ISSN: 2687 - 4539

CHAOS

THEORY AND APPLICATIONS

IN APPLIED SCIENCES AND ENGINEERING

Special Issue: Dissemination and Research in the Study of Complex Systems and their Applications (EDIESCA 2022)

VOLUME 4, ISSUE 4, DECEMBER 2022 (SPECIAL ISSUE)

AN INTERDISCIPLINARY JOURNAL OF NONLINEAR SCIENCE

ISSN: 2687 - 4539

CHAOS

THEORY AND APPLICATIONS

IN APPLIED SCIENCES AND ENGINEERING

Chaos Theory and Applications (CHTA)
Volume: 4 – Issue No: 4 (December 2022) - Special Issue (EDIESCA 2022)
https://dergipark.org.tr/en/pub/chaos/issue/73767

Editorial Advisory Board Members

Language Editors

Technical Coordinator

ISSN: 2687 - 4539

CHAOS

THEORY AND APPLICATIONS

IN APPLIED SCIENCES AND ENGINEERING

Chaos Theory and Applications (CHTA)
Volume: 4– Issue No:4(December2022) - Special Issue (EDIESCA 2022)
https://dergipark.org.tr/en/pub/chaos/issue/73767

Contents

CHAOS
Theory and Applications
in Applied Sciences and Engineering

e-ISSN: 2687-4539
RESEARCH ARTICLE
Vol.4 / No.4 / 2022 / pp.179-196
Special Issue (EDIESCA 2022)
https://doi.org/10.51537/chaos.1184952

Comparison Between Some Nonlinear Controllers for the Position Control of Lagrangian-type Robotic Systems

Sahar Jenhani [a,1], **Hassène Gritli** [a,b,2] **and Giuseppe Carbone** [c,3]

[a]Laboratory of Robotics, Informatics and Complex Systems (RISC Lab, LR16ES07), National Engineering School of Tunis, University of Tunis El Manar, BP. 37, Le Belvédère, 1002 Tunis, Tunisia, [b]Higher Institute of Information and Communication Technologies, University of Carthage, 1164 Borj Cedria, Tunis, Tunisia, [c]Department of Mechanical, Energy and Management Engineering, University of Calabria, Via Bucci Cubo 46C, 87036, Rende (Cs), Italy.

ABSTRACT This work addresses the set-point control problem of the position state of fully-actuated Lagrangian-type robotic systems by means of some nonlinear control laws. We adopt four different nonlinear control laws: the PD plus gravity compensation controller, the PD plus desired gravity compensation controller, the computed-torque controller and the augmented PD plus gravity compensation controller. An in-depth comparison between these control laws and their application is achieved. Indeed, using some properties, we design some conditions on the matrix feedback gains of the nonlinear controllers ensuring the stability in the closed loop of the zero-equilibrium point and its uniqueness. At the end of this paper, we adopt a planar two-degree-of-freedom robotic manipulator to illustrate via simulation the difference between and the efficiency of the adopted nonlinear controllers.

KEYWORDS
Lagrangian-type robotic systems
Nonlinear dynamics
Approximate linear model
Position feedback control
Nonlinear controllers
Stability
Stabilization
Solution uniqueness

INTRODUCTION

Robotics is a field of activity covering the study, design and manufacture of robots or automated machines (Koditschek 2021). Nowadays, robots are omnipresent in several sectors, and each robot is created and modified in such a way that it can perform certain desired tasks (Biswal and Mohanty 2021; Chai *et al.* 2021; da Costa Barros and Nascimento 2021; Gonzalez-Aguirre *et al.* 2021; González *et al.* 2021; Gualtieri *et al.* 2021; Tipary and Erdos 2021). Robotic systems have been introduced and employed in different fields such as the medical field for the rehabilitation of upper and lower limbs by building robotic-based orthosis, prosthetic leg robot and exoskeleton devices (Ahmed *et al.* 2021; Islam *et al.* 2020; Jafari *et al.* 2023; Kalita *et al.* 2021; Narayan and Dwivedy 2021; Tarnita *et al.* 2022; Wang *et al.* 2021). An historical overview of control theory applied to robotic manipulators and fundamental theoretical foundations of robot control were reported in (Spong 2022).

Manuscript received: 6 October 2022,
Revised: 27 October 2022,
Accepted: 28 October 2022.

[1]saharjenhani1@hotmail.com
[2]grhass@yahoo.fr (**Corresponding author**)
[3]giuseppe.carbone@unical.it

The different types of robotic systems can be subdivided into three main classes, depending on the degree number of their actuation (Choukchou-Braham *et al.* 2014; Gritli and Belghith 2021; Krafes *et al.* 2018; Liu and Yu 2013). The first class being the underactuated robotic systems Choukchou-Braham *et al.* (2014); Liu and Yu (2013); Zilong Zhang (2022). This type has less of actuators than the degrees of freedom (DoF), such as the acrobot, the pendubot and the inverted pendulum on a cart, and the inertia wheel inverted pendulum, just to mention a few (Choukchou-Braham *et al.* 2014; Gritli and Belghith 2018, 2021; Krafes *et al.* 2018; Liu and Yu 2013; Parulski *et al.* 2021, 11; Zilong Zhang 2022). The second class is called the fully-actuated robotic systems. In this class, the number of actuators in the robotic system is equal to the degrees of freedom (Li *et al.* 2020; Zhang and Wu 2021). Finally, the third class is the overactuated robotic systems, for which the number of control actuators is more than the number of degrees of freedom such as the over-actuated hexapod robot (Bjelonic *et al.* 2016).

In order to control these different types of mechanical systems, a suitable controller must be designed and hence applied. In the literature, as in (Abbas *et al.* 2021; Abdul-Adheem *et al.* 2021; Choukchou-Braham *et al.* 2014; Gritli 2020; Gu 2013; Kelly *et al.* 2005; Krafes *et al.* 2018; Kurdila and Ben-Tzvi 2019; Liu *et al.* 2020; Liu and Yu 2013; Mobayen *et al.* 2017; Perrusquia *et al.* 2020; Spong *et al.* 2020), we find different control techniques for robotic sys-

tems. These controllers can be subdivided into two main families: (1) the linear controllers such as the Proportional-Derivative (PD) control law, the Proportional-Integral-Derivative (PID) control law, the Linear Quadratic Regulator (LQR) control law, and the state-feedback control law (Chawla and Singla 2021; Kelly *et al.* 2005; Narayan and Dwivedy 2021; Singla and Singh 2017), and (2) the nonlinear controllers like the PD plus gravity compensation control law, the computed-torque control (CTC) law, the sliding mode control law, the PD plus desired gravity compensation control law, among others (Hasan and Dhingra 2021; Jiang *et al.* 2020; Kelly *et al.* 2005; Mobayen *et al.* 2017; Nho and Meckl 2003; Perrusquia *et al.* 2020). These several types of control laws have been proven to be applicable for settlement at desired configuration states (position control problem), i.e. to control and then stabilize the robotic system at some desired position/state, or for regulation to reference trajectories (tracking problem) i.e. to control the trajectory of the robot.

Recently, in (Gritli *et al.* 2022; Jenhani *et al.* 2022b,c), and using the developed approximate linear dynamic model, we proposed an affine PD-based control law in order to solve the position control problem of robotic systems. Indeed, in (Gritli *et al.* 2022; Jenhani *et al.* 2022b), the approximate linear dynamic was used to develop the conditions ensuring the stability of the closed-loop robotic system. Moreover, in (Jenhani *et al.* 2022b) we presented a comparison between the affine PD-based control law and the computed-torque control law. The numerical simulations demonstrated the efficiency and validity of the proposed affine PD-based control law. Some LMI stability conditions and improved ones for the stabilization of the controlled robotic system using the affine PD-based controller have been developed in (Jenhani *et al.* 2022f,g). Moreover, we performed in (Jenhani *et al.* 2022a) a comparison between this affine PD-based controller and the PD plus gravity compensation controller and also the PD plus desired gravity compensation controller. In addition, the control problem of underactuated robotic systems via the affine PD-based controller has been considered in (Jenhani *et al.* 2022d). Furthermore, in (Jenhani *et al.* 2022e), we applied an affine PID-based controller to control the Lagrangian robotic systems using the dynamical model which described the difference into the nonlinear dynamics and its approximated linear model.

In this research work, we will be interested in solving the position feedback control problem for fully-actuated Lagrangian-type robotic systems (Choukchou-Braham *et al.* 2014; Kelly *et al.* 2005; Spong *et al.* 2020). Thus, to control the robotic systems and then to ensure stability at the desired position, we will adopt four nonlinear control laws, namely the PD plus gravity compensation controller, the PD plus desired gravity compensation controller, the computed-torque controller, and the augmented PD plus gravity compensation controller. Additionally, we will construct conditions on the matrix feedback gains of these proposed control laws to ensure stabilization at the desired state. Moreover, for each case of control problem, we will develop the conditions on these matrix gains guaranteeing the uniqueness of the solution, that is the zero-equilibrium point of the closed-loop robotic system. Furthermore, a comparison between these controllers will be achieved. Finally, we will adopt a 2-DoF planar robotic manipulator as an illustrative robotic system, to check the validity of the developed conditions of stability and uniqueness of the zero-equilibrium state of the controlled Lagrangian-type robotic system, and hence the efficiency of the adopted nonlinear controllers.

The remaining and following sections of this article are organized like so. The second section presents the dynamic model of Lagrangian robotic systems and the problem considered in this research article. Some useful properties of the nonlinear dynamics of Lagrangian-type mechanical robot systems are given. The third section describes the design procedure of the matrix feedback gains of the PD plus gravity compensation controller. The fourth section is devoted to developing the stabilizing conditions on the feedback gain matrices of the PD plus desired gravity compensation control law. The fifth section presents the computed-torque controller and the condition on its matrix feedback gains. The design of certain conditions on the matrix gains of the augmented PD plus gravity compensation control law will be performed in the sixth section. The seventh section will be dedicated for the simulation results by introducing the 2-DoF manipulator robot. In the eighth section, a discussion about the obtained results and the efficiency of the proposed control laws is presented. Finally, at the end of this paper and in the last section, a conclusion and a future direction of this article will be drawn.

DYNAMIC MODEL OF LAGRANGIAN ROBOTIC SYSTEMS AND PROBLEM FORMULATION

Nonlinear Dynamics of Lagrangian-type Robotic Systems

In this present work, and for the reason of simplicity, we will ignore the presence of frictional and elastic forces, unmodeled dynamics, external disturbances, and structured and unstructured uncertainties in the nonlinear dynamics of Lagrangian-type mechanical robotic (or mechatronic) systems. Therefore, the dynamics of these robotic systems under such assumptions is given by the following nonlinear (and complex) expression:

$$\mathcal{M}(q)\ddot{q} + \mathcal{H}(q,\dot{q})\dot{q} + \mathcal{G}(q) = \mathcal{D}(q)\mathcal{U} \tag{1}$$

where in this previous model (1), we have the following notations:

- $q \in \mathbb{R}^{n\times 1}$ is the positions' vector of the different joints/articulations of the Lagrangian robotic system,
- $\dot{q} \in \mathbb{R}^{n\times 1}$ refers to the vector of corresponding velocities,
- $\ddot{q} \in \mathbb{R}^{n\times 1}$ is the vector of corresponding accelerations,
- $\mathcal{U} \in \mathbb{R}^{n\times 1}$ represents the input vector of available actuators applied to the Lagrangian robotic system,
- $\mathcal{M}(q) \in \mathbb{R}^{n\times n}$ represents the inertia matrix of the robot,
- $\mathcal{H}(q,\dot{q})\dot{q} \in \mathbb{R}^{n\times 1}$, where $\mathcal{H}(q) \in \mathbb{R}^{n\times n}$, is a vector containing two types of terms containing $\dot{q}_i\dot{q}_j$, which are called the centrifugal terms (for the cases $i = j$) and the Coriolis terms (for the cases $i \neq j$), for all $i, j = 1, \ldots, n$,
- $\mathcal{G}(q) \in \mathbb{R}^{n\times 1}$ stands for the gravity matrix of the robotic system, and
- $\mathcal{D}(q) \in \mathbb{R}^{n\times n}$ denotes the input matrix or the distribution matrix of all the actuators applied to the Lagrangian-type robotic system.

Remark 1 *It is worth to indicate that the nonlinear dynamic model (1) has been considered in some previous works, like (Krafes* et al. *2018; Liu* et al. *2020; Liu and Yu 2013). This general for the nonlinear dynamics (1) can model several types of robotic systems manipulator robots and wheeled mobile manipulator robots. Furthermore, in several works of the literature, the vector of control inputs, saying τ, in the dynamic model (1) was taken to be without the matrix $\mathcal{D}(q)$, and then $\tau = \mathcal{D}(q)\mathcal{U}$.*

Problem Formulation

Among the most important axes in the field of robotics research is the control of the robotic system to solve the stabilization problem. Such a stabilization problem can be classified into two main classes. The first is the problem of controlling the position of the robotic

system and then bringing it from its current configuration state to some desired one. The second stabilization problem is the trajectory/motion control, where the goal is to move the robot through control to a desired path/trajectory. Thus, to achieve these stabilization problems, we need to design a controller adapted and simple to apply in practice to the robot.

Our main objective in this article is to solve the position control problem of fully-actuated Lagrangian-type robotic systems. Then, our goal is to design an appropriate and simple controller $\mathcal{U}$ for the mechanical system where its (joint) motion is represented by its nonlinear dynamic model (1). Hence, the objective is to find and develop an expression of the nonlinear control law $\mathcal{U}$ that allows the robot to change its current configuration state q to a desired position state q_d. In this paper, we will adopt four nonlinear control laws: (i) the PD plus gravity compensation controller, (ii) the PD plus desired gravity compensation controller, (iii) the computed-torque control law, and (iv) the augmented PD plus gravity compensation controller.

Moreover, we will focus in this work on developing some feasible conditions to help in the right selection of the matrix feedback gains of the controllers ensuring the stabilization of the zero state, as the unique equilibrium, of the controlled Lagrangian robotic system. In addition, we will develop other conditions to guarantee the unicity of the zero origin as the unique possible equilibrium point of the controlled nonlinear dynamical system (1) of the Lagrangian robot systems.

In the sequel, let us consider $\phi = q - q_d$. Then, for the position control of the Lagrangian robot systems, and since q_d is constant, we have $\dot{\phi} = \dot{q}$ and hence $\ddot{\phi} = \ddot{q}$. Thus, the nonlinear dynamics' model (1) can be reformulated under the following equivalent nonlinear dynamic model:

$$\mathcal{M}(q)\ddot{\phi} + \mathcal{H}(q,\dot{\phi})\dot{\phi} + \mathcal{G}(q) = \mathcal{D}(q)\mathcal{U} \tag{2}$$

Such nonlinear system (2) represents the nonlinear dynamics of the position error of the Lagrangian-type robotic system. Thus, hereafter, we will use the nonlinear dynamic model (2) for the development of the proposed nonlinear control laws $\mathcal{U}$ too solve the set-point control problem of the position state of fully-actuated Lagrangian-type robot systems.

Useful Properties and Theorem

In this part, in order to develop some feasible conditions on the matrix gains of the nonlinear control laws to develop in the sequel, we present here some properties on the various matrices in the nonlinear dynamics (1) or the position error dynamics (2) of the robotic systems.

Useful Properties

We consider first the following useful properties (Jenhani *et al.* 2022a,c; Kelly *et al.* 2005).

Property 1 *In the nonlinear dynamic model (2), $\mathcal{M}(q)$ is such that:*

$$\mathcal{M}(q) = \mathcal{M}(q)^{\mathrm{T}} > 0, \qquad \forall\, q \in \mathbb{R}^n \tag{3}$$

Property 2 *For all vector $q \in \mathbb{R}^n$ and all vector $\dot{q} \in \mathbb{R}^n$, the inertia matrix $\mathcal{M}(q)$ and the matrix $\mathcal{H}(q,\dot{q})$ in (1) satisfy the following equality constraint:*

$$\xi^{\mathrm{T}}\left[\dot{\mathcal{M}}(q) - 2\mathcal{H}(q,\dot{q})\right]\xi = 0 \tag{4}$$

for all vector $\xi \in \mathbb{R}^n$.

Property 3 *For all vector $q \in \mathbb{R}^n$, the gravity matrix $\mathcal{G}(q)$ satisfies the following Lipschitz condition:*

$$\|\mathcal{G}(x) - \mathcal{G}(y)\| \leq k_g \|x - y\| \tag{5}$$

for all $x \in \mathbb{R}^n$ and $y \in \mathbb{R}^n$, and where k_g satisfies:

$$k_g \geq n \max_{i,j,q} \left| \frac{\partial \mathcal{G}_i(q)}{\partial q_j} \right| \tag{6}$$

or the following condition:

$$k_g \geq \lambda_{max}\left\{ \frac{\partial \mathcal{G}(q)}{\partial q} \right\} \tag{7}$$

where λ_{max} stands for the largest eigenvalue.

Contraction Mapping Theorem

In the sequel and in order to check the uniqueness of the zero solution of an equation constraint, we need to use the contraction map (Jenhani *et al.* 2022c; Kelly *et al.* 2005), which is introduced via the following theorem.

Theorem 1 (Contraction Map (Jenhani *et al.* 2022c)) *Consider $\Psi \subset \mathbb{R}^m$, a parameters' vector $\Theta \in \Psi$ and the continuous nonlinear function $F : \mathbb{R}^n \times \Psi \to \mathbb{R}^n$.*

Suppose that there is a constant scalar $\gamma > 0$ such that for all vectors $x \in \mathbb{R}^n$ and $y \in \mathbb{R}^n$, and all vector $\Theta \in \Psi$, we obtain:

$$\|F(x,\Theta) - F(y,\Theta)\| \leq \gamma \|x - y\| \tag{8}$$

If the constant scalar γ is such that the following condition is well verified:

$$\gamma < 1 \tag{9}$$

then, for all vector $\Theta^\star \in \Psi$, the nonlinear function $F(z,\Theta^\star)$ has only one and unique fixed point $z^\star \in \mathbb{R}^n$, satisfying this expression:

$$F(z^\star,\Theta^\star) = z^\star \tag{10}$$

DESIGN OF THE PD PLUS GRAVITY COMPENSATION CONTROL LAW

In this present section, we will consider the first nonlinear control law, namely the PD plus gravity compensation controller, to control the Lagrangian-type robotic system by its own nonlinear dynamics (1) or (2), in order to control it to and hence stabilize it at the desired position vector q_d.

The Nonlinear PD Plus Gravity Compensation Controller

Let us consider the following nonlinear PD plus gravity compensation control law:

$$\mathcal{U} = \mathcal{D}^{-1}(q)(\mathcal{G}(q) + \mathcal{K}_p\phi + \mathcal{K}_v\dot{\phi}) \tag{11}$$

where $\mathcal{K}_p$ and $\mathcal{K}_v$ stand for the two matrix feedback gains of the nonlinear controller (11), that need to be produced in this part. Moreover, notice that $\mathcal{K}_p \in \mathbb{R}^{n\times n}$ and $\mathcal{K}_v \in \mathbb{R}^{n\times n}$.

Therefore, our main objective is to develop some feasible constraints on the two feedback gain matrices $\mathcal{K}_p$ and $\mathcal{K}_v$ of the adopted nonlinear control law (11) ensuring the stability of the zero state of the nonlinear dynamics (2) of the position state error of the Lagrangian robotic systems.

Conditions on the Feedback Gains

The nonlinear dynamic model (2) of the Lagrangian robot systems under the proposed nonlinear controller (11), and hence in the closed loop, is reformulated like so:

$$\mathcal{M}(q)\ddot{\phi} + \mathcal{H}(q,\dot{\phi})\dot{\phi} - \mathcal{K}_p\phi - \mathcal{K}_v\dot{\phi} = 0 \tag{12}$$

Then, in order to design and establish some possible conditions on the two matrix gains that ensure the control to and hence the stabilization of the closed-loop robotic system at the desired configuration state q_d, let us propose the following nonlinear Lyapunov function:

$$\mathcal{V}(\phi,\dot{\phi}) = \frac{1}{2}\dot{\phi}^{\mathrm{T}}\mathcal{M}(q)\dot{\phi} - \frac{1}{2}\phi^{\mathrm{T}}\mathcal{K}_p\phi \tag{13}$$

Notice that since the matrix $\mathcal{M}(q)$ satisfies the Property 1, and by considering the following condition on the feedback gain $\mathcal{K}_p$:

$$\mathcal{K}_p = \mathcal{K}_p^T < 0 \tag{14}$$

it stands as a result that $\mathcal{V}(\phi,\dot{\phi}) > 0$.

The derivative the adopted candidate Lyapunov function (13) is described as follows:

$$\begin{aligned}\dot{\mathcal{V}}(\phi,\dot{\phi}) =& \frac{1}{2}\ddot{\phi}^{\mathrm{T}}\mathcal{M}(q)\dot{\phi} + \frac{1}{2}\dot{\phi}^{\mathrm{T}}\dot{\mathcal{M}}(q)\dot{\phi} \\ &+ \frac{1}{2}\dot{\phi}^{\mathrm{T}}\mathcal{M}(q)\ddot{\phi} - \frac{1}{2}\dot{\phi}^{\mathrm{T}}\mathcal{K}_p\phi - \frac{1}{2}\phi^{\mathrm{T}}\mathcal{K}_p\dot{\phi}\end{aligned} \tag{15}$$

As $\mathcal{M}(q) = \mathcal{M}^{\mathrm{T}}(q)$ (according to Property 1) and $\mathcal{K}_p = \mathcal{K}_p^T$, then expression (15) is simplified as follows:

$$\dot{\mathcal{V}}(\phi,\dot{\phi}) = \frac{1}{2}\dot{\phi}^{\mathrm{T}}\dot{\mathcal{M}}(q)\dot{\phi} + \dot{\phi}^{\mathrm{T}}\mathcal{M}(q)\ddot{\phi} - \dot{\phi}^{\mathrm{T}}\mathcal{K}_p\phi \tag{16}$$

Additionally, by solving for $\mathcal{M}\ddot{q}$ in the closed-loop dynamic model (12) and substituting it in (16), it follows that:

$$\dot{\mathcal{V}}(\phi,\dot{\phi}) = \frac{1}{2}\dot{\phi}^{\mathrm{T}}\dot{\mathcal{M}}(q)\dot{\phi} - \dot{\phi}^{\mathrm{T}}\mathcal{H}(q,\dot{\phi})\dot{\phi} + \dot{\phi}^{\mathrm{T}}\mathcal{K}_v\dot{\phi} \tag{17}$$

Moreover, by taking into consideration Property 2, and then relation (4), it follows from (17) that $\frac{1}{2}\dot{\phi}^{\mathrm{T}}\mathcal{M}(q)\dot{\phi} - \dot{\phi}^{\mathrm{T}}\mathcal{H}(q,\dot{\phi})\dot{\phi} = 0$.

Thus, the expression (17) of the derivative of the Lyapunov function can be simplified as follows:

$$\dot{\mathcal{V}}(\phi,\dot{\phi}) = \dot{\phi}^{\mathrm{T}}\mathcal{K}_v\dot{\phi} \tag{18}$$

Therefore, to guarantee the stabilization of the zero point of the position state error dynamics model (12), we should ensure that $\dot{\mathcal{V}}(\phi,\dot{\phi}) < 0$. Hence, the matrix gain $\mathcal{K}_v$ must satisfy this condition:

$$\mathcal{K}_v = \mathcal{K}_v^T < 0 \tag{19}$$

Condition Ensuring Equilibrium Unicity

The equilibrium state must satisfy the following conditions $\ddot{\phi} = 0$ and $\dot{\phi} = 0$. Then, the expression (12) becomes:

$$\mathcal{K}_p\phi = 0 \tag{20}$$

According to condition (14), it follows that $\mathrm{rank}(\mathcal{K}_p) = n$. Then, the only solution of the equality (20) is $\phi = 0$, and then it follows that the position vector $q = q_d$ is the unique admissible solution of the condition (20). Thus, the designed conditions (14) and (19) on the two matrix gains $\mathcal{K}_p$ and $\mathcal{K}_v$, respectively, ensure the stabilization (and hence stability) of the robotic system under the proposed PD plus gravity compensation controller (11) at the desired position vector q_d.

Final Stabilization Conditions

Based on inequalities (14) and (19), and in order to ensure the control and therefore the stabilization of the Lagrangian robotic system, we developed the following conditions on the two gain matrices of the adopted nonlinear PD plus gravity compensation control law (20):

$$\mathcal{K}_p = \mathcal{K}_p^T < 0 \tag{21a}$$

$$\mathcal{K}_v = \mathcal{K}_v^T < 0 \tag{21b}$$

DESIGN OF THE PD PLUS DESIRED GRAVITY COMPENSATION CONTROL LAW

This part is dedicated to present a different and simple controller, namely the PD plus desired gravity compensation controller. As before, our main objective is to develop conditions on the two matrix feedback gains of the proposed control law achieving the control of the Lagrangian robot system and therefore its stabilization at the desired state q_d.

The PD Plus Desired Gravity Compensation Controller

In order to stabilize the dynamical system (2), we will consider the following nonlinear PD plus desired gravity compensation control law:

$$\mathcal{U} = \mathcal{D}(q)^{-1}(\mathcal{G}(q_d) + \mathcal{K}_p\phi + \mathcal{K}_v\dot{\phi}) \tag{22}$$

where $\mathcal{K}_p$ and $\mathcal{K}_v$ are the two matrix feedback gains to design in the sequel.

It is obvious that compared to the control law (11), the gravity matrix $\mathcal{G}(q)$ is here constant in the adopted controller (22) and is evaluated at the desired position q_d and therefore equal to the quantity $\mathcal{G}(q_d)$. Notice that expression of the controller (22) is simpler than expression (11). Indeed, the controller (11) is more complex than (22) in realization in practice since it needs much time to be computed because of the gravity matrix $\mathcal{G}(q)$ that takes more time to be calculated at each iteration, or at each computation and application of the controller $\mathcal{U}$ via expression (11). However, in (22), we only need the computation of the matrix $\mathcal{D}(q)$.

We will focus now on designing the conditions on the matrix feedback gains $\mathcal{K}_p$ and $\mathcal{K}_v$ of the nonlinear control law (22) to ensure the control to and consequently the stabilization of the zero-equilibrium point of the position error dynamics (2) under such control law (22), and then guarantee the control/stabilization of the Lagrangian robot system to/at the desired position state q_d.

Conditions on the Feedback Gains

The nonlinear dynamics (2) under the PD plus desired gravity compensation control law $\mathcal{U}$ expressed by (22) is given as follows:

$$\mathcal{M}(q)\ddot{\phi} + \mathcal{H}(q,\dot{\phi})\dot{\phi} + \mathcal{G}(q) - \mathcal{G}(q_d) - \mathcal{K}_p\phi - \mathcal{K}_v\dot{\phi} = 0 \tag{23}$$

To determinate the stability conditions of the controlled system (22), we consider the following candidate Lyapunov function:

$$\begin{aligned}\mathcal{V}(\phi,\dot{\phi}) =& \frac{1}{2}\dot{\phi}^{\mathrm{T}}\mathcal{M}(q)\dot{\phi} + \mathcal{P}_e(q) - k_u - \frac{1}{2}\phi^{\mathrm{T}}\mathcal{K}_p\phi \\ &- \phi^{\mathrm{T}}\mathcal{G}(q_d) - \frac{1}{2}\mathcal{G}(q_d)^{\mathrm{T}}\mathcal{K}_p^{-1}\mathcal{G}(q_d)\end{aligned} \tag{24}$$

where $\mathcal{P}_e(q)$ defines the potential energy. Such quantity $\mathcal{P}_e(q)$ is linked to the gravity vector $\mathcal{G}(q)$ like so:

$$\mathcal{G}(q) = \frac{\partial \mathcal{P}_e(q)}{\partial q} \tag{25}$$

Moreover, the parameter k_u in (24) is defined like so:

$$k_u = \min_q \{\mathcal{P}_e(q)\} \tag{26}$$

Accordingly, from (24) it follows that:

$$\mathcal{P}_e(q) - k_u \geq 0 \tag{27}$$

Moreover, it is straightforward to demonstrate that:

$$\frac{1}{2}\phi^{\mathrm{T}}\mathcal{K}_p\phi + \phi^{\mathrm{T}}\mathcal{G}(q_d) + \frac{1}{2}\mathcal{G}(q_d)^{\mathrm{T}}\mathcal{K}_p^{-1}\mathcal{G}(q_d) = \frac{1}{2}\begin{bmatrix} \phi \\ \mathcal{G}(q_d) \end{bmatrix}^{\mathrm{T}} \begin{bmatrix} \mathcal{K}_p & \mathcal{I} \\ \mathcal{I} & \mathcal{K}_p^{-1} \end{bmatrix} \begin{bmatrix} \phi \\ \mathcal{G}(q_d) \end{bmatrix} \tag{28}$$

By taking the following condition on the feedback gain matrix $\mathcal{K}_p$:

$$\mathcal{K}_p = \mathcal{K}_p^T < 0 \tag{29}$$

it is easy to demonstrate, based on the Schur complement lemma (Gritli and Belghith 2018; Turki *et al.* 2020), that

$$\begin{bmatrix} \mathcal{K}_p & \mathcal{I} \\ \mathcal{I} & \mathcal{K}_p^{-1} \end{bmatrix} \leq 0 \tag{30}$$

Therefore, based on inequality (28), it follows that:

$$\frac{1}{2}\phi^{\mathrm{T}}\mathcal{K}_p\phi + \phi^{\mathrm{T}}\mathcal{G}(q_d) + \frac{1}{2}\mathcal{G}(q_d)^{\mathrm{T}}\mathcal{K}_p^{-1}\mathcal{G}(q_d) \leq 0 \tag{31}$$

Moreover, since $\mathcal{M}(q) = \mathcal{M}(q)^{\mathrm{T}} > 0$ (according to Property 1), and relying on conditions (27) and (31), we demonstrate that the adopted candidate Lyapunov function (24) is positive, and hence we ensure that: $\mathcal{V}(\phi, \dot{\phi}) > 0$.

Based on relation (25), the derivative of the candidate Lyapunov function (24) can be formulated as follows:

$$\begin{aligned}\dot{\mathcal{V}}(\phi, \dot{\phi}) =& \frac{1}{2}\dot{\phi}^{\mathrm{T}}\dot{\mathcal{M}}(q)\dot{\phi} + \dot{\phi}^{\mathrm{T}}\mathcal{M}(q)\ddot{\phi} \\ &+ \dot{\phi}^{\mathrm{T}}\mathcal{G}(q) - \phi^{\mathrm{T}}\mathcal{K}_p\dot{\phi} - \dot{\phi}^{\mathrm{T}}\mathcal{G}(q_d)\end{aligned} \tag{32}$$

From the dynamics (23), we can write the following relation:

$$\mathcal{M}(q)\ddot{\phi} = -\mathcal{H}(q, \dot{\phi})\dot{\phi} - \mathcal{G}(q) + \mathcal{G}(q_d) + \mathcal{K}_p\phi + \mathcal{K}_v\dot{\phi} \tag{33}$$

By replacing this last quantity $\mathcal{M}(q)\ddot{\phi}$ in expression (32), we obtain:

$$\begin{aligned}\dot{\mathcal{V}}(\phi, \dot{\phi}) =& \frac{1}{2}\dot{\phi}^{\mathrm{T}}\dot{\mathcal{M}}(q)\dot{\phi} - \dot{\phi}^{\mathrm{T}}\mathcal{H}(q, \dot{\phi})\dot{\phi} + \dot{\phi}^{\mathrm{T}}\left(\mathcal{G}(q_d) - \mathcal{G}(q)\right) \\ &+ \dot{\phi}^{\mathrm{T}}\mathcal{K}_p\phi + \dot{\phi}^{\mathrm{T}}\mathcal{K}_v\dot{\phi} + \dot{\phi}^{\mathrm{T}}\mathcal{G}(q) \\ &- \phi^{\mathrm{T}}\mathcal{K}_p\dot{\phi} - \dot{\phi}^{\mathrm{T}}\mathcal{G}(q_d)\end{aligned} \tag{34}$$

This previous expression can be simplified as follows:

$$\dot{\mathcal{V}}(\phi, \dot{\phi}) = \frac{1}{2}\dot{\phi}^{\mathrm{T}}\dot{\mathcal{M}}(q)\dot{\phi} - \dot{\phi}^{\mathrm{T}}\mathcal{H}(q, \dot{\phi})\dot{\phi} + \dot{\phi}^{\mathrm{T}}\mathcal{K}_v\dot{\phi} \tag{35}$$

By virtue of Property 2, the previous function is simplified and equal to:

$$\dot{\mathcal{V}}(\phi, \dot{\phi}) = \dot{\phi}^{\mathrm{T}}\mathcal{K}_v\dot{\phi} \tag{36}$$

Therefore, to guarantee the stabilization of the zero-equilibrium point of the position error dynamic model (23), the following condition must be satisfied:

$$\mathcal{K}_v = \mathcal{K}_v^T < 0 \tag{37}$$

Condition Ensuring Equilibrium Unicity

Note that at the equilibrium state, we have $\dot{\phi} = 0$ and $\ddot{\phi} = 0$. Then, relation (23) can be rewritten and therefore simplified as follows:

$$\mathcal{G}(q) - \mathcal{G}(q_d) - \mathcal{K}_p\phi = 0 \tag{38}$$

Since the gain matrix $\mathcal{K}_p$ satisfies the condition (29), it is then a non-singular matrix. Hence, we can write from (38) the following relation/condition:

$$\phi = \mathcal{K}_p^{-1}(\mathcal{G}(q) - \mathcal{G}(q_d)) \tag{39}$$

It is straightforward to demonstrate that $\phi = q - q_d = 0$ is a solution of the condition (39). Nevertheless, such solution is not the only one of the constraint (39). This equation (39) can generate other solutions. Then, as the condition (39) depends on the feedback gain $\mathcal{K}_p$, our main goal is to develop a condition on such matrix feedback gain $\mathcal{K}_p$ guaranteeing the equilibrium unicity, that is $\phi = 0$. Then, to achieve this objective, we should refer to the contracting mapping presented in Theorem 1.

Consider the following nonlinear function:

$$F(\phi, q_d) = \mathcal{K}_p^{-1}(\mathcal{G}(q) - \mathcal{G}(q_d)) \tag{40}$$

Then, relying on (8), our main objective is to search for some condition on the parameter γ, with $\gamma < 1$, satisfying the following constraint:

$$\|F(\phi_2, q_d) - F(\phi_1, q_d)\| \leq \gamma \|\phi_2 - \phi_1\| \tag{41}$$

Using equation (40), we can write the following expression:

$$F(\phi_2, q_d) - F(\phi_1, q_d) = \mathcal{K}_p^{-1}(\mathcal{G}(\phi_2) - \mathcal{G}(\phi_1)) \tag{42}$$

and therefore, we obtain:

$$\|F(\phi_2, q_d) - F(\phi_1, q_d)\| = \left\|\mathcal{K}_p^{-1}(\mathcal{G}(\phi_2) - \mathcal{G}(\phi_1))\right\| \tag{43}$$

Moreover, it is evident that:

$$\left\|\mathcal{K}_p^{-1}(\mathcal{G}(\phi_2) - \mathcal{G}(\phi_1))\right\| \leq \left\|\mathcal{K}_p^{-1}\right\| \times \|\mathcal{G}(\phi_2) - \mathcal{G}(\phi_1)\| \tag{44}$$

By taking into account the condition (29) on $\mathcal{K}_p$, inequality (44) is recast as follows:

$$\left\|\mathcal{K}_p^{-1}(\mathcal{G}(\phi_2) - \mathcal{G}(\phi_1))\right\| \leq \lambda_{\max}(-\mathcal{K}_p^{-1}) \|\mathcal{G}(\phi_2) - \mathcal{G}(\phi_1)\| \tag{45}$$

Since

$$\lambda_{\max}(-\mathcal{K}_p^{-1}) = \frac{1}{\lambda_{\min}(-\mathcal{K}_p)} \tag{46}$$

it follows that the inequality condition (45) is reformulated as follows:

$$\left\|\mathcal{K}_p^{-1}(\mathcal{G}(\phi_2) - \mathcal{G}(\phi_1))\right\| \leq \frac{1}{\lambda_{\min}(-\mathcal{K}_p)} \|\mathcal{G}(\phi_2) - \mathcal{G}(\phi_1)\| \tag{47}$$

By considering Property 3 on the gravity matrix $\mathcal{G}(q)$, we get the following expression:

$$\left\|\mathcal{K}_p^{-1}(\mathcal{G}(q) - \mathcal{G}(q_d))\right\| \leq \frac{k_g}{\lambda_{\min}(-\mathcal{K}_p)} \|\phi_2 - \phi_1\| \tag{48}$$

where k_g is determined by means of the condition (6).

Hence, relying on expression (43), it follows that:

$$\|F(\phi_2, q_d) - F(\phi_1, q_d)\| \leq \frac{k_g}{\lambda_{\min}(-\mathcal{K}_p)} \|\phi_2 - \phi_1\| \tag{49}$$

By comparing to condition (41), we can deduce that

$$\gamma = \frac{k_g}{\lambda_{\min}(-\mathcal{K}_p)} \tag{50}$$

Accordingly, by taking into account expressions (39) and (40), and in order to guarantee that the zero state $\phi = 0$ is the unique solution of the following relation:

$$\phi = F(\phi, q_d) \tag{51}$$

the following condition (since $\gamma < 1$) must be satisfied:

$$\frac{k_g}{\lambda_{\min}(-\mathcal{K}_p)} < 1 \tag{52}$$

This previous condition (52) can be rewritten like so:

$$\lambda_{\max}(\mathcal{K}_p) < -k_g \tag{53}$$

Final Stabilization Conditions

Finally, relying on constraints (29), (37) and (53), the conditions on the two matrix feedback gains of the adopted control law (20), that is the PD plus desired gravity compensation controller, guaranteeing the control to and hence the stabilization of the Lagrangian-type robot at the point q_d, are reformulated like so:

$$\mathcal{K}_p = \mathcal{K}_p^T < -k_g\, \mathcal{I}_n \tag{54a}$$

$$\mathcal{K}_v = \mathcal{K}_v^T < 0 \tag{54b}$$

where here in (54a) and in the sequel, $\mathcal{I}_n$ stands for the identity matrix with dimension $(n \times n)$.

Moreover, recall that the constant k_g in (54a) should be computed according to expression (6) or expression (7).

DESIGN OF THE COMPUTED-TORQUE CONTROL LAW

In this part, to control the Lagrangian robot system via its nonlinear dynamics (1) to the desired point q_d, we will adopt a computed-torque controller. Thus, our goal in this present section is to design some possible and realizable conditions on the two gain matrices $\mathcal{K}_p$ and $\mathcal{K}_v$ of such controller guaranteeing the stabilization of the zero-equilibrium state $\phi = 0$ of the position error dynamics (2).

The Computed-Torque Controller

The expression of the proposed computed-torque control law has the following form:

$$\mathcal{U} = \mathcal{D}^{-1}(q)(\mathcal{M}(q)v + \mathcal{H}(q,\dot{\phi})\dot{\phi} + \mathcal{G}(q)) \tag{55}$$

where the input v is given by:

$$v = \mathcal{K}_p\phi + \mathcal{K}_v\dot{\phi} \tag{56}$$

Next, we will determinate some feasible conditions on the two gain matrices of the proposed control law $\mathcal{U}$ defined by (55) and (56) in order to achieve the stabilization of the Lagrangian-type robot system under control.

Conditions on the Feedback Gains

Under the adopted computed-torque controller $\mathcal{U}$ defined in (55)-(56), the nonlinear dynamic model (2) of the Lagrangian robot system becomes like so:

$$\mathcal{M}(q)\ddot{\phi} = \mathcal{M}(q)(\mathcal{K}_p\phi + \mathcal{K}_v\dot{\phi}) \tag{57}$$

Based on Property 1, expression (57) becomes:

$$\ddot{\phi} - \mathcal{K}_v\dot{\phi} - \mathcal{K}_p\phi = 0 \tag{58}$$

First design approach of stability conditions

To look for stability conditions of the zero state (defined by $\phi = 0$ and $\dot{\phi} = 0$) of this previous linear system (58), we take a such candidate Lyapunov function defined as follows:

$$\mathcal{V}(\phi,\dot{\phi}) = \frac{1}{2}\dot{\phi}^{\mathrm{T}}\dot{\phi} - \frac{1}{2}\phi^{\mathrm{T}}\mathcal{K}_p\phi \tag{59}$$

It is clear that if we take the following condition:

$$\mathcal{K}_p = \mathcal{K}_p^T < 0 \tag{60}$$

then, the Lyapunov function (59) is positive.

The derivative with respect to time of the Lyapunov function (59) is formulated like so:

$$\dot{\mathcal{V}}(\phi,\dot{\phi}) = \dot{\phi}^{\mathrm{T}}\ddot{\phi} - \phi^{\mathrm{T}}\mathcal{K}_p\dot{\phi} \tag{61}$$

Using the linear dynamics (58) in expression (61), we obtain then:

$$\dot{\mathcal{V}}(\phi,\dot{\phi}) = \dot{\phi}^{\mathrm{T}}\mathcal{K}_v\dot{\phi} \tag{62}$$

Thus, by taking the following condition on the matrix gain $\mathcal{K}_v$:

$$\mathcal{K}_v = \mathcal{K}_v^T < 0 \tag{63}$$

we obtain then $\dot{\mathcal{V}}(\phi,\dot{\phi}) < 0$.

Therefore, the two conditions guaranteeing the stabilization of the zero state of the linear dynamic model (58) are defined like so:

$$\mathcal{K}_p = \mathcal{K}_p^T < 0 \tag{64a}$$

$$\mathcal{K}_v = \mathcal{K}_v^T < 0 \tag{64b}$$

Second design approach of the stability conditions

In the sequel, we look for designing other conditions on the two feedback gain matrices of the computed-torque controller (55)-(56). Thus, let us consider a decoupled controlled linear dynamics (58) and then the gain matrices $\mathcal{K}_p$ and $\mathcal{K}_v$ are diagonal. Moreover, we impose the desired poles of the controlled system (58). Then, our main objective here is to find conditions on theses two gain matrices ensuring the stabilization of the controlled Lagrangian robot system by imposing some desired motion (defined with respect to the desired poles) of a decoupled stable linear system. Then, suppose that all the position variables, q_i with $i = 1, \cdots, n$, of the Lagrangian-type robot system under the proposed computed-torque control law and then of the linear dynamics (58) are completely decoupled and therefore the desired closed-loop linear dynamics of the position q_i is like so:

$$\ddot{\phi}_i - (p_{1i} + p_{2i})\,\dot{\phi}_i + (p_{1i} \times p_{2i})\,\phi_i = 0 \tag{65}$$

where in the previous model, $\phi_i = q_i - (q_d)_i$, and the two parameters p_{1i} and p_{2i} denote together the desired poles of the controlled robotic system.

It is worth to note that the two poles p_{1i} and p_{2i} should be with negative real parts in order to have a stable linear dynamical system (65). In the case they are complex, they should be imperatively complex conjugate.

Relying on (65), the desired decoupled dynamics of the controlled robotic system defined by such linear reference model given as follows:

$$\ddot{\phi} + \Omega_v\dot{\phi} + \Omega_p\phi = 0 \tag{66}$$

where the matrices Ω_v and Ω_p are diagonal and positive definite ($\Omega_v > 0$ and $\Omega_p > 0$). They are defined like so:

$$\Omega_p = \text{diag}\,(p_{11} \times p_{21}, p_{12} \times p_{22}, \cdots, p_{1n} \times p_{2n}) \tag{67a}$$

$$\Omega_v = -\text{diag}\,(p_{11} + p_{21}, p_{12} + p_{22}, \cdots, p_{1n} + p_{2n}) \tag{67b}$$

Then, in order to obtain an appropriate choice of Ω_v and Ω_p, the two poles p_{1i} and p_{2i} are adopted to be entirely real. Moreover, we impose that $p_{1i} = p_{2i} = -w_i$, where here the parameter w_i is such that $w_i > 0$, and it denotes the desired natural frequency of the subsystem.

Comparing the closed-loop system (58) with that defined by (66), the two feedback gains are then defined as follows:

$$\mathcal{K}_p = -\Omega_p \tag{68a}$$

$$\mathcal{K}_v = -\Omega_v \tag{68b}$$

Recall here that the two matrix gains $\mathcal{K}_p$ and $\mathcal{K}_v$ are diagonal matrices.

Condition Ensuring Equilibrium Unicity

As previously, at the equilibrium state, we have $\dot{\phi} = 0$ and $\ddot{\phi} = 0$. Then, the controlled dynamics defined by (58) can be simplified as follows:

$$\mathcal{K}_p \phi = 0 \tag{69}$$

Since $\Omega_p > 0$, then according to (68a), it follows that $\mathcal{K}_p < 0$ and then $\text{rank}(\mathcal{K}_p) = n$. Notice that the condition $\mathcal{K}_p < 0$ was already determined in (64a), where $\mathcal{K}_p$ is not diagonal. However, by adopting the desired closed-loop decouple dynamics, the gain matrix $\mathcal{K}_p$ is diagonal. Hence, since $\text{rank}(\mathcal{K}_p) = n$, it follows that the state $\phi = 0$ is the only possible solution of the constraint (69).

Final Stabilization Conditions

In the previous development of the conditions on the two matrix feedback gains $\mathcal{K}_p$ and $\mathcal{K}_v$ of the computed-torque controller (55)-(56), we adopted two approaches. In the first approach using the Lyapunov method, we developed the two conditions (64a) and (64b) on $\mathcal{K}_p$ and $\mathcal{K}_v$, which are not diagonal matrices. Therefore, by taking into account the results achieved to check the unicity of the zero equilibrium, these two conditions (64a) and (64b) on the two matrix feedback gains $\mathcal{K}_p$ and $\mathcal{K}_v$ induce the stabilization of the Lagrangian robot system under the computed-torque controller (55)-(56), at the desired position q_d.

However, by adopting a different design approach by imposing a desired decoupled linear dynamics in the closed loop, we developed the two conditions/expressions (68a) and (68b) on the feedback gains $\mathcal{K}_p$ and $\mathcal{K}_v$. Thus, relying on expressions in (67), and by taking $p_{1i} = p_{2i} = -w_i$, with $w_i > 0$ for all $i = 1, 2, \ldots, n$, the two expressions of $\mathcal{K}_p$ and $\mathcal{K}_v$ are formulated as follows:

$$\mathcal{K}_v = -2\,\text{diag}\,(w_1, w_2, \cdots, w_n) \tag{70a}$$

$$\mathcal{K}_p = -\text{diag}\left(w_1^2, w_2^2, \cdots, w_n^2\right) \tag{70b}$$

Accordingly, by selecting positive values of the parameters w_1, $w_2, \cdots, w_n$, the two conditions on the matrix feedback gains $\mathcal{K}_p$ and $\mathcal{K}_v$ defined by (70a) and (70b) ensure the stabilization of the Lagrangian robot system under the computed-torque controller (55) at the desired state q_d.

DESIGN OF THE AUGMENTED PD PLUS GRAVITY COMPENSATION CONTROL LAW

In this present section, we will propose a different controller, namely the PD$^+$ controller or the augmented PD plus gravity compensation control law, to achieve the stabilization of Lagrangian-type robotic systems at the desired position vector q_d. Such augmented control law depends chiefly on the PD plus gravity compensation control law (11). Thus, as in the previous sections, our goal is to build some practicable conditions on the two matrix gains of the augmented control law to ensure the control/stabilization of the Lagrangian robotic system, modeled by its nonlinear dynamic model (1), to/at the desired point q_d.

The Augmented PD Plus Gravity Compensation Controller

The augmented PD plus gravity compensation control law (or simply the PD$^+$ controller) is defined:

$$\begin{aligned}\mathcal{U} =& \mathcal{D}^{-1}(q)\left(\mathcal{G}(q) + \mathcal{K}_p\phi + \mathcal{K}_v\dot{\phi}\right) \\ & - \mathcal{D}^{-1}(q)\left(\mathcal{M}(q)\Omega\dot{\phi} + \mathcal{H}(q,\dot{\phi})\Omega\phi\right)\end{aligned} \tag{71}$$

where the matrix Ω is given as follows:

$$\Omega = \mathcal{K}_v^{-1}\mathcal{K}_p \tag{72}$$

with $\mathcal{K}_p$ and $\mathcal{K}_v$ are the two matrix gains to determine in the sequel.

It is obvious that the control law (71) contains the part of the PD plus gravity compensation controller (11). Such part is the first line in the expression (71). The second line in (71) is the augmented part in the controller and aims at improving the stabilization process of the robotic system.

Then, our objective in the following is to design the conditions on the gain matrices $\mathcal{K}_p$ and $\mathcal{K}_v$ guaranteeing the stabilization of the Lagrangian robotic system under the proposed controller (71) at the desired state q_d.

Condition on the Feedback Gains

By considering and applying the adopted augmented PD plus gravity compensation control law (71), the nonlinear dynamics (2) becomes:

$$\mathcal{M}(q)\ddot{\phi} + \mathcal{H}(q,\dot{\phi})\dot{\phi} = \mathcal{K}_p\phi + \mathcal{K}_v\dot{\phi} - \mathcal{M}(q)\Omega\dot{\phi} - \mathcal{H}(q,\dot{\phi})\Omega\phi \tag{73}$$

This expression (73) of the closed-loop nonlinear dynamics can be rearranged and simplified as follows:

$$\mathcal{M}(q)(\ddot{\phi} + \Omega\dot{\phi}) + \mathcal{H}(q,\dot{\phi})(\dot{\phi} + \Omega\phi) - \mathcal{K}_v(\dot{\phi} + \Omega\phi) = 0 \tag{74}$$

We emphasize that the equilibrium point of the closed-loop system (74) is $\phi = 0$, with $\dot{\phi} = 0$ and $\dot{\phi} = 0$. The proof will be provided in the next section.

Posing in the sequel

$$\psi = \dot{\phi} + \Omega\phi \tag{75}$$

Then, $\psi = 0$ defines the new equilibrium state. Therefore, using this previous variable change, expression (74) can be written like this:

$$\mathcal{M}(q)\dot{\psi} + (\mathcal{H}(q,\dot{\phi}) - \mathcal{K}_v)\psi = 0 \tag{76}$$

Thus, let us adopt a such candidate Lyapunov function defined as follows:

$$\mathcal{V}(\psi) = \frac{1}{2}\psi^{\mathrm{T}}\mathcal{M}(q)\psi \tag{77}$$

The derivative with respect to time of the adopted candidate Lyapunov function (77) is expressed like so:

$$\dot{\mathcal{V}}(\psi) = \psi^{\mathrm{T}}\mathcal{M}(q)\dot{\psi} + \frac{1}{2}\psi^{\mathrm{T}}\dot{\mathcal{M}}(q)\psi \tag{78}$$

Moreover, by solving $\mathcal{M}\dot{\psi}$ in the closed-loop dynamic model (76) and substituting it into (78), we obtain:

$$\dot{\mathcal{V}}(\psi) = \psi^{\mathrm{T}}\mathcal{K}_v\psi + \psi^{\mathrm{T}}\left(\frac{1}{2}\dot{\mathcal{M}}(q) - \mathcal{H}(q,\dot{\phi})\right)\psi \tag{79}$$

Furthermore, based on Property 2, it follows that expression (79) is simplified like so:

$$\dot{\mathcal{V}}(\psi) = \psi^{\mathrm{T}}\mathcal{K}_v\psi \tag{80}$$

Therefore, to ensure the stability of the transformed closed-loop nonlinear system (76) at the zero-equilibrium point $\psi = 0$, we should have $\dot{\mathcal{V}}(\psi) < 0$, and the following condition on the matrix feedback gain $\mathcal{K}_v$ must be verified:

$$\mathcal{K}_v = \mathcal{K}_v^T < 0 \tag{81}$$

Moreover, since $\psi = \dot{\phi} + \Omega\phi$, and as $\psi = 0$ is the stable equilibrium point of the dynamic model (76), it follows then that the state ϕ evolves with respect to the following linear dynamics:

$$\dot{\phi} + \Omega\phi = 0 \tag{82}$$

The clear condition for the stabilization of the zero equilibrium, $\phi = 0$, is that $\Omega > 0$. Therefore, as the matrix Ω is defined by expression (72) and by taking into account the condition (81) on the gain $\mathcal{K}_v$, we emphasize that the position feedback gain $\mathcal{K}_p$ should satisfy the following condition:

$$\mathcal{K}_p = \mathcal{K}_p^T < 0 \tag{83}$$

Condition Ensuring Equilibrium Unicity

Consider the previously closed-loop nonlinear dynamic model (74) of the Lagrangian robotic system. As in the previous parts, the equilibrium of such system must satisfy $\dot{\phi} = 0$ and $\ddot{\phi} = 0$. Then, according to these evaluations and by taking into account expression (72), the nonlinear dynamics (74) at the equilibrium is simplified as follows:

$$\mathcal{K}_p\phi = \mathcal{H}(q,0)\Omega\phi \tag{84}$$

Relying on condition (83), it follows that $\mathrm{rank}(\mathcal{K}_p) = n$. Then, relation (84) is rewritten like so:

$$\phi = \mathcal{K}_p^{-1}\mathcal{H}(\phi,0)\Omega\phi \tag{85}$$

It is easy to show that $\phi = 0$ is a solution of the obtained expression (85), however it is not the only one. It is feasible to obtain other solutions satisfying this equation (85). Thus, our main goal in the sequel is to design some possible but feasible conditions on the two matrix gains $\mathcal{K}_v$ and $\mathcal{K}_p$ guaranteeing the uniqueness of the solution $\phi = 0$. Then, to achieve this objective, we will rely on Theorem 1 of the contracting mapping.

To apply such contracting mapping, let us pose first the following nonlinear function $\varphi(\phi)$:

$$\varphi(\phi) = \mathcal{K}_p^{-1}\mathcal{H}(\phi,0)\Omega\phi \tag{86}$$

and then expression (85) becomes:

$$\phi = \varphi(\phi) \tag{87}$$

Then, to guarantee the uniqueness of the zero solution (that is $\phi = 0$) and from expression (85), it is easy to expand the following inequality:

$$\begin{aligned}\|\varphi(\phi_1) - \varphi(\phi_2)\| \leq &\left\|\mathcal{K}_p^{-1}\right\| \times \|\Omega\| \\ &\times \|\mathcal{H}(\phi_1,0)\phi_1 - \mathcal{H}(\phi_2,0)\phi_2\|\end{aligned} \tag{88}$$

Using expression of the matrix Ω defined by (72), and by taking into consideration the two conditions (83) and (81) respectively on $\mathcal{K}_p$ and $\mathcal{K}_v$, we can develop the following relation:

$$\|\Omega\| \leq \lambda_{\max}(-\mathcal{K}_v^{-1})\lambda_{\max}(-\mathcal{K}_p) \tag{89}$$

Since

$$\lambda_{\max}(-\mathcal{K}_v^{-1}) = \frac{1}{\lambda_{\min}(-\mathcal{K}_v)} \tag{90}$$

it follows then that condition (89) becomes:

$$\|\Omega\| \leq \frac{\lambda_{\max}(-\mathcal{K}_p)}{\lambda_{\min}(-\mathcal{K}_v)} \tag{91}$$

Therefore, relying on condition (91), expression (88) is simplified as follows:

$$\begin{aligned}\|\varphi(\phi_1) - \varphi(\phi_2)\| \leq &\frac{1}{\lambda_{\min}(-\mathcal{K}_p)}\frac{\lambda_{\max}(-\mathcal{K}_p)}{\lambda_{\min}(-\mathcal{K}_v)} \\ &\|\mathcal{H}(\phi_1,0)\phi_1 - \mathcal{H}(\phi_2,0)\phi_2\|\end{aligned} \tag{92}$$

Supposing that the matrix $\mathcal{H}(\phi,\dot{\phi})\phi$ satisfies the following Lipschitz constraint:

$$\|\mathcal{H}(\phi_1,\dot{\phi_1})\phi_1 - \mathcal{H}(\phi_2,\dot{\phi_2})\phi_2\| \leq k_c\|\phi_1 - \phi_2\| \tag{93}$$

where k_c is some positive constant like so:

$$k_c \geq n^2 \max_{k,i,j,q,\dot{q}}\left|\mathcal{H}_{i,j}(q_k,\dot{q}_k)\right| \tag{94}$$

Using then the constraint (93) in (92), we obtain hence the following condition:

$$\|\varphi(\phi_1) - \varphi(\phi_2)\| \leq \frac{1}{\lambda_{\min}(-\mathcal{K}_p)}\frac{\lambda_{\max}(-\mathcal{K}_p)}{\lambda_{\min}(-\mathcal{K}_v)}k_c\|\phi_1 - \phi_2\| \tag{95}$$

Relying on the contraction mapping in Theorem 1, and to guarantee that $\phi = 0$ is a solution and the unique one of the equation (85) or (87), we obtain the following condition:

$$\frac{k_c}{\lambda_{\min}(-\mathcal{K}_p)}\frac{\lambda_{\max}(-\mathcal{K}_p)}{\lambda_{\min}(-\mathcal{K}_v)} < 1 \tag{96}$$

As we can write the following equivalent equalities:

$$\lambda_{\min}(-\mathcal{K}_p) = -\lambda_{\max}(\mathcal{K}_p) \tag{97a}$$

$$\lambda_{\max}(-\mathcal{K}_p) = -\lambda_{\min}(\mathcal{K}_p) \tag{97b}$$

$$\lambda_{\min}(-\mathcal{K}_v) = -\lambda_{\max}(\mathcal{K}_v) \tag{97c}$$

then the previous condition (96) can be recast as follows:

$$\frac{k_c}{\lambda_{\max}(\mathcal{K}_p)}\frac{\lambda_{\min}(\mathcal{K}_p)}{\lambda_{\max}(\mathcal{K}_v)} > -1 \tag{98}$$

From this condition (98), and since $\mathcal{K}_p < 0$ and $\mathcal{K}_v < 0$, therefore we expand such condition on the feedback gain $\mathcal{K}_v$, given as follows:

$$\lambda_{\max}(\mathcal{K}_v) < -k_c\frac{\lambda_{\min}(\mathcal{K}_p)}{\lambda_{\max}(\mathcal{K}_p)} \tag{99}$$

that ensures the uniqueness of the zero solution $\phi = 0$ of the nonlinear equation (85).

Final Stabilization Conditions

By considering the three previously established conditions (81), (83) and (99) on the feedback gains, we obtain the following two simplified conditions:

$$\mathcal{K}_p = \mathcal{K}_p^T < 0 \tag{100a}$$

$$\mathcal{K}_v = \mathcal{K}_v^T < -k_c \frac{\lambda_{\min}(\mathcal{K}_p)}{\lambda_{\max}(\mathcal{K}_p)} \mathcal{I}_n \tag{100b}$$

We can conclude therefore that the two conditions (100a) and (100b) on the two feedback gain matrices $\mathcal{K}_p$ and $\mathcal{K}_v$ of the proposed augmented PD plus gravity compensation controller (71), guarantee the control of the Lagrangian robot system to the desired point q_d and hence its stabilization at q_d.

SIMULATION RESULTS

This present section is devoted to presenting the numerical simulation and graphical results of the different control laws proposed in this research work, and then to illustrate the efficiency of the built conditions of the two feedback gain matrices $\mathcal{K}_p$ and $\mathcal{K}_v$ of these control laws to control and stabilize the position of Lagrangian-type robot systems to the desired point q_d. Then, we will propose the planar 2-DoF robot manipulator shown in Fig. 1 as an illustrative example. Such robot system contains two joints/articulations with absolute angular positions q_1 and q_2. Thus, let the vector $q = \begin{bmatrix} q_1 & q_2 \end{bmatrix}^T$ defines the state vector of absolute angular positions.

Using the nonlinear dynamics (1) and according to the relative position coordinates q_1 and q_2, the various matrices of the planar 2-DoF manipulator robot are described as follows (Gritli *et al.* 2022; Jenhani *et al.* 2022a,b,c):

$$\mathcal{M}(q) = \begin{bmatrix} m_1 a_1^2 + m_2 l_1^2 + I_1 & m_2 l_1 a_2 \cos(q_1 - q_2) \\ m_2 l_1 a_2 \cos(q_1 - q_2) & m_2 a_2^2 + I_2 \end{bmatrix} \tag{101a}$$

$$\mathcal{H}(q, \dot{q}) = \sin(q_1 - q_2) \begin{bmatrix} 0 & m_2 l_1 a_2 \dot{q}_2 \\ -m_2 l_1 a_2 \dot{q}_1 & 0 \end{bmatrix} \tag{101b}$$

$$\mathcal{G}(q) = g \begin{bmatrix} (m_1 a_1 + m_2 l_1)\cos(q_1) \\ m_2 a_2 \cos(q_2) \end{bmatrix} \tag{101c}$$

$$\mathcal{D}(q) = \mathcal{D} = \begin{bmatrix} 1 & -1 \\ 0 & 1 \end{bmatrix} \tag{101d}$$

Moreover, the values and descriptions of the various parameters found in these matrices (101) are defined in Table 1.

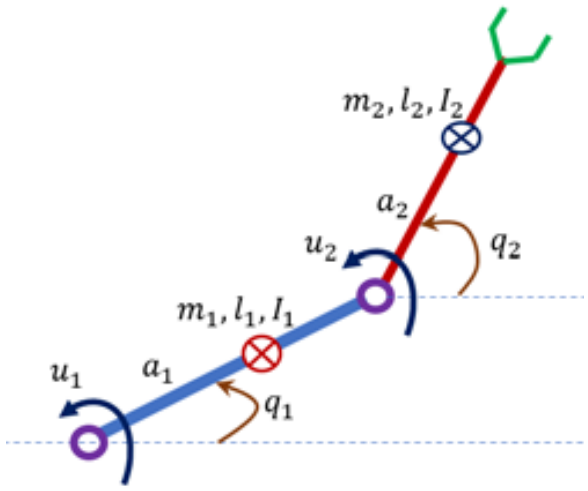

Figure 1 The adopted two-degree-of-freedom planar manipulator robot and its associated geometric and inertial parameters.

It is clear that the manipulator robotic system is composed of two links that are both controlled. Then, the control input vector $\mathcal{U}$ is composed of two control sub-inputs u_1 and u_2. The first joint is controlled via the input u_1, whereas the second joint is controlled via the second input u_2. Thus, we have $\mathcal{U} = \begin{bmatrix} u_1 \\ u_2 \end{bmatrix}$.

Let consider in the sequel the desired configuration state q_d to be as follows:

$$q_d = \begin{bmatrix} 90^\circ \\ -45^\circ \end{bmatrix} \tag{102}$$

Furthermore, and in order to make a comparison with the evolution of the controlled manipulator robot, all the simulation simulations with the proposed control laws start at the same initial position point:

$$q_0 = \begin{bmatrix} 0^\circ \\ 0^\circ \end{bmatrix} \tag{103}$$

Table 1 Used parameters and their values for the numerical simulation of the 2-DoF manipulator robotic system in Fig. 1.

Parameter	Value	Description
m_1	2 Kg	Mass of the first pendulum of the manipulator robot
a_1	0.375 m	Distance taken from the first articulation of the robot to the center of mass (CoM) of its first pendulum
m_2	1 Kg	Mass of the second pendulum of the manipulator robot
a_2	0.25 m	Distance taken from the second joint to the CoM of the second pendulum of the robotic manipulator
l_1	0.5 m	Length of the first pendulum of the manipulator robot
I_1	0.02 kg.m^2	Rotational inertia parameter of the first pendulum of the manipulator robotic system
l_2	0.4 m	Length of the second pendulum of the manipulator robot
I_2	0.01 kg.m^2	Rotational inertia parameter of the second pendulum of the manipulator robot
g	9.81 m/s^2	Gravitational constant

Simulation Results Obtained Using the PD Plus Gravity Compensation Controller

In this first part, we will consider and use the PD plus gravity compensation controller (11). Thus, based on the two conditions (21a) and (21b), the feedback gains $\mathcal{K}_v$ and $\mathcal{K}_p$ of the adopted nonlinear control law are computed to be like so:

$$\mathcal{K}_p = \begin{bmatrix} -20.0 & 5.0 \\ 5.0 & -10.0 \end{bmatrix} \tag{104a}$$

$$\mathcal{K}_v = \begin{bmatrix} -10.0 & 5.0 \\ 5.0 & -20.0 \end{bmatrix} \tag{104b}$$

It is straightforward to verify that the eigenvalues of two matrices $\mathcal{K}_p$ and $\mathcal{K}_v$ are real (since they are symmetric) and negative. Therefore, the two inequality constraints (21a) and (21b) on these feedback gains have been well satisfied.

It is worth to mention that the values of the two gain matrices $\mathcal{K}_p$ and $\mathcal{K}_v$ adopted in (104a) and (104b), are selected in order to compare with the augmented PD plus gravity compensation control law (71) by choosing the same gains (113a) and (113b).

Using the two feedback gain matrices (104a) and (104b) in the adopted PD plus gravity compensation controller defined by expression (11), the 2-DoF robot manipulator will be then controlled to and stabilize at the point q_d. Fig. 2(a) demonstrates the temporal evolution of the two angular positions q_1 and q_2 (or the position vector q) of the robotic system in question. It is clear from the curves of q_1 and q_2 that these two states converge to q_d. Moreover, Fig. 2(b) demonstrates that the temporal variation of the angular velocities $\dot{q}_1$ and $\dot{q}_2$ tends to zero. Furthermore, Fig. 2(c) presents the evolution of the PD plus gravity compensation controller $\mathcal{U}$. It is obvious that when the robotic system is controlled and hence stabilized at q_d, the control subinputs u_1 and u_2 (of the control law $\mathcal{U}$) converge towards the constant value 1.7342.

As noted previously, the two gains (104a) and (104b) adopted for the PD with gravity compensation control law are equal to (113a) and (113b), which will be adopted for the augmented PD plus gravity compensation control law. We consider now other values of the matrix feedback gains $\mathcal{K}_v$ and $\mathcal{K}_p$ different to those in (104a) and (104b) as follows:

$$\mathcal{K}_p = \begin{bmatrix} -2.0 & 1.0 \\ 1.0 & -2.0 \end{bmatrix} \tag{105a}$$

$$\mathcal{K}_v = \begin{bmatrix} -2.0 & 1.0 \\ 1.0 & -2.0 \end{bmatrix} \tag{105b}$$

Notice that the eigenvalues of these matrix gains (105a) and (105b) are -1 and -3. Then, the two conditions (21a) and (21b) are well satisfied. We emphasize that these two gains (105a) and (105b) will not satisfy the conditions (100a) and (100b) for the augmented PD plus gravity compensation control law.

By introducing the two feedback gain matrices (105a) and (105b) in the PD plus gravity compensation controller defined by expression (11), we obtain the results in Fig. 3 revealing the control and hence stabilization of the 2-DoF robotic manipulator at q_d. Moreover, the Fig. 3(a) demonstrates the temporal evolution of the positions q_1 and q_2. It is clear from the curves of q_1 and q_2 that these two states converge to q_d. In addition, the Fig. 3(b) depicts the variation of the angular velocities $\dot{q}_1$ and $\dot{q}_2$. Compared to the results in Fig. 2(a) and Fig. 2(b), the stabilization/convergence time at/to the desired point q_d is almost the same, about 7 $[s]$. Nevertheless, the obvious difference between the two results lies in the response of the angular velocities of the two links. Indeed, in Fig. 2(a), the angular velocity $\dot{q}_1$ reaches a high value about 150 $[deg/s]$ before its rapid and asymptotic decrease to zero. However, in Fig. 3(a), the angular velocity $\dot{q}_1$ reaches a relatively small value around 60 $[deg/s]$ before its convergence to zero. In contrast, the angular velocity $\dot{q}_2$ in Fig. 2(a) decreases to the minimal value $\approx -50\,[deg/s]$, whereas in Fig. 3(a) reaches the minimal value $\approx -80\,[deg/s]$.

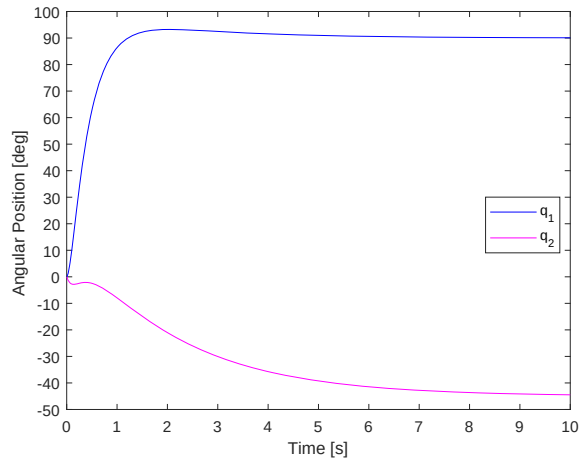

(a)

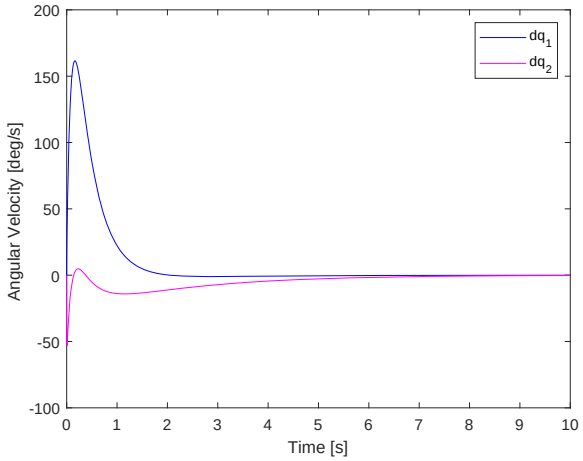

(b)

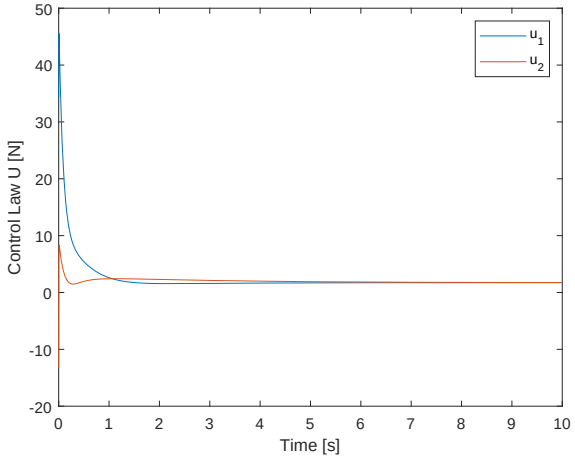

(c)

Figure 2 Temporal evolution of: (a) the two angular positions q_1 and q_2, (b) the two corresponding angular velocities $\dot{q}_1$ and $\dot{q}_2$, and (c) the PD with gravity compensation control law $\mathcal{U} = [u_1 \ u_2]^{\mathrm{T}}$, by adopting the two matrix feedback gains (104a) and (104b).

Furthermore, the curves in Fig. 3(c) illustrate the temporal variation of the controller $\mathcal{U}$ applied to the manipulator robot system. As in Fig. 2(c), when the manipulator robot was control to and hence stabilized at q_d, the two inputs of control u_1 and u_2 converge together towards the constant effort 1.7342. Compared to the results in Fig. 2(c) where u_1 (resp. u_2) reached the maximal value about 45 $[N]$ (resp. -15 $[N]$), in Fig. 3(c) the controller u_1 (resp. u_2) reaches the maximal value around 16 $[N]$ (resp. 3 $[N]$). Hence, the difference between the two control results is evident.

Numerical Results Obtained with the PD Plus Desired Gravity Compensation Controller

In this subsection, we will focus on the simulation results obtained by applying the the PD plus desired gravity compensation controller. Such control law and the associated conditions on its feedback gains are presented in the forth section. Expression of such controller is defined by (22) and the designed stabilization conditions are defined by the two constraints (54a) and (54b). The computation of the value of the constant k_g in the condition (54a) according to expression (6) gives:

$$k_g = 12.2625 \tag{106}$$

Then, according to these conditions (54a) and (54b), and by adopting the previous value of k_g in (106), we select the following matrices of $\mathcal{K}_p$ and $\mathcal{K}_v$:

$$\mathcal{K}_p = \begin{bmatrix} -15.0 & -1.0 \\ -1.0 & -20.0 \end{bmatrix} \tag{107a}$$

$$\mathcal{K}_v = \begin{bmatrix} -2.0 & -1.0 \\ -1.0 & -6.0 \end{bmatrix} \tag{107b}$$

The eigenvalues of the matrix $\mathcal{K}_p$ are -20.1926 and -14.8074. Since, $\lambda_{\max}(\mathcal{K}_p) = -14.8074 < -k_g = -12.2625$, then the first condition (54a) has been well respected. Moreover, it is obvious that the matrix $\mathcal{K}_v$ is negative definite.

By introducing the two matrix feedback gains (107a) and (107b) into the PD plus the desired gravity compensation controller (22), the manipulator robot system will be then controlled to and therefore stabilized at q_d. Figure 4(a) presents the angular positions q_1 and q_2, where q_1 and q_2 converge towards q_d. Additionally, we reveal from Fig. 4(b) that the temporal behavior of the two corresponding angular velocities $\dot{q}_1$ and $\dot{q}_2$ of the robotic system converge to zero. Moreover, Fig. 4(c) shows the behavior of the proposed PD plus the desired gravity compensation controller $\mathcal{U}$. Obviously, the two sub-controllers u_1 and u_2 converge together to the same constant value 1.7342, as in the previous control case.

Actually, in order to demonstrate the importance of the unicity condition of the zero solution established for the development of the stabilizing gains of the control law $\mathcal{U}$, we slightly modified the matrix $\mathcal{K}_p$ in order that the first condition (54a) will be not respected. Thus, we select the following matrix gain $\mathcal{K}_p$:

$$\mathcal{K}_p = \begin{bmatrix} -10.0 & -1.0 \\ -1.0 & -20.0 \end{bmatrix} \tag{108}$$

Such matrix (108) has the following eigenvalues : -20.0990 and -9.9010. It is evident that $\lambda_{\max}(\mathcal{K}_p) = -9.9010 > -k_g = -12.2625$. Therefore, the first condition (54a) has not been satisfied.

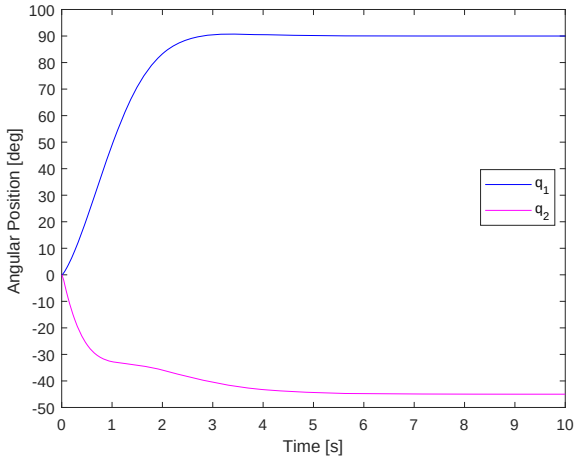

(a)

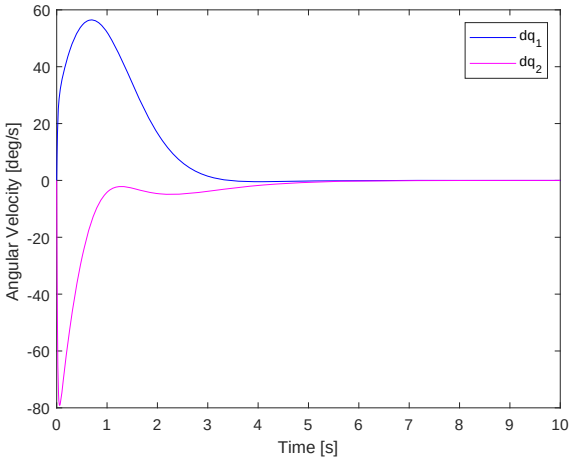

(b)

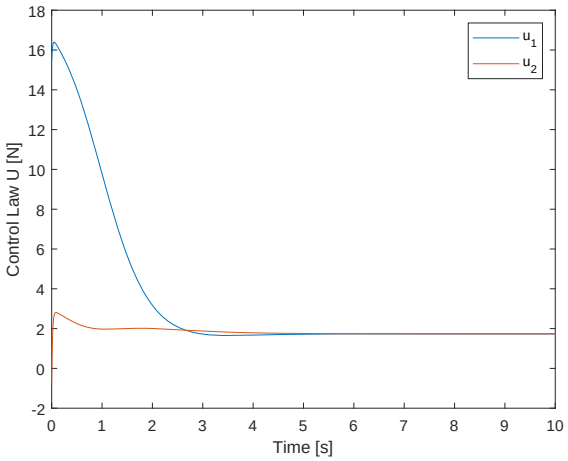

(c)

Figure 3 Temporal evolution of: (a) the two angular positions q_1 and q_2, (b) the two corresponding angular velocities $\dot{q}_1$ and $\dot{q}_2$, and (c) the PD plus gravity compensation controller $\mathcal{U} = [u_1 \;\; u_2]^{\mathrm{T}}$ by adopting the two matrix feedback gains (105a) and (105b).

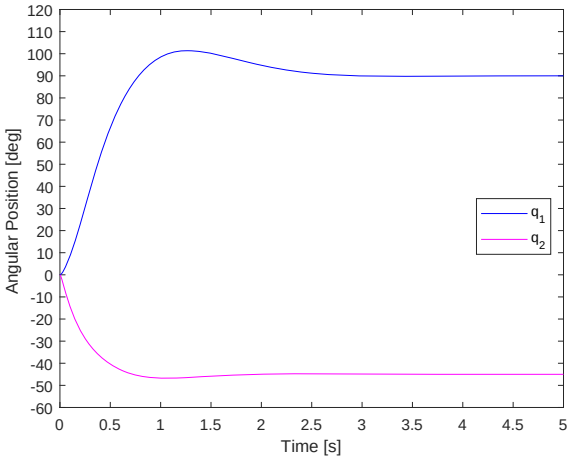

(a)

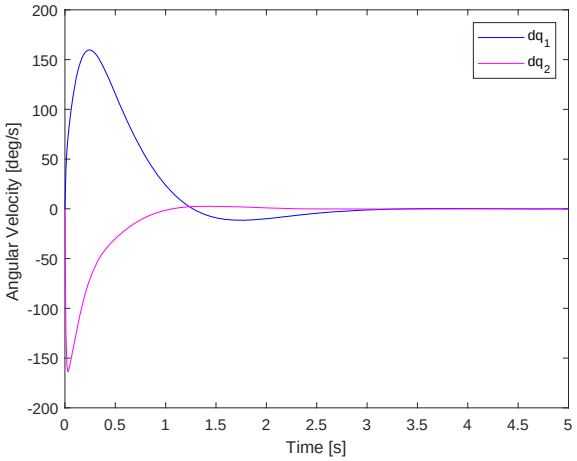

(b)

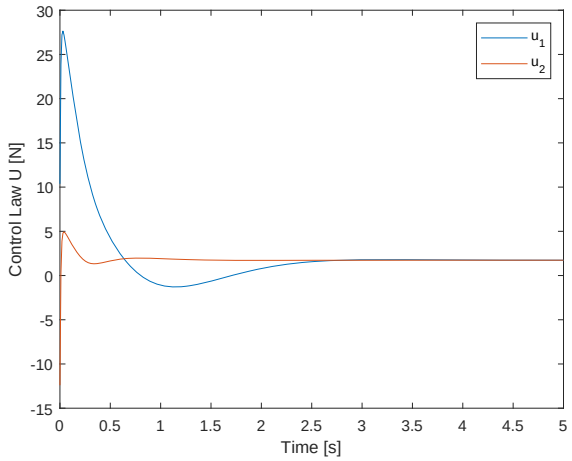

(c)

Figure 4 Temporal variation of: (a) the two angular positions q_1 and q_2, (b) the two corresponding angular velocities $\dot{q}_1$ and $\dot{q}_2$, and (c) the PD plus desired gravity compensation control law, by adopting the two matrix feedback gains (107a) and (107b).

The objective behind this previous modification is to show the evolution of the robotic system and its stabilization at a position state completely different to the desired one q_d. By using then the PD plus desired gravity compensation controller $\mathcal{U}$ according the position gain $\mathcal{K}_p$ in (108) and the velocity gain $\mathcal{K}_v$ in (107b), using its nonlinear dynamic model (1), we demonstrate the simulation results in Fig. 5. It is clear from the temporal variation of the angular position of the manipulator robot in Fig. 5(a) and that of the angular velocity in Fig. 5(b), the robot is stabilized at the position $q_\infty = \begin{bmatrix} 27.2468^\circ & -42.1061^\circ \end{bmatrix}^{\mathrm{T}}$. Thus, this final state q_∞ is entirely different to the desired one q_d, which was already defined in (102). Moreover, the evolution of the controller in Fig. 5(a) is completely different to that in Fig. 4(c). These results demonstrate accordingly the importance of establishing the condition on the gains of the controller to guarantee the uniqueness of the desired position q_d when the robotic system is stabilized.

Numerical Results Obtained Under the Computed-Torque Control Law

The computed-torque controller is defined by expressions (55) and (56). The designed conditions on the two matrix feedback gains $\mathcal{K}_p$ and $\mathcal{K}_v$ are (70a) and (70b). Using these conditions and by taking $w_1 = w_2 = 2$, we get the following diagonal matrices of $\mathcal{K}_p$ and $\mathcal{K}_v$:

$$\mathcal{K}_p = \begin{bmatrix} -4 & 0 \\ 0 & -4 \end{bmatrix} \tag{109a}$$

$$\mathcal{K}_v = \begin{bmatrix} -4 & 0 \\ 0 & -4 \end{bmatrix} \tag{109b}$$

Thus, by introducing these feedback gains in the proposed computed-torque control law (55)-(56), the robotic system, that is the 2-DoF manipulator robot, will be controlled to q_d. Figure 6(a) denotes the dynamic behavior of q_1 and q_2 of the manipulator robot, where q_1 and q_2 converge towards q_d. Thus, the temporal simulation of the corresponding angular velocities is illustrated in Fig. 6(b), where it reveals that $\dot{q}_1$ and $\dot{q}_2$ converge together to zero. Moreover, the Fig. 6(c) shows the temporal behavior of the applied computed-torque controller. In the present case, the control subinputs u_1 and u_2 converge together to 1.7342, as in the two previous cases.

Numerical Results Obtained with the Augmented PD Plus Gravity Compensation Control Law

The augmented PD with gravity compensation controller is defined by expression (71). Moreover, the established stabilization conditions are defined by the two inequality constraints (100a) and (100b). According to condition (100b), the feedback gain $\mathcal{K}_v$ depends on the constant k_c and the gain matrix $\mathcal{K}_p$. Recall that the constant k_c should be computed via condition (94). According to expression (101b) of the matrix $\mathcal{H}(q, \dot{q})$ and the values of the parameters of the 2-DoF manipulator robotic system in Table 1, it easy to show that condition (94) leads to the following inequality:

$$k_c \geq 0.5 \tag{110}$$

We take here the same gain matrix $\mathcal{K}_p$ adopted for the PD plus gravity compensation controller, that is (104a). The value

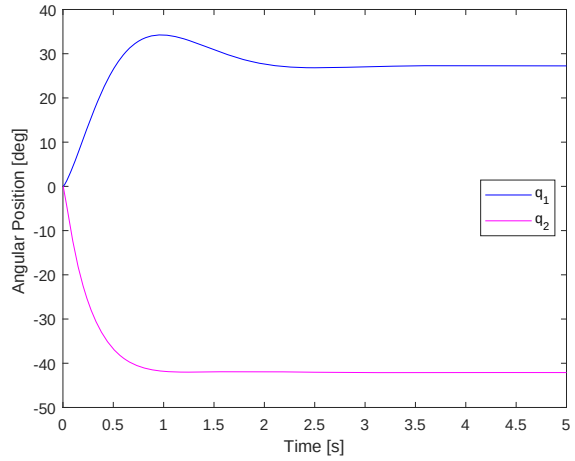

(a)

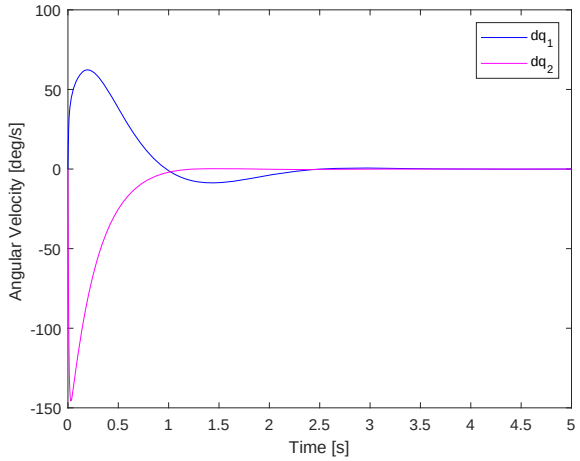

(b)

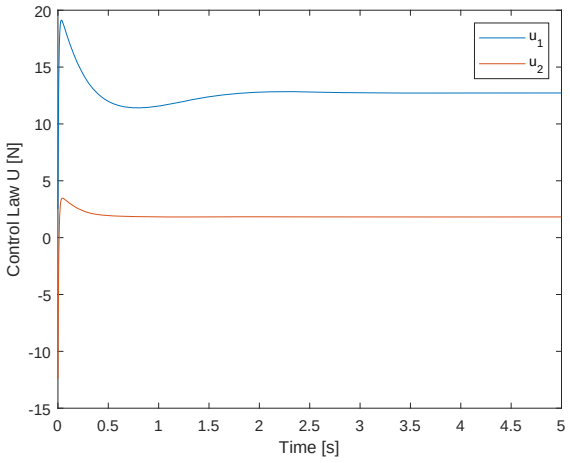

(c)

Figure 5 Simulation results of the controlled robot by selecting a different matrix (108) of $\mathcal{K}_p$: (a) q_1 and q_2, (b) $\dot{q}_1$ and $\dot{q}_2$, (c) the applied PD plus desired gravity compensation controller, by adopting the position gain $\mathcal{K}_p$ in (108) and the velocity gain $\mathcal{K}_v$ in (107b).

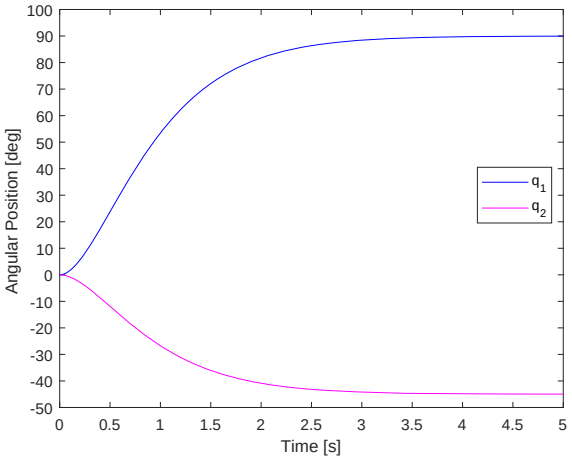

(a)

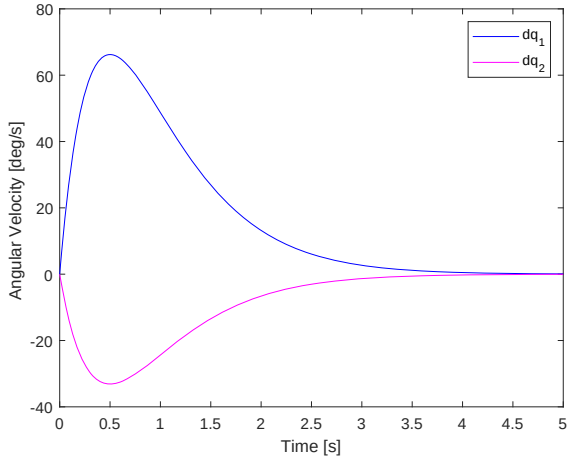

(b)

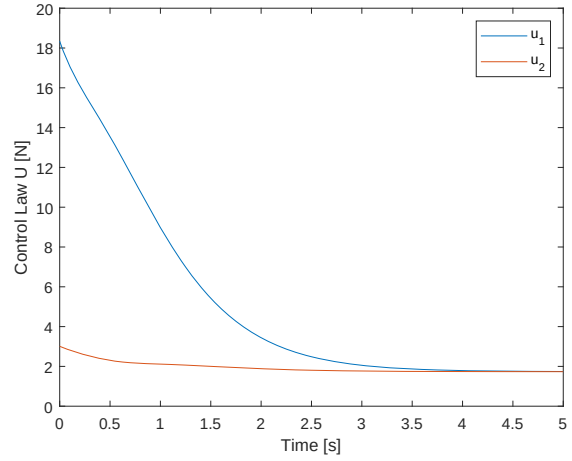

(c)

Figure 6 Temporal variation of: (a) the two angular positions q_1 and q_2 of the manipulator robot, (b) the two corresponding angular velocities $\dot{q}_1$ and $\dot{q}_2$, and (c) the applied computed-torque controller $\mathcal{U}$, by adopting the two matrix feedback gains (109a) and (109b).

of the feedback gain $\mathcal{K}_v$ should be selected via condition (100b). According to the matrix (104a) of $\mathcal{K}_p$, we obtain:

$$\lambda_{\min}(\mathcal{K}_p) = -22.0711 \tag{111a}$$

$$\lambda_{\max}(\mathcal{K}_p) = -7.9289 \tag{111b}$$

Hence, using expressions (111a) and (111b) and inequality (110), it is straightforward to show that according to the condition (100b), the feedback gain $\mathcal{K}_v$ should satisfy and be selected according to the following constraint:

$$\mathcal{K}_v = \mathcal{K}_v^T < -1.3918\, \mathcal{I}_n \tag{112}$$

Then, to satisfy this condition (112), we will adopt the same value (104b) of the feedback gain $\mathcal{K}_v$ adopted for the PD plus gravity compensation control law. Hence, for the controller in question, we will take the following values of $\mathcal{K}_p$ and $\mathcal{K}_v$:

$$\mathcal{K}_p = \begin{bmatrix} -20.0 & 5.0 \\ 5.0 & -10.0 \end{bmatrix} \tag{113a}$$

$$\mathcal{K}_v = \begin{bmatrix} -10.0 & 5.0 \\ 5.0 & -20.0 \end{bmatrix} \tag{113b}$$

It is obvious that these gains (113a) and (113b) are similar to those in (104a) and (104b) of the PD plus gravity compensation controller. The eigenvalues of the two matrices $\mathcal{K}_p$ and $\mathcal{K}_v$ are -22.0711 and -7.9289. It is clear that the condition (112) is well respected.

Using these two gains (113a) and (113b) in the augmented PD controller defined in (71), the planar 2-DoF manipulator is then controlled to q_d as revealed via Fig. 7(a), where convergence of the two angular positions q_1 and q_2 towards q_d is clear. In the Fig. 7(b), we show that the two angular velocities converges to zero, which justifies the stabilization at the desired point q_d. Moreover, Fig. 7(c) illustrates the applied controller $\mathcal{U}$. As in the previous cases, u_1 and u_2 converge progressively to the same value, which is almost equal to 1.734.

We consider now two other values of the two feedback gain matrices $\mathcal{K}_p$ and $\mathcal{K}_v$, and then we select the same gains (105a) and (105b) that were adopted for the PD plus gravity compensation controller. Since the eigenvalues of these two matrices $\mathcal{K}_p$ and $\mathcal{K}_v$ are -1 and -3, it follows then that the condition (112) was not verified. To satisfy this stabilization condition (112), we make a slight change in the two matrices $\mathcal{K}_p$ and $\mathcal{K}_v$, and we will take the following values:

$$\mathcal{K}_p = \begin{bmatrix} -3.0 & 1.0 \\ 1.0 & -2.0 \end{bmatrix} \tag{114a}$$

$$\mathcal{K}_v = \begin{bmatrix} -2.0 & 1.0 \\ 1.0 & -3.0 \end{bmatrix} \tag{114b}$$

It is easy to show that the eigenvalues of $\mathcal{K}_p$ and $\mathcal{K}_v$ are -1.3820 and -3.6180. Moreover, we can demonstrate via condition (100b) that the matrix $\mathcal{K}_v$ satisfies the following constraint:

$$\mathcal{K}_v = \mathcal{K}_v^T < -1.3090\, \mathcal{I}_n \tag{115}$$

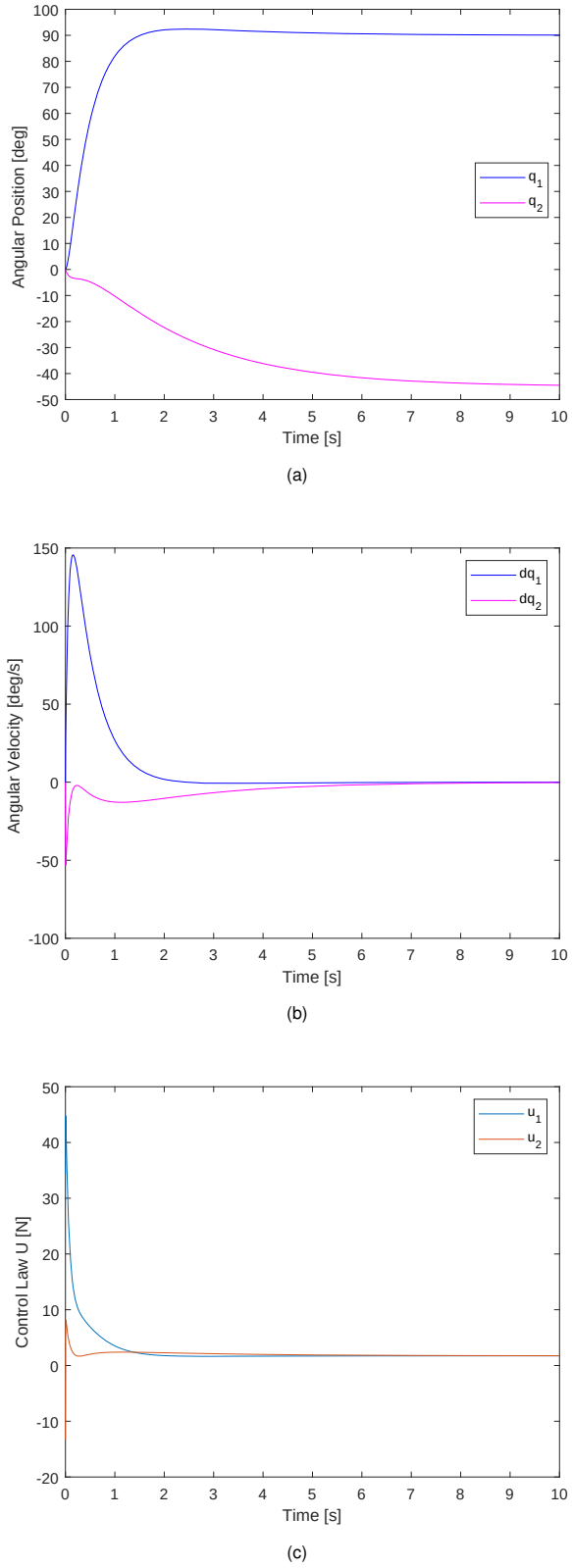

Figure 7 Temporal variation of: (a) the two angular positions q_1 and q_2 of the manipulator robot, (b) the two corresponding angular velocities $\dot{q}_1$ and $\dot{q}_2$, and (c) the augmented PD plus gravity compensation controller, by adopting the two feedback gains (113a) and (113b).

which is respected by adopting the gain (114b), since $\lambda_{\max}(\mathcal{K}_v) = -1.3820$.

Using then the two matrix feedback gains (114a) and (114b) in the adopted augmented PD plus gravity compensation controller defined by expression (71), the 2-DoF manipulator robot will be controlled to q_d. Fig. 8 shows the obtained outputs of the controlled manipulator robot. The Fig. 8(a) reveals the convergence of q_1 and q_2 towards q_d. Moreover, the Fig. 8(b) shows that the two angular velocities $\dot{q}_1$ and $\dot{q}_2$ converge to zero. In addition, the Fig. 8(c) depicts the controller $\mathcal{U}$ applied to the robotic system. As in the previous cases, the applied control subinputs u_1 and u_2 converge progressively and simultaneously to 1.7342.

Compared to the results obtained in Fig. 3 for the stabilization by means of the PD plus gravity compensation controller, the simulation results illustrated in Fig. 8 are found to be almost similar. The slight difference lies in the maximal values reached by the two subinputs u_1 and u_2 and also in the maximum values reached by the two angular velocities $\dot{q}_1$ and $\dot{q}_2$. This small difference can be explained by the fact that the adopted feedback gains (114a) and (114b) are higher (in terms of eigenvalues) than those in (105a) and (105b).

DISCUSSION

It is important to specify that the four proposed nonlinear controllers can control the position of robotic systems, and more particularly the 2-DoF manipulator in Fig. 1, and stabilize it at some desired state. As we have shown previously in the Fig. 2(a), the Fig. 4(a), the Fig. 6(a) and the Fig. 7(a), the manipulator robot is controlled to the desired point q_d. Furthermore, in all four cases, the angular velocity presented in Fig. 2(b), Fig. 4(b), Fig. 6(b) and Fig. 7(b) converges to zero and therefore the robot is well stabilized. In addition, as reported previously and revealed from Fig. 2(c), Fig. 4(c), Fig. 6(c) and Fig. 7(c), the control subinputs u_1 and u_2 converge together to the constant value $u_\infty \approx 1.734$. Such control effort is the necessary amount needed to keep the robotic manipulator at the desired state q_d. This result reveals that at the stabilization at the desired equilibrium point q_d, a small control effort is required/applied.

Furthermore, we showed that using the PD plus gravity compensation control law (11), the robotic system has been stabilized in almost 10 seconds, although the selected gains $\mathcal{K}_p$ and $\mathcal{K}_v$ are relatively high. But, by using the PD plus desired gravity compensation controller (22), almost 4 seconds were needed for the stability of the robot system at q_d. Furthermore, by applying the computed-torque control law (55)-(56), the manipulator robot was found to be stabilized at the desired point q_d in about 5 seconds. In addition, by applying the augmented PD plus gravity compensation controller (71), the robotic system has been stabilized in almost 6 seconds.

It is worth to note that compared to the PD plus gravity compensation controller (11), the augmented version (71) is more efficient. Indeed, by observing the plots of the angular velocity illustrated in Fig. 2(b) and Fig. 7(b), it is clear that by applying the PD plus gravity compensation controller (11), the angular velocities of the two joints reach higher values than those obtained by applying the augmented PD controller (71). Furthermore, according to Fig. 2(c) and Fig. 7(c), the control efforts u_1 and u_2 applied to the two joints is slightly small for the case of the augmented PD plus gravity compensation control law. This result demonstrates that the augmented/added term in the augmented control law (71), compared to the PD plus gravity compensation controller (11), contributes in (slightly) reducing the controller effort applied to the robot system.

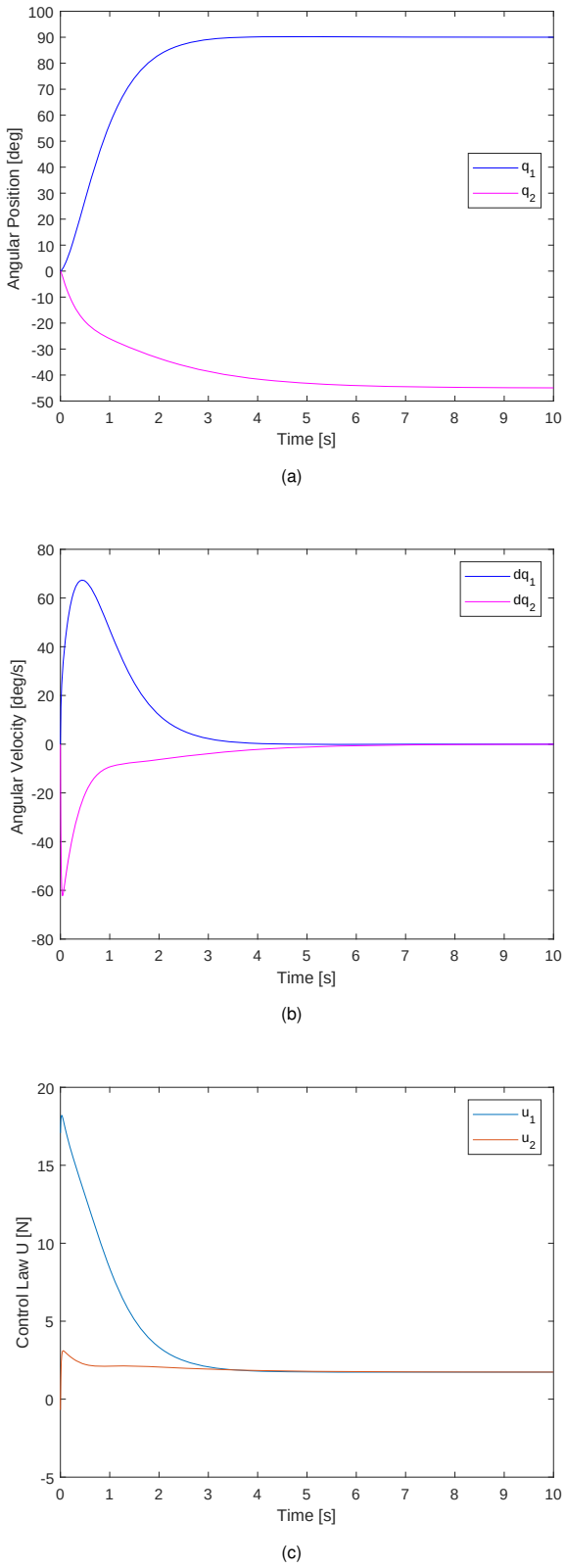

Figure 8 Temporal variation of: (a) the two angular positions q_1 and q_2 of the manipulator robot, (b) the two corresponding angular velocities $\dot{q}_1$ and $\dot{q}_2$, and (c) the augmented PD plus gravity compensation controller, by adopting the two feedback gains (114a) and (114b).

After this previous discussion, we can conclude that the four controllers proved to be globally effective for the control of Lagrangian-type robotic systems, for at least for the planar 2-DoF manipulator in Fig. 1. Nevertheless, more experiences should be achieved to further study the efficiency of these four controllers by considering the effect of external disturbances, unmodeled dynamics and the presence of frictions in the nonlinear dynamic model of the Lagrangian-like robotic systems. In these cases, robust controllers should be designed to deal with these uncertainties and disturbances.

From practical point-of-view, it is important to indicate that the design and application of the four proposed nonlinear controllers require the previous knowledge of all and some parts of the dynamic model of the robotic system to control. In fact, the PD plus desired gravity compensation controller (22) only needs information on a single matrix, namely the distribution input matrix $\mathcal{D}(q)$, which needs to be evaluated on-line at each time. Moreover, the PD plus gravity compensation controller (11) needs the previous knowledge of the matrix $\mathcal{D}(q)$ and also of the gravity matrix $\mathcal{G}(q)$. Thus, this controller is more complicated and needs more time to be executed than the PD plus desired gravity compensation controller. Indeed, the control law (11) requires information on the measurement of the position vector q and the velocity vector $\dot{q}(t)$ at each instant while the robotic system is moving for the computation of the two matrices and $\mathcal{D}(q)$ and $\mathcal{G}(q)$. Furthermore, the computed-torque controller (55)-(56) depends on all the matrices of the nonlinear dynamic model (1) of the Lagrangian robot system. It is usually called as the model-based controller, which explicitly use the full knowledge of the matrices $\mathcal{M}(q)$, $\mathcal{H}(q,\dot{q})$, $\mathcal{G}(q)$ and $\mathcal{D}(q)$ of the dynamic robot model (1). Similarly, the augmented PD plus gravity compensation controller (71) requires the full knowledge of the previous four matrices of the robotic system for its computation. Compared to the computed-torque control law, the augmented controller contains more nonlinear terms, and then its computation requires much time.

CONCLUSION AND FUTURE WORKS

In this research work, we adopted four different nonlinear controllers to solve the control and stabilization problem of the Lagrangian-type robotic systems to some set-point position. Then, the main goal was to control the robotic system through its nonlinear dynamic model to change its current configuration state into a desired position state. In order to achieve this objective, we adopted the PD plus gravity compensation controller, the PD plus desired gravity compensation controller, the computed-torque controller and the augmented PD plus gravity compensation controller. In addition, by applying these control laws in the nonlinear dynamic model of the Lagrangian robotic systems, we developed some feasible conditions on the gain matrices $\mathcal{K}_v$ and $\mathcal{K}_p$ ensuring the stability at the desired state and also guaranteeing the uniqueness of the desired equilibrium. Finally, we proposed the planar manipulator robot with 2-DoF, as an illustrative example, in order to present the simulation results by using the different adopted nonlinear controllers and a comparison between them was therefore achieved.

A a possible future direction of this research work, we aim at analyzing the efficiency of the adopted nonlinear controllers by considering the effect of external perturbations, unmodeled dynamics and parametric uncertainties.

Acknowledgments

The authors acknowledge with thanks the Ministry of Higher Education and Scientific Research (MESRS) of Tunisia, for its financial and technical support under the PEJC research project no. 20PEJC 06-02.

Availability of data and material

Not applicable.

Conflicts of interest

The authors declare that there is no conflict of interest regarding the publication of this paper.

LITERATURE CITED

Abbas, M., S. Al Issa, and S. K. Dwivedy, 2021 Event-triggered adaptive hybrid position-force control for robot-assisted ultrasonic examination system. Journal of Intelligent & Robotic Systems **102**: 84–102.

Abdul-Adheem, W. R., I. K. Ibraheem, A. J. Humaidi, and A. T. Azar, 2021 Model-free active input–output feedback linearization of a single-link flexible joint manipulator: An improved active disturbance rejection control approach. Measurement and Control **54**: 856–871.

Ahmed, T., M. Assad-Uz-Zaman, M. R. Islam, D. Gottheardt, E. McGonigle, *et al.*, 2021 Flexohand: A hybrid exoskeleton-based novel hand rehabilitation device. Micromachines **12**.

Biswal, P. and P. K. Mohanty, 2021 Development of quadruped walking robots: A review. Ain Shams Engineering Journal **12**: 2017–2031.

Bjelonic, M., N. Kottege, and P. Beckerle, 2016 Proprioceptive control of an over-actuated hexapod robot in unstructured terrain. In *2016 IEEE/RSJ International Conference on Intelligent Robots and Systems (IROS)*, pp. 2042–2049.

Chai, H., Y. Li, R. Song, G. Zhang, Q. Zhang, *et al.*, 2021 A survey of the development of quadruped robots: Joint configuration, dynamic locomotion control method and mobile manipulation approach. Biomimetic Intelligence and Robotics p. 100029.

Chawla, I. and A. Singla, 2021 Real-time stabilization control of a rotary inverted pendulum using LQR-based sliding mode controller. Arabian Journal for Science and Engineering **46**: 2589–2596.

Choukchou-Braham, A., B. Cherki, M. Djemai, and K. Busawon, 2014 *Analysis and Control of Underactuated Mechanical Systems*. Springer-Verlag, New York.

da Costa Barros, I. R. and T. P. Nascimento, 2021 Robotic mobile fulfillment systems: A survey on recent developments and research opportunities. Robotics and Autonomous Systems **137**: 103729.

Gonzalez-Aguirre, J. A., R. Osorio-Oliveros, K. L. Rodriguez-Hernandez, J. Lizarraga-Iturralde, R. M. Menendez, *et al.*, 2021 Service robots: Trends and technology. Applied Sciences **11**: 10702.

González, C., J. E. Solanes, A. Muñoz, L. Gracia, V. Girbés-Juan, *et al.*, 2021 Advanced teleoperation and control system for industrial robots based on augmented virtuality and haptic feedback. Journal of Manufacturing Systems **59**: 283–298.

Gritli, H., 2020 LMI-based robust stabilization of a class of input-constrained uncertain nonlinear systems with application to a helicopter model. Complexity **2020**: 7025761.

Gritli, H. and S. Belghith, 2018 Robust feedback control of the underactuated Inertia Wheel Inverted Pendulum under parametric uncertainties and subject to external disturbances: LMI formulation. Journal of The Franklin Institute **355**: 9150–9191.

Gritli, H. and S. Belghith, 2021 LMI-based synthesis of a robust saturated controller for an underactuated mechanical system subject to motion constraints. European Journal of Control **57**: 179–193.

Gritli, H., S. Jenhani, and G. Carbone, 2022 Position control of robotic systems via an affine PD-based controller: Comparison between two design approaches. In *2022 5th International Conference on Advanced Systems and Emergent Technologies (IC_ASET)*, pp. 424–432.

Gu, E. Y. L., 2013 *Control of Robotic Systems*, volume 1. Springer, Berlin, Heidelberg.

Gualtieri, L., E. Rauch, and R. Vidoni, 2021 Development and validation of guidelines for safety in human-robot collaborative assembly systems. Computers & Industrial Engineering p. 107801.

Hasan, S. K. and A. K. Dhingra, 2021 Development of a model reference computed torque controller for a human lower extremity exoskeleton robot. Proceedings of the Institution of Mechanical Engineers, Part I: Journal of Systems and Control Engineering **235**: 1615–1637.

Islam, M. R., M. Assad-Uz-Zaman, and M. H. Rahman, 2020 Design and control of an ergonomic robotic shoulder for wearable exoskeleton robot for rehabilitation. International Journal of Dynamics and Control **8**: 312–325.

Jafari, M., S. Mobayen, F. Bayat, and H. Roth, 2023 A nonsingular terminal sliding algorithm for swing and stance control of a prosthetic leg robot. Applied Mathematical Modelling **113**: 13–29.

Jenhani, S., H. Gritli, and G. Carbone, 2022a Design and computation aid of command gains for the position control of manipulator robots. In *2022 International Conference on Decision Aid Sciences and Applications (DASA)*, pp. 1558–1564.

Jenhani, S., H. Gritli, and G. Carbone, 2022b Design of an affine control law for the position control problem of robotic systems based on the development of a linear dynamic model. In *2022 5th International Conference on Advanced Systems and Emergent Technologies (IC_ASET)*, pp. 403–411.

Jenhani, S., H. Gritli, and G. Carbone, 2022c Determination of conditions on feedback gains for the position control of robotic systems under an affine PD-based control law. In *2022 5th International Conference on Advanced Systems and Emergent Technologies (IC_ASET)*, pp. 518–526.

Jenhani, S., H. Gritli, and G. Carbone, 2022d LMI-based optimization for the position feedback control of underactuated robotic systems via an affine PD controller: Case of the pendubot. In *2022 International Conference on Data Analytics for Business and Industry (ICDABI) (DATA'22)*, pp. 768–774, virtual, Bahrain.

Jenhani, S., H. Gritli, and G. Carbone, 2022e Position control of Lagrangian robotic systems via an affine PID-based controller and using the LMI approach. In *Advances in Italian Mechanism Science*, edited by V. Niola, A. Gasparetto, G. Quaglia, and G. Carbone, pp. 727–737, Cham, Springer International Publishing.

Jenhani, S., H. Gritli, and G. Carbone, 2022f Position feedback control of Lagrangian robotic systems via an affine PD-based control law. Part 1: Design of LMI conditions. In *2022 IEEE 2nd International Maghreb Meeting of the Conference on Sciences and Techniques of Automatic Control and Computer Engineering (MI-STA)*, pp. 171–176.

Jenhani, S., H. Gritli, and G. Carbone, 2022g Position feedback control of Lagrangian robotic systems via an affine PD-based

control law. Part 2: Improved results. In *2022 IEEE 2nd International Maghreb Meeting of the Conference on Sciences and Techniques of Automatic Control and Computer Engineering (MI-STA)*, pp. 177–182.

Jiang, Y., K. Lu, C. Gong, and H. Liang, 2020 Robust composite nonlinear feedback control for uncertain robot manipulators. International Journal of Advanced Robotic Systems **17**: 1729881420914805.

Kalita, B., J. Narayan, and S. K. Dwivedy, 2021 Development of active lower limb robotic-based orthosis and exoskeleton devices: A systematic review. International Journal of Social Robotics **3**: 775–793.

Kelly, R., V. S. Davila, and A. Loría, 2005 *Control of Robot Manipulators in Joint Space*. Advanced Textbooks in Control and Signal Processing, Springer-Verlag, London.

Koditschek, D. E., 2021 What is robotics? why do we need it and how can we get it? Annual Review of Control, Robotics, and Autonomous Systems **4**: 1–33.

Krafes, S., Z. Chalh, and A. Saka, 2018 A review on the control of second order underactuated mechanical systems. Complexity **2018**: 9573514.

Kurdila, A. J. and P. Ben-Tzvi, 2019 *Dynamics and Control of Robotic Systems*. Control Process & Measurements, Wiley, first edition.

Li, X., B. Liu, and L. Wang, 2020 Control system of the six-axis serial manipulator based on active disturbance rejection control. International Journal of Advanced Robotic Systems **17**: 1729881420939476.

Liu, P., M. N. Huda, L. Sun, and H. Yu, 2020 A survey on underactuated robotic systems: Bio-inspiration, trajectory planning and control. Mechatronics **72**: 102443.

Liu, Y. and H. Yu, 2013 A survey of underactuated mechanical systems. IET Control Theory Applications **7**: 921–935.

Mobayen, S., F. Tchier, and L. Ragoub, 2017 Design of an adaptive tracker for n-link rigid robotic manipulators based on super-twisting global nonlinear sliding mode control. International Journal of Systems Science **48**: 1990–2002.

Narayan, J. and S. K. Dwivedy, 2021 Robust LQR-based neural-fuzzy tracking control for a lower limb exoskeleton system with parametric uncertainties and external disturbances. Applied Bionics and Biomechanics **2021**: 5573041.

Nho, H. C. and P. Meckl, 2003 Intelligent feedforward control and payload estimation for a two-link robotic manipulator. IEEE/ASME transactions on mechatronics **8**: 277–282.

Parulski, P., P. Bartkowiak, and D. Pazderski, 2021, 11 Evaluation of linearization methods for control of the pendubot. Applied Sciences **11**: 1–13.

Perrusquia, A., J. A. Flores-Campos, and C. R. Torres-San-Miguel, 2020 A novel tuning method of PD with gravity compensation controller for robot manipulators. IEEE Access **8**: 114773–114783.

Singla, A. and G. Singh, 2017 Real-time swing-up and stabilization control of a cart-pendulum system with constrained cart movement. International Journal of Nonlinear Sciences and Numerical Simulation **18**: 525–539.

Spong, M. W., 2022 An historical perspective on the control of robotic manipulators. Annual Review of Control, Robotics, and Autonomous Systems **5**: 1–31.

Spong, M. W., S. Hutchinson, and M. Vidyasagar, 2020 *Robot Modeling and Control*. Robotics, John Wiley & Sons Inc, second edition.

Tarnita, D., I. D. Geonea, D. Pisla, G. Carbone, B. Gherman, *et al.*, 2022 Analysis of dynamic behavior of parreex robot used in upper limb rehabilitation. Applied Sciences **12**.

Tipary, B. and G. Erdos, 2021 Generic development methodology for flexible robotic pick-and-place workcells based on digital twin. Robotics and Computer-Integrated Manufacturing **71**: 102140.

Turki, F., H. Gritli, and S. Belghith, 2020 An LMI-based design of a robust state-feedback control for the master-slave tracking of an impact mechanical oscillator with double-side rigid constraints and subject to bounded-parametric uncertainty. Communications in Nonlinear Science and Numerical Simulation **82**: 105020.

Wang, J., W. Chen, X. Xiao, Y. Xu, C. Li, *et al.*, 2021 A survey of the development of biomimetic intelligence and robotics. Biomimetic Intelligence and Robotics **1**: 100001.

Zhang, C. and Y. Wu, 2021 P-Rob six-degree-of-freedom robot manipulator dynamics modeling and anti-disturbance control. IEEE Access **9**: 141403–141420.

Zilong Zhang, C. S. S., 2022 Underactuated mechanical systems – a review of control design. Journal of Vibration Testing and System Dynamics **6**: 21–51.

How to cite this article: Jenhani, S., Gritli, H., and Carbon G. Comparison Between Some Nonlinear Controllers for the Position Control of Lagrangian-type Robotic Systems. *Chaos Theory and Applications*, 4(4), 179-196, 2022.

CHAOS
Theory and Applications
in Applied Sciences and Engineering

e-ISSN: 2687-4539
RESEARCH ARTICLE
Vol.4 / No.4 / 2022 / pp.197-204
Special Issue (EDIESCA 2022)
https://doi.org/10.51537/chaos.1196653

The Unreasonable Effectiveness of the Chaotic Tent Map in Engineering Applications

Nithin Nagaraj [a,1]
[a] National Institute of Advanced Studies, Indian Institute of Science Campus, Bengaluru, India.

ABSTRACT From decimal expansion of real numbers to complex behaviour in physical, biological and human-made systems, deterministic *chaos* is ubiquitous. One of the simplest examples of a nonlinear dynamical system that exhibits chaos is the well known 1-dimensional piecewise linear Tent map. The Tent map (and their skewed cousins) are instances of a larger family of maps namely Generalized Lüroth Series (GLS) which are studied for their rich number theoretic and ergodic properties. In this work, we discuss the unreasonable effectiveness of the Tent map and their generalizations (GLS maps) in a number of applications in electronics, communication and computer engineering. To list a few of these applications: (a) GLS-coding: a lossless data compression algorithm for i.i.d sources is Shannon optimal and is in fact a generalization of the popular Arithmetic Coding algorithm used in the image compression standard JPEG2000; (b) GLS maps are used as neurons in the recently proposed Neurochaos Learning architecture which delivers state-of-the-art performance in classification tasks; (c) GLS maps are ideal candidates for chaos-based computing since they can simulate XOR, NAND and other gates and for dense storage of information for efficient search and retrieval; (d) Noise-resistant versions of GLS maps are useful for signal multiplexing in the presence of noise and error detection; (e) GLS maps are known to be useful in a number of cryptographic protocols - for joint compression and encryption, and also in generating pseudo-random numbers. The unique properties and rich features of the Tent Map (GLS maps) that enable these wide variety of engineering applications will be investigated. A list of open problems are indicated as well.

KEYWORDS
Tent map
Chaos
Generalized Lüroth Series
Compression
Coding
Cryptography
Neurochaos Learning
Ergodicity

INTRODUCTION

Deterministic Chaos refers to the seemingly random-like complicated (and often strange) behaviour of simple dynamical systems (Alligood *et al.* 2000; Devaney 2018). From decimal expansion of real numbers to complex behaviour in physical, biological and human-made systems, deterministic chaos is ubiquitous (Strogatz 2018). One of the simplest examples of a nonlinear dynamical system that exhibits chaos is the well known 1-dimensional piecewise linear Tent map (Alligood *et al.* 2000). The Tent map is topologically conjugate to the Logistic Map (the other popular 1D chaotic map) and finds numerous engineering applications in electronics, communications, compression, coding, computing and cryptography.

Manuscript received: 30 October 2022,
Revised: 20 November 2022,
Accepted: 22 November 2022.

[1] nithin@nias.res.in (**Corresponding author**)

The Tent map and their skewed cousins (Skew Tent map) are instances of a larger family of maps namely Generalized Lüroth Series (GLS) which are studied for their rich number theoretic and ergodic properties (Dajani and Kraaikamp 2002; Barrera and Robert 2022). In this work, we discuss the unreasonable effectiveness of the Tent map and their generalizations (GLS maps) in a number of applications in electronics, communication and computer engineering. To list a few of these applications: (a) GLS-coding (Nagaraj *et al.* 2009): a lossless data compression algorithm for independent and identically distributed (i.i.d) sources is Shannon optimal and is in fact a generalization of the popular Arithmetic Coding (Rissanen and Langdon 1979) algorithm used in the image compression standard JPEG2000; (b) GLS maps are used as neurons in a recently proposed novel *Neurochaos Learning* (Balakrishnan *et al.* 2019; Harikrishnan and Nagaraj 2021; Harikrishnan *et al.* 2022b) architecture which delivers state-of-the-art performance in classification tasks; (c) GLS maps are ideal candidates for chaos-based comput-

ing since they can simulate XOR, NAND and other gates (Sinha and Ditto 1998; Ditto *et al.* 2010; Jaimes-Reátegui *et al.* 2014) and for dense storage of information for efficient search and retrieval (Miliotis *et al.* 2008); (d) Noise-resistant versions of GLS maps are useful for signal multiplexing in the presence of noise (Nagaraj and Vaidya 2009) and error detection (Nagaraj 2019); (e) GLS maps are shown to be useful in a number of cryptographic protocols (Nagaraj 2012) - for joint source coding and encryption (Nagaraj *et al.* 2009; Wong *et al.* 2010) and also for generating pseudo-random numbers (Palacios-Luengas *et al.* 2019; Addabbo *et al.* 2006); (f) Skew-tent maps have been employed in chaos based communications (Hasler and Schimming 2000). The unique properties and rich features of the Tent Map and its skewed cousins (GLS maps) that enable these wide variety of engineering applications will be discussed.

This paper is organized as follows. In the next section we introduce the Tent map, Binary map and Generalized Lüroth Series (GLS). The unique properties of GLS are enumerated. What makes these GLS maps so attractive to a host of engineering applications? In the following section, the unreasonable effectiveness of the chaotic Tent map/GLS maps are discussed. We conclude with some open issues and suggest a few pointers for exciting future research.

TENT MAP, BINARY MAP AND GENERALIZED LÜROTH SERIES (GLS)

In this section, we define the Tent map and other closely related maps. We shall also describe the properties of these maps.

The Tent map (Figure 1(a)) is defined as $T : [0,1) \rightarrow [0,1)$:

$$T(x) = \begin{cases} 2x, & 0 \leq x < 0.5, \\ 2-2x, & 0.5 \leq x < 1. \end{cases} \tag{1}$$

The Skew-Tent map (Figure 1(b)) is a generalization of the Tent map and is defined as $T_b : [0,1) \rightarrow [0,1)$:

$$T_b(x) = \begin{cases} \frac{x}{b}, & 0 \leq x < b, \\ \frac{(1-x)}{(1-b)}, & b \leq x < 1, \end{cases} \tag{2}$$

where $0 < b < 1$ is the skew parameter. Setting $b = 0.5$ in Eq. 2 gives us the Tent map $T(x)$.

The Binary map (also known as Bernoulli Shift map, Figure 1(e)) is defined as $T : [0,1) \rightarrow [0,1)$:

$$T_{binary}(x) = \begin{cases} 2x, & 0 \leq x < 0.5, \\ 2x-1, & 0.5 \leq x < 1. \end{cases} \tag{3}$$

A similar extension to Skew Binary map is also possible. In these examples, the maps are piecewise linear onto $[0,1)$ with either a positive slope or negative slope. Generalizing this to an arbitrary finite number of intervals yields the 1D Generalized Lüroth Series or GLS maps (Figure 1(f)). The GLS map is defined as $T_{GLS} : [0,1) \rightarrow [0,1)$:

$$T_{GLS}(x) = \begin{cases} \frac{x}{p_1}, & 0 \leq x < p_1, \\ \frac{x-p_1}{p_2}, & p_1 \leq x < p_1+p_2. \\ \ldots & \\ \frac{x-\sum_1^{N-1} p_i}{p_N}, & \sum_1^{N-1} p_i \leq x < 1, \end{cases} \tag{4}$$

where the set of intervals $\{a_1, a_2, \ldots, a_N\}$ have lengths $\{p_1, p_2, \ldots, p_N\}$ respectively (note: $\sum_1^N p_i = 1$). In each of the intervals a_i, we have a linear mapping with a positive slope, but we could have chosen a line with negative slope instead. Thus, there are 2^N different GLS maps (piecewise linear) having the exact same set of intervals with the same lengths. They only differ in the sign of the slope of the linear mapping in one or more of the intervals (without any intrinsic change in chaotic dynamics).

It is easy to see that the Tent map, Binary map and their skewed cousins are all special instances of this family of 1D Generalized Lüroth Series (GLS) maps which we have defined above. We have to appropriately choose the set of intervals $\{a_i\}$ and their lengths $\{p_i\}$. Note that the set of intervals forms a Generating Markov Partition (GMP) on $[0,1)$ for the GLS map.

Properties of GLS

GLS maps exhibit several interesting properties. We list a few of them here:

1. Continuity: GLS maps are piecewise linear and could be either continuous or not. This depends on the transition of the linear mapping across adjacent intervals a_i, a_j - whether there is a corner or not. Even if a GLS is continuous, it is not differentiable at the corner points.

2. Lebesgue measure and invariant distribution: GLS maps preserve the Lebesgue measure (Dajani and Kraaikamp 2002; Boyarski and Gora 1998) and has the uniform distribution on $[0,1)$ as the invariant distribution (Figure 1(d)).

3. Generating Markov Partition: the set of intervals $\{a_1, a_2, \ldots, a_N\}$ with lengths $\{p_1, p_2, \ldots, p_N\}$ forms a Generating Markov Partition (GMP).

4. Symbolic dynamics on GLS: given the GMP on the GLS, we can associate symbols from the alphabet $\{'0', '1', \ldots, 'N-1'\}$ to the N intervals $\{a_1, a_2, \ldots, a_N\}$ respectively. Every initial value on the GLS yields a trajectory which can be associated with a *unique symbolic sequence* consisting of symbols from this alphabet (Dajani and Kraaikamp 2002; Nagaraj 2008).

5. Relationship between Lyapunov Exponent and Shannon Entropy: the lyapunov exponent λ of GLS map with the GMP defined in Figure 1(f) is given by:

$$\lambda_{GLS} = -\sum_{i=1}^{N} p_i \log(p_i). \tag{5}$$

The Shannon Entropy H of the symbolic sequence on the GLS is given by:

$$H_{GLS} = -\sum_{i=1}^{N} p_i \log_2(p_i) \ \ bits/symbol. \tag{6}$$

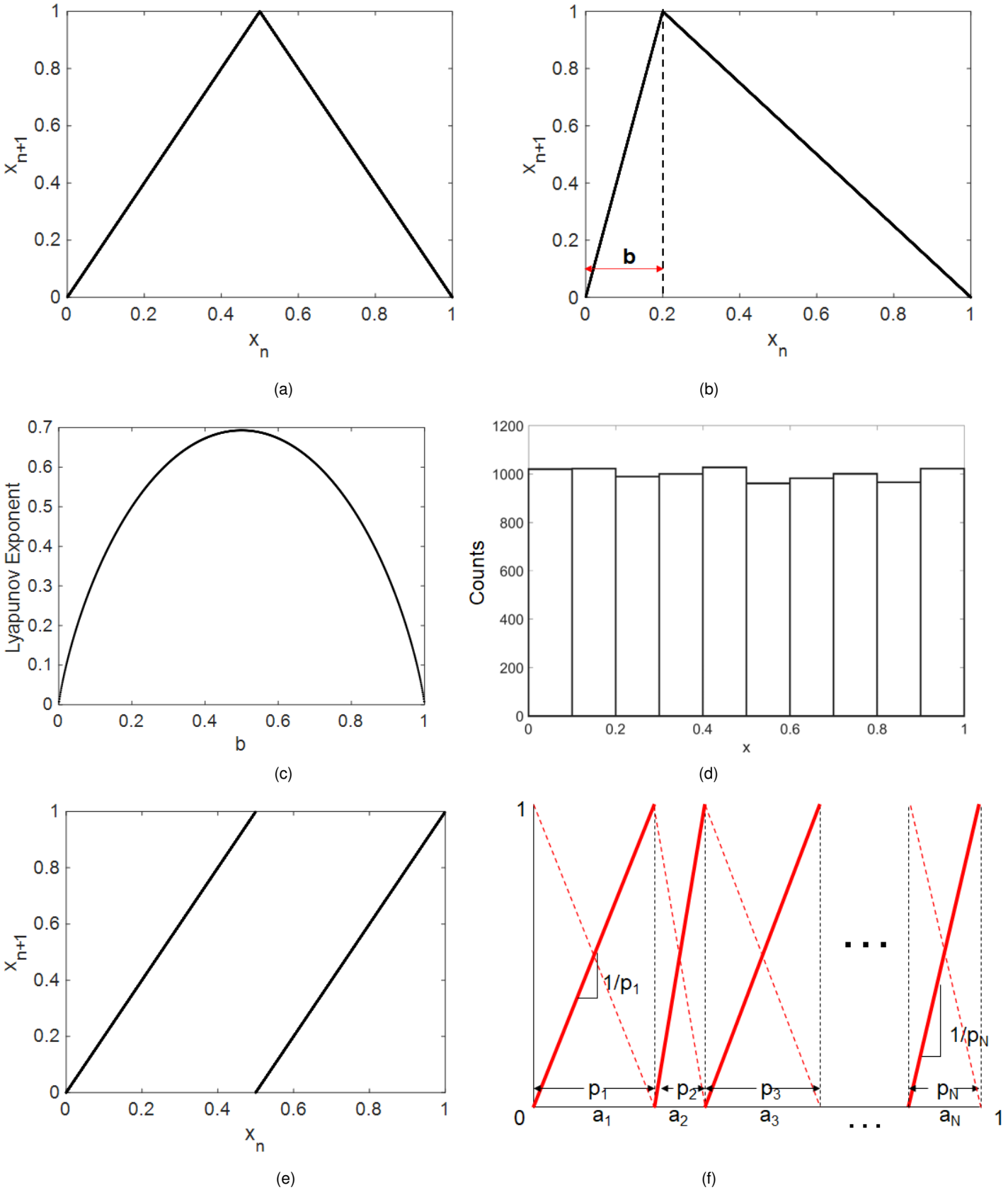

Figure 1 (a) Tent map, (b) Skew Tent Map, (c) Lyapunov exponents of the skew tent maps for different values of skew parameter b, (d) Histogram of a trajectory on the Tent map for a randomly chosen initial value, (e) Binary map, (f) Generalized Lüroth Series (GLS).

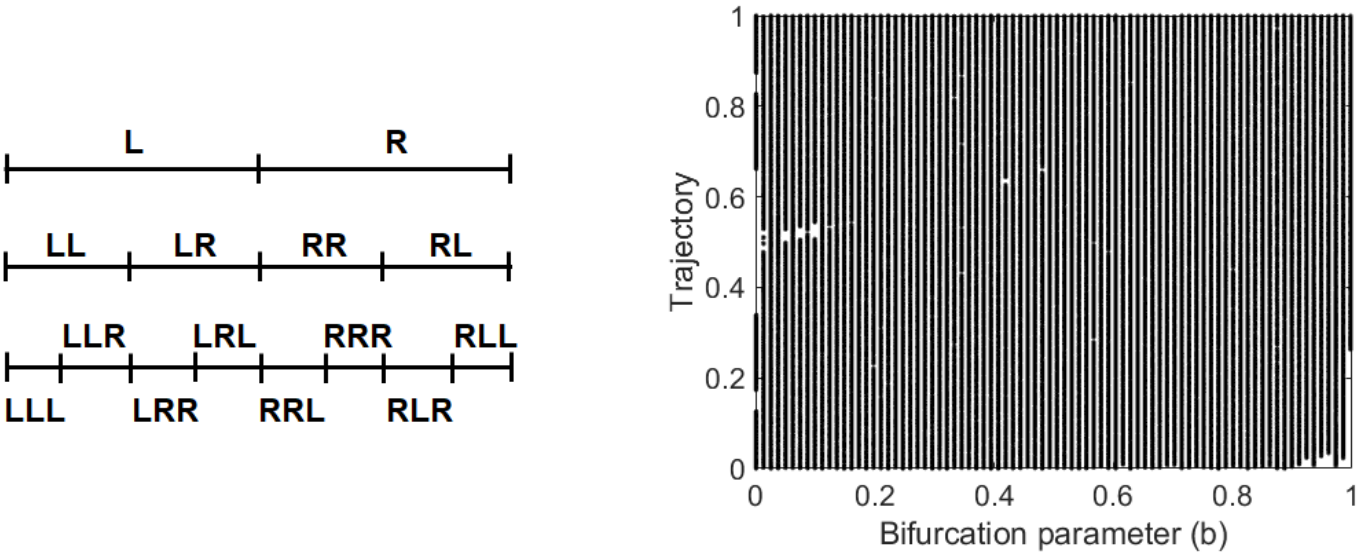

(a) (b)

Figure 2 (a) Symbolic sequences of different orders on the Tent map. These form a *Gray Code*, (b) Bifurcation diagram for the Skew Tent Map. Absence of *windows* or attracting periodic orbits indicating *Robust Chaos*.

If the base of the logarithm is chosen as 2 in computation of the lyapunov exponent in Eq. 5, then we have $\lambda_{GLS} = H_{GLS}$ (Nagaraj 2008). We can interpret the lyapunov exponent as the number of bits of information of the initial value that is revealed at every iteration of the map. This equality plays a very significant role in lossless data compression of i.i.d sources (Nagaraj *et al.* 2009).

6. Periodic, quasi-periodic and chaotic behaviour: it is well known that the Tent map, Binary map, their skewed versions - all of these maps exhibit chaotic behaviour (Devaney 2018). This is indicated both by a positive lyapunov exponent (Figure 1(c)) for every value of $0 < b < 1$ and by the bifurcation diagram that reveals the fact that the entire family of GLS maps exhibit *Robust Chaos* (Banerjee *et al.* 1998; Glendinning 2017) - characterized by complete absence of attracting periodic orbits (Figure 2(b)), also known as *windows*. This is a very desirable property for a number of applications such as pseudorandom number generators (Nagaraj *et al.* 2008), chaos based cryptographic protocols and joint compression and encryption algorithms. As per Devaney's definition of chaos (Devaney 2018), GLS maps also have countably infinite number of periodic and quasi-periodic orbits that are dense, uncountably infinity of non-periodic trajectories and also exhibit sensitive dependence on initial values (the *Butterfly Effect*). The topological entropy of GLS is positive.

7. Ergodicity, mixing properties - as already noted, GLS maps preserve the Lebesque measure. They are also known to be ergodic and exhibit mixing. Variations of GLS show different degrees of mixing - weak and strong mixing. For more details, the reader is referred to Dajani and Kraaikamp (2002).

8. Topological transitivity and Universal orbits: GLS maps exhibit topological transitivity property defined as follows.

   Topological transitivity: for every pair of non-empty open sets $A, B \in [0,1)$, there exists a non-negative integer m such that $T^m(A) \cap B \neq \varnothing$. Equivalently, there exists at least one initial value in A which when iterated a finite number of times ($m \geq 0$ iterations) reaches B.

   Universal orbits (also known as *dense orbits*) are special non-periodic trajectories which visit every possible non-empty neighbourhoods of $[0,1)$. Equivalently, there exists an initial value $x_0 \in [0,1)$ such that the set $\{x_0, T(x_0), T^2(x_0), \ldots, T^k(x_0), \ldots\}$ is dense in $[0,1)$. This property is of utmost importance in Neurochaos Learning (NL) (Balakrishnan *et al.* 2019).

9. Number theoretic properties - Dajani and Kraaikamp (2002) discuss number theoretic properties of GLS and other variations of GLS (β expansions).

10. Implementation in software and hardware: given the piecewise linear nature of Tent map (and GLS), it enjoys a very low computational complexity for software implementation. There have been a number of hardware/electronic circuit realizations of the Tent map (Valtierra *et al.* 2017; Kumar *et al.* 2018; Hernandez *et al.* 2003; Campos-Cantón *et al.* 2009).

11. Nonlinear GLS: Nagaraj *et al.* (2009) propose a non-linear extension to GLS which preserves the Lebesgue measure that finds applications in joint compression and encryption techniques.

Table 1 Details of research works that have employed Tent/GLS maps (or their variations) in applications pertaining to electronics, communication (coding, error correction/detection, encryption) and computer science and engineering. This is not an exhaustive list.

Reference	Properties of GLS used	Applications
Hasler et al., 2000	Chaotic synchronization	Chaos shift keying using iterations of the skew tent map, chaotic communication systems.
Dajani et al., 2002	Ergodicity, mixing	Number theory.
Miliotis et al., 2008	"Be-headed" Tent map	Efficient and flexible storage, very fast search, amenable for parallel implementation.
Nagaraj et al., 2009	$\lambda_{GLS} = H_{GLS}$	GLS-coding: Shannon optimal lossless compression for i.i.d sources. Generalization of Arithmetic Coding that is used in JPEG2000.
Nagaraj et al., 2009	Noise-resistant GLS maps, symbolic sequence invariance	Multiplexing and de-multiplexing chaotic signals in the presence of noise.
Campos-Cantón et al., 2013	Chaos and ergodicity of the Tent map	Reconfigurable logical cell using evolutionary computation.
Wong et al., 2010	GLS maps with key-based switching	Simultaneous arithmetic coding or GLS-coding and encryption.
Nagaraj, 2012	Ergodicity/mixing	Joint compression and encryption. One-Time Pads that achieve unbreakable encryption (Perfect Secrecy) are nothing but switched GLS-coding.
Nagaraj, 2019	Cantor sets on GLS maps with a forbidden symbol	Error detection, joint compression and error control coding.
Palacios-Luengas et al., 2019	Ergodcity/mixing properties of Skew-Tent map	Psuedo Random Number Generators.
Balakrishnan et al., 2019	GLS used as a neuron. Topological transitivity, universal orbits, chaotic features	Brain-inspired machine learning (Neurochaos Learning or NL) for classification. State-of-the-art performance in low training sample regime.
Balakrishnan et al., 2021	Stochastic resonance at a GLS neuron	NL for classification tasks.
Balakrishnan et al., 2022	Topological transitivity, universal orbits, chaotic features of trajectories on GLS	Efficient classification of SARS-CoV-2 viral genome sequences using NL.
Balakrishnan et al., 2022	Causality preservation property of network of GLS neurons	Causality and machine Learning using NL. Deep learning fails to preserve causality.
Ajai et al., 2022	Heterogeneous network of GLS and Logistic map neurons	Classification tasks, further boost in performance of heterogeneous NL architecture

UNREASONABLE EFFECTIVENESS OF TENT/GLS MAPS

Table 1 is an attempt to succinctly summarize some of the published past research works that employ the Tent/GLS maps (or their variations) for applications in electronics and communications, computer science and engineering. It is by no means an exhaustive list of such published research. The specific maps used and the properties of these maps that enable these applications are also mentioned.

Why not Logistic map?

One may be wondering why we have not discussed the logistic map which is also an equally popular 1D chaotic map. In fact, logistic map is continuous and differentiable (unlike GLS maps which can only be continuous at best). There are a number of published research papers on properties and applications of the logistic map as well.

One of the most important reasons why the Tent map and GLS maps are preferable (over the Logistic map) in engineering applications is due to the piecewise linear nature of these maps. This enables an easy implementation of these maps in hardware and software. Furthermore, one of the important issues in the implementation of any dynamical system is finite numerical precision. Given an arbitrarily long symbolic sequence from a GMP of a GLS, it is possible to find the initial value to arbitrary precision. This is made possible because of the connection between GLS and Arithmetic Coding. Using ideas of finite precision implementation (such as scaling and re-normalization) of Arithmetic Coding, we can determine the initial value of a given arbitrarily long symbolic sequence on the GLS. This is used in GLS-coding as well as in multiplexing and de-multiplexing of chaotic signals in the presence of noise. Please see Nagaraj and Vaidya (2009) (Appendix) which describes this algorithm in detail.

This is also the reason that other 1D/2D maps such as the Standard Map, Sine Map, Circle Map, Hénon Map etc. are not preferred in practical engineering applications where finite precision effects can lead to problems.

Symbolic dynamics on GLS

Figure 2(a) depicts the symbolic sequences on the Tent map upto order 3. These sequences produces a *Binary Gray code*. A Gray code has the unique property that successive codes differ only in one location. A binary Gray code would have the property that consecutive codewords differ by exactly one hamming distance. Gray codes are widely employed in electromechanical switches to prevent spurious outputs and also in digital communications to enable error correction. This property can be extended to N-ary Gray codes using GLS with N intervals. The requirement for Gray codes is that the GLS should be continuous on the entire set $[0, 1)$.

Nagaraj and Vaidya (2009) construct noise-resistant versions of the Tent map (and Binary map) to enable efficient multiplexing and de-multiplexing of chaotic signals in the presence of noise. They employ the symbolic sequence invariance property and provide a finite precision implementation of finding the initial condition of an arbitrarily long symbolic sequence on the Tent/Binary map. Their scheme is able to multiplex/de-multiplex up to 20 chaotic signals in the presence of additive noise.

Compression, Coding and Cryptography Applications

GLS maps find applications in lossless data compression, joint compression and error detection and in several cryptographic schemes. The reason for the success of GLS maps in these kind of applications is due to the unique property that $\lambda_{GLS} = H_{GLS}$ (along with the property of chaos and ergodcity/mixing). To the best of one's knowledge, such a property is not true with any other map. This allows a very efficient handshake between dynamical properties with infotheoretic properties. The well known Kraft–McMillan inequality and its converse for prefix-free codes and the celebrated Huffman Coding are both related to symbolic dynamics on GLS maps (Nagaraj 2009, 2011).

The Tent map (and GLS maps) preserves the Lebesgue measure, has an uniform distribution as invariant, positive lyapunov exponent for all values of the bifurcation parameter, positive topological entropy and is ergodic. This is highly desirable for cryptographic algorithms, methods and protocols. Block ciphers and stream ciphers are required to have the properties of *confusion* and *diffusion*. These can be translated to strong mixing/ergodicity of the underlying chaotic map (Alvarez and Li 2006). The fact that Skew Tent map with the skew parameter b exhibits *Robust Chaos* for all values of b is very desirable for hardware implementation of cryptographic methods. Since there are no *windows* or attracting periodic orbits for any value of b, this means that perturbations to the parameter b due to noise in hardware implementations do not result in low periodicity. This is the problem with most maps that exhibit *fragile chaos*, i.e., the presence of windows or attracting periodic orbits. The logistic family of maps with the bifurcation parameter a: $x_{n+1} = ax_n(1 - x_n)$ exhibits fragile chaos which is problematic in cryptography applications.

Researchers have also employed GLS maps for simultaneous compression and encryption (Wong *et al.* 2010; Nagaraj *et al.* 2009; Nagaraj 2008, 2019).

Chaos based computing applications

The power of chaotic maps is their ability to generate a wide variety of patterns. This feature is available in even simple 1D maps that exhibit chaos such as the Logistic map and Tent map. Sinha and Ditto (1998) proposed, for the very first time, thresholded logistic map to emulate logic gates, encode numbers and perform simple arithmetic operations such as addition, multiplication and least common multiplier of a given sequence of integers. Since the publication of this pioneering work by Sinha and Ditto, several other researchers have contributed to this rich field of chaos-based computing. Ditto *et al.* (2010) proposes the *Chaogate* – a dynamical universal computing device which can be rapidly morphed to serve as any desired logic gate. Experimental realization of the same using a chaotic circuit has also been accomplished (Murali *et al.* 2005).

While the above research works focused on the Logistic map, it is easily translatable to the Tent map since there exists a topological conjugacy between these two maps (Alligood *et al.* 2000). There have been attempts also to use the Tent map for designing a reconfigurable logical cell (Campos-Cantón *et al.* 2013). Miliotis *et al.* (2008) employs the "be-headed" Tent map (or thresholded Tent map) ingeniously to efficiently and flexibly store information. They demonstrate how a single element can store M items (M could potentially be very large) and a very fast search by means of a single global shift operation is possible. Such a scheme is amenable for parallel implementation of chaos-based computing architectures.

Machine Learning: Neurochaos Learning using GLS neurons

One of the recent applications of GLS maps is in the design and construction of a novel neural network composed of GLS neurons as the input layer. This learning architecture is dubbed *Neurochaos Learning* or NL (Balakrishnan *et al.* 2019; Harikrishnan and Nagaraj 2021; Harikrishnan *et al.* 2022b). NL draws inspiration from the empirical fact that chaos is ubiquitous in the brain and found to manifest at several spatiotemporal scales - at the level of single neurons, coupled neurons and network of neurons (Korn and Faure 2003). The performance of NL on publicly available datasets for classification tasks in the domains of medical diagnosis, banknote fraud detection, environmental applications and spoken-digit classification is impressive and comparable to state-of-the-art Machine Learning (ML) and Deep Learning (DL) algorithms. Sethi *et al.* (2022) propose a hybrid learning architecture composed of chaos-based features from GLS neurons (NL) fed to classical ML algorithms such as Support Vector Machines, Logistic Regression, AdaBoost, Decision Trees, Random Forest, $k-$Nearest Neighbours and Naive Bayes classifiers. Such an approach provides a significant boost to the performance of standalone ML algorithms thereby indicating the efficacy of chaos-based features extracted from GLS neurons.

GLS neurons are shown to satisfy a version of the *Universal Approximation Theorem* (UAT) (Harikrishnan *et al.* 2022b) which is very desirable for learning algorithms since it allows for approximating complicated decision boundaries. The property of topological transitivity combined with presence of universal/dense orbits and ergodic/mixing properties of GLS makes it effective for machine learning applications. Another surprising property of GLS neurons is that an intermediate amount of noise added to the input is beneficial for classification performance in NL architecture (Harikrishnan and Nagaraj 2021). This is the well known *Stochastic Resonance* or noise-enhanced signal processing property found in certain nonlinear systems. Ajai *et al.* (Sep. 2022) provide a heterogeneous Neurochaos Learning architecture using both GLS neurons and logistic map neurons to further enhance classification performance. GLS neurons also help preserve causality unlike Deep Learning architectures (Harikrishnan *et al.* 2022a).

CONCLUSION AND FUTURE WORKS

In this paper, we have explored the unique properties of the chaotic Tent map and more generally of Generalized Lüroth Series (GLS) maps. The Tent map, Binary map, Skew Tent maps are all examples of 1D GLS maps. We have discussed which specific properties of these maps contribute to their effectiveness in various engineering applications. To conclude, we shall list some pointers and directions for further research:

1. Harikrishnan *et al.* (2022b) have proven a version of the Universal Approximation Theorem (UAT) using GLS maps as neurons in the input layer of a novel learning architecture (NL). Further explorations on various versions of UAT and connections to standard Artificial Neural Networks (ANNs) and NL is a research direction worth investigating.

2. Coupled GLS maps for Neurochaos Learning: currently NL architecture consists of an input layer of 1D GLS maps which are independent of each other. Going forward, it would be interesting to explore addition of hidden layers to the network that consists of GLS maps which are coupled to the previous layers. Coupling between GLS neurons within each layer also needs to be explored. Such a *Deep* Neurochaos Learning architecture could further boost classification performance.

3. GLS maps have already proved their effectiveness in lossless data compression, joint compression and error detection and joint compression and encryption. However, incorporating an efficient error correction property along with compression and/or encryption has been elusive. This is an open problem.

4. GLS maps and other 1D chaotic maps (such as Logistic map) have shown promise in chaos based computing schemes. Have these matured to a stage where they can give serious competition to classical computer architectures?

5. GLS and their variations, especially β expansions have rich number theoretic properties. Is it possible to use these in practical engineering applications?

6. It is well understood that digital implementation of dynamical systems results in degradation of chaotic and ergodic properties (Li *et al.* 2005). Have we realized the full implications of these in practical applications involving GLS maps? What corrections are necessitated to combat the dynamical degradation of digital piecewise chaotic maps?

7. Another open problem is an efficient software implementation of determining the initial value for an arbitrarily long symbolic sequence on other 1D maps such as the Logistic map (without running into numerical precision issues). As mentioned earlier, such a method exists for the Tent map (GLS maps) but no such efficient method is known for other maps which are not piecewise linear.

To conclude, we foresee exciting novel applications of GLS maps in new domains. The (un)reasonable effectiveness of GLS maps (Tent map included) in engineering applications owe to a unique set of properties which other maps do not enjoy.

Acknowledgments

This work is dedicated to (late) Prof. Prabhakar G. Vaidya who introduced me to the fascinating world of chaos, fractals and specifically the Tent map and its amazing properties. I am also grateful to Dr. Kishor G. Bhat for introducing me to the rich literature on Generalized Lüroth Series.

Availability of data and material

Not applicable.

Conflicts of interest

The author declares that there is no conflict of interest regarding the publication of this paper.

LITERATURE CITED

Addabbo, T., M. Alioto, A. Fort, S. Rocchi, and V. Vignoli, 2006 The digital tent map: Performance analysis and optimized design as a low-complexity source of pseudorandom bits. IEEE Transactions on Instrumentation and Measurement **55**: 1451–1458.

Ajai, R. A., H. N. Balakrishnan, and N. Nagaraj, Sep. 2022 Analysis of logistic map based neurons in neuorchaos learning architectures for data classification. Meeting for the Dissemination and Research in the Study of Complex Systems and their Applications (EDIESCA 2022) .

Alligood, K. T., T. Sauer, and J. A. Yorke, 2000 *Chaos: an introduction to dynamical systems*. Springer New York.

Alvarez, G. and S. Li, 2006 Some basic cryptographic requirements for chaos-based cryptosystems. International journal of bifurcation and chaos **16**: 2129–2151.

Balakrishnan, H. N., A. Kathpalia, S. Saha, and N. Nagaraj, 2019 Chaosnet: A chaos based artificial neural network architecture for classification. Chaos: An Interdisciplinary Journal of Nonlinear Science **29**: 113125.

Banerjee, S., J. A. Yorke, and C. Grebogi, 1998 Robust chaos. Physical Review Letters **80**: 3049.

Barrera, R. A. and G. G. Robert, 2022 Chaotic sets and hausdorff dimension for lüroth expansions. Journal of Mathematical Analysis and Applications p. 126324.

Boyarski, A. and P. Gora, 1998 Laws of chaos. invariant measures and dynamical systems in one dimension. APPLICATIONS OF MATHEMATICS-PRAHA- **43**: 480–480.

Campos-Cantón, I., E. Campos-Cantón, J. Murguía, and H. Rosu, 2009 A simple electronic circuit realization of the tent map. Chaos, Solitons & Fractals **42**: 12–16.

Campos-Cantón, I., L. M. Torres-Treviño, E. Campos-Cantón, and R. Femat, 2013 Generation of a reconfigurable logical cell using evolutionary computation. Discrete Dynamics in Nature and Society **2013**.

Dajani, K. and C. Kraaikamp, 2002 Ergodic theory of numbers, volume 29 of carus mathematical monographs. Mathematical Association of America, Washington, DC p. 1.

Devaney, R. L., 2018 *An introduction to chaotic dynamical systems*. CRC press.

Ditto, W. L., A. Miliotis, K. Murali, S. Sinha, and M. L. Spano, 2010 Chaogates: Morphing logic gates that exploit dynamical patterns. Chaos: An Interdisciplinary Journal of Nonlinear Science **20**: 037107.

Glendinning, P., 2017 Robust chaos revisited. The European Physical Journal Special Topics **226**: 1721–1738.

Harikrishnan, N., A. Kathpalia, and N. Nagaraj, 2022a Cause-effect preservation and classification using neurochaos learning. NeurIPS 2022 p. accepted.

Harikrishnan, N. and N. Nagaraj, 2021 When noise meets chaos: Stochastic resonance in neurochaos learning. Neural Networks **143**: 425–435.

Harikrishnan, N., S. Pranay, and N. Nagaraj, 2022b Classification of sars-cov-2 viral genome sequences using neurochaos learning. Medical & Biological Engineering & Computing pp. 1–11.

Hasler, M. and T. Schimming, 2000 Chaos communication over noisy channels. International Journal of Bifurcation and Chaos **10**: 719–735.

Hernandez, E. D. M., G. Lee, and N. H. Farhat, 2003 Analog realization of arbitrary one-dimensional maps. IEEE Transactions on Circuits and Systems I: Fundamental Theory and Applications **50**: 1538–1547.

Jaimes-Reátegui, R., S. Afanador-Delgado, R. Sevilla-Escoboza, G. Huerta-Cuellar, J. H. García-López, *et al.*, 2014 Optoelectronic flexible logic gate based on a fiber laser. The European Physical Journal Special Topics **223**: 2837–2846.

Korn, H. and P. Faure, 2003 Is there chaos in the brain? ii. experimental evidence and related models. Comptes rendus biologies **326**: 787–840.

Kumar, D., K. Nabi, P. K. Misra, and M. Goswami, 2018 Modified tent map based design for true random number generator. In *2018 IEEE International Symposium on Smart Electronic Systems (iSES)(Formerly iNiS)*, pp. 27–30, IEEE.

Li, S., G. Chen, and X. Mou, 2005 On the dynamical degradation of digital piecewise linear chaotic maps. International journal of Bifurcation and Chaos **15**: 3119–3151.

Miliotis, A., S. Sinha, and W. L. Ditto, 2008 Exploiting nonlinear dynamics to store and process information. International Journal of Bifurcation and Chaos **18**: 1551–1559.

Murali, K., S. Sinha, and W. L. Ditto, 2005 Construction of a reconfigurable dynamic logic cell. Pramana **64**: 433–441.

Nagaraj, N., 2008 *Novel applications of chaos theory to coding and cryptography*. Ph.D. thesis, NIAS.

Nagaraj, N., 2009 A dynamical systems proof of kraft–mcmillan inequality and its converse for prefix-free codes. Chaos: An Interdisciplinary Journal of Nonlinear Science **19**: 013136.

Nagaraj, N., 2011 Huffman coding as a nonlinear dynamical system. International Journal of Bifurcation and Chaos **21**: 1727–1736.

Nagaraj, N., 2012 One-time pad as a nonlinear dynamical system. Communications in Nonlinear Science and Numerical Simulation **17**: 4029–4036.

Nagaraj, N., 2019 Using cantor sets for error detection. PeerJ Computer Science **5**: e171.

Nagaraj, N., M. C. Shastry, and P. G. Vaidya, 2008 Increasing average period lengths by switching of robust chaos maps in finite precision. The European Physical Journal Special Topics **165**: 73–83.

Nagaraj, N. and P. G. Vaidya, 2009 Multiplexing of discrete chaotic signals in presence of noise. Chaos: An Interdisciplinary Journal of Nonlinear Science **19**: 033102.

Nagaraj, N., P. G. Vaidya, and K. G. Bhat, 2009 Arithmetic coding as a non-linear dynamical system. Communications in Nonlinear Science and Numerical Simulation **14**: 1013–1020.

Palacios-Luengas, L., J. Pichardo-Méndez, J. Díaz-Méndez, F. Rodríguez-Santos, and R. Vázquez-Medina, 2019 Prng based on skew tent map. Arabian Journal for Science and Engineering **44**: 3817–3830.

Rissanen, J. and G. G. Langdon, 1979 Arithmetic coding. IBM Journal of research and development **23**: 149–162.

Sethi, D., N. Nagaraj, and H. N. Balakrishnan, 2022 Neurochaos feature transformation for machine learning. in EDIESCA 2022 .

Sinha, S. and W. L. Ditto, 1998 Dynamics based computation. physical review Letters **81**: 2156.

Strogatz, S. H., 2018 *Nonlinear dynamics and chaos: with applications to physics, biology, chemistry, and engineering*. CRC press.

Valtierra, J. L., E. Tlelo-Cuautle, and Á. Rodríguez-Vázquez, 2017 A switched-capacitor skew-tent map implementation for random number generation. International Journal of Circuit Theory and Applications **45**: 305–315.

Wong, K.-W., Q. Lin, and J. Chen, 2010 Simultaneous arithmetic coding and encryption using chaotic maps. IEEE Transactions on Circuits and Systems II: Express Briefs **57**: 146–150.

How to cite this article: Nagaraj, G. The Unreasonable Effectiveness of the Chaotic Tent Map in Engineering Applications. *Chaos Theory and Applications*, 4(4), 197-204, 2022.

CHAOS
Theory and Applications
in Applied Sciences and Engineering

e-ISSN: 2687-4539
RESEARCH ARTICLE
Vol.4 / No.4 / 2022 / pp.205-211
Special Issue (EDIESCA 2022)
https://doi.org/10.51537/chaos.1185892

Multi-scroll Systems Synchronization on Strongly Connected Digraphs

Eber J. Ávila-Martínez [*,1], **J.L. Echenausía-Monroy** [α,2] **and A. Ruiz-Silva** [β,3]

[*] Innovaciones Tecnológicas Mercado S.A. de C.V., Av. Sierra Leona 418, Lomas 2a Secc., 78210, San Luis Potosí, S.L.P., México., [α] Applied Physics Division, Center for Scientific Research and Higher Education at Ensenada, CICESE. Carr. Ensenada-Tijuana 3918, Zona Playitas, Ensenada, 22860, B. C., México., [β] Programa de Ingeniería en Sistemas Biomédicos. Universidad Estatal de Sonora, Unidad Hermosillo, Ley Federal del Trabajo, Col. Apolo, 83100, Hermosillo, Sonora, México.

ABSTRACT In this paper, we study the synchronization problem in complex dynamic networks of Piece Wise Linear (PWL) systems. PWL systems exhibit multi-scrolls and belong to a special class of Unstable Dissipative Systems (UDS). We consider strongly connected digraphs and linear diffusive couplings. The synchronization regions are computed using the concept of disagreement vectors, generalized algebraic connectivity of the network topology, and Lyapunov functions, which provide lower bounds on the coupling gain of the network. Then, different combinations of linear diffusive coupling are explored by changing the observed and measured variables to illustrate the contribution of our results. The theoretical results are validated by numerical simulations.

KEYWORDS
Synchronization; Complex networks
Digraphs
Multi-Scroll attractors
Unstable dissipative systems.

INTRODUCTION

In the last decade, the study of synchronization phenomena in a group of coupled Piece-Wise Linear (PWL) in the context of nonlinear systems theory has attracted considerable attention due to its wide application in fields such as physics, biology, and engineering, among others (Muñoz-Pacheco *et al.* 2012; Anzo-Hernández *et al.* 2019; Carbajal-Gómez and Sánchez-López 2019; Ruiz-Silva *et al.* 2021; Echenausía-Monroy *et al.* 2021; Ruiz-Silva *et al.* 2022).

One way to analyze these kinds of interconnected systems is to model them as complex networks whose nodes are the individual dynamical systems and the coupling is represented by a static graph. One of the most important aspects in the study of complex networks and their emergent behaviour is the structural analysis of the topology and dynamical properties of their nodes, to determine the conditions under which a set of interconnected dynamical systems achieve stable collective behaviour (Boccaletti *et al.* 2006; Wu 2007; Ávila-Martínez and Barajas-Ramírez 2018, 2021; Ávila-Martínez 2022). In this context, the term *synchronization* refers to the collective phenomenon in which two or more elements exhibit temporally coordinated dynamical behaviour (Boccaletti *et al.* 2002; Pikovsky *et al.* 2002).

A starting point for the study of synchronization in complex networks, whether a PWL or other non-linear system, is the assumption that nodes are identical, links are static, and coupling is diffusive. The diffusive condition is a basic assumption in this type of problem because it is a requirement that occurs naturally in many real-world networks and is a relatively soft condition on the structure of the network model (Chen *et al.* 2014). On the other hand, to achieve synchronization in a complex network, it is possible to consider different properties of the network links, such as unidirectional couplings (Anzo-Hernández *et al.* 2019; Posadas-Castillo *et al.* 2014), bidirectional or symmetric couplings (Ruiz-Silva *et al.* 2022; Soriano-Sánchez *et al.* 2016), connections with weights (Ruiz-Silva *et al.* 2021; Ontañón-García *et al.* 2021) or changes in the nature of the coupling functions (Echenausía-Monroy *et al.* 2021; Mishra *et al.* 2022). All these properties are reflected in the stability analysis of the synchronized behaviour, and some of them simplify it.

In this paper, we focus on the synchronization problem for a complex network under a fixed communication structure, where the dynamics of each node belongs to a class of affine linear systems. Traditionally, this problem can be approached by studying the system stability of the error around the synchronization solution using the λ_2 criterion (Chen *et al.* 2014), or the master stability function method (Pecora and Carroll 1998; Huang *et al.* 2009).

The method proposed in this paper is essentially compatible

Manuscript received: 7 October 2022,
Revised: 12 November 2022,
Accepted: 12 November 2022.

[1] phd.eber.avila.martinez@gmail.com (**Corresponding author**).
[2] echenausia@cicese.mx
[3] adriana.ruiz@ues.mx

with the λ_2 criterion since Lyapunov stability theory is used for the node dynamics and synchronization of the complex network. However, it presents a different point of view since the analysis is performed using the stability region of the nodes, the concept of disagreement vectors, and the generalized algebraic connectivity of the network topology (Li *et al.* 2010; Yu *et al.* 2010). First, we focus on the individual dynamics of the nodes and the internal coupling matrix, since unbounded stability regions must be determined to simplify the analysis of network synchronization. Then, using the disagreement vectors, we analyze the effect of the network topology on the stability regions of the nodes, which can be adjusted by the strength of the network coupling. Moreover, it is important to mention that an advantageous feature of this approach is that it can be used in bidirectional or unidirectional topologies as long as they represent strongly connected structures.

The rest of the document is structured as follows: We introduce first the multi-scroll system, the network model, and some helpful graph theory results. Then, we analyze the synchronized behaviour of strongly connected digraphs using the Lyapunov stability theory. We later present a case of study, followed by some numerical simulations illustrating our results. In the end, we discuss some conclusions.

PRELIMINARIES

Multi-Scroll System

It is known that the generation of attractors with multiple scrolls depends on both the stability of the generated equilibrium points and the type of switching function implemented (Echenausía-Monroy *et al.* 2020). It is possible to analyze the stability of the equilibrium points of this type of systems using the Unstable Dissipative Systems (UDS) theory, which describes a variety of three-dimensional systems with dissipative and conservative components. The coexistence of both components leads to the appearance of the so-called attractors with multi-scrolls (Campos-Cantón *et al.* 2010, 2012; Campos-Cantón 2016).

As in previous works (Gilardi-Velázquez *et al.* 2017; Echenausía-Monroy and Huerta-Cuellar 2020), we consider that each dynamical system is defined by a class of affine linear systems given by:

$$\dot{x}_i = Ax_i + B(x_i), \tag{1}$$

where $x_i = [x_{i1},\ x_{i2},\ x_{i3}]^T \in \mathbb{R}^3$ is the state vector of the i-th system, the constant matrix, $A = \{a_{ij}\} \in \mathbb{R}^{3\times 3}$, is the linear operator of the system, and $B = [b_1,\ b_2,\ b_3]^T \in \mathbb{R}^3$ is a vector with real entries. It should be noted that the behavior of the system (1) is determined by the eigen-spectrum of the matrix A, which can produce a variety of combinations and thus different dynamic behaviors.

The class of affine linear systems considered here are UDS of type 1, i.e., the eigenvalues associated with the linear operator A correspond to a hyperbolic saddle point where one eigenvalue is real negative and the other two are complex conjugate with a positive real component. Moreover, the sum of these values must be less than zero (Campos-Cantón *et al.* 2010, 2012; Campos-Cantón 2016). If the affine linear system given by Eq. (1) satisfies the UDS I definition with $B = 0$, then it is possible to generate an attractor with multi-scrolls by constructing a commutation law, in this case a PWL function. The purpose of the commutation function is to generate as many equilibrium points as desired and to control their visitation, which is achieved by coexisting a large number of unstable single-spiral trajectories (Echenausía-Monroy and Huerta-Cuellar 2020; Echenausía-Monroy *et al.* 2020).

Next, before we present the concept of a complex network, we introduce some preliminaries of algebraic graph theory.

Algebraic Graph Theory

A *directed graph* (in short, a *digraph*) of order N, is a pair $\mathcal{G} = (\mathcal{V}, \mathcal{E})$, where $\mathcal{V} = \{1, \ldots, N\}$ is a set of elements called nodes and $\mathcal{E} \subseteq \mathcal{V} \times \mathcal{V}$ is a set of ordered pair of nodes. For $i, j \in \mathcal{V}$ the ordered pair $(j, i) \in \mathcal{E}$ denotes an edge that starts on node j and ends in node i. The neighbourhood of node i is defined as $\mathcal{N}_i := \{j \in \mathcal{V} : (j, i) \in \mathcal{E}\}$. In $\mathcal{G}$ a *directed path* of length m from node i to j is a sequence of edges with distinct nodes n_k, with $k = 1, 2, \ldots, m$, such that $(i, n_1), (n_1, n_2), \ldots, (n_m, j) \in \mathcal{E}$. A graph $\mathcal{G}$ is *strongly connected* if there exists a directed path connecting every nodes pair. A digraph $\mathcal{G}$ is called *weighted* if for every edge $(j, i) \in \mathcal{E}$ there is an associated *weight* $w_{ij} > 0$.

The Laplacian matrix of a weighted digraph $\mathcal{G}$ is a zero row sum non-negative matrix $L = [l_{ij}] \in \mathbb{R}^{N\times N}$ defined as:

$$l_{ij} := \begin{cases} -w_{ij} & \text{if } (j, i) \in \mathcal{E}, \\ \sum_{i=1, j\neq i}^{N} w_{ij} & \text{if } i = j. \end{cases}$$

Now, we present some results related to matrix Laplacians.

Lemma 1. *(Li 2015) Suppose that $\mathcal{G}$ is strongly connected. Then, there is a positive left eigenvector $z = [z_1, \cdots, z_N]^T \in \mathbb{R}^N$ of L associated with the zero eigenvalue and $\hat{L} := ZL + L^TZ \geq 0$, where $Z = Diag(z_1, \cdots, z_N)$.*

Lemma 2. *(Li 2015) For a strongly connected graph $\mathcal{G}$ with Laplacian L, define its generalized algebraic connectivity as*

$$\alpha := \min_{z^Tx=0, x\neq 0} \left\{ \frac{x^T\hat{L}x}{x^TZx} \right\}, \tag{2}$$

where z and Z are defined as in Lemma 1. Then, $\alpha > 0$.

Lemma 3. *(Yu et al. 2010) The generalized algebraic connectivity of a strongly connected digraph $\mathcal{G}$ can be computed by the following:*

$$\begin{aligned} &max && \mu, \\ &subject\ to && Q^T\left(\frac{1}{2}\hat{L} - \mu Z\right)Q \geq 0, \end{aligned} \tag{3}$$

where $Q = \begin{pmatrix} \mathcal{I}_{N-1} \\ -\hat{z}^T/z_N \end{pmatrix} \in \mathbb{R}^{N\times(N-1)}$ *and* $\hat{z} = [z_1, \ldots, z_{N-1}]^T \in \mathbb{R}^{N-1}$.

The Complex Dynamical Network Models

A complex dynamic network is defined as a set of interconnected systems, being each system a fundamental entity whose dynamics depend on the nature of the network (Chen *et al.* 2014). The interaction structure or network topology is modeled by a graph $\mathcal{G} = (\mathcal{V}, \mathcal{E})$, where $\mathcal{V}$ is the set of fundamental units, and an edge $(i, j) \in \mathcal{E}$ depicts the interaction between nodes i and j. Therefore, the state describing the dynamic network are as follows:

$$\dot{x}_i = f(x_i) - c\sum_{j\in\mathcal{N}_i} w_{ij}\Gamma(x_i - x_j), \qquad i \in \mathcal{V}, \tag{4}$$

where $x_i = [x_{i1},\ x_{i2},\ x_{i3}]^T \in \mathbb{R}^3$ is the state vector of node i, the function $f(x_i) = Ax_i + B(x_i)$ can be derived from Eq. (1), and determines the dynamics of an isolated multi-scroll system.

The constant $c > 0$ denotes the uniform coupling strength of the network. Let $\Gamma = Diag(\gamma_1, \gamma_2, \gamma_3) \in \mathbb{R}^{3\times 3}$ be a constant matrix describing the internal coupling between the systems in the network, constructed as follows: if $\gamma_k > 0$ indicates that the ith node and the jth node are coupled by their kth state variable, otherwise $\gamma_k = 0$. The value $w_{ij} > 0$ is the weight of the ij-th edge, portraying the external coupling. The network described by Eq. (4) can be rewritten in terms of the matrix Laplacian entries as follows:

$$\dot{x}_i = Ax_i + B(x_i) - c\sum_{j\in\mathcal{N}_i} \ell_{ij}\Gamma x_j, \qquad i \in \mathcal{V}, \tag{5}$$

which in vector form is given by

$$\dot{x} = \Big((\mathcal{I}_N \otimes A) - c(L\otimes\Gamma)\Big)x + \tilde{B}(x), \tag{6}$$

where $x = [x_1^T, x_2^T, \cdots, x_N^T]^T \in \mathbb{R}^{3N}$, $\tilde{B}(x) = [B(x_1)^T, \cdots, B(x_N)^T]^T \in \mathbb{R}^{3N}$, $\mathcal{I}_N$ is the identity matrix of size $N \times N$, and $\otimes$ denotes the Kronecker product. It is worth noting that the network model describes all kinds of topologies, where they can consider connection patterns with uniform weights or non-uniform connections.

SYNCHRONIZATION PROBLEM AND MAIN RESULTS

One of the most-studied collective behaviors for a set of interconnected systems is the synchronization phenomenon, which emerges when the dynamics of the systems correlate over time (see (Chen *et al.* 2014; Boccaletti *et al.* 2002; Pecora and Carroll 1998; Arenas *et al.* 2008) and references therein). Although there are several definitions of synchronization in dynamic networks, this study focuses on *complete synchronization*. Mathematically, this is defined as follows:

Definition 1. *(Chen* et al. *2014) It is said that the dynamic network* (4) *achieves complete asymptotic synchronization when*

$$\lim_{t\to\infty} \|x_i - x_j\| = 0, \qquad i, j \in \mathcal{V}, \tag{7}$$

where $\|\cdot\|$ *is the Euclidean norm of a vector.*

The goal of this paper is to find sufficient conditions for the nodes in the network to achieve complete synchronization, i.e., to ensure that Eq. (7) is satisfied regardless of the initial conditions. Since the linear operator A, the constant vector $B(\cdot)$, and the matrix Γ have a particular form, synchronization must be achieved by suitably designing the coupling strength, taking into account the structural properties of the network.

Stability Analysis on Strongly Connected Digraphs

Inspired by (R. Olfati-Saber and R. M. Murray 2004; Li *et al.* 2010), we introduce *disagreement functions* to perform stability analysis of the synchronous behavior of the network (6).

Let $z \in \mathbb{R}^N$ be defined as in Lemma 1 such that $z^T\mathbf{1} = 1$, where $\mathbf{1} \in \mathbb{R}^N$ denotes the vector where all entries are ones. Thus, the *disagreement vector* is defined as:

$$\delta := \Big((\mathcal{I}_N - \mathbf{1}z^T)\otimes\mathcal{I}_3\Big)x, \tag{8}$$

where $\delta = [\delta_1^T, \delta_2^T, \ldots, \delta_N^T] \in \mathbb{R}^{3N}$ satisfies the condition $(z^T \otimes I_3)\delta := \mathbf{0}$. It is important to emphasize that $\delta_i = x_i - \sum_{k=1}^N z_k x_k$ and $\delta_i - \delta_j = x_i - x_j$. Thus, by the Definition 1, the synchronization state is reached if and only if $\delta \to \mathbf{0}$ is $t \to 0$. Also, it can be proved that δ evolves according to the development given by *disagreement dynamics*:

$$\dot{\delta} = \Big[(\mathcal{I}_N \otimes A) - c(L\otimes\Gamma)\Big]\delta + \Big[(\mathcal{I}_N - \mathbf{1}z^T)\otimes\mathcal{I}_3\Big]\tilde{B}(x). \tag{9}$$

To show the stability for each of the disagreement vectors, the following assumptions are required for the remainder of this paper:

Assumption 1. *For each configuration of the matrix* $\Gamma = Diag(\gamma_1, \gamma_2, \gamma_3) \in \mathbb{R}^{3\times 3}$ *with* $\Gamma > 0$, *there exist constants* $d > 0$ *and* $\eta > 0$ *such that*

$$A + A^T - d\Gamma \le -\eta\mathcal{I}_3, \tag{10}$$

where $\mathcal{I}_3$ *is the identity matrix of size* 3×3.

Assumption 2. *Let us assume that there are known or unknown non-negative constants* $\beta_{ij} \ge 0$, *so that*

$$\|B(x_i) - B(x_j)\| \le \beta_{ij}\|x_i - x_j\|, \tag{11}$$

with $i \ne j$, *for* $i, j = 1, 2, \cdots, N$.

Under these assumptions, we establish the following result:

Theorem 1. *Suppose that the Assumption 1 holds and that the dynamic network described by Eq.* (6) *is strongly connected. If the coupling strength c satisfies the condition*

$$c \ge \frac{d^*}{\alpha}, \tag{12}$$

where d^* *is a non-positive constant and* α *is the generalized algebraic Fielder's connectivity of* $\mathcal{G}$. *Then the disagreement dynamics is asymptotically stable at the equilibrium, or equivalently* $\delta_i \to 0$, *for any* $i = 1, 2, \cdots, N$. *Consequently, the complex dynamical network* (6) *achieves synchronization.*

Proof. Define the Lyapunov function candidate as:

$$V(\delta) := \frac{1}{2}\delta^T(Z\otimes\mathcal{I}_3)\delta, \tag{13}$$

with the positive matrix $Z = Diag(z_1, z_2, \cdots, z_N) > 0$ defined as in Lemma 1.

The time derivative of Eq. (13) along the trajectories of (9) yields:

$$\dot{V}(\delta) = \delta^T(Z\otimes\mathcal{I}_3)\dot{\delta} = U(\delta) + W(\delta, \tilde{B}(x)), \tag{14}$$

with

$$U(\delta) := \frac{1}{2}\delta^T\Big[\Big(Z\otimes(A + A^T)\Big) - c\,(\hat{L}\otimes\Gamma)\Big]\delta$$
$$W(\delta, \tilde{B}(x)) := \delta^T\Big[Z(\mathcal{I}_N - \mathbf{1}z^T)\otimes\mathcal{I}_3\Big]\tilde{B}(x).$$

Using Lemma 1 and Lemma 2 in $U(\delta)$ we obtain

$$\begin{aligned} U(\delta) &\le \frac{1}{2}\delta^T\Big[\Big(Z\otimes(A + A^T)\Big) - c\alpha\,(Z\otimes\Gamma)\Big]\delta \\ &= \frac{1}{2}\delta^T\Big[\Big(Z\otimes(A + A^T - c\alpha\Gamma)\Big)\Big]\delta \\ &= \frac{1}{2}\sum_{i=1}^N z_i\delta_i^T\Big(A + A^T - c\alpha\Gamma\Big)\delta_i, \end{aligned} \tag{15}$$

where α is the generalized algebraic connectivity of the graph $\mathcal{G}$. For $W(\delta, \tilde{B}(x))$ it is also true that

$$\begin{aligned} W(\delta,\tilde{B}(x)) &= \sum_{i=1}^{N} z_i\delta_i^T\left(B(x_i)-\sum_{k=1}^{N} z_k B(x_k)\right) \\ &= \sum_{i=1}^{N} z_i\delta_i^T\left(B(x_i)-B(\bar{x})+B(\bar{x})-\sum_{k=1}^{N} z_k B(x_k)\right) \\ &= \sum_{i=1}^{N} z_i\delta_i^T\Big(B(x_i)-B(\bar{x})\Big) \\ &\quad +\left(B(\bar{x})-\sum_{k=1}^{N} z_k B(x_k)\right)^T\sum_{i=1}^{N} z_i\delta_i \\ &= \sum_{i=1}^{N} z_i\delta_i^T\Big(B(x_i)-B(\bar{x})\Big), \end{aligned} \tag{16}$$

where $\bar{x} := \sum_{k=1}^{N} z_k x_k$, and we use the fact that $\sum_{i=1}^{N} z_i\delta_i = \mathbf{0}$.

Under Assumption 2, it follows that

$$\begin{aligned} \left\|\sum_{i=1}^{N} z_i\delta_i^T\left(B(x_i)-B(\bar{x})\right)\right\| &\leq \sum_{i=1}^{N} z_i\,\|\delta_i\|\,\|B(x_i)-B(\bar{x})\| \\ &\leq \sum_{i=1}^{N}\beta z_i\,\|\delta_i\|\,\|x_i-\bar{x}\| \\ &\leq \sum_{i=1}^{N}\beta z_i\|\delta_i\|^2, \end{aligned} \tag{17}$$

with $\beta > 0$ is the largest Lipschitz constant of the function $B(\cdot)$.

Substitute Eqs. (15) and (17) into Eq. (14), we get:

$$\begin{aligned} \dot{V} &\leq \frac{1}{2}\sum_{i=1}^{N} z_i\delta_i^T\left(A+A^T-c\alpha\Gamma\right)\delta_i+\sum_{i=1}^{N}\beta z_i\delta_i^T\delta_i \\ &= \sum_{i=1}^{N} z_i\delta_i^T\Big(\frac{1}{2}(A+A^T-c\alpha\Gamma)+\beta\mathcal{I}_3\Big)\delta_i. \end{aligned} \tag{18}$$

Let $d = c\alpha$, then under the Assumption 1 it follows that

$$A + A^T - c\alpha\Gamma \leq -\eta\mathcal{I}_3, \tag{19}$$

with $d^* \leq d = c\alpha$ and $\eta > 0$. Since $d^* > 0$ and $\alpha > 0$, we solve for c from the inequality $d^* \leq c\alpha$ and we have the condition (12). Therefore, the inequality (18) can be rewritten as

$$\dot{V}(\delta) \leq \sum_{i=1}^{N} z_i\Big(\beta-\frac{\eta}{2}\Big)\,\|\delta_i\|^2. \tag{20}$$

Note that the right-hand side of the previous inequality is a quadratic function and $z_i > 0$ for $i = 1, 2, \cdots, N$. Thus, if we choose $\eta > 2\beta$, it follows that $\dot{V}(\delta) < 0$. Consequently, $\delta_i \to \mathbf{0}$ as $t \to \infty$, *i.e.* the network (6) asymptotically synchronizes. □

It should be emphasized that the Assumption 1 provides a bound on the stability of the linear operator A, while the Assumption 2 indicates that the vector B around zero is a fading perturbation. Moreover, the value of α can be computed as in Lemma 3. Up to this point, the Theorem 1 gives such a value for the coupling strength c that $\|\delta_i\| \to 0$ as $t \to \infty$. Thus, there is a certain range for the coupling strength in which the synchronization of the digraph is guaranteed. Notice that other values that can lead to synchronization of the network are not excluded.

A CASE OF STUDY

Consider a multi-scroll system whose dynamics is described by Eq. (1). In particular, take the following dynamic system:

$$\begin{bmatrix}\dot{x}_{i1}\\ \dot{x}_{i2}\\ \dot{x}_{i3}\end{bmatrix} = \underbrace{\begin{bmatrix}0 & 1 & 0\\ 0 & 0 & 1\\ -a & -a & -a\end{bmatrix}}_{A}\begin{bmatrix}x_{i1}\\ x_{i2}\\ x_{i3}\end{bmatrix} + \underbrace{\begin{bmatrix}0\\ 0\\ ab(x_i)\end{bmatrix}}_{B(x_i)}, \tag{21}$$

where $x_i = [x_{i1},\ x_{i2},\ x_{i3}]^T \in \mathbb{R}^3$ is the state vector, a is a dynamical parameter modifying the Lyapunov exponent, the order and the magnitude of the attractor (Echenausía-Monroy *et al.* 2018), and $b(\cdot) : \mathbb{R}^3 \mapsto \mathbb{R}$ is a PWL function given as:

$$b(x_i) = \begin{cases} -6 & \text{if } x_i \in \mathcal{D}_1 = \{\boldsymbol{x_i} \mid x_{i1} < -5\},\\ -4 & \text{if } x_i \in \mathcal{D}_2 = \{\boldsymbol{x_i} \mid -5 \leq x_{i1} < -3\},\\ -2 & \text{if } x_i \in \mathcal{D}_3 = \{\boldsymbol{x_i} \mid -3 \leq x_{i1} < -1\},\\ 0 & \text{if } x_i \in \mathcal{D}_4 = \{\boldsymbol{x_i} \mid -1 \leq x_{i1} < 1\},\\ 2 & \text{if } x_i \in \mathcal{D}_5 = \{\boldsymbol{x_i} \mid 1 \leq x_{i1} < 3\},\\ 4 & \text{if } x_i \in \mathcal{D}_6 = \{\boldsymbol{x_i} \mid 3 \leq x_{i1} < 5\},\\ 6 & \text{if } x_i \in \mathcal{D}_7 = \{\boldsymbol{x_i} \mid x_{i1} \geq 5\}, \end{cases} \tag{22}$$

where $\mathcal{D} = \{\mathcal{D}_1, \cdots, \mathcal{D}_7\}$ is a finite partition of the phase space. As mentioned before, the parameter a in Eq. (21) determines the system's equilibrium points stability, and must satisfy the UDS I conditions (Campos-Cantón *et al.* 2010; Anzo-Hernández *et al.* 2018). To achieve this, a can only take values from the set $a \in (0, 1)$ and thus, generating the same number of scrolls as equilibrium points in the system.

To illustrate that Eqs. (21)-(22) form a multi-scroll system, take $a = 0.6$. Hence, the matrix A has a negative real eigenvalue and two complex conjugate eigenvalues whose sum is negative, i.e.[5]

$$\sigma(A) = \{-0.794,\ 0.097 \pm 0.863\mathbf{i}\},\ \text{and}\ \sum_{i=1}^{3}\sigma_i = -0.6. \tag{23}$$

Under these conditions, system described by Eq. (21) is a UDS type I system. Figure 1 shows its state trajectories with an initial condition $x_i^0 = [5,\ 1,\ 0.13]^T$. In Figure 1(a) we show the projection of the multi-scroll attractor onto the planes $(x_{i1} - x_{i2})$ and $(x_{i1} - x_{i3})$. Figure 1(b) corresponds to the temporal behaviour of the states x_{i1}, x_{i2} and x_{i3} with arbitrary units (a.u.) time.

Dynamical Network

For ease of illustration, consider a network of N identical multi-scroll systems with dynamics described by Eq. (21), with linear and diffusive couplings. Thus, we describe the dynamic network by Eq. (5) and $\beta_{ij} = \beta > 0$, for all $i, j \in \mathcal{V}$, in Assumption 2.

Theorem 1 must satisfy the Assumption 1 and satisfy the inequality (12). Note that in order to obtain an appropriate value for the coupling gain in Eq. (12), we need to compute d as shown in Assumption 1, and Eq. (10) imposes a Hurwitz condition over the

[5] Here $\mathbf{i}$ stands for the imaginary unit.

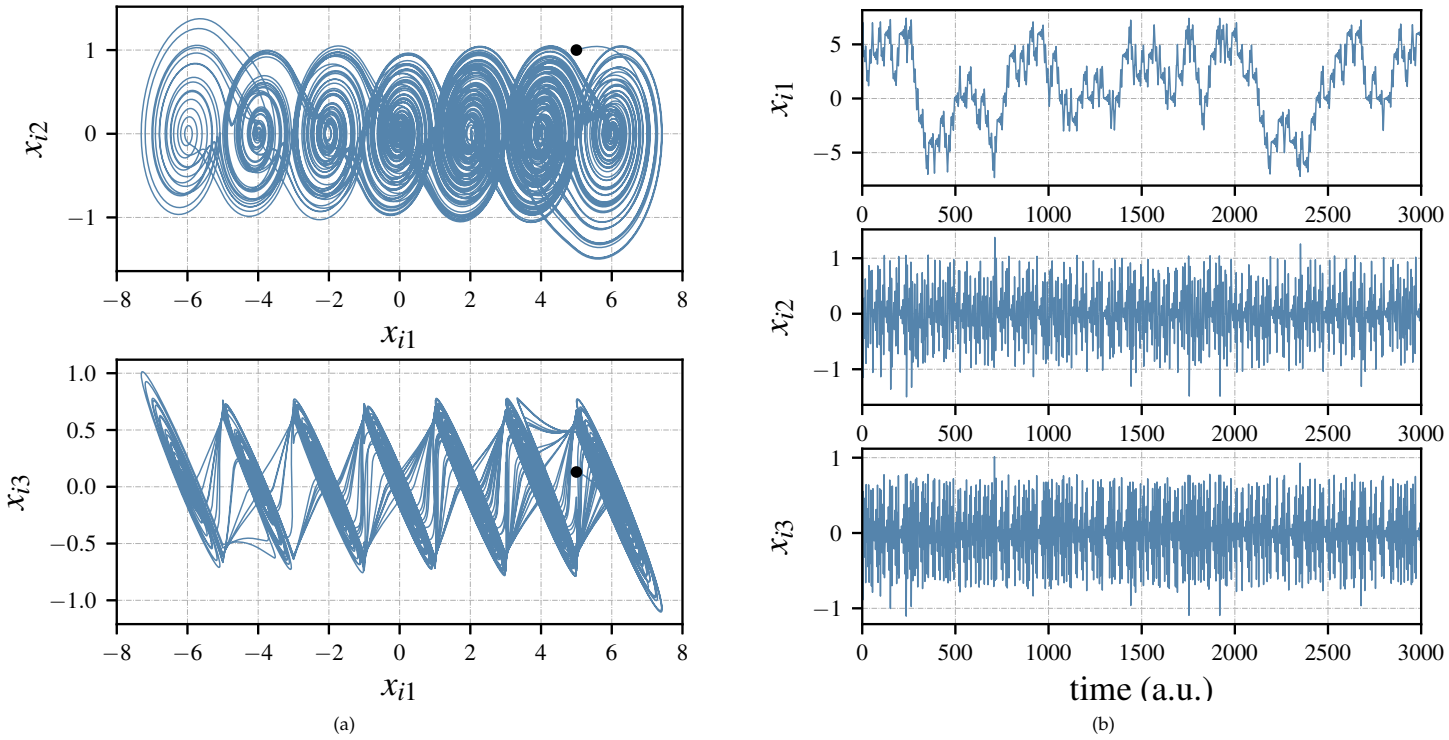

Figure 1 Attractor and states behaviour generated by Eqs. (21)-(22) with $a = 0.6$.

matrix $A + A^T - d\Gamma$. Therefore, in this section we are interested in finding a method to design the internal coupling matrix Γ and the external coupling gain c to achieve synchronization. Inspired by the λ_2 criterion (Chen *et al.* 2014) and the Master Stability Function (MSF) (Pecora and Carroll 1998; Huang *et al.* 2009), we compute synchronizability regions over an $(a-d)$-plane from which we can choose a particular matrix Γ and values for d and hence for c.

From the Eq. (10), described in Assumption 1, and the linear operator A defined in Eq. (21) we obtain the following matrix:

$$M := A + A^T - d\Gamma = \begin{bmatrix} -d\gamma_1 & 1 & -a \\ 1 & -d\gamma_2 & 1-a \\ -a & 1-a & -(2a+d\gamma_3) \end{bmatrix}, \quad (24)$$

with characteristic polynomial

$$p(M) := \sigma^3 + \kappa_2\sigma^2 + \kappa_1\sigma + \kappa_0, \quad (25)$$

where

$$\begin{aligned} \kappa_2 &= 2a + d(\gamma_1+\gamma_2+\gamma_3), \\ \kappa_1 &= d^2(\gamma_1\gamma_2+\gamma_1\gamma_3+\gamma_2\gamma_3) + 2ad(\gamma_1+\gamma_2) \\ &\quad -2\left(a+(1-a)^2\right), \\ \kappa_0 &= d^3\gamma_1\gamma_2\gamma_3 + 2ad\gamma_1(1+d\gamma_2) - a^2(2+d\gamma_1) \\ &\quad -d(\gamma_1+\gamma_3). \end{aligned}$$

Note that M is symmetric and therefore all its eigenvalues are real. Denote by σ_k, with $k \in \mathcal{K} := \{1,2,3\}$, the eigenvalues of the matrix M. For all $k \in \mathcal{K}$, $\sigma_k < 0$ holds if and only if M satisfies the Routh-Hurwitz stability criterion, namely

$$\kappa_2 > 0,\ \kappa_1 > 0,\ \kappa_0 > 0,\ \text{and}\ \kappa_2\kappa_1 - \kappa_0 > 0. \quad (26)$$

Recall that a is in $(0,1)$, so two different values of a can lead to different multi-scroll systems with different parameters for $p(M)$. Therefore, a particular matrix Γ and a particular value for d may not be appropriate for every choice. To accommodate a variety of multi-scroll systems, the proposed method is to choose an internal coupling matrix Γ and numerically solve the inequalities of Eq. (26) as a function of a and d. The result is a synchronizability region in the $(a-d)$ plane. In Figure 2 we show some examples of this; The blue regions indicate values for which inequalities in Eq. (26) hold.

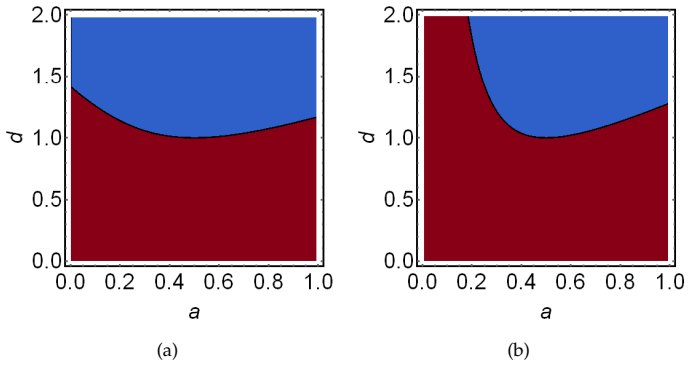

Figure 2 Synchronizability region (blue) of the matrix M subject to parameters a and d with: (a) $\Gamma = Diag(1,1,1)$ and, (b) $\Gamma = Diag(1,1,0)$.

Remark 1. *Although there are up to eight different combinations of the values for γ_1, γ_2, and γ_3, a quick examination of the inequalities from Eq. (26) shows that six of them cannot satisfy them. Synchronization can be achieved only if $\gamma_1 > 0$, $\gamma_2 > 0$ and $\gamma_3 \geq 0$.*

Remark 2. *In Assumption 1, notice that, by the min-max theorem (Allaire and Kaber 2007), we can choose* $\eta = \min_{k\in\mathcal{K}}\{|\sigma_k|\}$.

NUMERICAL ILLUSTRATION

Let the inner coupling matrix $\Gamma = Diag(1,1,1) \in \mathbb{R}^3$, and let the topology of the network be as shown in Figure 3, whose elements satisfy the conditions of a strongly connected graph. Therefore, the Laplacian matrix and its left eigenvector are given by:

$$L := \begin{bmatrix} 1 & -1 & 0 & 0 & 0 & 0 \\ 0 & 6 & -2 & 0 & -2 & -2 \\ 0 & -2 & 2 & 0 & 0 & 0 \\ 0 & 0 & -3 & 3 & 0 & 0 \\ 0 & 0 & 0 & -4 & 4 & 0 \\ -1 & 0 & 0 & 0 & -5 & 6 \end{bmatrix} \text{ and } z = \begin{bmatrix} 0.168 \\ 0.237 \\ 0.168 \\ 0.118 \\ 0.118 \\ 0.188 \end{bmatrix}.$$

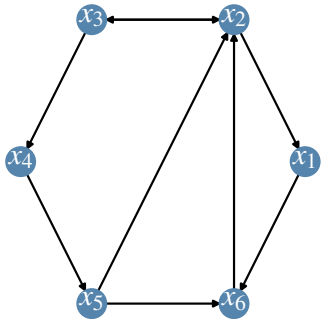

Figure 3 A strongly connected digraph of order $N = 6$.

As mentioned in the previous section, for each configuration of the internal coupling matrix and each value of the parameter a, there are critical values d such that $A + A^T - d\Gamma$ is a negative definite matrix. For this example, it is possible to choose the value of d using Figure 2(a), let $d = 1.5$ hold, which is valid for all $a \in (0,1)$. Then the generalized algebraic connectivity for the graph shown in Figure 3 is $\alpha \approx 0.7017$. Thus, to ensure synchronization in the nodes, the coupling strength must satisfy $c > d/\alpha \approx 2.13$ according to the Theorem 1.

To illustrate the above in more detail, Figure 4 shows the time series of coupled systems (5) with randomly chosen initial conditions. In the numerical simulations, the Figure 4(a) corresponds to the time series of the network state with parameter $a = 0.45$ and $\Gamma = Diag(1,1,1)$; while the Figure 4(b) corresponds to the time series of states for a network with $a = 0.6$ and $\Gamma = Diag(1,1,0)$. In both simulations, it is assumed that for $t < 1000$ $(a.u.)$ the nodes are decoupled, so that each solution evolves its own attractor. While for $t > 1000$ $(a.u.)$ the nodes are connected in a network structure with a coupling strength $c = 2.14$. Moreover, it can be observed how the trajectories of all nodes collapse in the three states, i.e., the nodes achieve complete synchronization.

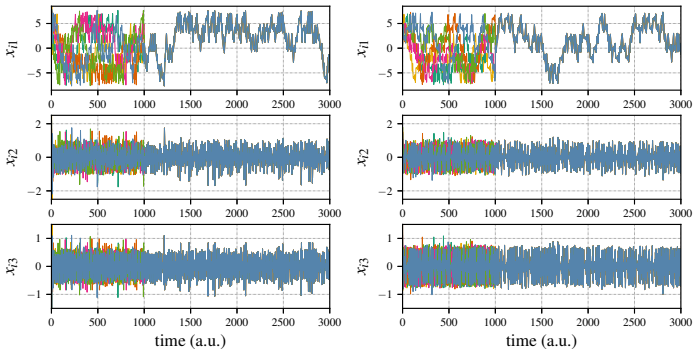

(a) (b)

Figure 4 Numerical simulation of the system from Eq. (5) with: (a) $a = 0.45$ and $\Gamma = Diag(1,1,1)$, (b) $a = 0.6$ and $\Gamma = Diag(1,1,0)$.

CONCLUSIONS

This paper studies the synchronization problem in a complex network where each node belongs to a class of PWL systems. The network's topology is directed and strongly connected with linear and diffusive couplings. Using graph theory and Lyapunov stability theory, we established synchronization conditions utilising the notion of disagreement vectors and generalized algebraic connectivity for digraphs. We then use our main result and the Routh-Hurwitz criterion to determine synchronizability regions for a given affine system, namely a UDS type-I system. For a given inner coupling matrix and a directed network topology, we compute the synchronizability regions as a function of a system parameter and a ratio between the generalized connectivity and the coupling strength. In this way, we determine minimum values for the coupling strength that allow synchronization. An advantageous feature of our approach is its flexibility in network structures. Although our main result is related to strongly connected digraphs, it is also suitable for undirected graphs.

In future work, we will further investigate the synchronization of UDS Type-I systems and provide a general method for computing synchronizability regions. We will also consider networks of systems with a different number of scrolls, including the effects of the performance parameters associated with the nonlinear functions on their electronic implementation.

Availability of data and material

Not applicable.

Conflicts of interest

The authors declare that there is no conflict of interest regarding the publication of this paper.

LITERATURE CITED

Allaire, G. and S. M. Kaber, 2007 *Numerical Linear Algebra*, volume 55 of *Texts in Applied Mathematics*. Springer-Verlag New York.

Anzo-Hernández, A., E. Campos-Cantón, and M. Nicol, 2019 Itinerary synchronization between pwl systems coupled with unidirectional links. Communications in Nonlinear Science and Numerical Simulation **70**: 102–124.

Anzo-Hernández, A., H. E. Gilardi-Velázquez, and E. Campos-Cantón, 2018 On multistability behavior of unstable dissipative

systems. Chaos: An Interdisciplinary Journal of Nonlinear Science **28**: 033613.

Arenas, A., A. Díaz-Guilera, J. Kurths, Y. Moreno, and C. Zhou, 2008 Synchronization in complex networks. Physics reports **469**: 93–153.

Ávila-Martínez, E. J., 2022 Obstacle avoidance flocking motion in multi-agent systems with limited sensing radius and heterogeneous input constraints. Advanced Robotics .

Ávila-Martínez, E. J. and J. G. Barajas-Ramírez, 2018 Distributed control for consensus on leader-followers proximity graphs. In *IFAC-PapersOnLine*, volume 51, pp. 240–245, Guadalajara, Jalisco, México.

Ávila-Martínez, E. J. and J. G. Barajas-Ramírez, 2021 Flocking motion in swarms with limited sensing radius and heterogeneous input constraints. Journal of The Franklin Institute **358**: 2346–2366.

Boccaletti, S., J. Kurths, G. Osipov, D. Valladares, and C. Zhou, 2002 The synchronization of chaotic systems. Physics reports **366**: 1–101.

Boccaletti, S., V. Latora, Y. Moreno, M. Chavez, and D.-U. Hwang, 2006 Complex networks: Structure and dynamics. Physics reports **424**: 175–308.

Campos-Cantón, E., 2016 Chaotic attractors based on unstable dissipative systems via third-order differential equation. International Journal of Modern Physics C **27**: 1650008.

Campos-Cantón, E., J. G. Barajas-Ramirez, G. Solis-Perales, and R. Femat, 2010 Multiscroll attractors by switching systems. Chaos: An Interdisciplinary Journal of Nonlinear Science **20**: 013116.

Campos-Cantón, E., R. Femat, and G. Chen, 2012 Attractors generated from switching unstable dissipative systems. Chaos: An Interdisciplinary Journal of Nonlinear Science **22**: 033121.

Carbajal-Gómez, V. H. and C. Sánchez-López, 2019 Determining accurate Lyapunov exponents of a multiscroll chaotic attractor based on SNFS. Nonlinear Dyn. **98**: 2389–2402.

Chen, G., X. Wang, and X. Li, 2014 *Fundamentals of Complex Networks*. John Wiley & Sons Singapore Pte. Ltd, Singapore.

Echenausía-Monroy, J., J. García-López, R. Jaimes-Reátegui, and G. Huerta-Cuéllar, 2020 Parametric control for multiscroll generation: Electronic implementation and equilibrium analysis. Nonlinear Analysis: Hybrid Systems **38**: 100929.

Echenausía-Monroy, J., L. Ontañón-García, and J. P. Ramirez, 2021 On synchronization of unidirectionally coupled multi-scroll systems: Dynamic vs static interconnections. IFAC-PapersOnLine **54**: 53–58.

Echenausía-Monroy, J. L., J. H. García-López, R. Jaimes-Reátegui, D. López-Mancilla, and G. Huerta-Cuellar, 2018 Family of bistable attractors contained in an unstable dissipative switching system associated to a SNLF. Complexity **2018**.

Echenausía-Monroy, J. L. and G. Huerta-Cuellar, 2020 A novel approach to generate attractors with a high number of scrolls. Nonlinear Analysis: Hybrid Systems **35**: 100822.

Gilardi-Velázquez, H. E., L. Ontañón-García, D. G. Hurtado-Rodriguez, and E. Campos-Cantón, 2017 Multistability in piecewise linear systems versus eigenspectra variation and round function. International Journal of Bifurcation and Chaos **27**: 1730031.

Huang, L., Q. Chen, Y.-C. Lai, and L. M. Pecora, 2009 Generic behavior of master-stability functions in coupled nonlinear dynamical systems. Physical Review E **80**: 036204.

Li, Z., 2015 *Cooperative Control of Multi-agent Systems: A Consensus Region Approach*. CRC Press, Boca Raton, Florida, first edition.

Li, Z., Z. Duan, G. Chen, and L. Huang, 2010 Consensus of multiagent systems and synchronization of complex networks: a unified viewpoint. IEEE Trans. Circuits Syst. I Regul. Pap. **57**: 213–224.

Mishra, A. K., S. Das, and V. K. Yadav, 2022 Finite-time synchronization of multi-scroll chaotic systems with sigmoid non-linearity and uncertain terms. Chinese Journal of Physics **75**: 235–245.

Muñoz-Pacheco, J. M., E. Zambrano-Serrano, O. Félix-Beltrán, L. C. Gómez-Pavón, and A. Luis-Ramos, 2012 Synchronization of pwl function-based 2d and 3d multi-scroll chaotic systems. Nonlinear Dynamics **70**: 1633–1643.

Ontañón-García, L., I. C. Cantón, and J. P. Ramirez, 2021 Dynamic behavior in a pair of lorenz systems interacting via positive-negative coupling. Chaos, Solitons & Fractals **145**: 110808.

Pecora, L. M. and T. L. Carroll, 1998 Master stability functions for synchronized coupled systems. Physical review letters **80**: 2109.

Pikovsky, A., M. Rosenblum, and J. Kurths, 2002 Synchronization: a universal concept in nonlinear science.

Posadas-Castillo, C., E. Garza-González, D. Diaz-Romero, E. Alcorta-García, and C. Cruz-Hernández, 2014 Synchronization of irregular complex networks with chaotic oscillators: Hamiltonian systems approach. Journal of applied research and technology **12**: 782–791.

R. Olfati-Saber and R. M. Murray, 2004 Consensus Problems in Networks of Agents with Switching Topology and Time-Delays. IEEE Trans. Automat. Contr. **49(9)**: 1520–1533.

Ruiz-Silva, A., B. Cassal-Quiroga, G. Huerta-Cuellar, and H. Gilardi-Velázquez, 2022 On the behavior of bidirectionally coupled multistable systems. The European Physical Journal Special Topics pp. 1–11.

Ruiz-Silva, A., H. Gilardi-Velázquez, and E. Campos, 2021 Emergence of synchronous behavior in a network with chaotic multistable systems. Chaos, Solitons & Fractals **151**: 111263.

Soriano-Sánchez, A. G., C. Posadas-Castillo, M. A. Platas-Garza, C. Cruz-Hernández, and R. M. López-Gutiérrez, 2016 Coupling strength computation for chaotic synchronization of complex networks with multi-scroll attractors. Applied Mathematics and Computation **275**: 305–316.

Wu, C. W., 2007 *Synchronization in Complex Networks of Nonlinear Dynamical Systems*. World Scientific, Singapore.

Yu, W., G. Chen, M. Cao, and J. Kurths, 2010 Second-Order consensus for multiagent systems with directed topologies and nonlinear dynamics. IEEE Trans. Syst. Man, Cybern. Part B Cybern. **40**: 881–891.

How to cite this article: Ávila-Martínez, E. J., Echenausía-Monroy, J. L., and Ruiz-Silva, A. Multi-scroll Systems Synchronization on Strongly Connected Digraphs. *Chaos Theory and Applications*, 4(4), 205-211, 2022.

CHAOS
Theory and Applications
in Applied Sciences and Engineering

e-ISSN: 2687-4539
RESEARCH ARTICLE
Vol.4 / No.4 / 2022 / pp.212-225
Special Issue (EDIESCA 2022)
https://doi.org/10.51537/chaos.1193078

The Effect of Agents' Psychology and Social Environment on the Opinion Formation: C/PA Relative Agreement Model in SW and SF Societies

Evguenii Kurmyshev *,[1] **and N. Leticia Abrica-Jacinto** *,[2]
*Centro Universitario de Los Lagos, Universidad de Guadalajara, México.

ABSTRACT Opinion dynamics in relative agreement models seen as an extension of bounded confidence ones, involve a new agents' variable usually called *opinion uncertainty* and have higher level of complexity than that of bounded confidence models. After revising the meaning of the opinion uncertainty variable we conclude that it has to be interpreted as the agent's opinion toleration, that changes the type of the variable from the social to the psychological one. Since the convergence rates to the stationary states in dynamics of sociological and psychological variables are in general different, we study the effect of agents' psychology and social environment interaction on the opinion dynamics, using concord and partial antagonism relative agreement model in small-world and scale-free societies. The model considers agents of two psychological types, concord and partial antagonism, that differs it from other relative agreement models. The analysis of opinion dynamics in particular scenarios was used in this work. Simulation results show the importance of this approach, in particular, the effect of small variations in initial conditions on the final state. We found significant mutual influence of opinion and toleration resulting in a variety of statistically stationary states such as quasi consensus, polarization and fragmentation of society into opinion and toleration groups of different configurations. Consensus was found to be rather rare state in a wide range of model parameters, especially in scale-free societies. The model demonstrates different opinion and toleration dynamics in small-world and scale-free societies.

KEYWORDS
Opinion dynamics
Psychological type
Psychological profile
Networked societies
Self-organization of opinion groups

INTRODUCTION

Public and personal opinions are key elements in a decision taking or making over a subject of interest. A decision is followed by actions that can be of crucial importance for the behavior or even existence of a social group or the whole society. As a consequence, both the empirical and theoretical, including mathematical, study of opinion dynamics is of great significance. Human psychology and sociology sciences consider the following factors to be important in formation of opinion: the status of a topic to be considered, a person awareness of the theme, the structure of the society, psychological type and profile of society members, pair or mixed way of interaction between persons, the influence of opinion leaders and/or mass media, a way of thinking of persons, among others. So, the process of opinion formation turns out to be a complex dynamical system when a combination of these factors is taken into account.

From nineties of the past century, the mathematical modeling of opinion dynamics turns out to be one of the important and efficient tools in studying of opinion formation, considering some of the features mentioned above. To formalize the study of the problem, different models of opinion dynamics have been proposed, which are used to explore the processes of opinion diffusion and evolution in human populations. Research of opinion dynamics covers a wide range of social phenomena: rise and popularity of subjects, spread and preservation of minority opinion, decision taking, consensus formation, emergence of political parties, spread of rumors, rise and influence of extremists, among others.

Manuscript received: 24 October 2022,
Revised: 25 November 2022,
Accepted: 5 December 2022.

[1]evguenii.kourmychev@academicos.udg.mx (**Corresponding author**).
[2]leticia.abrica@gmail.com

A formal theory of social power by French (French Jr 1956) can be considered as the origin of formal opinion dynamics research followed by a series of opinion dynamics models and their variations; those differ each other in representation of opinion space (discrete or continuous), opinion updating rules, dynamics (regimes) of agents' interaction and the structure of a social group, basically. The key models of opinion dynamics in discrete opinion space are the voter model (Clifford and Sudbury 1973; Galam 2008), the Sznajd model (Sznajd-Weron and Sznajd 2000), the Axelrod cultural diffusion (dissemination) model (Axelrod 1997); the bounded confidence (BC) and relative agreement (RA) models take opinion as a continuous variable (Dittmer 2001; Deffuant *et al.* 2001, 2002; Hegselmann *et al.* 2002). For more detailed and structured review of models on opinion dynamics we refer to the work of Xia et al. (Xia *et al.* 2011), S. Galam (Galam 2022) and, Dong et al. (Dong *et al.* 2018).

In the beginning of sociophysics different models and methods of mathematical physics were adapted to study various social phenomena, in particular, to explore the processes of opinion diffusion (propagation, spreading) and evolution in human populations. Later on new models, based on theories and principles of social sciences, have arisen to give more realistic features to simulation dynamics. In continuous opinion space, bounded confidence (BC) and relative agreement (RA) models, being ones of the closest to the social experience and sociological theories, were proposed for the studying of opinion dynamics in networked societies; BC models (Deffuant *et al.* 2001; Hegselmann *et al.* 2002; Wang 2022) being predecessors of the RA ones (Deffuant *et al.* 2002) are still popular in opinion evolution simulation. As in any dynamical system, the convergence and final states of opinion evolution are considered to be one of the main problems to study. Both BC and RA opinion models demonstrate convergence to the states of consensus, polarization or fragmentation of opinion at different combinations of their parameters and with different convergence rate (Dittmer 2001; Deffuant *et al.* 2001, 2002; Deffuant 2006; Hegselmann *et al.* 2002; Douven and Riegler 2010; Pineda *et al.* 2013). The state variable of an agent in BC models is the opinion only, while in RA ones the uncertainty of opinion is used as an additional variable along with the opinion; the psycho-social meaning of the latter variable was not formally defined in psycho-social sense but interpreted as a range of self-reliance of an agent on its own opinion. Nevertheless, the meaning of that variable as the opinion uncertainty is somehow confusing if not wrong, because it is not measurable (see Section *Conclussions and Discussion* at the end of article). In addition, in this case it is considered as one more sociological variable analogous to the opinion, leaving out of the consideration the influence of agents' psychology on opinion formation.

In order to overcome these constraints of RA models, the differentiation of agents in psychological types was first considered in (Kurmyshev *et al.* 2011; Abrica-Jacinto *et al.* 2017) assigning to each agent one of the two psychological types, Concord (C) or Partial Antagonism (PA); the latter was reflected in the rules of opinion updating at agents' interaction. In addition, after being analyzed the notion of the psychological profile of human individuals (open or closed mind persons), we reinterpret the meaning of the variable *opinion uncertainty* giving to it the notion of personal *toleration* to the opinions of others. New interpretation gives mayor conceptual consistency to the RA models since it allows to study effects of interrelation and mutual influence of the opinion (social variable) and the personal toleration (psychological variable) in evolution of opinion in artificial societies of different structures.

The main conceptual difference between BC and RA models is the criterion of the opinion updating. In BC models (homogeneous or heterogeneous) an agent changes its opinion if and only if the distance between the opinions of influenced (passive) agent and influential (active) ones is less than a certain threshold, that depends on closeness of opinions only. In RA models an influenced (passive) agent changes its opinion if and only if the opinion intervals of interacting agents overlap each other, that depends on both the opinion closeness and the opinion uncertainty. The rate of convergence to a stationary opinion state is regulated by a convergence parameter $\mu \in (0, 0.5]$ along with other factors. The μ parameter is the intensity of agents' opinion interaction and it shows how much other opinions influence the opinion of an agent. In homogeneous and heterogeneous BC models the influence of μ on convergence rate and opinion patterns in opinion dynamics was studied in (Urbig and Lorenz 2007; Deffuant 2006; Lorenz 2008; Huang *et al.* 2018). It was found that its value, along with other parameters of the model, influence both the convergence rate and the final opinion groups distribution; even though, most of the works on opinion dynamics in BC and RA models use the only value $\mu = 0.5$. Systematic study of this influence in RA models was not done. Moreover, when the *opinion uncertainty* is now reinterpreted as the toleration to others' opinions we have to admit the difference in convergence rates of variables, expressing them through the two convergence parameters μ_1 and μ_2 for the opinion and toleration respectively. Because the evolution of persons' psychology is used to be slower than that of their opinions, we consider opinion and toleration dynamics through the variation of μ_2 under the condition $\mu_r = \frac{\mu_2}{\mu_1} \leq 1$.

Another essential feature of models are communication regimes in opinion dynamics that in real life can be quite different, ranging from pair interactions to meetings of agents or including various combinations between them (Urbig and Lorenz 2007; Yu *et al.* 2017). Random selection of agents for the updating of opinion is usually used in simulation. The latter turns out the system into a stochastic one, and as a consequence one has to choose between the analysis of particular scenarios or the averaging of results of many similar experiments. In this respect, the influence of initial conditions on opinion dynamics in a stochastic system has to be taken into account (Yu *et al.* 2020).

This work is aimed mainly to the studying of toleration (psychological variable) and opinion (sociological variable) dynamics of agents in artificial societies of different structure (SW and SF networks) in the frame of C/PA relative agreement model. We pay special attention to particular scenarios at small variation in initial conditions in a wide range of model parameters. The rest of this document is organized as follows. In next section (*C/PA model*) we set out the problem to be studied and briefly describe the C/PA relative agreement opinion dynamics model. Later, in section *Desing of experiments* describes the design of computational experiments and parameters of the model. The results of extensive simulations are presented and analyzed in *Simulation results and analysis*. Finally, *Conclusions and discussion* are given.

C/PA MODEL

Agent based mathematical models of opinion dynamics in networked societies are characterized by four basic elements (Kurmyshev *et al.* 2011):

- *Networked society* – represents a communication system between agents of a society by means of a graph where nodes represent agents and communication channels between agents are represented by links.

- *Opinion space* – a discrete or continuous set of values that represents the opinions of agents. The *toleration* and respective space is used along with the opinion in RA models.
- *Interaction dynamics* – establish the manner and sequence of agents' interaction and conditions under which agents update their state variables.
- *Updating rule* – basically, the model equations describing opinion change as a result of agents' interaction.

Opinion dynamics models are usually distinguished by their specific updating rules and updating dynamics, while other elements are shared. In this article, we use the C/PA relative agreement opinion dynamics agent based model (Kurmyshev *et al.* 2011) that is an extension of the DW model (Deffuant *et al.* 2002). The C/PA model contemplates societies of agents of two psychological types, concord C-agents and partial antagonism agreement PA-agents; any substrate network is admitted. Given a society of $N = N_C + N_{PA}$ agents, a subset of $N_C = p \cdot N$ agents are C-type agents and the rest, $N_{PA} = (1-p) \cdot N$ are PA-agents, where $p \in [0,1]$ is the fraction (proportion) of C-agents. At each instant of time t, the state of i-agent is described by the two continuous variables, its opinion $x_i(t) \in [-1,1]$ and toleration (ex-uncertainty) $u_i(t) \in (0,1]$, where $i = 1,2,\ldots,N$.

The interaction dynamics in C/PA-model is stochastic. Agents can change their states as a result of pair interaction in a discrete time. At each instant t, M edges of a network are selected at random. Each edge connects a pair (i,j) of interacting agents and one of them is selected at random to be receptive (influenced), say j-agent, and the other, i-agent, to be influential. So, unidirectional pair interaction of agents is chosen.

For a pair of selected agents (i,j), the social condition for their interaction in RA models is defined by the overlap of the opinion segments,

$$s_i(t) = [x_i(t) - u_i(t), x_i(t) + u_i(t)]. \tag{1}$$

Toleration $u_i(t)$ defines the borderlines of acceptability of other agents' opinions. The overlap of segments is calculated as

$$\begin{aligned} h_{ij}(t) = &\min\{x_i(t) + u_i(t), x_j(t) + u_j(t)\} \\ &- \max\{x_i(t) - u_i(t), x_j(t) - u_j(t)\}. \end{aligned} \tag{2}$$

When $h_{ij}(t) \leq 0$, neither opinion nor toleration of the influenced agent j from (i,j) pair are modified. If $h_{ij}(t) > 0$, then the receptive j-agent of the interacting pair updates the opinion $x_j(t)$ and toleration $u_j(t)$ according to its psychological C or PA-type, following the equations:

$$x_j(t+1) = x_j(t) + \mu_1 \cdot ra_{ij}^{C,PA}(t) \cdot [x_i(t) - x_j(t)], \tag{3}$$

$$u_j(t+1) = u_j(t) + \mu_2 \cdot ra_{ij}^{C,PA}(t) \cdot [u_i(t) - u_j(t)], \tag{4}$$

where $\mu_1, \mu_2 \in (0, 1/2]$ are convergence parameters (intensity of interactions) for the opinion and toleration, respectively. Relative agreement $ra_{ij}^{C,PA}(t)$ of receptive agent with an active one depends on the psychological type of the former and is calculated as

$$ra_{ij}^{C}(t) = \frac{h_{ij}(t)}{u_i(t)}, \tag{5}$$

$$ra_{ij}^{PA}(t) = \frac{h_{ij}(t)}{2u_i(t)} \left[\frac{h_{ij}(t)}{u_i(t)} - 1 \right], \tag{6}$$

In the C/PA model (Kurmyshev *et al.* 2011), the interaction of passive C-agents is always attractive in the opinion space, its opinion always gets closer to that of the active one as in the DW model (Deffuant *et al.* 2002). Nevertheless, dynamics of passive PA-agents can be repulsive-attractive in accord to the relative agreement $ra_{ij}^{PA}(t)$, depending on the overlap of opinion intervals $h_{ij}(t)$ (see Eq. 2).

Usually, most of the BC and RA opinion dynamics models handle the convergence parameter equal to $\mu = 0.5$. The exceptions are (Lorenz 2010; Huang *et al.* 2018). In (Lorenz 2010) the convergence of opinion in function of different values of the convergence parameter was studied in the BC Deffuant model. In (Huang *et al.* 2018) the heterogeneous convergence parameter, depending on the distance between the opinions of interacting agents, was proposed for the BC Deffuant model. The use of heterogeneous parameters has converted the BC model into a kind of RA one. In general, the RA models use the same convergence parameter equal to $\mu = \mu_1 = \mu_2 = 0.5$ for both variables, x_i and u_i (Deffuant *et al.* 2002; Meadows and Cliff 2012; Kurmyshev *et al.* 2011). But x_i describes the social manifestation and u_i corresponds to the psychological profile of agent; so they can have different time scales in evolution. In addition, agents' social manifestation (opinion) and psychological profile (toleration) influence each other (Abrica-Jacinto *et al.* 2017). In our work, we study the opinion and toleration dynamics and their mutual influence varying the ratio of convergence parameters $\mu_r = \frac{\mu_2}{\mu_1}$ in the frame of C/PA relative agreement model on the SW and SF networks. With the features being integrated into the model, complex system dynamics emerge that has resemblance to the real social processes, at least qualitatively.

DESING OF EXPERIMENTS

We study opinion and toleration dynamics in artificial societies of two types, small world (SW) and scale free (SF), consisting of $N = 10^3$ agents each. It is an intermediate size society that can get the insight into particularities of evolution of both small and large societies. SW-network (undirected graph) is generated according to the Watts-Strogatz algorithm with the probability of reconnection $\beta = 0.25$ and average degree $< k >= 40$ (average number of neighbors of each node); it has $M_{SW} = 20 \times 10^3$ links (Watts and Strogatz 1998). SW-network can be considered as a prototype of democratic society without noticeable leadership. SF-network is constructed according to the Barabási-Albert model (Barabási and Albert 1999), with following parameters: $N_0 = 2$, with $m = m_0 = 1$; that has $M_{SF} = 999$ links. SF-network is a *structured* network with an intention of hubs to leadership.

Mixed societies composed of C- and PA-agents with the C-agents' fractions $p = 0.3$ and 0.7 are studied. To our opinion, the two compositions are quite representative to see the difference in dynamics of opinion and toleration in societies composed of agents of different psychological types. We understand the term society as a network (graph), with a particular psychological type (C or PA) assignment to each agent. For a given value of the p parameter, two societies represented by the same graph are considered different if they have different psychological type assigning to the agents.

In C/PA model, the initial mean value of agents' toleration is an important parameter, to which was given the following values $U = 0.3, 0.5, 0.7$. Societies with $U = 0.3$ can be considered as composed of agents with relatively low toleration (enclosed agent), while $U = 0.7$ corresponds to high tolerant agents (open agent).

In order to evaluate the effect of convergence parameters on the opinion and toleration dynamics and their mutual influence, we set the convergence parameter of opinion at the value $\mu_1 = 1/2$ and

varied the convergence of toleration, $\mu_2 = 1/2, 1/6, 1/10, 1/20$, so that the ratio of convergence parameters was $\mu_r = \frac{\mu_2}{\mu_1} = 1, 1/3, 1/5, 1/10$. Finally, each of the experiments are characterized by the quaternion $(Network, p, U, \mu_r)$ in parametric space.

The updating dynamics of the model is a stochastic one, and we were faced with the decision of studying particular scenarios or the averaged results of many individual experiments. Pilot simulations showed that the averaging of experimental results (see also (Kurmyshev *et al.* 2011; Abrica-Jacinto *et al.* 2017)) capture opinion evolution tendencies, while interesting and important characteristics of each particular scenario can be lost. On the other hand, the analysis of particular scenarios shows rather general trends of opinion evolution in addition to salient particularities. For that reason, we decided to explore individual scenarios systematically in a wide range of parameters offered by the model. For a given society, a *particular scenario* of opinion and toleration dynamics is defined by the following elements: given initial opinion and toleration conditions, and the particular realization of updating dynamics (a sequence of nodes selected for the opinion and toleration updating). *Particular experiment* begins with the setting of initial conditions for the variables:

- Uniform distribution on the interval $[-1, 1]$ is used to assign the initial opinion to agents.
- Uniform distribution on the interval $[U - 0.15, U + 0.15]$ is used to assign the initial toleration to agents.

Particular realizations of the uniform distribution are not identical, being of the same type but with variations due to the generator of random numbers. To see how much the result of experiment is sensitive to initial conditions (IC) in the frame of stochastic updating dynamics, we carry out each experiment at four particular realizations (A, B, C, D) of IC.

After setting the initial conditions, the simulation is conducted according to the following algorithm:

- M edges are chosen at random.
- On each selected edge (i, j), the receptive agent is chosen at random.
- The overlap h_{ij} of opinion intervals is calculated, Eq. 2.
- If $h_{ij} > 0$, the opinion and toleration of the receptive agent are updated according to their psychological type, Eqs. 3 and 4. If $x_i(t) \leq -1$ or $x_i(t) \geq 1$, then we take $x_i(t)$ to be -1 or 1, respectively. Similarly, the toleration is retained in the interval $u_i(t) \leq [0.05, 1]$.
- In regard to $h_{ij} \leq 0$, neither opinion nor toleration of the receptive agent are modified.

Agents with $u_i(t) = 0$, if they were, are unexpressive. They are not willing to change their opinion neither toleration despite being connected in the network, because they have zero opinion interval overlap with other agents. These agents can be considered as apathetic or socially closed because they do not admit interaction with other agents. That was the reason to maintain at least a nominal interaction, so that a small margin (0.05) was left in toleration for keeping opinion exchange.

Unlike the SW, the SF networks have hubs as "distinguished" members. In order to maintain the degree, psychological type and position of hubs in the network, and, finally, to have a detailed control over the influence of parameters μ_r and U on the dynamics of system, we design experiments in SF societies in the following manner. The SF network was generated once for all experiments. The three largest degree nodes (Hubs) had 35, 25 and 23 links and we assigned them PA, C, C and psychological type, respectively. The uniform random distribution was used to assign the psychological type to the rest of the nodes of network at each of the two values $p = 0.3$ and $p = 0.7$. The structure of the society is preserved for a part of experiments; afterwards, the psychological type of Hubs is inverted, C to PA and PA to C, maintaining the psychological type of the rest of agents. So, we have conducted experiments with two societies, differed each other in opposed psychological type of Hubs.

The uniform initial conditions were generated four times (A, B, C, D) for both SW and SF networks. In order to see the effect of μ_r and IC on the dynamics, for each pair of parameters (p, U) we run $16 = 4 \times 4$ experiments simultaneously under the same (stochastic) updating dynamics for all combinations of initial conditions ($\times 4$) and values of parameter μ_r ($\times 4$). In experiments we used the following values for $p = 0, 3, 0.7$ and $U = 0.3, 0.5, 0.7$.

The advantage of this scheme is that the influence of parameters can be analyzed separately, under the same stochastic updating dynamics. To see the influence of μ_r, one has to analyze the results of experiments along the lines at fixed IC, but the influence of variation in IC is analyzed along the columns. Through the preliminary experimentation we noticed that the evolution time in SF networks is greater than that for the SW. So, for the SF experiments we extended the evolution time from 2000 to 6000 steps.

In order to compare the convergence of opinion and toleration in networks of different type, SW and SF, one has to choose equal number of edges to ensure near the same number of agents update their opinion and tolerance. The empiric rule in most of the publications is to choose at random in each time step the number of edges equal to the number of agents in the network. So, near a half of agents has an opportunity to update their opinion and tolerance.

We use a SF network of 1000 agents that has 999 edges in accord to the Barabasi-Albert algorithm (Barabási and Albert 1999); the number of edges in a SF network is much smaller than that of SW with equal numbers of agents. In opinion dynamics, random selection (with regression) of network edges for a unit time step can result in a multiple selection of a link between one agent and the others. So, one agent can have a number of interactions with others during unit time step; in particular, it is quite possible between a hub and common agents, and a hub can participate as a passive or active agent several times for a time step. Nevertheless, in accord to the Eqs. 3 and 4, only the ultimate interaction has an effect on changing the opinion and tolerance; one can see all previous interactions of the stage as an exploration of the issue (opinion and toleration situation).

SIMULATION RESULTS AND ANALYSIS

The number of simulated particular scenarios is 192: 2 (networks, SW and SF) $\times 2$ (composition of society, $p = 0.3$ and 0.7) $\times 3$ (U's values, $U = 0.3, 0.5, 0.7$) $\times 4$ (μ_r's values) $\times 4$ (initial conditions, A, B, C, D) $= 2 \cdot 2 \cdot 3 \cdot 4 \cdot 4 = 192$. In order to exclude the influence of variations in generation of networks on results of simulation, we use the same SW or SF graph in all experiments with SW and SF societies; each was generated only once. In this work, no specific quantitative criteria are used to analyze multiple aspects of the opinion and uncertainty dynamics; analysis and conclusions are qualitative more than quantitative. Each experiment was carrying out up to 2000 generations for SW and 6000 generations for SF networks. These numbers were chosen on base of preliminary simulations, because the tracking of evolution trajectories has shown convergence to a steady state.

Along with the data files, each experiment provides two plots of opinion and toleration trajectories of each and all agents, two color palette histograms of opinion and toleration evolution and two histograms of final distributions of opinion and toleration – those are for the visual qualitative analysis. We see that the plots of agents' opinion and toleration trajectories can be often confusing and difficult for individual tracking because of their multiple overlapping. In that cases the evolutionary histograms are of great benefit. Since the representation of simulation results in a graphic manner is extensive, we resume them by some instructive examples and qualitative description. Histograms of opinion are given in the interval $[-1,1]$ and for the toleration in the interval $[0.05,1]$, both with 21 bins. In order to facilitate comparison of simulation results, we comment them by similar phrases in a repetitive manner.

Experiments in SW-networks

Each experiment is characterized by the quaternion (SW,p,U,μ_r) and by the same set of four realizations of initial conditions (A,B,C,D); we chose at random $M=1000$ links of total number $M_{SW}=20\times10^3$ links in each experiment. We think that the selection of links in each experiment does not influence much on the updating dynamics, since each node of the network has in average the same degree.

SW society at $p=0.3$. The cross-analysis of plots and histograms of the opinion and toleration evolution in SW society with C-agents' fraction equal to $p=0.3$, for the set of parameters $\mu_r=\{1,1/3,1/5,1/10\}$ ($\mu_r=\mu_2/\mu_1$) reveals the following features in opinion and toleration dynamics (see Figure 1).

At $U=0.3$, for the decreasing ratio of convergence coefficients μ_r's: 1. We observe the opinion fragmentation; the number of opinion groups is decreasing from 7 to 4 with the decrease of μ_r. 2. No regular change in the rate of toleration convergence is detected with the decrease of the convergence parameter μ_r; toleration converges to the values smaller than U and agents show more toleration ($u_i\approx U$) for the societies with less convergence parameter μ_r, meanwhile most of the agents become low tolerant ($u_i\approx0.06$) at $\mu_r=1$. Sometimes toleration tends to split into few close groups. 3. The four generations of initial conditions, even being each of the same type uniform distribution, are not identical, and the effects of relatively small variations in IC and stochastic updating dynamics on the final opinion and toleration distributions were observed through the variation in size and position of principal peaks.

At $U=0.5$, for the decreasing ratio μ_r (Figure 2 as an example): 1. We observe polarization and, sometimes, fragmentation of opinion into three groups. The slowing down of toleration convergence is observed as μ_r decreases and, as consequence, the opinion evolution is elongated also (Figure 2.b). 2. Toleration shows a slowing down of convergence with the decrease of μ_r; toleration converges to values smaller than U, so agents become less tolerant in average; the final values of toleration frequently split into two groups, one of them is a group of low toleration agents. 3. Between groups dynamics is observed in evolution of opinion and tolerance, that is seen in plots of trajectories but almost not seen in histograms; trajectories of agents migrating from one to another opinion group are observed – those are bridges connecting groups of different opinions. 4. The effects of IC on the final opinion and toleration distributions are observed as the variation in size and position of principal peaks, those are more noticeable than that in case of $U=0.3$. That is an indication of instability in toleration and opinion dynamics, $U=0.5$ looks to be near the bifurcation point.

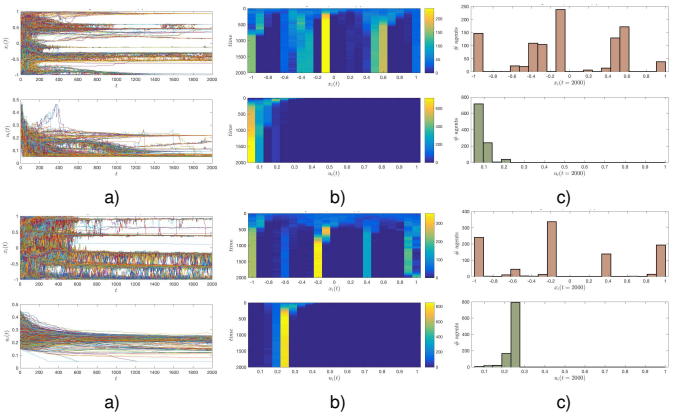

Figure 1 Opinion and toleration evolution in SW network at $(p,U)=(0.3,0.3)$ IC$-A$. Columns: a) trajectories and b) color palette histograms of agents' opinion and toleration evolution, c) final distribution of opinion and toleration. First double line for $\mu_r=1$, second double line for $\mu_r=1/10$.

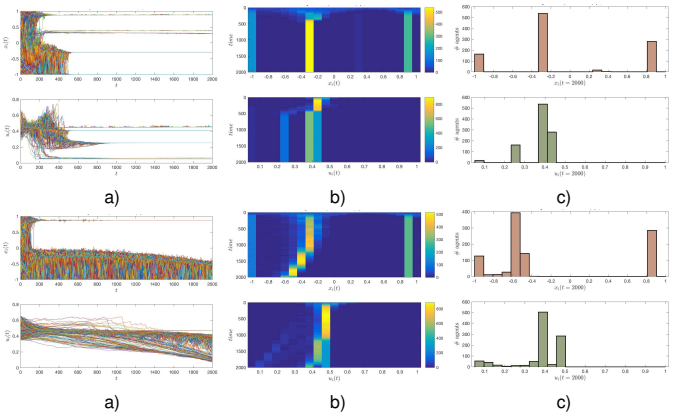

Figure 2 Opinion and toleration evolution in SW network at $(p,U)=(0.3,0.5)$, IC$-A$. Other conditions are the same as in Figure 1.

At $U=0.7$, for convergence coefficients μ_r (see Figure 3) we observe: 1. Opinion polarization into two asymmetric groups with final positions generally fluctuating in the opinion space at small variations of IC (sometimes, fragmentation into three groups at $\mu_r=1$); decreasing of μ_r (slowing down of toleration convergence) causes increasing of opinion convergence. 2. Toleration shows the slowing down of convergence with the decrease of μ_r, converging to values smaller but close to U. At $\mu_r=1$ toleration sometimes converges to two values, $u_i\approx0.65$ and $u_i\approx0.05$, the latter corresponds to low toleration agents, enclosed or unwilling to collaborate. 3. Between groups dynamics is observed in evolution of opinion and tolerance, that is seen in plots of trajectories but almost not seen in histograms; trajectories of agents migrating from one to another opinion group are observed – those are bridges connecting groups of different opinions.

It is important to note that in SW societies at $p=0.3$ (societies with a predominant number of PA agents) an opinion consensus was not observed at any value of U and μ_r.

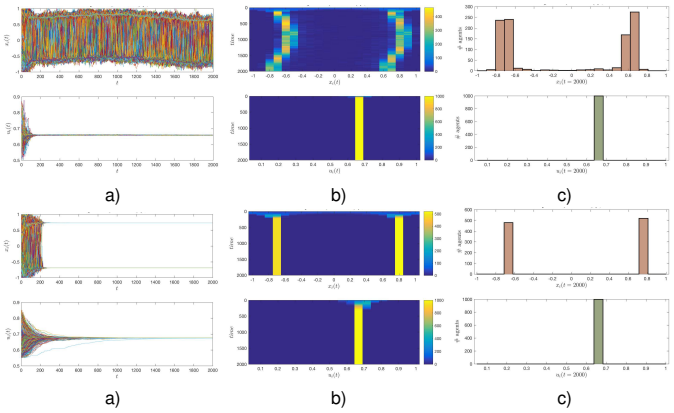

Figure 3 Opinion and toleration evolution in SW network at $(p, U) = (0.3, 0.7)$, IC$-A$. Other conditions are the same as in Figure 1.

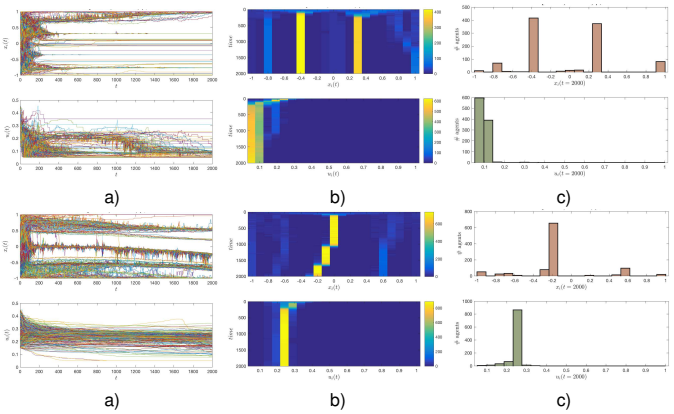

Figure 4 Opinion and toleration evolution in SW network at $(p, U) = (0.7, 0.3)$, IC$-A$. Other conditions are the same as in Figure 1.

SW society at $p = 0.7$. When the psychological composition of the society is changed from $p = 0.3$ to $p = 0.7$ (C-agents are predominant), the analysis of plots and histograms of the opinion and toleration evolution, for the set of parameters $U = 0.3, 0.5, 0.7$ and $\mu_r = \{1, 1/3, 1/5, 1/10\}$, shows the following characteristics of the opinion and toleration dynamics.

At $U = 0.3$, for μ_r's (Figure 4): 1. In the range of $\mu_r = 1/3, 1/5, 1/10$ we observe the convergence of opinion into one dominating group (quasi consensus). Centrist dominating group *drifts* in opinion space to one of the extremes (see, for example Figure 4.b); the effect is most noticeable at $\mu_r = 1/5$ while it is less visible at $\mu_r = 1/10$ and absent at $\mu_r = 1, 1/3$. Final value of opinion depends on the parameter μ_r and IC, even though no regular pattern of this dependence was found. In addition, several minority groups are formed. In case of $\mu_r = 1$, polarization or fragmentation into three dominant groups is observed; several minority groups are also observed. At all values of μ_r small groups of opposed extremists emerge. 2. Decreasing in the rate of toleration convergence is observed with the decrease of the convergence parameter μ_2, that is not trivial. Predominant compact group of agents with toleration less than U is formed and, moreover, agents become less tolerant when the convergence parameter μ_r increases. In case of $\mu_r = 1$, toleration converges to small values, in general, less than 0.1, so that the society evolves into a state with low toleration agents. 3. The effects of relatively small variations in IC and stochastic updating dynamics on the final opinion and toleration distributions were observed through the variation in size and position of principal peaks.

At $U = 0.5$, for μ_r's (Figure 5 as an example): 1. We observe the convergence of opinion of agents into one dominant group that *flips* its position due to small variations in uniform IC. The final value of the dominant opinion group seems to depend on the IC mainly and on the parameter μ_r partially, even though no regular pattern of this dependence was found. In addition, one or two small extremist groups are formed. 2. Composition of SW society of agents of different psychological type has significant influence on the formation of opinion. At $p = 0.3$ (minority of C-agents), the society tends to separate into two or three opinion and tolerance groups. Nevertheless, at $p = 0.7$ (minority of PA-agents), the trend to formation of a single dominant group is observed. In some scenarios, at both $p = 0.3$ and $p = 0.7$, the formation of a compact single one or various groups are observed soon after the beginning of interaction between agents, then the group evolves (drifts) as a whole. 3. An interesting and important effect of convergence parameters in opinion evolution is observed at $(p, U) = (0.7, 0.5)$. When $\mu_r = 1, 1/10$ the dominant both opinion and toleration groups after being formed remain stable in opinion and toleration spaces (Figure 5.b), but at the intermediate values of $\mu_r = 1/3, 1/5$ a notable drift is observed, especially at $\mu_r = 1/5$. With the decrease of the convergence parameter μ_2, the opinion converges faster than the toleration due to $\mu_1 > \mu_2$. 4. Toleration of agents converges to a value smaller than U (predominant compact group of agents with close tolerances less than U is formed) and, in addition, agents show more toleration ($u_i \approx U$) in the societies with a less convergence parameter μ_2. In some cases, toleration converges to rather small values (in general, less than 0.2), so that the majority of the society advances into the group of agents with low tolerance. Drift of the dominant toleration group toward to $U \approx 0.3$ is also observed at $\mu_r = 1/5$. 5. Effects of relatively small variations in IC and stochastic updating dynamics on the final opinion and toleration distributions are observed through the variation in position of dominant groups.

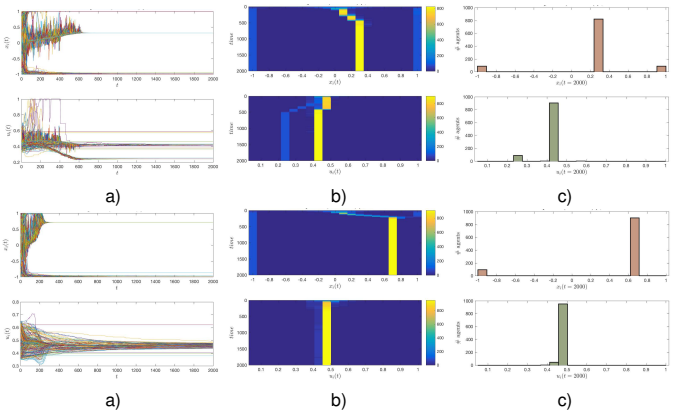

Figure 5 Opinion and toleration evolution in SW network at $(p, U) = (0.7, 0.5)$, IC$-A$. Other conditions are the same as in Figure 1.

At $U = 0.7$, for μ_r's (see Figure 6): 1. Similar to the case $U = 0.5$, we clearly observe two stages both in the opinion and toleration dynamics: first a dominant compact group of opinion and toleration is formed and, then this group evolves in opinion or toleration space as a whole; drift is obvious, especially at $\mu_r = 1/5, 1/10$ (Figure 6.b). 2. In the range of $\mu_r = 1/3, 1/5, 1/10$, the toleration convergence time grows up with the decreasing of convergence

parameter μ_2; toleration of agents converges to the values smaller than U and, in addition, toleration normally converges to rather small values $u_i \approx 0.1$, so that the society evolves into a state with low toleration. 3. In the range of $\mu_r = 1, 1/3, 1/5, 1/10$ we observe the convergence of opinion into a single consensus group. Final value of the opinion depends on the parameter μ_r and IC, even though no regular pattern of this dependence was found. At $\mu_r = 1$ the position of dominant group tends to the center ($x_i \approx 0$), nevertheless, for $\mu_r = 1/3, 1/5, 1/10$ the group takes one of the extremist positions, $x_i \approx -1$ or $x_i \approx +1$, depending on IC and updating dynamics. 4. Effects of relatively small variations in IC and stochastic updating dynamics on the final opinion and toleration distributions is observed through the variation in position of dominant groups.

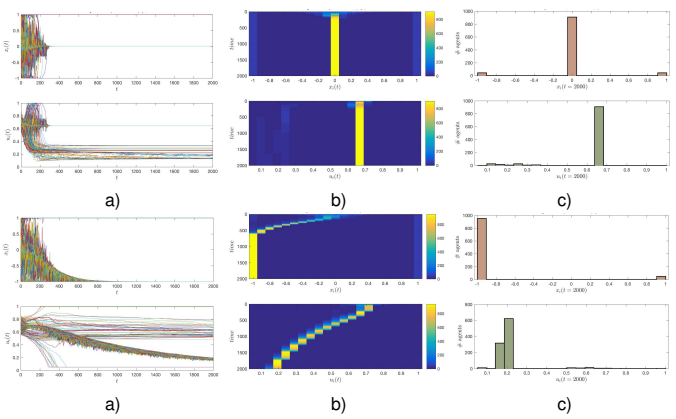

Figure 6 Opinion and toleration evolution in SW network at $(p, U) = (0.7, 0.7)$, IC$-A$. Other conditions are the same as in Figure 1.

It is instructive to revise the histograms of final distributions of opinion and toleration for the several IC and values of $U = 0.3, 0.5, 0.7$, at $p = 0.3, 0.7$ (Figures 7 and 8). Polarization of opinion is predominant at $p = 0.3$ and $U = 0.5, 0.7$ (Figure 7), while at $p = 0.7$ and $U = 0.5, 0.7$ an asymmetric quasi-consensus accompanied by small extremist groups is observed (Figure 8). Small variations in IC, A and B, cause noticeable change in position of opinion groups, at $U = 0.5, 0.7$ especially (see Figure 8, second and third columns).

Experiments on SF-networks

Trajectories and histograms of agents' opinion and toleration evolution and the histograms of final distributions of opinion and toleration were obtained in experiments. To observe the evolution of the hubs' opinion and toleration, the trajectories of the three hubs in figures of temporal evolution are presented in black, cyan and magenta, respectively. In histograms of final distributions of opinion and tolerance, the bins containing the hubs are shown in yellow.

SF society and $p = 0.3$**.** When the psychological composition of the society is $p = 0.3$, the cross-analysis of plots and histograms of the opinion and toleration evolution, for the set of parameters $U = 0.3, 0.5, 0, .7$ and $\mu_r = 1, 1/3, 1/5, 1/10$, shows the following tendencies and particularities of opinion and toleration dynamics.

For the decreasing ratio of convergence coefficients $\mu_r = 1, 1/3, 1/5, 1/10$ and $U = 0.3$: 1. The great majority of (if not all) individual trajectories in opinion and toleration space are straight lines of steady state after some evolution time, that is rather different of SW networks where only a stochastic steady states are observed (see Figures 9 and 10). This interesting effect is the result of combination of the three causes: the structure of SF network, high proportion of PA-agents and relatively low toleration of agents. Agents with close opinion are located far each other (they are not nearest neighbors) or close to agents with rather distinct opinion in the SF network, and for that reason can't interact each other (their opinion segments have no overlap in the opinion space). 2. No substantial changes in the opinion compared to its initial distribution are observed, neither fragmentation no polarization of the opinion (Figures 9.c and 10.c). The final distributions of opinion at $\mu_r = 1, 1/3, 1/5, 1/10$ differs each other not much but in the position of hubs mainly. The opinion convergence time increases with the decreasing of μ_r. 3. The trajectory of principal PA-hub opinion is much stable and regular than that of the two smaller C-hubs, each hub behaves similar to Brownian particle (irregular interaction with neighboring agents causes chaotic motion in opinion space). We observe an irregular change of the final position of hubs in opinion space with the change of μ_r. 4. No regular change in the rate of toleration convergence is detected with the decrease of the convergence parameter μ_r; toleration converges to the values smaller than U, forming a kind of bell distribution.5. The four generations of IC are not identical (the hubs are included), even being each of the same type uniform distribution, and the effects of variations in IC on the final opinion and toleration distributions were observed, in particular, through the variation of hubs position and size of bins that include hubs (Figures 9 and 10).

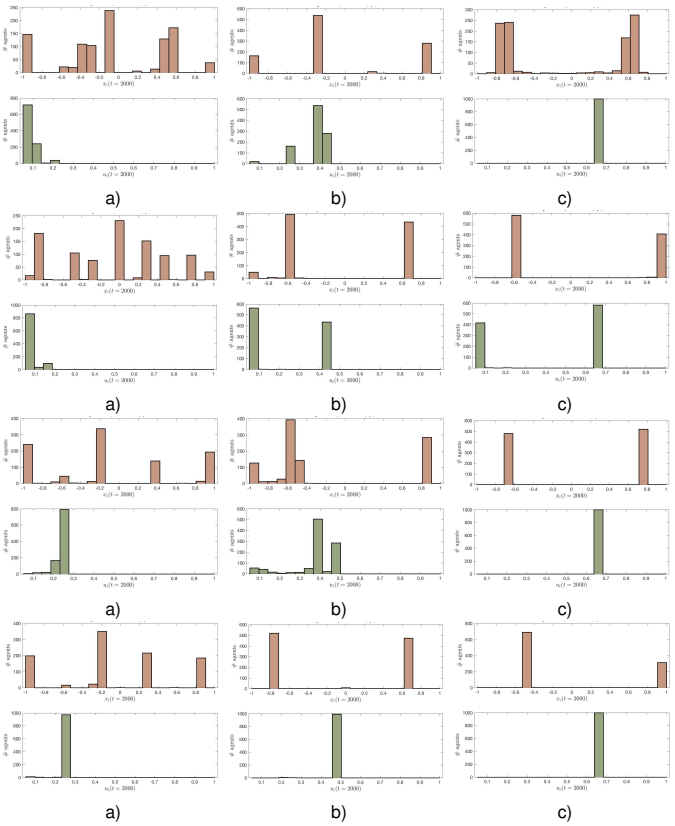

Figure 7 Final distributions of opinion and toleration on SW network at $p = 0.3$. Columns: a) $U = 0.3$, b) $U = 0.5$ and c) $U = 0.7$. First double line for IC$-A$, $\mu_r = 1$; second double line for IC$-B$, $\mu_r = 1$; third double line for IC$-A$, $\mu_r = 1/10$ and fourth double line for IC$-B$, $\mu_r = 1/10$. Brown histograms – opinion, green histograms – toleration.

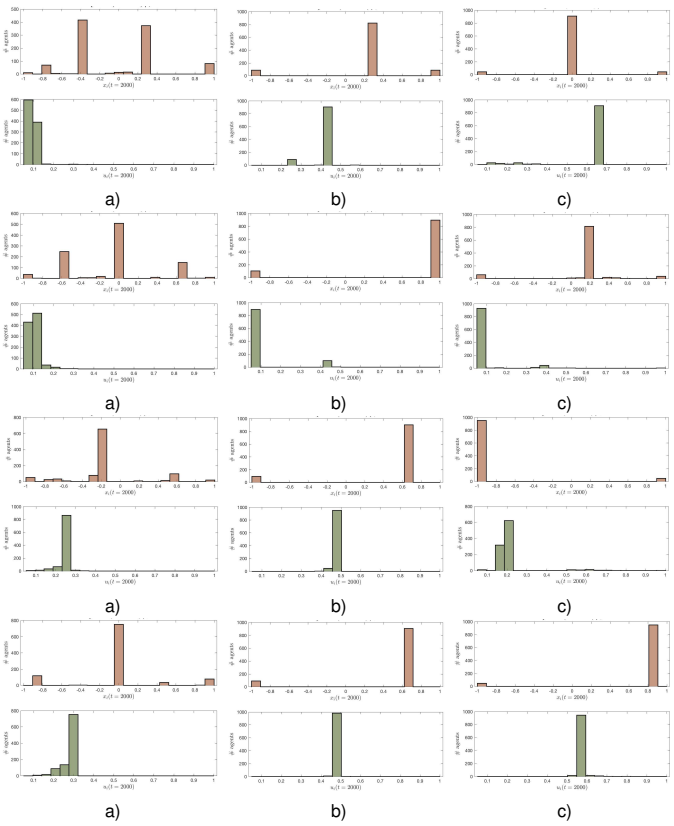

Figure 8 Final distributions of opinion and toleration on SW network at $p = 0.7$. Other conditions are the same as in Figure 7.

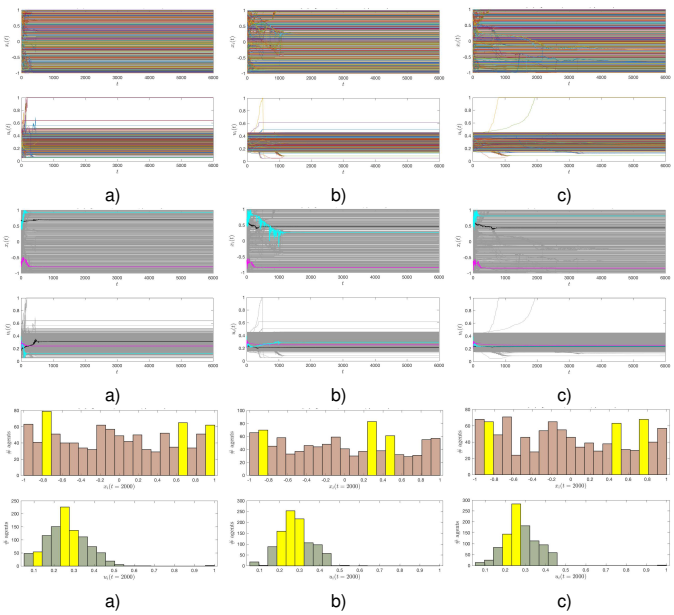

Figure 9 Opinion and toleration evolution on SF network at $(p, U) = (0.3, 0.3)$, IC$-A$. First double line – trajectories of agents' opinion and toleration evolution, second double line – trajectories of hubs' opinion and toleration evolution, third double line – final distributions of opinion (brown histograms) and toleration (green histograms), yellow bins include hubs. Columns: a) $\mu_r = 1$, b) $\mu_r = 1/5$ and c) $\mu_r = 1/10$.

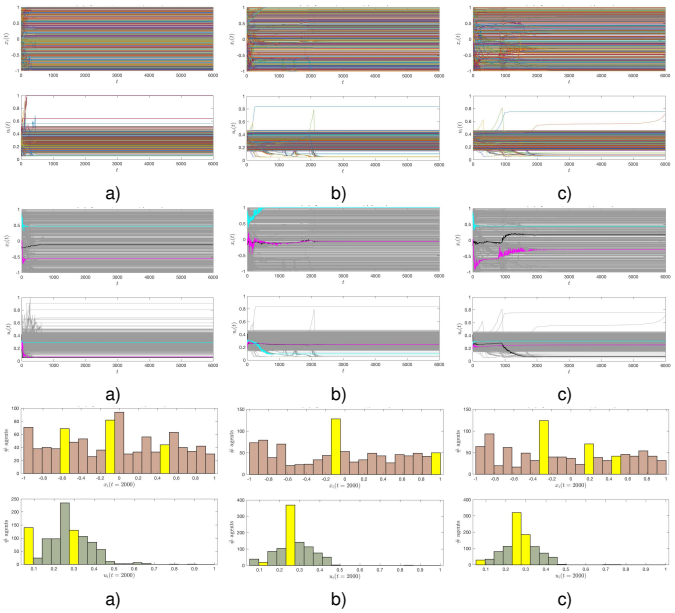

Figure 10 The same conditions as in Figure 9 but for IC$-B$.

For $U = 0.5$ and the decreasing ratio of convergence coefficients, μ_r's: 1. The time to reach an opinion stationary state increases when μ_r decreases and that is much greater than the time for SW networks. At $\mu_r = 1$ neither happens after that time, all trajectories of opinion evolution are parallel lines. Nevertheless, the evolution to stationary state is much longer and increasing for decreasing $\mu_r = 1/3, 1/5, 1/10$ (see Figure 11, first double line). 2. At $\mu_r = 1, 1/3, 1/5$, final distributions of opinion are similar each other and show a tendency to fragmentation in three opinion groups, but at $\mu_r = 1/10$ we observe a tendency to polarization (Figure 11, third double line). 3. The trajectory of principal PA-hub opinion is much stable and regular than that of the two smaller C-hubs, hubs behave similar to Brownian particles. We detect an irregular change of the final position of hubs in opinion space with the change of μ_r (Figure 11, second double line). 4. No regular change in the rate of toleration convergence is detected with the decrease of the convergence parameter μ_2. Toleration converges to the values smaller than U, forming two groups: one of them is a kind of bell distribution and the other consists of low tolerant agents. 5. The four generations of IC are not identical (the hubs are included), even being each of the same type uniform distribution, and the effects of their variations on the final opinion and toleration distributions were observed, in particular, through the variation of hubs' position and the size of bins that include hubs.

For $U = 0.7$ and decreasing ratio of convergence coefficients, μ_r's: 1. The time to reach an opinion stationary state (the hubs included) increases when μ_r decreases and that is much greater than the time for SW networks. Neither happens after that time, all trajectories of opinion evolution are parallel lines. The evolution to stationary state takes more time and is increasing for decreasing $\mu_r = 1, 1/3, 1/5, 1/10$ (see Figure 12). 2. Final distributions of opinion, being dependent of initial conditions noticeably, show a tendency to fragmentation or polarization at $\mu_r = 1, 1/3, 1/5, 1/10$ (Figure 12, third double line). 3. The trajectory of principal PA-hub opinion is more stable and regular than that of the two smaller C-hubs, hubs behave similar to Brownian particles. We detect an irregular change of the final position of hubs in opinion space with the change of μ_2, that depends of initials conditions also (igure

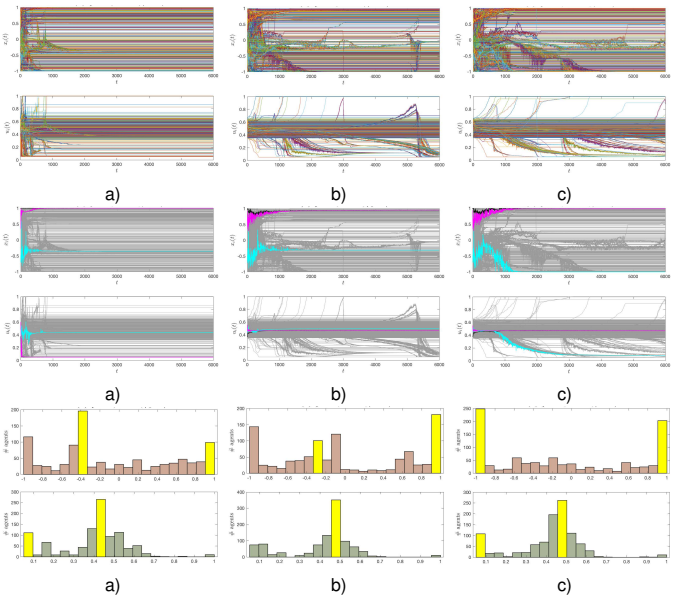

Figure 11 Opinion and toleration evolution in SF network at $(p, U) = (0.3, 0.5)$, IC$-A$. Other conditions are the same as in Figure 9.

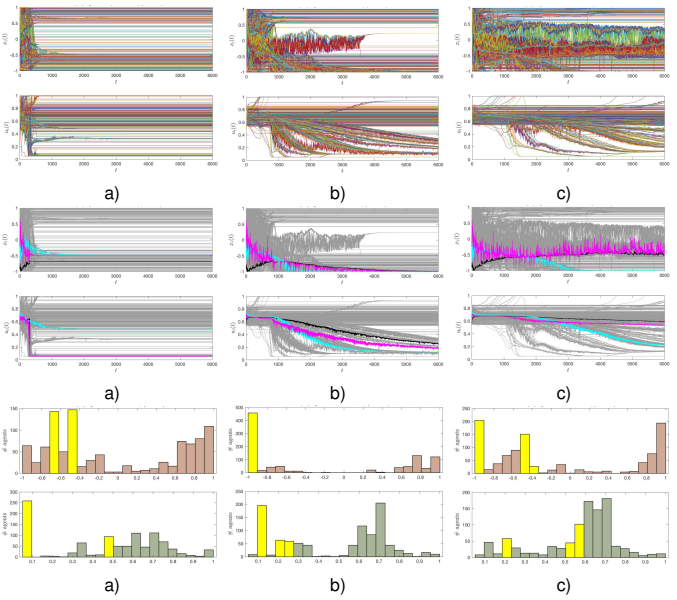

Figure 12 Opinion and toleration evolution in SF network at $(p, U) = (0.3, 0.7)$, IC$-A$. Other conditions are the same as in Figure 9.

12, second double line). A hub is frequently located in one of the important bins. Nevertheless, a hub does not represent an attractor of opinions because we observe final states when it belongs to a minority group. 4. Convergence of toleration is decreasing with decrease of the convergence parameter μ_2. Toleration converges to the values smaller than U, forming two groups: one of them is a kind of bell distribution and the other consists of a compact group of low tolerant agents, except for the case of low rate evolution of tolerance, $\mu_r = 1/10$ .5. The four generations of IC are not identical (the hubs are included), even being each of the same type uniform distribution, and the effects of initial conditions' variation on the final opinion and toleration distributions were observed, in particular, through the variation of hubs position and the size of bins that include hubs.

Finally, in SF societies at $p = 0.3$ no compact centrist opinion groups (a kind of local consensus) were detected and, in general, final opinion distributions look wide-ranging at almost all U and μ_r.

***SF society and* $p = 0.7$.** When the psychological composition of the society is $p = 0.7$ (C-agents are predominant), the cross-analysis of plots and histograms of the opinion and toleration evolution, for the set of parameters $U = 0.3, 0.5, 0.7$ and $\mu_r = 1, 1/3, 1/5, 1/10$, shows the following tendencies and peculiarities of opinion and toleration dynamics.

For $U = 0.3$ and the ratio of convergence coefficients, μ_r's: 1. The time to reach an opinion stationary state increases when decreases and that is greater than the time for SW networks. Nothing happens after that time, all trajectories of opinion and toleration are parallel lines (see Figure 13). The reason is that agents with close opinion have no common links or they have no overlap of opinion segments due to the distant opinions, so they are not pairs of interacting agents. 2. The trajectory of principal PA-hub opinion is much stable and regular than that of the two smaller C-hubs, all hubs behave similar to Brownian particles. We detect an irregular change of the final position of hubs in opinion space with the change of μ_2 (Figure 13, second double line). 3. We observe a tendency to fragmentation in the final opinion distribution, with noticeable opinion groups associated to the hubs. The final distributions of opinion for different $\mu_r = 1, 1/3, 1/5, 1/10$ differ each other not much, being different in position and size of hubs mainly (Figure 14). 4. No regular change in the rate of toleration convergence is detected with the decrease of the convergence parameter μ_2; toleration converges to the values smaller than U, with a tendency to form a kind of bell distribution.5. The four generations (A, B, C, D) of IC are not identical (the hubs are included), even being each of the same type uniform distribution, and the effects of variations in IC on the final opinion and toleration distributions were observed, in particular, through the variation in the position of hubs and size of bins that include hubs. In addition, groups of centrists are observed in contrast to that for the case of $(p, U) = (0.3, 0.3)$ (Figure 14).

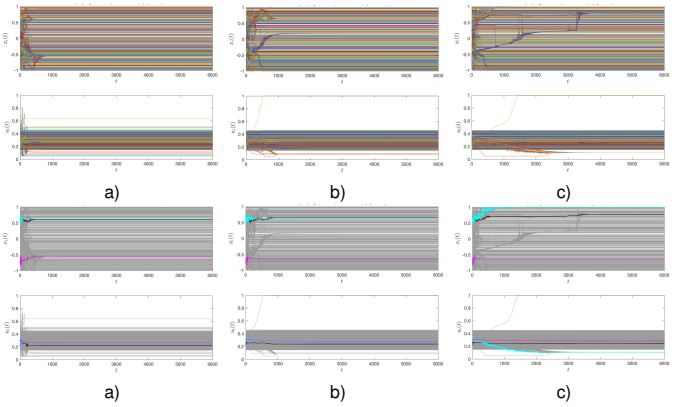

Figure 13 Opinion and toleration evolution in SF network at $(p, U) = (0.7, 0.3)$, IC$-A$. First double line – trajectories of agents' opinion and toleration evolution, second double line – trajectories of hubs' opinion and toleration evolution. Columns: a) $\mu_r = 1$, b) $\mu_r = 1/5$ and c) $\mu_r = 1/10$.

Figure 14 Final distributions of opinion and toleration (yellow bins include hubs) in network at $(p, U) = (0.7, 0.3)$: first double line is for the initial conditions A, second double line for IC$-B$, third double line for IC$-C$ and the fourth double line is for IC$-D$. Columns: a) $\mu_r = 1$, b) $\mu_r = 1/5$ and c) $\mu_r = 1/10$.

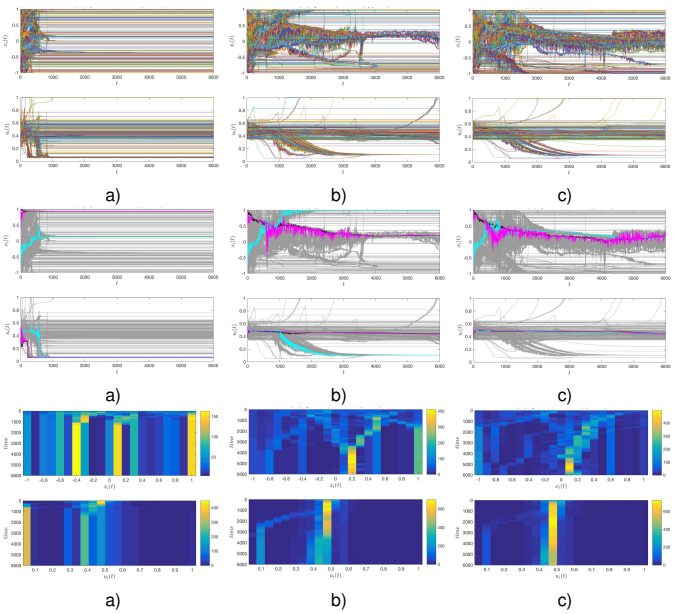

Figure 15 Opinion and toleration evolution in SF network at $(p, U) = (0.7, 0.5)$, IC$-A$. First double line – trajectories of agents' opinion and toleration evolution, second double line – trajectories of hubs' opinion and toleration evolution, third double line – color palette histogram of opinion and toleration evolution. Columns: a) $\mu_r = 1$, b) $\mu_r = 1/5$ and c) $\mu_r = 1/10$.

For the decreasing ratio of convergence coefficients, $\mu_r = 1, 1/3, 1/5, 1/10$ and $U = 0.5$: 1. The time to reach a quasi-stationary opinion state increases when μ_r decreases and that is much greater than the time for SW networks; an increasing number of bridges between opinion groups is also observed (Figure 15). 2. The trajectory of principal PA-hub opinion is much stable and regular than that of the two smaller C-hubs, all hubs behave similar to Brownian particles. We detect an irregular change of the final position of hubs in opinion space with change of μ_r (Figures 15 and 16, second double line). 3. A decrease in the rate of toleration convergence is detected with the decrease of the convergence parameter μ_2; toleration converges to the values smaller than U, with a tendency of forming a group of low tolerant agents, while the rest of agents are aggregated in a group with the toleration near U; in the case of $\mu_r = 1/10$ the toleration converges to a compact distribution centered almost at U (Figures 15, 16 and 17). 4. Significant difference in final distributions of opinion is observed as a result of change of μ_2 and relatively small variations in initial conditions (A, B, C, D) (Figure 17). In general, hubs are located in majority opinion groups. The states of polarization and consensus at different values of opinion and, sometimes, a tendency to fragmentation are observed. The latter indicates a kind of instability of the opinion in the C-PA society at $(p, U) = (0.7, 0.5)$.

For the decreasing ratio of convergence coefficients, $\mu_r = 1, 1/3, 1/5, 1/10$ and $U = 0.7$: 1. The time to reach a quasi-stationary opinion state increases when μ_r decreases and that is much greater than the time for SW networks; a number of bridges between opinion groups is large and increasing, so that the opinion variations are continuing for a long time (Figures 18 and 19). 2.

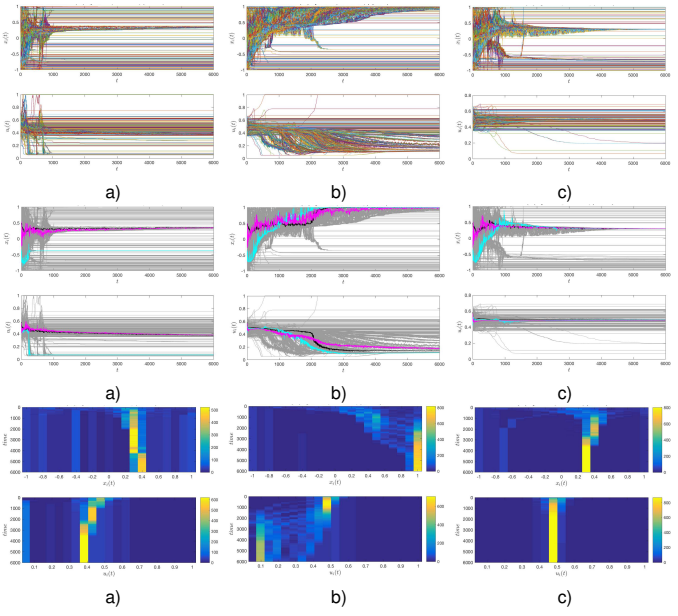

Figure 16 The same conditions as in Figure 15 but for IC$-B$.

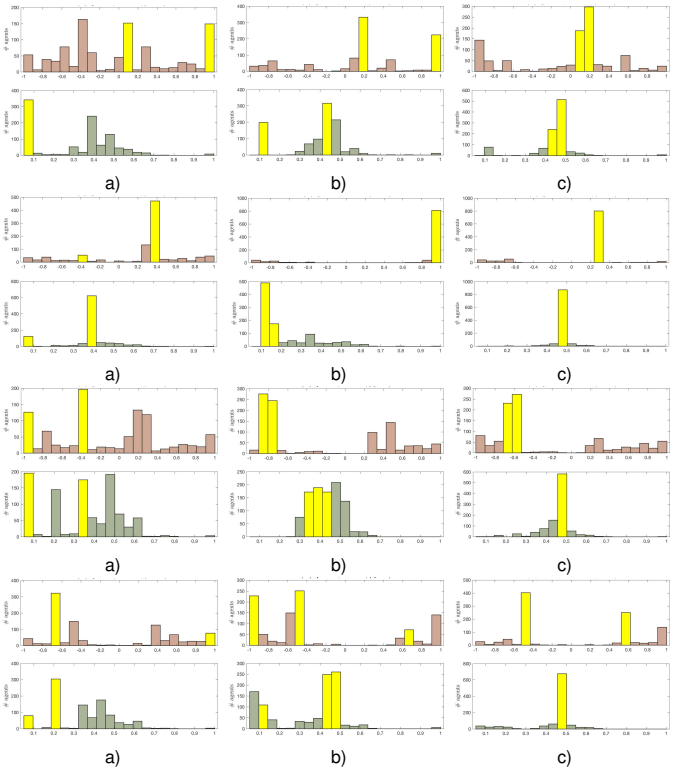

Figure 17 Final distributions of opinion and toleration (yellow bins include hubs) in network at $(p, U) = (0.7, 0.5)$: other conditions are the same as in Figure 14.

The trajectory of principal PA-hub opinion is much stable and regular than that of the two smaller C-hubs, all hubs behave similar to Brownian particles. We detect an irregular change of the final position of hubs in opinion space with change of μ_r (Figures 18 and 19, second double line; Figure 20). 3. A decrease in the rate of toleration convergence is detected with the decrease of the convergence parameter μ_2; toleration converges to the values smaller than U, with a tendency of forming a group of low tolerant agents at $\mu_r = 1, 1/3, 1/5$ especially, while the rest of agents are aggregated in a group with the toleration near U; large variations in final distributions of tolerance, associated to small variations in IC, are observed (Figures 18, 19 and 20). 4. Significant difference in final distributions of opinion is observed as a result of change of μ_r and of small variations in IC (Figure 20-(A, B, C, D)). In general, hubs are located in opinion majority groups. The states of polarization and consensus at different values of opinion and, sometimes a tendency to fragmentation are observed. The latter indicates a kind of instability of the opinion in the C-PA society at $(p, U) = (0.7, 0.7)$. Groups of centrists are not observed.

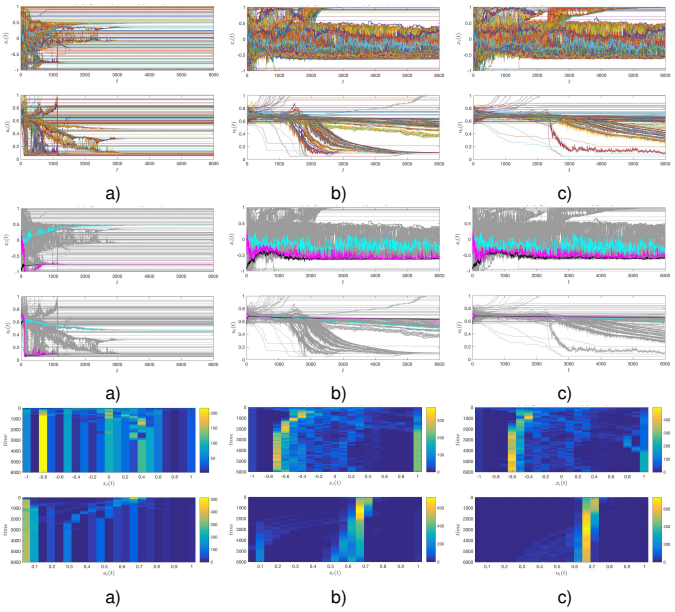

Figure 18 Opinion and toleration evolution in SF network at $(p, U) = (0.7, 0.7)$. Other conditions are the same as in Figure 15.

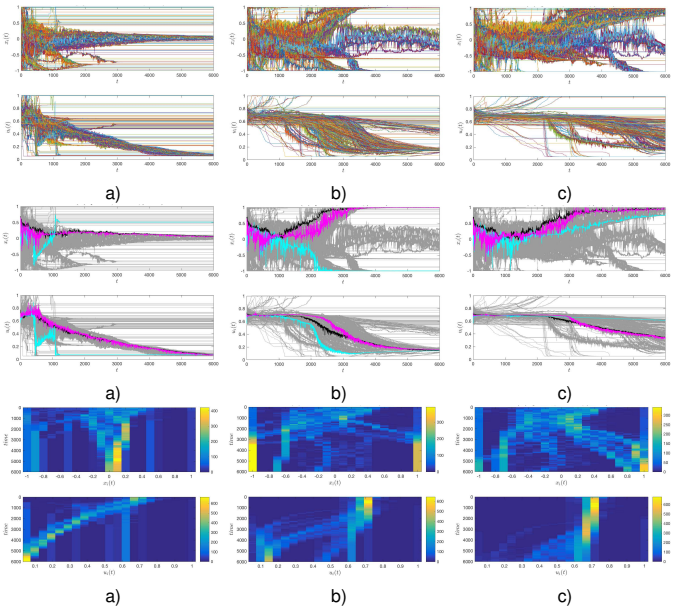

Figure 19 The same conditions as in Figure 18 but for IC$-B$.

Turning over the psychological type of hubs in society

Hubs of a social network, having a large number of links to other agents, interact more frequently with other agents than that do ordinary agents. We have turned over the psychological type of three hubs from PA, C and C to C, PA and PA, in order to see if it is important in opinion dynamics and run a series of experiments identical to that of the previous section. Comparative cross analysis of trajectories and final distributions of opinion and toleration of previous section show that evolution of opinion and toleration of hubs are notably affected by their psychological type and the ratio of timescales μ_r (Figure 21 as an example).

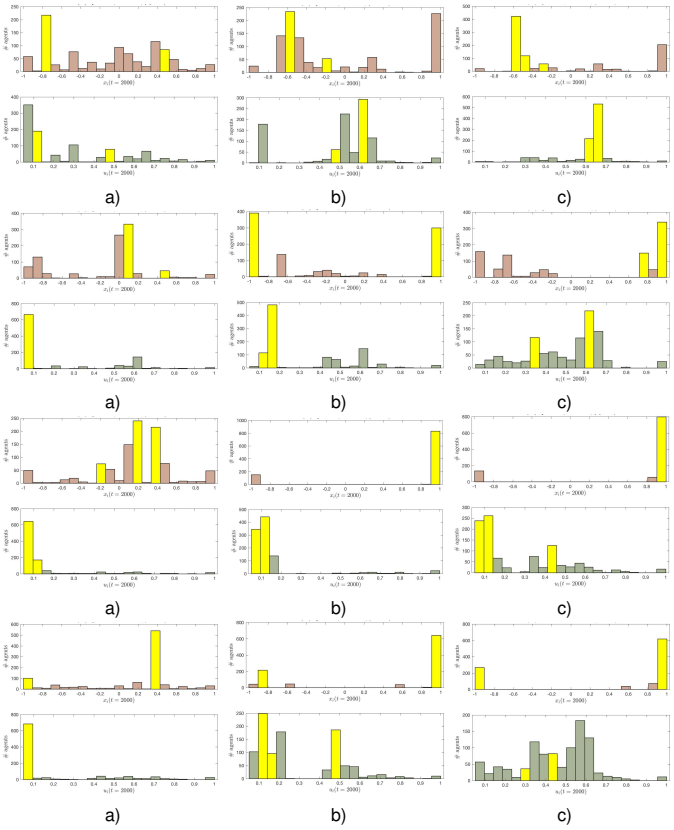

Figure 20 Final distributions of opinion and toleration (yellow bins include hubs) in network at $(p, U) = (0.7, 0.7)$: other conditions are the same as in Figures 14 and 17.

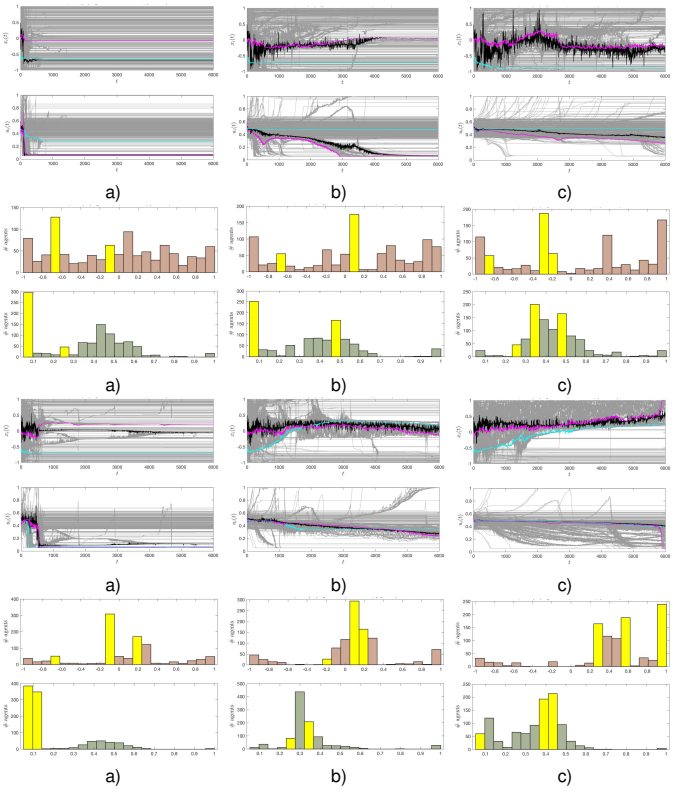

Figure 21 Opinion and toleration evolution in SF network for IC$-B$ at $(p, U) = (0.3, 0.5)$ and $(p, U) = (0.7, 0.5)$. Psychological type of hubs is C, PA and PA, that is inverted compared to Figures 11 and 15, respectively. Double lines one and three show trajectories of hubs' opinion and toleration evolution, lines two and four show final distributions of opinion and toleration. Columns: a) $\mu_r = 1$, b) $\mu_r = 1/3$ and c) $\mu_r = 1/10$.

CONCLUSION AND DISCUSSION

In the frame of C/PA relative agreement model of opinion dynamics we have analyzed mutual influence of social environment (SW and SF societies) and psychological aspects (psychological C/PA type and psychological profile) of agents on the opinion and toleration evolution in SW and SF artificial societies.

Mutual influence of social and psychological aspects of agents in mathematical models of opinion dynamics was treated systematically for the first time. Agents of C and PA psychological type were organized in SW and SF artificial societies. Psychological profile of each agent was represented by the *toleration* variable $u_i(t)$, that was interpreted vague as the opinion uncertainty in all previous works; the initial average toleration of society was regulated by the parameter U. C or PA psychological type responds for the agents' reaction on the opinion of others during agents' interaction, while the toleration shows the range of acceptability of others' opinions (wideness of agent's opinion interval). To study the mutual influence of opinion x_i and toleration u_i we took into account different time scale of opinion and toleration evolution by varying the relative parameter $\mu_r = \mu_2/\mu_1$, keeping in mind that opinion is the social characteristic and toleration expresses the psychological profile of agent.

1. Results of simulation demonstrate notable mutual influence of opinion and toleration on the dynamics of both, in particular, showing a split of toleration in two or three groups that was not revealed in other models. In general, the final toleration of agents shows a tendency to values lower than the initial U. In SW and SF societies the effects appear in different manner, being influenced by C/PA composition also. In other words, we observe how social environment influences psychology of agents, and vice versa. The peculiarity of opinion and toleration dynamics on SF networks comes from its tree-type topology, with communication channels that can be obstructed by the lack of relative agreement between the adjacent neighbors of network; the effect is observed through the straight line parallel individual trajectories in opinion and toleration evolution.

2. Consensus, being an opinion state desirable in some real life situations, unfortunately is not a typical one in a real society. In this concern, we found the consensus in mixed C/PA societies is the state rare to reach, in contrast to the results reported by other models (Yu *et al.* 2017). Opinion polarization and fragmentation accompanied by the formation of extremist groups resulted to be more recurrent states. In addition, the model shows the formation of groups of agents with a low toleration (agents closed for the interaction with others). In recent work (Huang *et al.* 2018) focused on the study of probability of opinion consensus emergence in SW societies, authors reported the consensus as a dominant state in a wide range of parameters of a modified DW model. It should be noted that modifications done to the original bounded confidence DW model have transformed it to a kind of relative agreement one, but without explicit use of toleration or uncer-

tainty as an agent's state variable. To some extent that model is similar to our one when the latter being applied to pure concord societies. When C-agents are predominant in C/PA societies, in our model the consensus is also observed more frequently.

3. The C/PA model used in this work is a dynamical system with stochastic elements; those are initial conditions for the variables and a stochastic updating dynamics through the random selection of interacting pairs of agents, even when the distribution of C and PA agents is fixed on a given network. When many simulations are done and the results of all scenarios are averaged, the latter will represent statistical tendencies in opinion and toleration evolution. The averaging of final opinion and toleration distributions, indicates general tendencies of opinion dynamics and can help to detect the bifurcation points of distributions (fragmentation, polarization or consensus) versus the parameter U. However, the averaged results can lead to confusing interpretation and explanation of opinion dynamics with respect to an individual scenario. For example, when single simulations show a dominant opinion bin in two alternating locations, then the averaging of these results will give exactly two groups of opinion and that is interpreted as splitting or polarization; that is not true for a single scenario, see the flips of position of predominant opinion groups $(SW, 0.7, 0.5, 1/10)$. This indicates the importance of particular scenarios analysis, one by one.

4. Dynamics of opinion and toleration in the C/PA societies on the SF networks is more complex and diverse than that on the SW networks. Both the process and final results of opinion and toleration evolution in C/PA model show significant difference for the SW and SF societies. That is due to the structural differences in organization of these societies; SF network has tree-like structure and agents-hubs. Having high degree of connection, hubs could be expected to be natural leaders of opinion, but our simulation experiments have shown it is not true. Even though hubs used to belong to majority but not outstanding groups, they behave like Brownian particles in opinion space more than leaders, their final states are not predictable. The size of the group of opinion followers depends on the degree of a hub and its psychological type. Sometimes, two hubs meet each other in the same group despite of different initial opinions. The final opinion and toleration states of SF society depend notably on small variations in initial conditions for the hubs (quasi leaders) and their psychological type, C or PA agent; the influence of timescale ratio μ_r is clearly important.

Few words in favor of toleration. In dynamical systems, any variable has to be measurable and that is evaluated by external measuring tool, in case of opinion models it is a kind of social enquiry. When the variable $u_i(t)$ is considered as an individual characteristic of i-agent at instant t and interpreted as the opinion uncertainty we meet a methodological difficulty if not a contradiction. In order to evaluate the state of a person, in sociology and psychology a specialist uses a kind of enquiry or a set of enquiries. To measure *opinion uncertainty* u_i at instant t one has to measure the opinion of an individual many times at an instant (in order to have statistical validation of the result), but that is not possible. Suppose we apply the individual enquiry for a short period of time. In this case the interval of time has to be so short that the opinion of the individual remains unvaried, and that has to be valid for each and every person of the society. That is also impossible because we don't know how fast or slow an individual opinion is changing. On the other hand, if we apply the enquiry to a set of persons, the result can't be considered as an individual characteristic. So, the "uncertainty" can't be measured instantaneously or it can't be considered as an individual variable.

The way to reconcile these contradictions is to interpret $u_i(t)$ as the toleration of i-agent to the opinions of others, that can be measured at each instant applying the same enquiry for a reasonably short interval of time (individual opinion remains unvaried) to each and every agent. *Opinion uncertainty*, as it was defined, can be self-evaluated only and, so there is no an objective criterion to validate it. Whereas the toleration (acceptability) can be measured, simply evaluating the range of opinions a person can accept. Acceptability is the base of agents' interaction and opinion exchange, but the opinion uncertainty of agent does not.

Opinion leadership is an important, if not crucial element in public opinion formation. So, for the future work we shall extent the model for the studying of the opinion leadership, using the self-organization of opinion and toleration in SW and SF societies of this work as the background. Pure mathematical study of the model is working on also.

Acknowledgments

Special thanks to the reviewers.

Availability of data and material

Not applicable.

Conflicts of interest

The authors declare that there is no conflict of interest regarding the publication of this paper.

LITERATURE CITED

Abrica-Jacinto, N. L., E. Kurmyshev, and H. A. Juárez, 2017 Effects of the interaction between ideological affinity and psychological reaction of agents on the opinion dynamics in a relative agreement model. Journal of Artificial Societies and Social Simulation **20**.

Axelrod, R., 1997 The complexity of cooperation. In *The Complexity of Cooperation*, Princeton university press.

Barabási, A.-L. and R. Albert, 1999 Emergence of scaling in random networks. science **286**: 509–512.

Clifford, P. and A. Sudbury, 1973 A model for spatial conflict. Biometrika **60**: 581–588.

Deffuant, G., 2006 Comparing extremism propagation patterns in continuous opinion models. Journal of Artificial Societies and Social Simulation **9**.

Deffuant, G., F. Amblard, G. Weisbuch, and T. Faure, 2002 How can extremism prevail? a study based on the relative agreement interaction model. Journal of artificial societies and social simulation **5**.

Deffuant, G., D. Neau, F. Amblard, and G. Weisbuch, 2001 Mixing beliefs among interacting agents. Advances in Complex Systems p. 11.

Dittmer, J. C., 2001 Consensus formation under bounded confidence. Nonlinear Analysis: Theory, Methods & Applications **47**: 4615–4621.

Dong, Y., M. Zhan, G. Kou, Z. Ding, and H. Liang, 2018 A survey on the fusion process in opinion dynamics. Information Fusion **43**: 57–65.

Douven, I. and A. Riegler, 2010 Extending the hegselmann–krause model i. Logic Journal of IGPL **18**: 323–335.

French Jr, J. R., 1956 A formal theory of social power. Psychological review **63**: 181.
Galam, S., 2008 Sociophysics: A review of galam models. International Journal of Modern Physics C **19**: 409–440.
Galam, S., 2022 Opinion dynamics and unifying principles: A global unifying frame. Entropy **24**: 1201.
Hegselmann, R., U. Krause, *et al.*, 2002 Opinion dynamics and bounded confidence models, analysis, and simulation. Journal of artificial societies and social simulation **5**.
Huang, C., Q. Dai, W. Han, Y. Feng, H. Cheng, *et al.*, 2018 Effects of heterogeneous convergence rate on consensus in opinion dynamics. Physica A: Statistical Mechanics and its Applications **499**: 428–435.
Kurmyshev, E., H. A. Juárez, and R. A. González-Silva, 2011 Dynamics of bounded confidence opinion in heterogeneous social networks: Concord against partial antagonism. Physica A: Statistical Mechanics and its Applications **390**: 2945–2955.
Lorenz, J., 2008 Fixed points in models of continuous opinion dynamics under bounded confidence. arXiv preprint arXiv:0806.1587 .
Lorenz, J., 2010 Heterogeneous bounds of confidence: meet, discuss and find consensus! Complexity **15**: 43–52.
Meadows, M. and D. Cliff, 2012 Reexamining the relative agreement model of opinion dynamics. Journal of Artificial Societies and Social Simulation **15**: 4.
Pineda, M., R. Toral, and E. Hernández-García, 2013 The noisy hegselmann-krause model for opinion dynamics. The European Physical Journal B **86**: 1–10.
Sznajd-Weron, K. and J. Sznajd, 2000 Opinion evolution in closed community. International Journal of Modern Physics C **11**: 1157–1165.
Urbig, D. and J. Lorenz, 2007 Communication regimes in opinion dynamics: Changing the number of communicating agents. arXiv preprint arXiv:0708.3334 .
Wang, C., 2022 Opinion dynamics with higher-order bounded confidence. Entropy **24**: 1300.
Watts, D. J. and S. H. Strogatz, 1998 Collective dynamics of 'small-world'networks. nature **393**: 440–442.
Xia, H., H. Wang, and Z. Xuan, 2011 Opinion dynamics: A multidisciplinary review and perspective on future research. International Journal of Knowledge and Systems Science (IJKSS) **2**: 72–91.
Yu, Y., V. X. Nguyen, and G. Xiao, 2020 Effects of initial state on opinion formation in complex social networks with noises. arXiv preprint arXiv:2004.00319 .
Yu, Y., G. Xiao, G. Li, W. P. Tay, and H. F. Teoh, 2017 Opinion diversity and community formation in adaptive networks. Chaos: An Interdisciplinary Journal of Nonlinear Science **27**: 103115.

How to cite this article: Kourmychev, E. and Abrica-Jacinto, N. L. A. The Effect of Agents' Psychology and Social Environment on the Opinion Formation: C/PA Relative Agreement Model in SW and SF Societies. *Chaos Theory and Applications*, 4(4), 212-225, 2022.

CHAOS
Theory and Applications
in Applied Sciences and Engineering

e-ISSN: 2687-4539
RESEARCH ARTICLE
Vol.4 / No.4 / 2022 / pp.226-233
Special Issue (EDIESCA 2022)
https://doi.org/10.51537/chaos.1197559

Effects of Optical Laser Injection in Multistable Erbium Fiber Lasers

J.O. Esqueda-de-la-Torre [*,1], **R. Jaimes-Reátegui** [*,2], **J.H. García-López** [*,3], **A. N. Pisarchik** [β,4] **and G. Huerta-Cuellar** [*,5]

[*]Dynamical Systems Laboratory, Centro Universitario de los Lagos, Universidad de Guadalajara, Enrique Díaz de León 1144, Paseos de la Montaña, 47460, Lagos de Moreno, Jalisco, Mexico , [β]Center for Biomedical Technology, Technical University of Madrid, Campus Montegancedo, 28223 Pozuelo de Alarcón, Madrid, Spain.

ABSTRACT During the past years, the study of optical injection has been intensely carried in theoretical and experimental realizations, showing interesting emergent behaviors, and synchronized states between other results. This work proposes an experimental scheme of an array of three driven erbium-doped fiber lasers (EDFLs), which dynamics exhibit the coexistence of multiple attractors. The laser array is controlled by a driver EDFL by injecting its optical intensity into the three coupled driven EDFLs array. The experimental realization was with the aim to induce an attractor tracking in the driving lasers, then to get coexisting states with increasing output power, and to study other emergent behavior given by the differences between doped fibers. To find the multistability regions, some bifurcation diagrams of the laser peak intensities are constructed. The obtained results are identified by comparing them with the modulation frequency. In some cases, the obtained results show that the intensity of the optical output signal of the driven systems is increased with respect to the initial individual response. In the case of synchronized states, it's possible to get an increased signal from the whole system. The obtained results could have important applications in repeaters of communications systems.

KEYWORDS
Erbium doped fiber laser
Multistability
Coupling
Non-linearity
Power increase

INTRODUCTION

Since some years ago, a rapid increase has been achieved in commercialization and research on erbium-doped fiber laser (EDFLs). This devices have been studied extensively for their flexible applications in several important optical systems as optical communications, laser surgery, nonlinear optics, optical sensing, and optical materials (Digonnet 2001; Luo and Chu 1998; Duarte 2009; Pisarchik *et al.* 2013; R. Mary and Kar 2014; Zhao *et al.* 2017). The EDFL active gain medium offers a long interaction length of pump light because the active ions that lead to a single transversal operation mode and a high gain produced by the correct choice of fiber parameters (Kir'yanov *et al.* 2013). Moreover, the signal amplification in optical fibers offers great advantages for technological applications due to its particular characteristics like electromagnetic field robustness, efficiency, reliability, compactness with an additional alignment-free structure, and spatial beam profile (Liu *et al.* 2020; Jafry *et al.* 2020). In that sense, the optical power increase is in constant evolution for the implementation of better fiber optical amplifiers capable of transmitting a signal in a fiber optical network along hundreds of kilometers with a minimum attenuation (Bouzid 2011).

It is well known that EDFL amplifiers wavelength, especially 1550 nm, shows very small losses in optical fibers (Castillo-Guzmán *et al.* 2008), as well as, a very rich dynamical behavior that the EDFL can exhibit (chaos, multistability, period-doubling,,etc.) (Reategui *et al.* 2004; Huerta-Cuellar *et al.* 2008) that can be have applications in different applications, such as, e.g., industrial micromachining (Kraus *et al.* 2010), medicine (Morin *et al.* 2009), spectral interferometry (Keren and Horowitz 2001), optical sensing (Wu *et al.* 2014), optical coherence tomography (Lim *et al.* 2005), optical metrology (Droste *et al.* 2016), and LiDAR systems (Philippov *et al.* 2004). In such systems, a particular state is determined by initial conditions (Pisarchik *et al.* 2005, 2011).

Manuscript received: 3 November 2022,
Revised: 28 November 2022,
Accepted: 29 November 2022.

[1]jose.edelatorre@alumnos.udg.mx
[2]rider.jaimes@academicos.udg.mx
[3]jhugo.garcia@academicos.udg.mx
[4]alexander.pisarchik@ctb.upm.es
[5]guillermo.huerta@academicos.udg.mx (**Corresponding author**).

Among many results showing the nonlinear behavior in EDFLs, few researchers are interested in the study of multistability in these lasers (Reategui *et al.* 2004; Huerta-Cuellar *et al.* 2008; Pisarchik *et al.* 2005; Huerta-Cuellar *et al.* 2009). EDFL's can exhibit up to four coexisting states under periodic modulation of the pump laser, in this sense, a high period attractor contains a high pulse energy (Pisarchik *et al.* 2011). Some other results in multistable systems show the possibility to obtain a monostable behavior by eliminating undesirable attractors, and in that sense some methods and results on attractor annihilation have been shown Sevilla-Escoboza *et al.* (2017); Pisarchik and Jaimes-Reategui (2009); Magallón *et al.* (2022). Recently Barba-Franco *et al.* (2023), shown the implementation of an electronical version of an EDFL based on differential equations.

The phenomenon of optical injection in lasers have been extensively studied since more than twenty years ago, and some recent results have been reported in VCSEL's Doumbia *et al.* (2022), showing the nonlinear dynamics and the polarization properties of a VCSEL by using a frequency comb. Between interesting results in the case of optical injection in semiconductor lasers, extreme events (EEs) have been recently investigated, and the probability of appearance of EEs can be controlled by the injection parameters applied to the locking regions of the diver-driving laser configuration (Huang *et al.* 2022). In the case of numerical injected semiconductor lasers modelated by the Lang-Kobayashi equations, different noise-induced transitions have been reported Tseng *et al.* (2022). Erbium doped fiber lasers has show different behaviors when optical injection is performed in this devices. In Xu *et al.* (2022), experimentally observed the evolutionary dynamics of convention solitons(CSs) in a simplified Erbium-doped fiber laser. An interesting phenomenon known as Q-switching was recently reported by Cai *et al.* (2022), they shown that the pulse evolution and dynamics of a pulsed erbium-doped fiber laser with plasmonic titanium nitride nanoparticles under different pump powers can result in two states: mode-locking and Q-switched mode-locking (QS-ML). Aditionally, the presence of noise-like behavior in doped fiber laser is one of the most interesting phenomena when the lasers are operating in a mode-looking regime, some results in this topic was presented by Soboń (2022).

Reported results about EDFL's injection shows the apparition of energetic pulses and some applications as the mentioned Q-switching phenomenon for certain laser type, but the dynamical response of a fiber laser depends on the doped level, and the distribution of the doping atoms in the fiber material as reported by Kir'yanov *et al.* (2013). In that sense, each of the implemented driven lasers were constructed with the same erbium doped fiber, but with different segments of fiber. With the aim of study the different possible behaviors when each of the EDFL's are injected by the driver EDFL, and looking for a high power emission in multistable EDFLs array, an experimental study of a four lasers system is implemented. Despite the existence of different results reported by injection into erbium-doped fiber lasers, this paper compares differences that may exist when using lasers implemented with different sections of the same doped fiber. The experimental setup is constructed by using a multistable driver EFDL Huerta-Cuellar *et al.* (2008), that injects an optical signal of a controlled state to three coupled multistable EFDLs.

This next sections of this paper is structured as follows. In Section 2, numerical model, materials and methods, the tools and basics of this work are shown, section 3, is about the experimental obtained results, and its discussion. Finally, the main conclusions of this work are given in section 4.

METHODS AND MATERIALS

Mathematical model

As first part of this research work, the model aproximation of the experimental setup is studied. The mathematical model of one normalized EDFL equations is shown in eq. 1:

$$\begin{aligned} \frac{dx}{dt} &= axy - bx + c(y + 0.3075), \\ \frac{dy}{dt} &= -\delta xy - (y + 0.3075) + \ldots \\ \ldots\ & P_{pump}(1 - exp(-18(1 - (y + 0.3075)/0.6150))), \end{aligned} \tag{1}$$

where the laser intensity is represented by x, the population inversion by y, the constants have the next values: $a = 6.6206 \times 10^7$, $b = 7.4151 \times 10^6$, $c = 0.0163$, and $\delta = 4.0763 \times 10^3$. The numerical model presented in 1, can reproduce periodic behavior depending on the combination of the initial conditions with the frequency of modulation for the bistable and multistable regions (as shown in 1(c))), and chaotic behavior as shown in Figure 1(a) for a modulation frequency (F_m), $0 < F_m < 12kHz$. Being a nonautonomous dynamic system, a pump function is required which is represented by eq. 2 where P_{pump} is the pump power, m is the modulation amplitude, and F_m is the modulation frequency.

$$P_{pump} = 506(1 + m * sin(2\phi F_m t)) \tag{2}$$

To obtain the numerical results, the Runge-Kutta method of 4^{th} order is implemented as in Reategui *et al.* (2004). As first annalysis of this laser model, a bifurcation diagram (BD) of local maxima of time series of the laser intensity x is constructed, as shown in Figure 1(a), as in Pisarchik *et al.* (2012); Esqueda-de-la Torre *et al.* (2022). This BD is obtained by sweeping the modulation frequency in a range $1kHz < F_m < 100kHz$, and by changing 30 times the initial conditions of the system. In this figure, the multistability region is obtained for a modulation frequency of $73kHz < F_m < 80kHz$ and $m = 1$ for which is $F_m = 84kHz$ is selected to generate the information of Figure 1(b), and (c), four labeled branches are distinguished for period one (P1), period three (P3), period four (P4), and period five (5) behavior, which represents coexistent states or multistable attractor. For the mentioned frequency $F_m = 80kHz$, in Figure 1(b), four time series of these coexistent attractors are shown with the pump power modulation signal P_{pump}, the ratio of the periodic attractors P1, P3, P4 and P5, are subharmonics of the modulation frequency F_m, respectively $\frac{P1}{F_m} = 1$, $\frac{P3}{F_m} = \frac{1}{3}$, $\frac{P4}{F_m} = \frac{1}{4}$, and $\frac{P5}{F_m} = \frac{1}{5}$, where P5 represents the higher intensity atractor. The Figure 1(c) shows the basin of attraction of the equation 1, with $F_m = 80kHz$, here, the colors yellow, red, blue, and green represent the initial conditions (x_0, y_0) where the EDFL shows periodic behavior represented by P1, P3, P4 and P5 respectively. Intial conditions (I.C.) used to obtain the periodical series shown in Figure 1(c), are the mentioned in table 1.

Table 1 Initial conditions used to get the periodic behavior shown in Figure 1(b).

	P1	P3	P4	P5
I.C. (x)	7.0614	24.2265	5.987	91.1913
I.C. (y)	0.0095	0.0542	0.0187	0.096

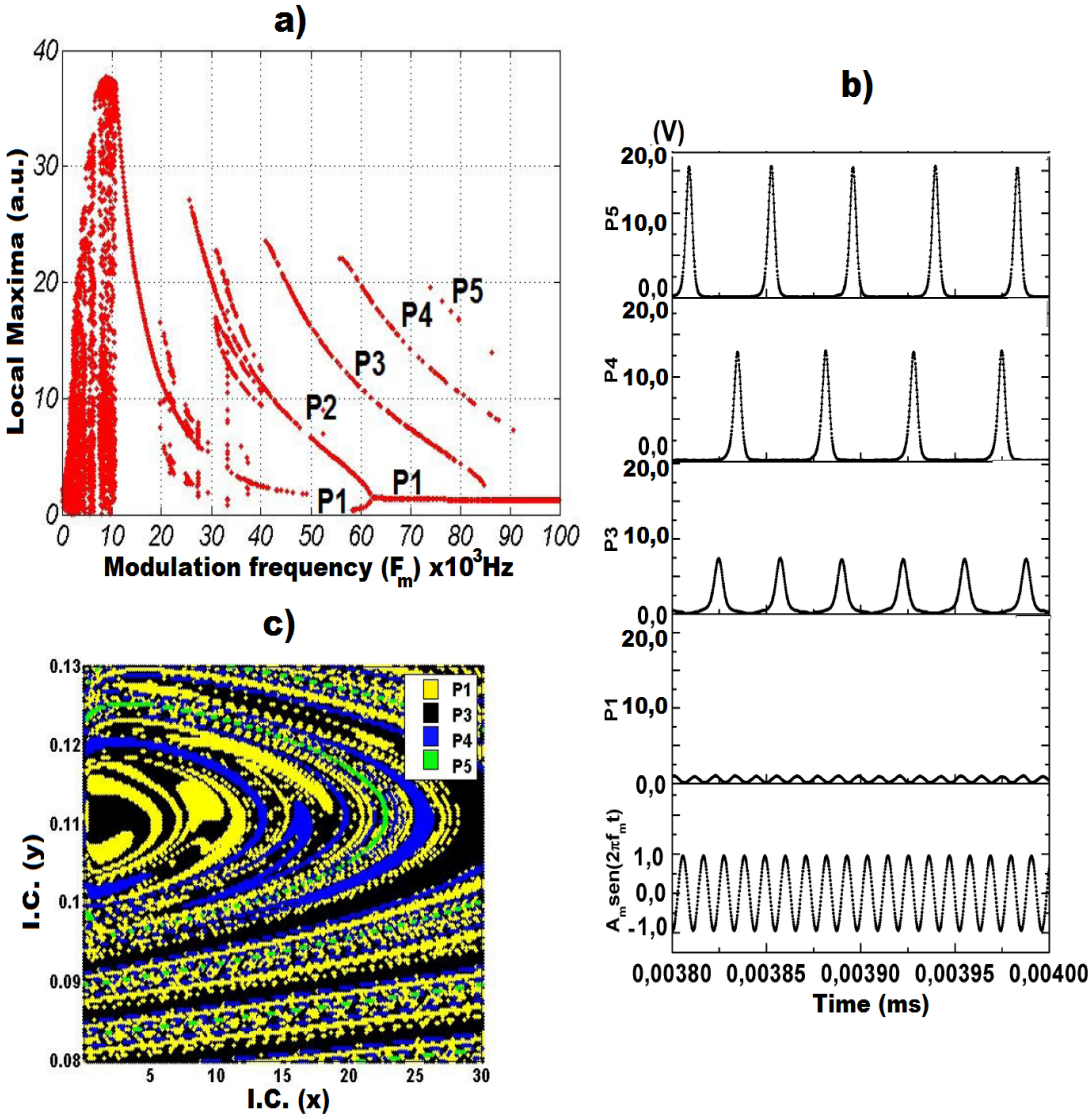

Figure 1 a) bifurcation diagram of the driver EDFL behavior , b) time series of multistable states, and pump frequency for a F_m= 80 kHz, and c) basin of attraction of the driver EDFL existing states for F_m= 80 kHz.

Experimental setup

The experimental setup of this work is shown in Figure 2, and is defined as in Esqueda-de-la Torre *et al.* (2022). The equipment and materials used are three temperature controllers ITC510, four function generators AFG3021B conected to the driver EDFL, four laser diodes BL976-PAG500, four EDFLs, eigth 1550nm Bragg gratings, four 980/1550nm wavelength divisor multiplexors WD9860BA, four photodetectors PBD481-AC, one data acquisition card NI BNC-2110, an Optical Attenuator and, a personal computer.

The driver laser (ML) which injects its optical power to the array of three erbium doped fiber lasers (SL's) is shown in Figure 2 (i). The bifurcation diagram of this laser is shown in Figure 3 (d). It has been chosen as driver due it has the richest dynamics over all the characterized lasers, showing a multistable behavior containing 5 behaviors. The injected information from the ML to the SLs could given by the for possible periodic states in the region of multistability, but in the presented results just the P5 and P4 behavior were used. It has its own function generator, current and temperature driver, a cavity and its output, as shown in Figure 2 (i).

Figure 2 (ii) shows an optical attenuator used to control the intensity of the driver laser signal, definning as coupling strength. The laser intensity variate by the optical attenuator from 8.5 V to 0 V, that corresponds to an attenuation from 0% to 100% respectively. Figures 2 (iii), (iv), and (v) represent the experimental implementation of each erbium-doped fiber driving lasers (SL's) whose bifurcation diagrams are shown in Figure 3 (a), (b), and (c) respectively. Each current Driver is being modulated by adding both the function generator and the coupling of the driver laser signal.

Figure 2 (vi) shows the data acquisition card (DAQ), previously configured in the PC to acquire the time series coming from the output optical detectors of the three erbium doped fiber driving lasers and the driver laser. In Figure 2 (vii) a personal computer appears, where all time series of the whole system are saved and analyzed to study their dynamics.

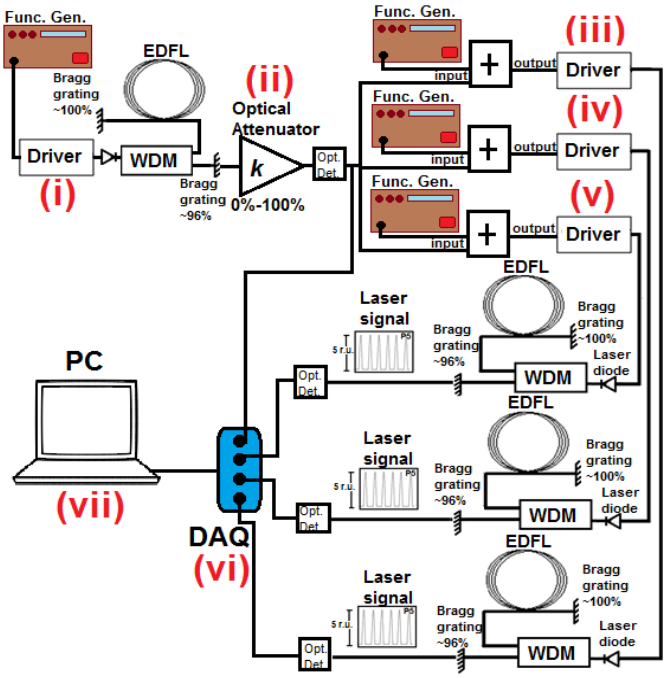

Figure 2 Experimental setup.

In the present work, the three SLs are constructed with commercial erbium doped fibers defined as type M5 Kir'yanov *et al.* (2013), and the ML is constructed by a highly doped erbium fiber laser wich presents a rich dynamical behavior as the obtained in Fig. 2 Pisarchik *et al.* (2012). As part of the characterization of the different EDFLs in this work, and in spite of the four EDFLs used in experiments are close in fiber type, and fiber measures, a bifurcation diagram of local maxima of time series for each EDFL is constructed, as shown in Huerta-Cuellar *et al.* (2008). In order to understand the behavior, modulation frequency ranges, and the multistability regime for each EDFL, the experimental bifurcation diagrams are shown in Figure 3.

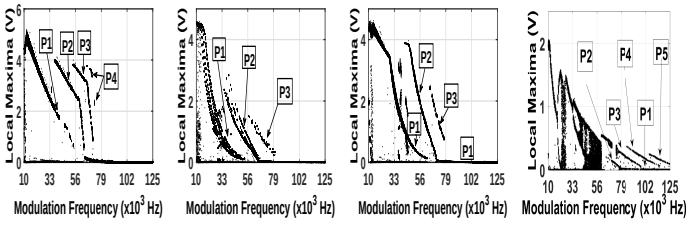

Figure 3 Bifurcation diagrams corresponding to to (a) SL1, (b) SL2, (c) SL3, and (d) ML.

RESULTS

In this section, experimental obtained results are shown. To guarantee that the behavior of the SLs is different to the behavior of the ML, each initial behavior (I.C.) is manually fixed by turning on and off the function generators shown in Figure 2(iii-v). As the results are obtained from the experimental setup, it isn't possible to know exactly the I. C. value, as in the case of numerical implementation. All of the different periodic behaviors in the EDFLs have dissimilar probability as shown in Pisarchik *et al.* (2012). From the later, is easy to obtain a P1 behavior, and it is difficult to obtain a P5 behavior, as has been experimentally shown by Huerta-Cuellar et. al. in Huerta-Cuellar *et al.* (2008).

One interesting result about optical injection was theoretically and experimentally shown by Doumbia *et al.* (2020), they uses an optical frequency comb to inject to a single frequency semiconductor, from that they obtained several dynamic behavior from periodical to chaos and other behaviors. Some dynamical effects of optical injection in multistable lasers has been recently considered by Pisarchik and Hramov (2022), from which the dynamical answer of optical injection is studied from gas lasers, semiconductor lasers, and VCELs.

Few works are devoted to studying the effects of optical injection in EDFLs. In this work, the dynamical response from three different injected EDFLs, whose were constructed from the same erbium-doped fiber are shown. The obtained results are ordered considering some of the different combinations, first by fixing the driven laser in P5 dynamics, and then it is fixed in P4, for each of the driving EDFLs (SLs), by showing what happens for each scenario for different coupling strengths. Experimental results whit coupling between ML with SLs are shown in the next sub-sections.

Fixing driver laser in period five (P5) In this subsection an evaluation of the coupling strenght between the ML and the SLs is revised. The Figure 4 shows the bifurcation diagrams of local maxima of time series for the three driving lasers (SL). Each of the SLs has been modulated by the driver laser (ML) with a previously fixed signal in P5 behavior, this can be obtained by changing the initial condition by turning on and off the function generator.

Having fixed the ML in a P5 behavior it has been applied a coupling strength k variation between the ML and each of the SLs (for SL1, SL2, and SL3). From obtained results, in Table 1 its possible to observe that the coupling value k, and the modulation amplitude are not the same, it is because the differences between the SLs behaviors that can be appreciated from Fig. 3. As result of the coupling strength between the ML and the SLs, also it is possible to see that the final behavior is not a tracking attractor from SLs to ML.

For the case that the SLs are initially in P1, Fig 4(a–c), the final obtained behavior corresponds to P5, here it worths to mention that P5 is not a possible behavior in those lasers, but the SLs reach a tracking attractor. For the coupling with SLs with a behavior different from P1, i.e. P2, and P3, the resulting behavior is not a tracking attractor between ML and SLs, and aditionally, in some cases, it is chaotic.

A comparision between the SLs is realized to know the obtained behavior after the ML perturbation. In order to see if the arrangement of three SLs reach the tracking attractor of the ML, the average values of their intensities differences has been done. When the value is close to zero, it implies the tracking attractor between the ML and the SLs, see Fig. 5.

In order to compare the obtained results from the optical injection of the ML to the SLs, the sums of the resulting behaviors of the SLs are achieved. In Fig. 6(a-d), it is possible to see from the obtained results, that in the case of SLs with initial behavior of P1, the similitude does not have a big change, while with the other initial states the results are too different between the SLs and the ML.

Fixing driver laser in period five (P4) In this subsection an evaluation of the coupling strenght between the ML and the SLs is

Table 2 Behavior of the SL for threshold k for ML P5 oscillation.

Figure	threshold k	Amplitude (V)	Modulation frequency (kHz)	LS number	Initial behavior	Final behavior
4 (a)	69	0.80	110	LS1	P1	P5
4 (b)	92	1.40	110	LS2	P1	P5
4 (c)	88	1.00	110	LS3	P1	P5
4 (d)	93	0.80	66	LS1	P2	CH
4 (e)	88	1.40	65	LS2	P2	P1
4 (f)	94	1.00	66	LS3	P2	CH
4 (g)	NA	0.80	66	LS1	P3	P3
4 (h)	NA	0.80	66	LS2	P3	P3
4 (i)	84	0.80	66	LS3	P3	CH

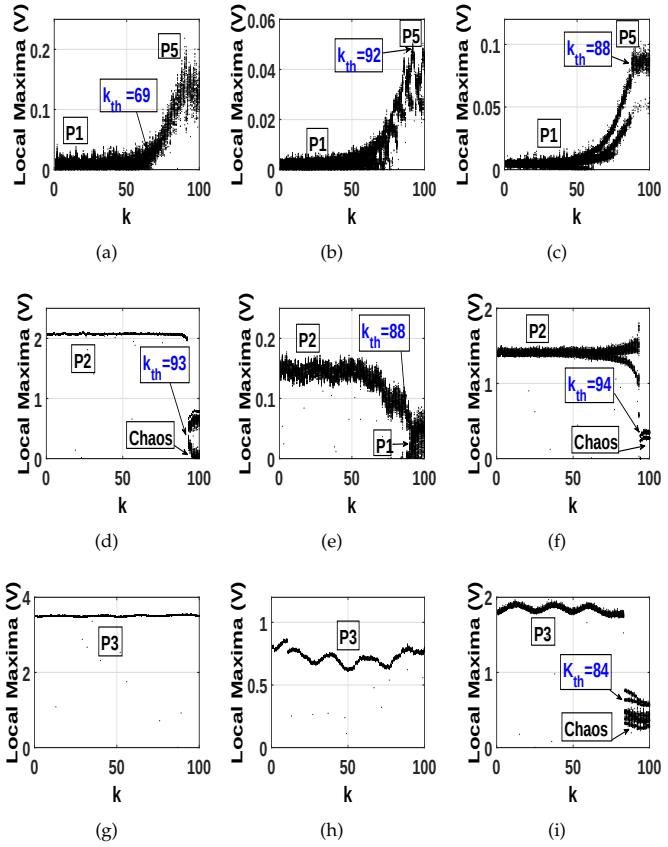

Figure 4 Bifurcation diagrams of the three SLs, under P5 periodic injected signal from the ML. The figures corresponds to the information shown in Table 2

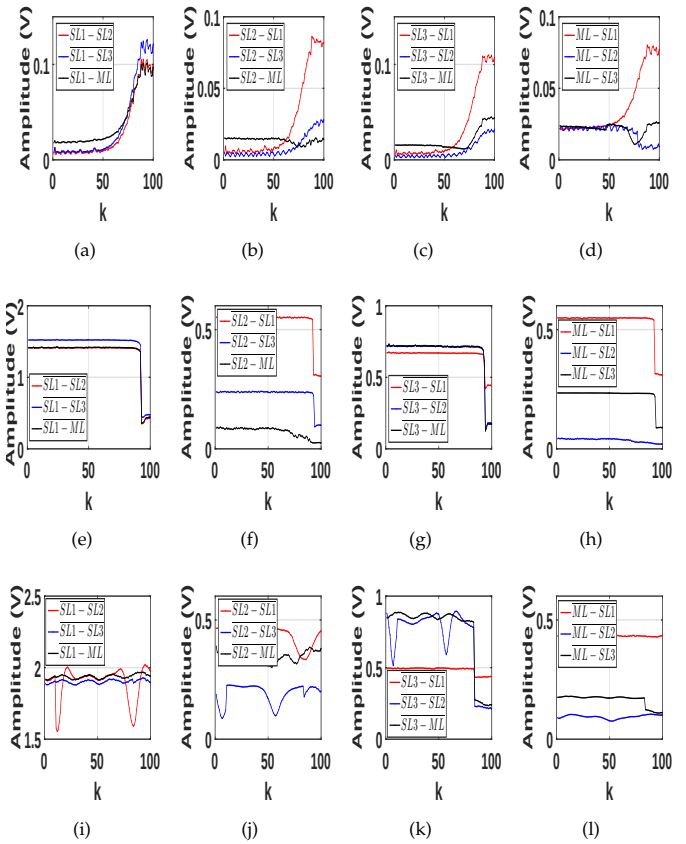

Figure 5 Average values of difference between: a) SL 2 (red color), SL 3 (blue color) and ML (black color) from SL 1, b) SL 1 (red color), SL 3 (blue color) and ML (black color) from SL 2, c) SL 1 (red color), SL 2 (blue color) and ML (black color) from SL 3, and d) SL 1 (red color), SL 2 (blue color) and SL 3 (black color) from ML laser.

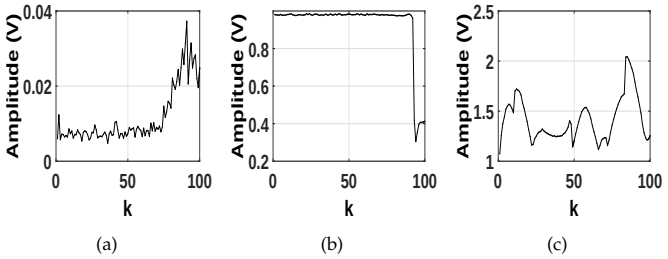

Figure 6 Average values of sum of the three SLs time series for each coupling strength value (k).

revised. The Figure 7 shows the bifurcation diagrams of local maxima of time series for the three driving lasers (SL). Each of the SLs has been modulated by the driver laser (ML) with a previously fixed signal in P4 behavior, this can be obtained by changing the initial condition by turning on and off the function generator. Having fixed the ML in a P4 behavior, it has been applied a coupling strength k variation between the ML and each of the SLs (for SL1, SL2, and SL3). From obtained results, in Table 2 its possible to observe that the coupling value k, and the modulation amplitude are not the same, it is because the differences between the SL behaviors that can be apreciated from Fig. 3. As result of the coupling strength between the ML and the SLs, also it is possible to see that the final behavior is not a tracking attractor between ML and SLs. For the case that the SLs are initially in P1, Fig 7(a–c), the final obtained behavior corresponds to P4, here it worths to mention that P4 is not a possible behavior in those lasers, but the SLs reach the tracking attractor. For the coupling with SLs with a behavior

different from P1, i.e. P2, see Figs. 7(d–f), and P3, see Figs. 7(g–i), the resulting behavior does not completely follow the P4 attractor, and aditionally, in some cases, it is chaotic.

Table 3 Behavior of the SL for threshold k for ML P4 oscillation.

Figure	threshold k	Amplitude (V)	Modulation frequency (kHz)	LS number	Initial behavior	Final behavior
7 (a)	74	0.80	110	LS1	P1	P4
7 (b)	84	1.40	110	LS2	P1	P4
7 (c)	61	1.00	110	LS3	P1	P4
7 (d)	96	0.80	66	LS1	P2	CH/P3
7 (e)	92 and 97	1.40	65	LS2	P2	CH/P4
7 (f)	95	1.00	66	LS3	P2	CH
7 (g)	73 and 85	0.80	66	LS1	P3	CH/P3
7 (h)	86	0.80	66	LS2	P3	CH
7 (i)	76	0.80	66	LS3	P3	CH

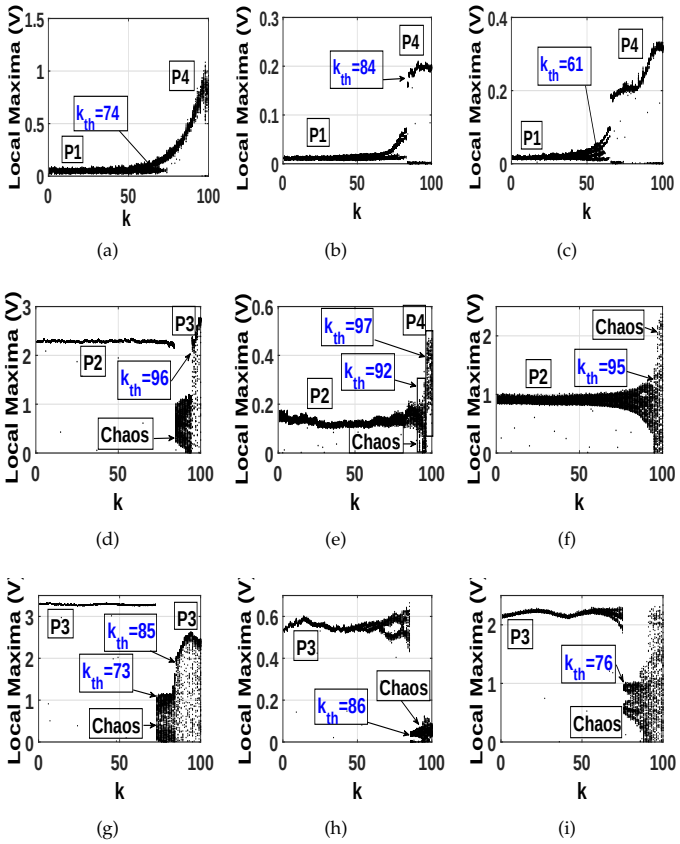

Figure 7 Bifurcation diagrams of the three SLs, under P5 periodic injected signal from the ML. The figures corresponds to the information shown in Table 3

A comparision between the SLs is realized to know the obtained behavior after the ML perturbation. In order to see if the arrangement of three SLs reach the tracking attractor of the ML, the average values of their intensities differences has been done. When the value is close to zero, it implies the tracking attractor between ML and SLs, see Fig. 8.

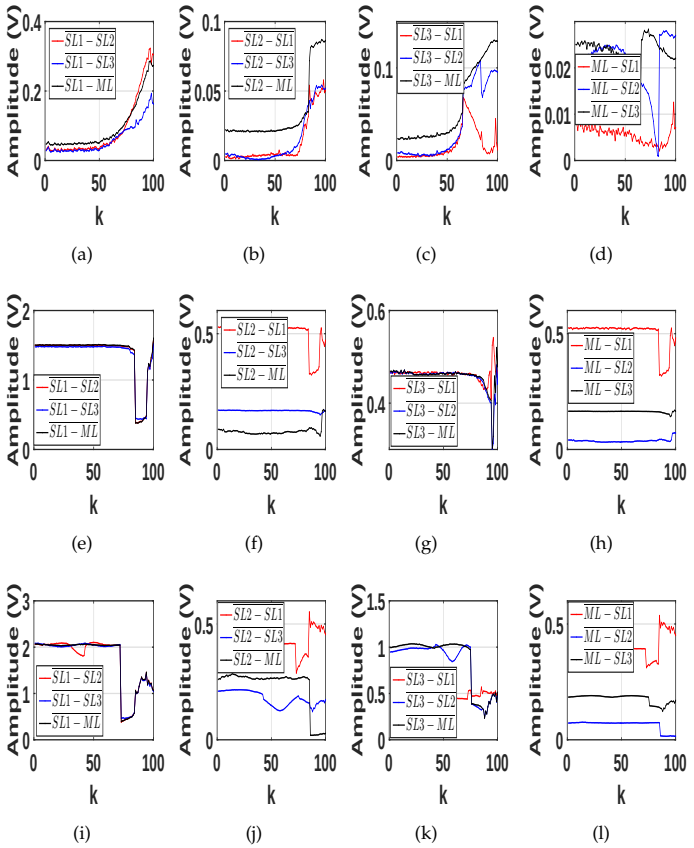

Figure 8 Average values of difference between: a) SL 2 (red color), SL 3 (blue color) and ML (black color) from SL 1, b) SL 1 (red color), SL 3 (blue color) and ML (black color) from SL 2, c) SL 1 (red color), SL 2 (blue color) and ML (black color) from SL 3, and d) SL 1 (red color), SL 2 (blue color) and SL 3 (black color) from ML laser.

In order to compare the obtained results from the optical injection of the ML to the SLs, the sums of the resulting behaviors of the SLs are achieved. In Fig. 9(a-d), it is possible to see from the obtained results, that in the case of SLs with initial behavior of P1, the similitude does not have a big change, while with the other initial states the results are too different between the SLs and the ML.

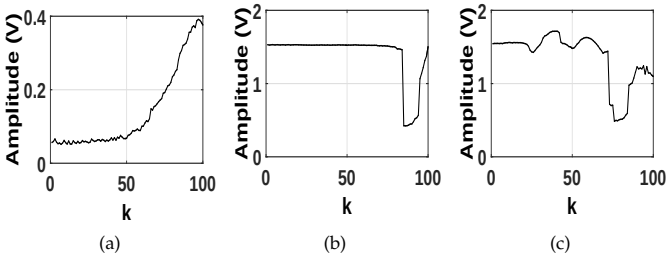

Figure 9 Average values of sum of the three SLs time series for each coupling strength value (k).

CONCLUSIONS

By considering that the SLs have different global behavior, as can be confirmed from Figure 3, the analysis of their answer to the same optical injection was made. The construction of the bifurcation diagram and basin of attraction of the coexistent states of EDFL, allowed us to know the multistable behavior in the driver laser output signal. The output signal from the ML was implemented as additional modulation to the pump power of the three multistable SLs array and in turn. The results obtained when the ML injects a P5, and P4 dynamical behavior shows an attractor tracker response, in this sense when SLs have P1 dynamics a phase synchronization to a single state is favored. This synchronization phenomenon has been reported and studied from other authors by different coupling techniques in other type of lasers, but in one-to-one coupling. In the case of synchronized lasers, a result through the suitable choice of the coupling strength value and the sum of the output signals of the three slave lasers allowed us to obtain maximal power. This optimal power crucially depends on the $k_{threshole}$ value.

Results obtained when the SLs have an initial behavior of P2, shown chaos and P1 monostable behavior when the ML operates in P5. In the case of P1 response, is a possible effect related with one of the three actual behavior of the SL but the answer of chaos reserves another analysis related with the interaction of different periodic states. The obtained results of the injected SLs when the ML is oscillating in P4, shown a richer dynamics in the case when bistable behavior of CH/P3, and CH/P4 is obtained. The activity of P4 is more related to harmonic behavior from the I.C. of the SL, while the P3 is one of the possible dynamics of the SLs.

The presented results are just an analysis of the possible answer of the SLs, that are implemented with the same erbium doped fiber, and the differences on the dynamical behavior are because this systems are real and the small differences in the erbium concentration can produce changes in the final result, as the chaos theory affirms. In this sense, more analysis and research could be implemented. In the case of SLs synchronized with the ML in P5 behavior, we consider that one possible application is in the repeaters of communication systems.

Acknowledgments

J.O.E. thanks Consejo Nacional de Ciencia y Tecnologia (CONACyT) for support provided to develop the studies of Doctorate in Science and Technology at CULagos in UdeG. R.J.-R. thanks CONACYT for financial support, project No. 320597. To AMVP, and VPS for their support with the final edition of the paper.

Availability of data and material

Not applicable.

Conflicts of interest

The authors declare that there is no conflict of interest regarding the publication of this paper.

LITERATURE CITED

Barba-Franco, J., L. Romo-Muñoz, R. Jaimes-Reátegui, J. García-López, G. Huerta-Cuellar, *et al.*, 2023 Electronic equivalent of a pump-modulated erbium-doped fiber laser. Integration **89**: 106–113.

Bouzid, B., 2011 New erbium doped fiber laser amplifier. In *2011 Saudi International Electronics, Communications and Photonics Conference (SIECPC)*, pp. 1–3, IEEE.

Cai, X., P. Gu, and Z. Zhang, 2022 Real-time observation of mode locking and q-switching in erbium-doped fiber laser using plasmonic titanium nitride nanoparticles. Journal of Russian Laser Research **43**: 169–175.

Castillo-Guzmán, A., G. Anzueto-Sánchez, R. Selvas-Aguilar, J. Estudillo-Ayala, R. Rojas-Laguna, *et al.*, 2008 Erbium-doped tunable fiber laser. In *Laser Beam Shaping IX*, volume 7062, pp. 214–217, SPIE.

Digonnet, M., 2001 *Rare-Earth-Doped Fiber Lasers and Amplifiers, Revised and Expanded*. CRC, second edition.

Doumbia, Y., T. Malica, D. Wolfersberger, K. Panajotov, and M. Sciamanna, 2020 Nonlinear dynamics of a laser diode with an injection of an optical frequency comb. Opt. Express **28**: 30379–30390.

Doumbia, Y., D. Wolfersberger, K. Panajotov, and M. Sciamanna, 2022 Two polarization comb dynamics in vcsels subject to optical injection. In *Photonics*, volume 9, p. 115, MDPI.

Droste, S., G. Ycas, B. R. Washburn, I. Coddington, and N. R. Newbury, 2016 Optical frequency comb generation based on erbium fiber lasers. Nanophotonics **5**: 196–213.

Duarte, F., 2009 *Tunable Laser Applications*. CRC, second edition.

Esqueda-de-la Torre, J., J. García-López, G. Huerta-Cuellar, and R. Jaimes-Reategui, 2022 Synchronization of two fiber lasers with optical logarithmic coupler: Experimental implementation. In *Complex Systems and Their Applications*, pp. 3–21, Springer.

Huang, Y., P. Zhou, Y. Zeng, R. Zhang, and N. Li, 2022 Evolution of extreme events in a semiconductor laser subject to chaotic optical injection. Physical Review A **105**: 043521.

Huerta-Cuellar, G., A. Pisarchik, A. Kir'yanov, Y. O. Barmenkov, and J. del Valle Hernández, 2009 Prebifurcation noise amplification in a fiber laser. Physical Review E **79**: 036204.

Huerta-Cuellar, G., A. N. Pisarchik, and Y. O. Barmenkov, 2008 Experimental characterization of hopping dynamics in a multistable fiber laser. Physical Review E **78**: 035202.

Jafry, A., N. Kasim, M. Rusdi, A. Rosol, R. Yusoff, *et al.*, 2020 Max phase based saturable absorber for mode-locked erbium-doped fiber laser. Optics & Laser Technology **127**: 106186.

Keren, S. and M. Horowitz, 2001 Interrogation of fiber gratings by use of low-coherence spectral interferometry of noiselike pulses. Optics Letters **26**: 328–330.

Kir'yanov, A. V., Y. O. Barmenkov, G. E. Sandoval-Romero, and L. Escalante-Zarate, 2013 er^{3+} concentration effects in commercial erbium-doped silica fibers fabricated through the mcvd and dnd technologies. IEEE Journal of Quantum Electronics **49**: 511–521.

Kraus, M., M. A. Ahmed, A. Michalowski, A. Voss, R. Weber, *et al.*, 2010 Microdrilling in steel using ultrashort pulsed laser beams with radial and azimuthal polarization. Optics express **18**: 22305–22313.

Lim, H., Y. Jiang, Y. Wang, Y.-C. Huang, Z. Chen, *et al.*, 2005 Ultrahigh-resolution optical coherence tomography with a fiber laser source at 1 μm. Optics letters **30**: 1171–1173.

Liu, J., X. Li, J. Feng, C. Zheng, Y. Wang, *et al.*, 2020 Zns nanospheres for optical modulator in an erbium-doped fiber laser. Annalen der Physik **532**: 1900454.

Luo, L. and P. Chu, 1998 Optical secure communications with chaotic erbium-doped fiber lasers. J. Opt. Soc. Amer. B **15**: 2524–2530.

Magallón, D. A., R. Jaimes-Reátegui, J. H. García-López, G. Huerta-Cuellar, D. López-Mancilla, *et al.*, 2022 Control of multistability in an erbium-doped fiber laser by an artificial neural network: A numerical approach. Mathematics **10**: 3140.

Morin, F., F. Druon, M. Hanna, and P. Georges, 2009 Microjoule

femtosecond fiber laser at 1.6 μm for corneal surgery applications. Optics letters **34**: 1991–1993.

Philippov, V., C. Codemard, Y. Jeong, C. Alegria, J. K. Sahu, *et al.*, 2004 High-energy in-fiber pulse amplification for coherent lidar applications. Optics letters **29**: 2590–2592.

Pisarchik, A. and R. Jaimes-Reategui, 2009 Control of basins of attraction in a multistable fiber laser. Physics Letters A **374**: 228–234.

Pisarchik, A., R. Jaimes-Reátegui, R. Sevilla-Escoboza, and G. Huerta-Cuellar, 2012 Multistate intermittency and extreme pulses in a fiber laser. Physical Review E **86**: 056219.

Pisarchik, A., R. Sevilla-Escoboza, R. Jaimes-Reátegui, G. Huerta-Cuellar, J. García-Lopez, *et al.*, 2013 Experimental implementation of a biometric laser synaptic sensor. Sensors pp. 17322–17331.

Pisarchik, A. N. and A. E. Hramov, 2022 Multistability in lasers. In *Multistability in Physical and Living Systems*, pp. 167–198, Springer.

Pisarchik, A. N., R. Jaimes-Reátegui, R. Sevilla-Escoboza, G. Huerta-Cuellar, and M. Taki, 2011 Rogue waves in a multistable system. Physical Review Letters **107**: 274101.

Pisarchik, A. N., A. V. Kir'yanov, Y. O. Barmenkov, and R. Jaimes-Reátegui, 2005 Dynamics of an erbium-doped fiber laser with pump modulation: theory and experiment. JOSA B **22**: 2107–2114.

R. Mary, D. C. and A. Kar, 2014 Eapplications of fiber lasers for the development of compact photonic devices. IEEE J. Sel. Top. Quantum Electron **20**: 0902513.

Reategui, R., A. Kir'yanov, A. Pisarchik, Y. O. Barmenkov, and N. Il'ichev, 2004 Experimental study and modeling of coexisting attractors and bifurcations in an erbium-doped fiber laser with diode-pump modulation. Laser Phys **14**: 1277–1281.

Sevilla-Escoboza, R., G. Huerta-Cuéllar, R. Jaimes-Reátegui, J. García-López, C. Medel-Ruiz, *et al.*, 2017 Error-feedback control of multistability. Journal of the Franklin Institute **354**: 7346–7358.

Soboń, G., 2022 Noise-like pulses in mode-locked fiber lasers. In *Dissipative Optical Solitons*, pp. 319–337, Springer.

Tseng, C.-H., J.-H. Yang, and S.-K. Hwang, 2022 Numerical study of noise-induced transitions in nonlinear dynamics of optically injected semiconductor lasers. Nonlinear Theory and Its Applications, IEICE **13**: 60–71.

Wu, Q., Y. Okabe, and J. Sun, 2014 Investigation of dynamic properties of erbium fiber laser for ultrasonic sensing. Optics express **22**: 8405–8419.

Xu, L., L. Zhang, Z. Zhang, Z. Gao, J. Tian, *et al.*, 2022 Conventional soliton dynamics of mode-locked erbium-doped fiber lasers. In *Second Optics Frontier Conference (OFS 2022)*, volume 12307, pp. 35–39, SPIE.

Zhao, L., D. Li, L. Li, X. Wang, Y. Geng, *et al.*, 2017 Route to larger pulse energy in ultrafast fiber lasers. IEEE Journal of Selected Topics in Quantum Electronics **24**: 1–9.

How to cite this article: Esqueda-de-la-Torre, J. O., Jaimes-Reátegui, R., García-López, J. H., Pisarchik, A. N., and Huerta-Cuellar, G. Effects of Optical Laser Injection in Multistable Erbium Fiber Lasers. *Chaos Theory and Applications*, 4(4), 226-233, 2022.

CHAOS
Theory and Applications
in Applied Sciences and Engineering

e-ISSN: 2687-4539
RESEARCH ARTICLE
Vol.4 / No.4 / 2022 / pp.234-240
Special Issue (EDIESCA 2022)
https://doi.org/10.51537/chaos.1196860

Generation of Multistability through Unstable Systems

Edgar Cristian Díaz González [*,β,1], **Arturo Guerra López** [*,2], **Baltazar Aguirre-Hernández** [β,3] **and Eric Campos Cantón** [*,4]

[*]División de Control y Sistemas Dinámicos, Instituto Potosino de Investigación Científica y Tecnológica A. C., Camino a la Presa San José 2055, col. Lomas 4a Sección, 78216 San Luis Potosí, SLP, México., [β]Departamento de Matemáticas, Universidad Autónoma Metropolitana – Iztapalapa, San Rafael Atlixco 186, CDMX, 09340, México.

ABSTRACT In this work, we propose an approach to generate multistability based on a class of unstable systems that have all their roots in the right complex half-plane. Multistability is the coexistence of multiple stable states for a set of system parameters. The approach is realized by using linear third order differential equations that consists of two parameters. The first bifurcation parameter transforms the unstable system with all its roots in the right complex half-plane into an unstable system with one root in the left complex half-plane and two roots remaining in the right complex half-plane. With this first transformation, the system is capable of generating attractors by means of a piecewise linear function and the system presents monostability. We then use the another bifurcation parameter to switch from a monostable multiscroll attractor to several multistable states showing a single-scroll attractor.

KEYWORDS
Chaos
Multistability
Switched systems
Attractors

INTRODUCTION

The coexistence of two or more attractors, for a given set of parameters, is called multistability and the convergence to one of the different attractors depends only on the initial condition. The coexistence of multiple behaviors is a universal phenomenon found in many area of science and in nature, from electronic devices and chemical reactions to weather and the brain. One of the pioneering studies on multistability was reported on visual perception (Attneave 1971). In electronic devices, the phenomenon of bistability has been widely explored and its applications in technological devices such as cell phones, computers, etc. Many studies have reported various multistability phenomena through different types of systems, for example, through coupled systems, delayed feedback systems, stochastic systems, among others (Feudel 2008).

There are different mechanisms for multistability emergence in dynamical systems. We can find in the reported literature the generation of multistable systems via Unstable Dissipative Systems (UDS). These dissipative systems with unstable dynamics defined in the space can be of type I or II. The system based on UDS-type I presents a one-dimensional stable manifold leading the trajectory to the equilibrium point and a two-dimensional unstable manifold leading the trajectory away from the equilibrium point. The UDS-type II presents a two-dimensional stable manifold and a one-dimensional unstable manifold, see Anzo-Hernández *et al.* (2018), Gilardi-Velázquez *et al.* (2017). In this work we focus on the creation of multistable systems from an proposed unstable system which is transformed into a system UDS-I.This class of systems UDS-I are useful for the generation of multiscroll attractors through a linear function by parts (PWL), and thus through a bifurcation parameter to obtain the multistability.

Recently, the fractional calculus has been used to make multistable systems based on fractional derivatives instead of integer derivatives in PWL systems that display multiple scrolls Echenausía-Monroy *et al.* (2022). The mechanisms that produce multistable behavior in integer and fractional PWL systems are currently a topic of research. In Gilardi-Velázquez *et al.* (2022) a PWL system showing multistable behavior was presented, in this system the nearest integer function was used to control the switching processes and the corresponding equilibrium between the individual switching surfaces was found.

In this paper our approach to generate chaotic systems is based on an transformation of unstable system to a class of *unstable dissipative systems* (UDS). Therefore, the chaotic self-excited attractor emerges from saddle equilibria. The manifolds of these hyperbolic equilibrium points are determined by the eigenvalues associated to the linear operator of the system. Therefore, the first requirement is to obtain a system based on a linear operator that has a complex conjugate eigenvalue pair with a positive real part and a negative real eigenvalue. With this first transformation, the system

Manuscript received: 31 October 2022,
Revised: 30 November 2022,
Accepted: 7 December 2022.

[1]dige.uam.cd18@gmail.com
[2]arturo.guerra@ipicyt.edu.mx
[3]bahe@xanum.uam.mx
[4]eric.campos@ipicyt.edu.mx (**Corresponding author**).

is capable of generating a monostable attractor. The next step is to switch the system from monostability to multistability.

The manuscript is organized in the following sections: In the first section , definitions are given for clarity in developing the approach to obtaining multistability. In the second section , we classify the types of unstable systems capable of generating families of systems that can generate multiscroll. In the third section by using another bifurcation parameter, we generate multistability in the given system. Finally, in the last section, the conclusions are given.

PRELIMINARIES

In this section, we give some basic definitions to understand the coexistence of multiple chaotic attractors. Two important features of chaotic system solutions are unpredictable behavior and trajectory divergence. A chaotic system usually displays the types of behavior listed above. The following definitions can be reviewed in Lynch (2004).

Definition 1 *A minimal closed invariant set A, $F(A) \subset A$, that attracts nearby trajectories that are in the basin of attraction B, $A \subset B$, towards it is called an* attractor.

Definition 2 *A* strange attractor *generated by a chaotic system is an attractor that shows fractal structure and sensitivity to initial conditions.*

There are many approaches to check that a system has chaotic behavior. For instance, *Lyapunov exponents* is a widely used method to verify whether a system is chaotic or not. A chaotic system presents a positive Lyapunov exponent and if the system presents two positive Lyapunov exponents it is called hyperchaotic. Other approach to generate chaotic behavior is by using homoclinic and heteroclinic orbits, this chaotic behavior is known as homoclinic and heteroclinic chaos. Two chaotic trajectories with very close initial conditions in the strange attractor will separate with a rate of divergence given by the positive Lyapunov exponent.

Lyapunov exponents can be computed by different methods and their performance can be consulted in Geist *et al.* (1990). Three-dimensional autonomous systems have been useful for modeling many phenomena of nature. For example, the highly simplified model of a convective fluid proposed by Edward Lorenz to generate meteorological data Lorenz (1963). A wide variety of behaviors was discovered in the simplified Lorenz model, finding that for some parameter values the system behave chaotically. Sparrow's work on the Lorenz system is an excellent reference for more details about the system, see Sparrow (1982).

The trajectories revolve around two equilibrium points C_1 and C_2 in an apparently stochastic way, which makes the trajectories unpredictable. This pioneer model has been widely study, for example, Guanrong Chen and Tetsushi Ueta introduced a variation on the Lorenz model. Another iconic chaotic system was introduced by Leon O. Chua in the mid-1980s, his system was implemented electronically and is known as the Chua circuit, and it exhibits a variety of behaviors. A review of Chua's circuit is presented in Madan (1993) and exhibits many interesting bifurcation and chaotic phenomena.

As the Lorenz system as the Chua system generate attractors that present a double scroll attractor. In this paper, one of our objectives is to *control* an attractor that present five scrolls, we called this attractor *multiscroll attractor*. One of the approaches used to generate a multiscroll attractor is by means the use of a piecewise linear function in the system $\dot{\mathbf{x}} = A\mathbf{x} + B$, see Campos-Cantón *et al.* (2010, 2012).

Dissipative systems and attractors

Let us consider a system given a set of nonlinear autonomous differential equations, as follows

$$\dot{\mathbf{x}} = F(\mathbf{x}),$$

where $\mathbf{x} \in \mathbb{R}^3$ is the state vector. Important information is obtained by the equilibrium points $\mathbf{x}^*$ that satisfy $F(\mathbf{x}^*) = 0$. These points give qualitative information about the local behaviors of its solutions. The local behavior of a nonlinear system is obtained by the Jacobian matrix $DF(\mathbf{x}^*)$. For a *hyperbolic equilibrium point*, the eigenvalues of the Jacobian matrix $DF(\mathbf{x}^*)$ are nonzero. Hartman-Grobman Theorem states that in a vicinity of a hyperbolic equilibrium point $\mathbf{x}^*$ in which the phase portrait for the nonlinear system $\dot{\mathbf{x}} = F(\mathbf{x})$ resembles the linearization. The linearization is given as follows:

$$\begin{aligned} \dot{\mathbf{x}} &= DF(\mathbf{x}^*) \\ &= A\mathbf{x}. \end{aligned} \tag{1}$$

What we have is that the phase portraits are qualitatively equivalent in the neighborhood of a hyperbolic critical point, see Hartman (1964). Other important concept is the volume contraction rate of a dynamical system

$$\dot{\mathbf{x}} = F(\mathbf{x}),$$

where $\mathbf{x} = (x, y, z)^T$ is the state vector and $F(\mathbf{x}) = (F_1(\mathbf{x}), F_2(\mathbf{x}), F_3(\mathbf{x}))$ determines the evolution of the system, then the volume contraction rate is given by:

$$\Lambda = \nabla \cdot F(\mathbf{x}) = \frac{\partial F_1}{\partial x} + \frac{\partial F_2}{\partial y} + \frac{\partial F_3}{\partial z}.$$

Notice that the time evolution in phase space is determined by $V(t) = V_0 e^{\Lambda t}$, where $V_0 = V(0)$ and Λ is a constant. When a system is capable of dissipating energy, it is known as a dissipative system and is given for a negative value of Λ. When Λ is negative it leads to a fast exponential shrinks of the volume in state space. If the system is dissipative, it can develop attractors. Without loss of generality we analyze a jerk system. On the other hand, for the given system to be dissipative, it is necessary and sufficient that the sum of the roots of the characteristic polynomial be a negative quantity. That is, the eigenvalues associated with the matrix $A \in \mathbb{R}^3$ of the system (1) is $\sum_{i=1}^{3} \lambda_i < 0$. The saddle equilibria of a system in $\mathbb{R}^3$ can be characterized into two types according to the eigenvalues associated with matrix A.

Definition 3 *Let us consider a system defined by (1) in the space with eigenvalues λ_j, $j = 1, \ldots, 3$ associated with matrix A. The system is called* Unstable Dissipative System *(UDS) Type I if one eigenvalue $\lambda_1 \in \mathbb{R}^-$, the other two $\lambda_{2,3} \in \mathbb{C}^+$, and the sum of the eigenvalues is negative. Where $\mathbb{R}^-$ and $\mathbb{C}^+$ denote the negative real numbers and complex conjugate numbers with a positive real part, respectively.*

Definition 4 *Let us consider a system given by (1) in $\mathbb{R}^3$ with eigenvalues λ_i, $i = 1, 2, 3$ associated with matrix A. The system is said UDS Type II if one eigenvalue λ_1 is positive real number and the other two are complex conjugate numbers with a negative real part, and the sum of the eigenvalues is negative.*

Attractors in $\mathbb{R}^3$ are generated by several kind of dynamical systems, and particularly PWL systems based on the aforementioned two types of UDS have been employed to generate multiscroll attractors. Also some systems present the two types of UDS's to generate attractors, For example, the Chua system mentioned above considers two UDS Type I equilibria to generate the scrolls of the attractos and another UDS Type II equilibrium point between the two UDS Type I equilibria. This last equilibrium point does not generate a scroll in the attractor.

FROM UNSTABLE SYSTEMS TO SYSTEMS THAT GENERATE ATTRACTORS

In this section we generate attractors that present multiscroll. In this work we are interested in continuous piecewise functions as controllers for the generation of multiscroll atractors. We use a similar technique as in Díaz-González *et al.* (2017) where a bifurcation parameter is used to generate a family of multiscroll attractors. The idea is to destabilize Hurwitz polynomial for the generation of a class of systems that display multiscroll attractor based on unstable dissipative systems. One of our goals in this paper is to explain how to transform a totally unstable system into an unstable system capable of generating attractor through a piecewise linear function.

Unstable systems

Let us propose the following controlled linear system

$$\dot{\mathbf{x}} = A\mathbf{x} + \mathbf{b}u(r,\nu) + B(\nu)S, \tag{2}$$

where $A \in \mathbb{R}^{3\times 3}$ is a linear operator, $\mathbf{b} = (0,0,1)^T$ is a constant vector, and $B = (0,0,\nu)^T$ with $\nu \in \mathbb{R}$. We apply a feedback of the form

$$u(r,\nu) = \mathbf{c}^T(r,\nu)\cdot\mathbf{x},$$

where $S = S(\mathbf{x})$ is the following step function:

$$S = \begin{cases} s_1 & \text{for } c_1 < x, \\ s_2 & \text{for } c_2 < x \leq c_1, \\ \vdots & \\ s_m & \text{for } x \leq c_m, \end{cases}$$

leads

$$\dot{\mathbf{x}} = A(\nu)\mathbf{x} + B(\nu)S. \tag{3}$$

which describes a closed-loop or feedback system. The way to select the values of $c_i's$ in such a way that they help to develop UDS systems will be explained below. For the generation of multiscroll attractors we take $\nu = 1$ to analyze the location of the parameter r. Our goal is to set the appropriate value of the parameter r in such a way that the control linear system generates multiscroll attractors. Firstly we assume that $u(r,\nu)$ equal to 0, $B = 0$ and $\mathrm{Re}(\lambda) > 0$ for all $\lambda \in \sigma(A)$ where $\sigma(A)$ is the set of eigenvalues of A. If *all* eigenvalues of A have positive real part, then the system is totally unstable. For the system (2), the equilibrium point 0 has a neighborhood such that every nonzero solution that starts in the neighborhood must eventually leave the neighborhood and not return in the future time. Without loss of generality we consider the matrix form of the third-order jerk equation $x''' + a_1x'' + a_2x' + a_3x + \beta = 0$, where $a_1, a_2, a_3, \beta \in \mathbb{R}$. The generated system is of the form (2) with $u \equiv 0$ where the matrix A has the following form:

$$A = \begin{pmatrix} 0 & 1 & 0 \\ 0 & 0 & 1 \\ -a_3 & -a_2 & -a_1 \end{pmatrix} \tag{4}$$

where $B = (b_1, b_2, b_3)^T$ is a vector with the following entries $B = (0,0,-\beta)^T$. The characteristic polynomial associated with A is defined by $p(t) = t^3 + a_1t^2 + a_2t + a_3$. We are going to characterize the unstable systems that can generate attractors through a bifurcation parameter. We begin with a test to characterize the roots of a polynomial of degree three.

Lemma 1 *The polynomial $p(t) = t^3 + a_1t^2 + a_2t + a_3$ has a positive real root and two complex conjugate roots $\alpha \pm \beta$ with $\alpha > 0$ and $\beta \neq 0$ if and only if $4a_2^3 + 27a_3^2 + 4a_1^3a_3 - a_1^2a_2^2 - 18a_1a_2a_3 > 0$.*

Proof 1 *Consider the polynomial $p(t)$given by the following form $p(t) = t^3 + a_1t^2 + a_2t + a_3$, we define $\Delta = 4a_2^3 + 27a_3^2 + 4a_1^3a_3 - a_1^2a_2^2 - 18a_1a_2a_3$. The proof is obtained from Cardano's formulas to obtain the roots of a cubic equation, see Uspensky (1987).*

Example 1 *If we consider the following polynomial $p(t) = t^3 - 0.86t^2 + 2.65t - 0.24$, we can see that it satisfies $4a_2^3 + 27a_3^2 + 4a_1^3a_3 - a_1^2a_2^2 - 18a_1a_2a_3 = 61.56 > 0$. That is, $p(t)$ satisfies condition from Lemma 1, so it has one real positive root and two roots in the form $\alpha + i\beta$ with $\alpha > 0$ and $\beta \neq 0$.*

Instability parameter to generate unstability and multiscrolls attractors

We will use a polynomial approach that will help us to find bounds that will allow us to obtain the necessary instability in UDS-I to generate attractors by using an instability parameter. The unstability parameter of $p(t)$ is set according to the following definition.

Definition 5 *Let $p(t)$ be the characteristic polynomial of A and t_1, t_2, ..., t_n are its zeros in the complex right half-plane ($\mathbb{C}^+$). The* abscissa of instability *σ_p of the polynomial $p(t)$ is defined as follows*

$$\sigma_p = \min_{1\leq i\leq n}\{\mathrm{Re}\,(t_i)\}. \tag{5}$$

If $\underline{\sigma_p}$ and $\overline{\sigma_p}$ are numbers such that $\underline{\sigma_p} \leq \sigma_p \leq \overline{\sigma_p}$, then they are named lower and upper bound, respectively.

Now we are going to follow a similar approach to Aguirre-Hernández *et al.* (2015) where a polynomial approach is given. The characteristic polynomial of the system (3) is given by $f_r(t) = p(t-r)$, note that $f_r(t)$ is a set of polynomials such that $f_0(t) = p(t)$ is an unstable polynomial. Now by Taylor's theorem $f_r(t)$ can be rewritten as

$$\begin{aligned} f_r(t) &= t^n + \frac{p^{(n-1)}(-r)}{(n-1)!}t^{n-1} + \cdots + \frac{p'(-r)}{1!}t + p(-r) \\ &= t^n + A_{n-1}(r)t^{n-1} + \cdots + A_1(r)t + A_0(r). \end{aligned} \tag{6}$$

Our goal is to generate the chaotic behavior with a translation of the characteristic polynomial with an upper bound of the abscissa of instability. The roots of $f_r(t)$ are in the imaginary axis when $r = -\sigma_p$. Therefore the system (2) could generate multiscroll attractors for r in an interval contained in $(-\overline{\sigma_p}, -\sigma_p)$, where $\overline{\sigma_p}$ is an upper bound of the abscissa of instability.

Maximal instability interval

It is important to know the maximum range of the r parameter in order to control that the system remains UDS-I. In addition, a necessary condition for generating attractors is that system (2) satisfies the condition of dissipativity. Thus we have the following lemma for a system of dimension three.

Lemma 2 *Let $p(t) = t^3 + a_1t^2 + a_2t + a_3$ be a real unstable characteristic polynomial with roots $t_1 = \alpha_1$, $t_2 = \alpha_2 + i\beta_2$ and $t_3 = \alpha_2 - i\beta_2$, $(\alpha_2 > \alpha_1)$, in the complex right half-plane. If $f_r(t) = p(t-r)$ is unstable and dissipative, then we have that the following conditions are fulfilled.*

i) $r < \frac{a_1}{3}$.

ii) $r > -\alpha_2$.

Proof 2 *If the sum of its roots,* $r + t_j$*, is negative, then the family* $f_r(t)$ *is dissipative if the sum of its roots. So,* $2\alpha_2 + \alpha_1 + 3r < 0$ *and hence* $r < \frac{-2\alpha_2 - \alpha_1}{3}$*. On the other hand*

$$\begin{aligned} p(t) &= t^3 - (\alpha_1 + 2\alpha_2)t^2 + (2\alpha_1\alpha_2 + \alpha_2^2 - \beta_2^2)t - \alpha_1\alpha_2^2 + \alpha_1\beta_2^2 \\ &= t^3 + a_1t^2 + a_2t + a_3. \end{aligned}$$

Therefore we have that $r < \frac{a_1}{3}$*. (ii) The roots of* $f_r(t)$ *are in the imaginary axis for* $r = -\sigma_u$*, if* $\alpha_2 + r > 0$*, then* $f_r(t)$ *is UDS-I. So* $r > -\alpha_2$.

Let us summarize all of this in a theorem.

Theorem 1 *Let* $p(t)$ *be the unstable polynomial of degree three with a pair of conjugate complex roots and one real root as in Lemma 2. Then* $f_r(t)$ *is UDS-type I if and only if* $r \in (-\alpha_2, \frac{a_1}{3})$.

Proof 3 *The proof follows from Lemma 2.*

Example 2 *Consider the system given by (2) for*

$$A = \begin{pmatrix} 0 & 1 & 0 \\ 0 & 0 & 1 \\ 0.15 & -2.36 & 0.687 \end{pmatrix}$$

whose characteristic polynomial is $p(t) = t^3 - 0.687t^2 + 2.36t - 0.15$*, from Lemma (1) we have that* $4a_2^3 + 27a_3^2 + 4a_1^3a_3 - a_1^2a_2^2 - 18a_1a_2a_3 = 46.3728 > 0$*. That is,* $p(t)$ *satisfies the condition from Lemma 1, so it has one real positive root and two roots in the form* $\alpha + i\beta$ *with* $\alpha > 0$ *and* $\beta \neq 0$*. The abscissa of instability of the polynomials is* $\sigma_u = 0.0647$*. Now we will use the result of Theorem 1 taking the value of* $r = -0.3$ *for the created* $f_r(t)$*. We obtain the polynomial* $f_{-0.3}(t) = t^3 + 0.663t^2 + 1.1342t + 1.1422$ *whose eigenvalues are* $\lambda_1 = -0.8695$*,* $\lambda_{2,3} = 0.1032 \pm i1.1415$.

Therefore, for $f_{-0.3}(t)$ we have an UDS type I capable of generating multiscroll attractors by using a piecewise linear function.

Generation of multiscroll

Now, let us consider a control PWL system to generate multiscroll attractors as follows

$$\dot{\mathbf{x}} = A\mathbf{x} + \mathbf{b}u(r) + BS \tag{7}$$

where $\mathbf{x} = (x, y, z)^T \in \mathbb{R}^3$ is the state vector, $\mathbf{b} = B = (0, 0, 1)^T$ is a constant vector, $\mathbf{A} = [a_{ij}] \in \mathbb{R}^{3\times3}$ with $i, j = 1, 2, 3$ denotes a nonsingular linear matrix.

We have that $p_A(t)$ is the characteristic polynomial of the system and S is a step function defined as follows

$$S = \begin{cases} s_1 & \text{for } c_1 < x, \\ s_2 & \text{for } c_2 < x \leq c_1, \\ \vdots & \\ s_m & \text{for } x \leq c_m. \end{cases}$$

Define the linear control $u = c^T(r) \cdot \mathbf{x} = [a_3 - A_0(r), a_2 - A_1(r), a_1 - A_2(r)] \cdot \mathbf{x}$, where $A_j(r) = \frac{p^j(-r)}{j!}$. Therefore the controlled system can be given as follows

$$\dot{\mathbf{x}} = \begin{pmatrix} 0 & 1 & 0 \\ 0 & 0 & 1 \\ -A_0(r) & -A_1(r) & -A_2(r) \end{pmatrix} \mathbf{x} + BS = A_c\mathbf{x} + BS. \tag{8}$$

Then, the closed-loop characteristic polynomial is given by:

$$\begin{aligned} f_r(t) &= t^3 + A_2(r)t^2 + A_1(r)t + A_0(r), \\ &= p_A(t - r). \end{aligned}$$

The equilibrium points of the system (8) are $\mathbf{x}_i^* = -A_c^{-1}BS$, with $i = 1, \ldots, m$, and each entry s_i of the PWL system is considered to preserve bounded trajectories of system and let the generation of an attractor. Therefore, the choice of $c_i's$ determines the atoms $D_i's$ in step function S. Each atom $D_i's$ of the partition of the space contains an equilibrium $\mathbf{x}_i^*$. The design of the s_i depends on the region we want to place the equilibrium point and the switching surfaces, we choose them so that the equilibrium point is in the center of these varieties, that is, we calculate the Euclidean distance

$$d(\mathbf{x}_0^*, \mathbf{x}_1^*) = \sqrt{(x_0^* - x_1^*)^2 + (y_0^* - y_1^*)^2 + (z_0^* - z_1^*)^2},$$

which has to be the same between each equilibrium point. Consider the following system to illustrate the generation of multiscroll attractors.

$$\dot{\mathbf{x}} = \begin{pmatrix} 0 & 1 & 0 \\ 0 & 0 & 1 \\ 0.15 & -2.36 & 0.687 \end{pmatrix} \mathbf{x} + \begin{pmatrix} 0 \\ 0 \\ 1 \end{pmatrix} u + \begin{pmatrix} 0 \\ 0 \\ 1 \end{pmatrix} S. \tag{9}$$

For this example, we define S as follows:

$$S(x) = \begin{cases} 1.0280, & \text{for } 0.7500 < x; \\ 0.6853, & \text{for } 0.4500 < x \leq 0.7500; \\ 0.3427, & \text{for } 0.1500 < x \leq 0.4500; \\ 0, & \text{for } -0.1500 < x \leq 0.1500; \\ -0.3427 & \text{for } x \leq -0.1500. \end{cases}$$

and $u(r) = (-0.15 - p(-r), 2.36 - \frac{p'(-r)}{1!}, -0.687 - \frac{p''(-r)}{2!})x$ where $p(t) = t^3 - 0.687t^2 + 2.36t - 0.15$ is unstable.

The controlled system is

$$\dot{\mathbf{x}} = \begin{pmatrix} 0 & 1 & 0 \\ 0 & 0 & 1 \\ -p(-r) & -\frac{-p'(-r)}{1!} & -\frac{-p''(-r)}{2!} \end{pmatrix} \mathbf{x} + \begin{pmatrix} 0 \\ 0 \\ 1 \end{pmatrix} S. \tag{10}$$

We have that $f_r(t) = t^3 + \frac{p''(-r)}{2!}t^2 + \frac{p'(-r)}{1!}t + p(-r)$. For $r = 0$, $f_0(t) = t^3 - 0.687t^2 + 2.36t - 0.15$ is a unstable polynomial and there is not multiscroll. The instability parameter of $f_0(t)$ is

$\sigma_{f_0} = 0.0647$. Then other behavior could appear when $r \in (-U_{diss(p_A)}, -\sigma_{p_A})$. By example 2 for $r = -0.3$ we have that $f_{-0.3}(t) = t^3 + 0.663t^2 + 1.1342t + 1.1422$. Hence $\sum_{j=1}^{3} t_j < 0$ consequently the system (10) is dissipative when $r = -0.3$.

Next, in the following Figure 1 the generation of the attractor from the system (10) is illustrated. The following Figure 2 shows

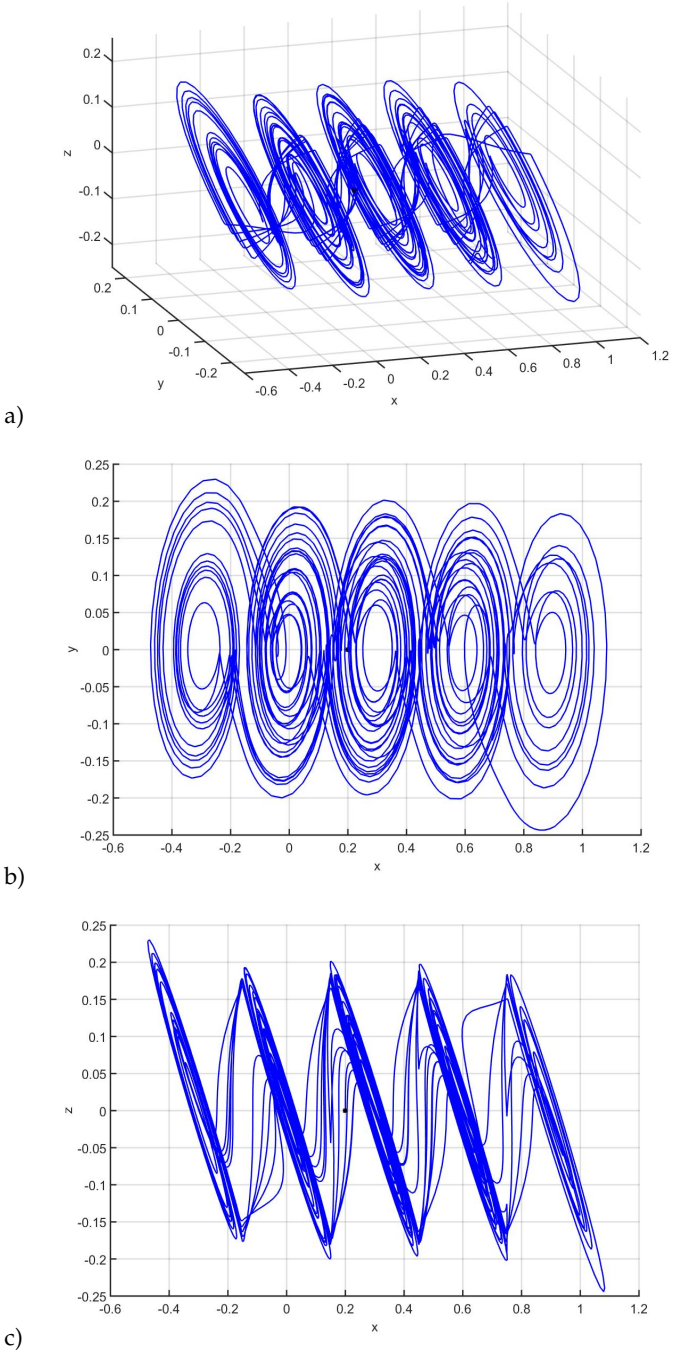

Figure 1 Attractor generated by the system (10) for $r = -0.30$. a) Solution of the system (10) with initial condition $\mathbf{x}_0 = (0.2, 0.0, 0.0)^T$. b) Projections of the attractor on the planes: b) (x, y). And c) (x, z).

the generation of attractors for five different conditions: a) $\mathbf{x}_0 = (-0.4, 0, 0)^T$, b) $\mathbf{x}_0 = (-0.1, 0.0, 0.0)^T$, c) $\mathbf{x}_0 = (0.2, 0.0, 0.0)^T$, d) $\mathbf{x}_0 = (0.5, 0.0, 0.0)^T$ and e) $\mathbf{x}_0 = (0.8, 0.0, 0.0)^T$.

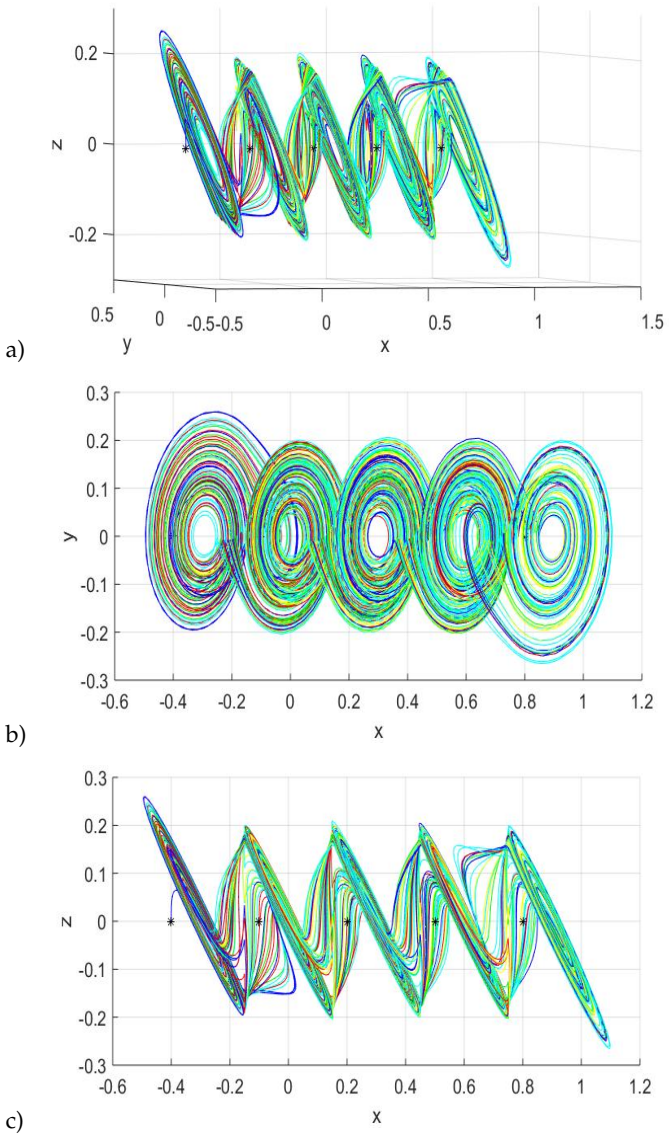

Figure 2 Generation of five attractors with five different conditions. a) [Blue, $\mathbf{x}_0 = (-0.4, 0.0, 0.0)^T$; red, $\mathbf{x}_0 = (-0.1, 0.0, 0.0)^T$; green, $\mathbf{x}_0 = (0.2, 0.0, 0.0)^T$; cyan, $\mathbf{x}_0 = (0.5, 0.0, 0.0)^T$ and yellow, $\mathbf{x}_0 = (0.8, 0.0, 0.0)^T$. Projections of the attractor on the planes: b) (x, y). And c) (x, z).

GENERATION OF MULTISTABILITY FROM INSTABILITY

In this section, we present the way to move from a system with monostability to a system that generates multistability through moving the stable and unstable varieties. The phenomenon of having two attractors coexisting generated by a nonlinear system has been reported by Arecchi *et al.* (1985), who called this behavior generalized multistability. Two problems related to the coexistence of attractions have been studied. The first problem is about choosing a desired attractor to which the system should converge, and the second problem is about excluding certain unwanted attractors from the dynamics (Pisarchik and Feudel 2014).

By moving the stable and unstable varieties of the system we can trap the trajectory of the system in different attractors, where any initial condition belonging to some basin of attraction will always converge to the same attractor, that is, a single attractor of the different ones that coexist. Depending on the initial condition that is split, the trajectory remains oscillating around of any of the equilibrium points of the system, and all the dynamics will be maintained in the attractor where the system's trajectory is enclosed. The region of coexistence of these attractors is critical, since a small noise can commute the physical system, adding a new characteristic to usual chaotic scenarios. In such cases, the properties of the areas of attraction are largely determined by the structure of saddle-type equilibrium points.

Description of the model

Consider the system UDS-I

$$\dot{\mathbf{x}} = A(\nu)\mathbf{x} + B(\nu)S \tag{11}$$

where $\mathbf{x} = (x, y, z) \in \mathbb{R}^3$ is vector states, $B = (0, 0, \nu)^T$ with $\nu \in \mathbb{R}$, S function linear piecewise and $A(\nu) = (a_{ij}) \in \mathbb{R}^3$ is of the form

$$A(\nu) = \begin{pmatrix} 0 & 1 & 0 \\ 0 & 0 & 1 \\ -\frac{p_{A_c}(-r)}{0!}\cdot\nu & -\frac{p'_{A_c}(-r)}{1!}\cdot\nu & -\frac{p''_{A_c}(-r)}{2!}\cdot\nu \end{pmatrix}. \tag{12}$$

The mission of the parameter ν, better known as the bifurcation parameter, is to control the stable and unstable varieties in each s_i to catch the trajectories in a single attraction. This parameter can affect the dissipativity of the system since the dissipativity is given by $-\frac{p''_{A_c}(-r)}{2!}\cdot\nu$. For $\nu = 1$ system (11) is a system capable of generating attractor multiscroll, when ν varies we need the system to remain dissipative, this is true if $-\frac{p''_{A_c}(-r)}{2!}\cdot\nu < 0$, which allows us to obtain qualitative information about the interval where ν can vary and generate multistability. If we take $-\frac{p''_{A_c}(-r)}{2!}\cdot\nu = -1$ we obtain that $\nu = 1.5383$ and for this value the system (11) can generate multistability as shown in the following example.

Example 3 *Consider the system*

$$\dot{\mathbf{x}} = A(\nu)\mathbf{x} + B(\nu)S \tag{13}$$

with

$$S(x) = \begin{cases} 1.028, & \text{for } 0.75 < x; \\ 0.6853, & \text{for } 0.45 < x \leq 0.75; \\ 0.3427, & \text{for } 0.15 < x \leq 0.45; \\ 0, & \text{for } -0.15 < x \leq 0.15; \\ -0.3427 & \text{for } x \leq -0.15. \end{cases}$$

and

$$A = \begin{pmatrix} 0 & 1 & 0 \\ 0 & 0 & 1 \\ -1.1422\cdot\nu & -1.1342\cdot\nu & -0.663\cdot\nu \end{pmatrix}$$

with characteristic polynomial $p(t) = t^3 + 0.663t^2 + 1.1342t + 1.1422$ *the system (13) is UDS-I for* $\nu = 1$. *As mentioned, our first challenge is that we need the sum of the eigenvalues of the system to be negative. Taking the value of* ν *from the equation* $-\frac{p''_{A_c}(-r)}{2!}\cdot\nu = -1$ *we have that* $\nu = 1.5083$. *For this value the system has the following form:*

$$\dot{\mathbf{x}} = \begin{pmatrix} 0 & 1 & 0 \\ 0 & 0 & 1 \\ -1.7228 & -1.7107 & -1 \end{pmatrix}\mathbf{x} + \begin{pmatrix} 0 \\ 0 \\ 1.5083 \end{pmatrix} S. \tag{14}$$

We can observe in the Figure 3 the graphical representation of multistability.

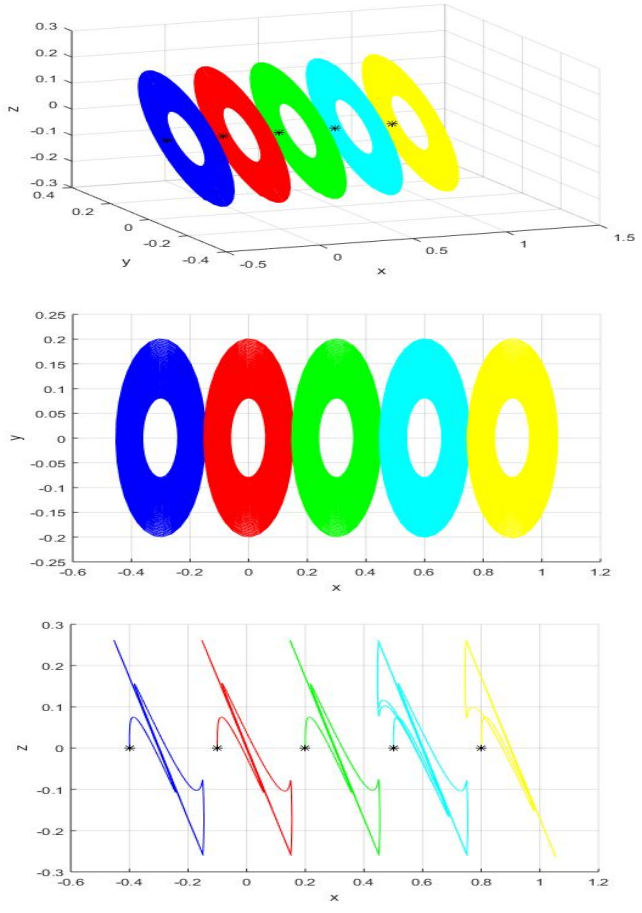

Figure 3 a) Attractors for five different initial conditions: (blue) $\mathbf{x}_0 = (-0.4, 0.0, 0.0)^t$, (red) $\mathbf{x}_0 = (-0.1, 0.0, 0.0)^t$, (green) $\mathbf{x}_0 = (0.2, 0.0, 0.0)^t$,(cian) $\mathbf{x}_0 = (0.5, 0.0, 0.0)^t$,(yellow) $\mathbf{x}_0 = (0.8, 0.0, 0.0)^t$. Projections of the attractors on the planes: b) (x, y); c) (x, z).

In Figure 3 we can see that for five different initial conditions, the dynamics of the system remains trapped in a single attractor of the five attractors coexisting, this depends on the initial condition is within the attraction basin of one of the five attractors that coexist. In the graph of the Figure 3 c) we can see how to move the bifurcation parameter ν such that the stable and unstable manifolds can be controlled, that is, at the moment trajectory of the system leaves by the unstable manifolds W^u, the stable manifolds W^s manages to catch the trajectory to again maintain it within the domain of the equilibrium point.

The initial conditions to generate multistability are the same as those used in the figure 2. Thus the dynamics of the system remain trapped in some region depending on the initial condition that is chosen.

CONCLUSION

By using a system of linear differential equations we generate multistability starting from a totally unstable system. First, we use a parameter for moving the eigenvalues of the associated matrix and to obtain a UDS-I system. Next, by means of another parameter we control the stable and unstable manifolds of the system to catch the generated trajectory from a given initial condition only in an attractor.

Acknowledgments

Díaz-González Edgar Cristian also wants to thank the support of CONACYT trough the postdoctoral fellowship and the IPICYT by the support in the realization of this paper. A. Guerra-López wants to thank to CONACYT for its Master's degree scholarship. E. Campos-Cantón acknowledges CONACYT for the financial support through Project no. A1-S-30433.

Availability of data and material

Not applicable.

Conflicts of interest

The authors declare that there is no conflict of interest regarding the publication of this paper.

LITERATURE CITED

Aguirre-Hernández, B., E. Campos-Cantón, J. A. López-Rentería, and E. C. Díaz-González, 2015 A polynomial approach for generating a monoparametric family of chaotic attractors via switched linear systems. Chaos, Solitons and Fractals **71**: 100–106.

Anzo-Hernández, A., H. E. Gilardi-Velázquez, and E. Campos-Cantón, 2018 On multistability behavior of unstable dissipative systems. Chaos: An Interdisciplinary Journal of Nonlinear Science **28**.

Arecchi, F. T., R. Badii, and A. Politi, 1985 Generalized multistability and noise-induced jumps in a nonlinear dynamical system. Physical Review A **32**.

Attneave, F., 1971 Multistability in perception. Scientific American **225**: 63–71.

Campos-Cantón, E., G. Barajas-Ramírez, J. G.and Solís-Perales, and R. Femat, 2010 Multiscroll attractors by switching systems. Chaos: An Interdisciplinary Journal of Nonlinear Science **20**: 013116.

Campos-Cantón, E., R. Femat, and G. Chen, 2012 Attractors generated from switching unstable dissipative systems. Chaos: An Interdisciplinary Journal of Nonlinear Science **22**.

Díaz-González, E. C., B. Aguirre-Herández, J. A. López-Rentería, E. Campos-Cantón, and C. A. Loredo-Villalobos, 2017 Stability and multiscroll attractors of control systems via the abscissa. Mathematical Problems in Engineering **2017**.

Echenausía-Monroy, J., H. Gilardi-Velázquez, N. Wang, R. Jaimes-Reátegui, J. García-López, *et al.*, 2022 Multistability route in a pwl multi-scroll system through fractional-order derivatives. Chaos, Solitons and Fractals **161**: 112355.

Feudel, U., 2008 Complex dynamics in multistable systems. International Journal of Bifurcation and Chaos **18**: 1607–1626.

Geist, K., U. Parlitz, and Lauterborn, 1990 Comparison of different methods for computing lyapunov exponents. Progress of Theoretical Physics **83**: 875–893.

Gilardi-Velázquez, H. E., J. L. Echenausia-Monroy, R. J. Escalante-González, B. B. Cassal-Quiroga, and G. Huerta-Cuellar, 2022 On the relationship between integer and fractional pwl systems with multistable behavior. In *Complex Systems and Their Applications*, edited by G. Huerta Cuéllar, E. Campos Cantón, and E. Tlelo-Cuautle, pp. 113–129, Cham, Springer International Publishing.

Gilardi-Velázquez, H. E., L. J. Ontañón García, D. G. Hurtado-Rodriguez, and E. Campos-Cantón, 2017 Multistability in piecewise linear systems versus eigenspectra variation and round function. International Journal of Bifurcation and Chaos **27**: 1730031.

Hartman, P., 1964 *Ordinary Differential Equations*. Wiley, New York.

Lorenz, E. N., 1963 Deterministic non-periodic flow. J. Atmos. Sci. **20**: 130–141.

Lynch, S., 2004 *Dynamical systems with applications using MATLAB*. Birkhäuser, Boston.

Madan, R. N., 1993 *Chua's Circuit: A paradigm for Chaos*. World Scientific, Singapore.

Pisarchik, A. N. and U. Feudel, 2014 Control of multistability. Physics Reports **540**: 167–218.

Sparrow, C., 1982 *The Lorenz Equation: Bifurcations, Chaos and Strange Attractors*. Springer-Verlag, New York.

Uspensky, J. V., 1987 *Teoría de ecuaciones*. Limusa, México.

How to cite this article: Díaz-González E.C., Guerra-López A., Aguirre-Hernández B., Campos-Cantón E. Generation of Multistability through Unstable Systems. *Chaos Theory and Applications*, 4(4), 234-240, 2022.

CHAOS
Theory and Applications
in Applied Sciences and Engineering

e-ISSN: 2687-4539
RESEARCH ARTICLE
Vol.4 / No.4 / 2022 / pp.241-245
Special Issue (EDIESCA 2022)
https://doi.org/10.51537/chaos.1190234

Dynamics of Indoctrination in Small Groups around Three Options

Maria Guadalupe Medina Guevara *,[1], **Evguenii Kurmyshev** *,[2] **and Hector Vargas-Rodriguez** *,[3]
*Departamento de Ciencias Exactas y Tecnología, Centro Universitario de los Lagos, Universidad de Guadalajara, Enrique Díaz de Leon 1144, Lagos de Moreno, Jalisco 47460, Mexico.

ABSTRACT In this work, we consider the dynamics of opinion among three parties: two small groups of agents and one very persuasive agent, the indoctrinator. Each party holds a position different from that of the others. In this situation, the opinion space is required to be a circle, on which the agents express their position regarding three different options. Initially, each group supports a unique position, and the indoctrinator tries to convince them to adopt her or his position. The interaction between the agents is in pairs and is modeled through a system of non-linear difference equations. Agents, in both groups, give a high weight to the opinion of the indoctrinator, while they give the same weight to the opinion of their peers. Through several computational experiments, we investigate the times required by the indoctrinator to convince both groups.

KEYWORDS
Opinion dynamics
Non-linear difference-equations
Indoctrination
Agent-based model

INTRODUCTION

The dynamics of opinion attempt to understand the processes of opinion formation in society through the use of different agent-based models, considering different social networks, different opinion updating rules, and different opinion spaces. To date, there are many models, and the topic is far from exhausted. Some reviews of the topic can be found in Noorazar *et al.* (2020); Dong *et al.* (2018). According to Zha *et al.* (2020), these models can be classified into two categories depending on whether opinions are discrete or continuous, and the dynamics associated with them evolve towards three stable states: consensus, polarization, or fragmentation.

Some models of opinion dynamics have used circles and n-dimensional spheres to study the formation of consensus and dissensus (Caponigro *et al.* 2015; Hegarty *et al.* 2016; Zhang *et al.* 2021, 2022). These spaces are very convenient for modeling the evolution of the preferences of a group of agents around a discrete set of options. For example, in Medina-Guevara *et al.* (2017); Medina Guevara *et al.* (2018), the evolution of preferences around three political options is considered.The opinion space is considered being a circle, where the options are separated at the same distance from each other, and the preference of the agents can freely evolve from one of them to any other, without approaching the third of them. For example, assuming that the options are located at the points 0°, 120° and 240°; an agent whose preference is 240° supports completely this option, while an agent whose opinion is 60° is insecure about the options at 0° and 120°, while completely rejects the option at 240°, this last agent has a diametrically opposed opinion (its opinion is in the opposed side of the circle, they are separated 180°). So, in order to give the agents the knowledge about where the options are located, a non linear map is used.

For certain values of the maps's parameter, it introduces three attractors, one for each option, however, for other values of that parameter, the map also offer the agents the possibility to reject all three options, or to manifest doubt when opinion converges with oscillation to the attractor, or a dilemma when the maps has a 2-cycle around the option. In this sense it is considered that this map emulates an internal reflexion process in the agents, allowing them to update their opinion according with their preferences regarding those three options.

In this work we use the model presented in Medina-Guevara *et al.* (2017), to study the process of indoctrination of a polarized group, the group is formed by two factions of equal size that support two different positions, and a highly influential agent, the indoctrinator, who tries to convince the rest of the agents to adopt a position different from theirs. As the interaction of the agents is in pairs, and to have an even number of agents, an additional agent is considered, who is undecided between the two majority options, but openly in opposition to the indoctrinator. In this work we use the term indoctrination in the same way as in Medina-Guevara *et al.*

Manuscript received: 17 October 2022,
Revised: 13 December 2022,
Accepted: 13 December 2022.

[1]maria.mguevara@academicos.udg.mx
[2]evguenii.kourmychev@academicos.udg.mx
[3]hvargas@culagos.udg.mx (**Corresponding author**).

(2019), so it is interpreted as the fact of trying to impose an opinion different from that of others. That the indoctrinated is influential is because the other agents give significant weight to his opinion. While they trust each other equally. Thus, the indoctrinator is an opinion leader like the one discussed in Boccaletti *et al.* (2018).

The work is organized in the following way. Section 1 presents the introduction. Section 2, The mathematical model, introduces the agent based model used in Medina-Guevara *et al.* (2017). Section 3, Numerical Experiment Settings, considers the initial conditions and settings under which the model emulates the dynamics of the indoctrination of two small groups that support opposite positions to those of the indoctrinator. Section 4, Results, presents the required average times to indoctrinate small groups of agents. Section 5 presents the conclusions of the work. For convenience we use both radians and degrees, in this sense radians are used in Section 2, while degrees are used in Section 3.

THE MATHEMATICAL MODEL

We employ the agent based model given in Medina-Guevara *et al.* (2017). In that model, a set of N agents manifest their opinion with regard to three options, in this sense their opinion space S^1 is a circle with the options located at the points: 0 rad, $2\pi/3$ rad, $4\pi/3$ rad. Agents have two attributes their opinion or preference x, and a personal parameter $\kappa \in K = [-1.5, 1.5]$, that allows them to have a posture and a behavior regarding those options.

Hence, in order to distinguish these three points in the opinion space, a non-linear function $\Xi : S^1 \times K \to S^1$ is introduced, it is defined as:

$$\Xi(x_n, \kappa) = x_n - \kappa \sin(3x_n). \tag{1}$$

For $0 < \kappa < 2/3$, the map $x_{n+1} = \Xi(x_n, \kappa)$ possesses three attractors in 0, $2\pi/3$, $4\pi/3$, and three repellers in $\pi/3$, π, $5\pi/3$, if $-2/3 < \kappa < 0$ the attracting nature of these fixed points reverses. The map also possess $n-$cycles which after a cascade of bifurcations lead to chaos, see Figure 1.

As it is already mentioned in Medina Guevara *et al.* (2018), the parameter κ can be used to model different behaviors in agents regarding those options. For example, when the preference of the agent is governed only by this map, and his personal parameter satisfies $0 < \kappa < 2/3$, the preference of the agent is attracted to those options, but an agent whose personal parameter satisfies $-2/3 < \kappa < 0$ rejects the options, and become attracted to the intermediate postures at $\pi/3$ rad, π rad and $5\pi/3$ rad; the preference of a secure agent, with $\kappa \in [0, 1/3]$, converges without oscillation to the options; but the preferences of a vacillating agent, the one with $\kappa \in [1/3, 2/3]$ converges with oscillation to the options; the preferences of an agent whose personal parameter satisfies $-1.045 < \kappa < -2/3]$ will evolve into a 2-cycle, a dilemma where the agent is insecure about two options, consider, for example, the case when its preference is initially near π, it will evolve to be jumping from preferences near $2\pi/3$ to preferences near $4\pi/3$.Perhaps, it is even possible to have agents whose preferences evolve chaotically in a scenario where information is changing every moment.

Hence the iterative model is the following:

1. In the first temporal step each agent is assigned an opinion and a personal parameter κ.

2. In the following steps, arbitrarily chosen pairs of agents interact according to the affinity of their opinions. To do this, an affinity parameter ϵ is introduced. Depending on how similar the opinions of the agents are, two different situations are contemplated:

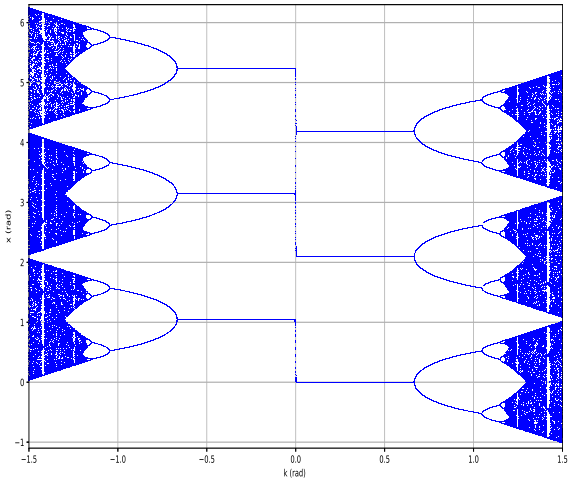

Figure 1 The figure shows the bifurcation diagram corresponding to the iterated map $x_{n+1} = \Xi(x_n, \kappa)$, it can be appreciated the fixed points corresponding to 0, $2\pi/3$ and $4\pi/3$ for $0 < \kappa < 2/3$; and $\pi/6$, π, $5\pi/3$ for $-2/3 < \kappa < 0$. Both axis are in radians. This maps allows the agents to identify three equal options in the opinion space, as well as to have different behaviors to update their opinions.

- **Agents' opinions are affine.** In this case, $|x_n^i - x_n^j| < \epsilon$, the opinions for the $(n+1)$th temporal step will be defined through:

$$\begin{cases} x_{n+1}^i &= a_{ii}\Xi(x_n^i, \kappa^i) + a_{ij}x_n^j, \\ x_{n+1}^j &= a_{ji}x_n^i + a_{jj}\Xi(x_n^j, \kappa^j), \end{cases} \tag{2}$$

  where the coefficients a_{ij} represent the relative weight that agent number i grants to the opinion of agent number j, they satisfied $0 \leq a_{ij} \leq 1$, $a_{ii} + a_{ij} = 1$ and $a_{ji} + a_{jj} = 1$.

- **Agents' opinions are not affine.** In this case, $|x_n^i - x_n^j| > \epsilon$ the agents update their opinions considering only their individual preferences. Thus,

$$\begin{cases} x_{n+1}^i &= \Xi(x_n^i, \kappa^i), \\ x_{n+1}^j &= \Xi(x_n^j, \kappa^j). \end{cases} \tag{3}$$

NUMERICAL EXPERIMENTS SETTINGS

As the initial conditions we consider

1. A small group of N agents formed by one indoctrinator supporting the choice 240°, two subgroups of equal size, the first one supporting choice 0° and the second one supporting choice 120°, and an indecisive agent with a posture 60° between those of the two subgroups. We consider group sizes $N = 4, 6, 8, ..., 22$.

2. We consider an affinity $\epsilon = 120°$, which prevents the indoctrinator to interact with the indecisive agent, notice that this

last agent has a diametrally opposed preference to that of the indoctrinator.

3. In order to have a very persuasive indoctrinator, agent number 1, we consider that all agents grant to her (or his) opinion a great relative weight,

$$a_{11} = \frac{a}{1+a}, \quad a_{1i} = \frac{1}{1+a}, \tag{4}$$

$$a_{i1} = \frac{a}{1+a}, \quad a_{ii} = \frac{1}{1+a} \tag{5}$$

where $a > 1$ and $i = 2, 3, ..., N$. While among themselves, they give each other the same weight.

$$a_{ii} = \frac{1}{2}, \quad a_{ij} = \frac{1}{2}, \tag{6}$$

$$a_{ji} = \frac{1}{2}, \quad a_{jj} = \frac{1}{2}, \tag{7}$$

here $i, j \neq 1$.

4. To measure the indoctrinator's convincing power we use a quantity defined in Medina-Guevara *et al.* (2019), the charisma, it is defined as in the following manner:

$$\eta_{ij} = \frac{a_{ij}}{a_{ii}}, \tag{8}$$

hence de charisma of the jth-agent as perceived by the ith-agent is simple the ratio of the relative weight of that agent relative to his own weight, for example, the perceived charisma of the indoctrinator is the number $\eta_{i1} = a$ for $i \neq 1$, while that of any other agent is $\eta_{ij} = 1$ for $i, j \neq 1$. We will consider indoctrinators with $a \in \{2, 3, 4, 5, 10\}$.

5. For simplicity, we consider a fixed value of the agents' parameter κ^i, we choose $\kappa^i = 28°$.

RESULTS

After performing 100 computational experiments for each of the above settings, we have the following results:

1. Table 1 presents the average number, $\bar{T}$ and the standard deviation, σ, of the temporal steps (computational cycles) required by a given indoctrinator to convince the groups of agents of her (or his) posture. There were cases when the indoctrinator was unable to convince the whole group, in those cases a dash is reported on the table. In all cases, the average number of cycles grows with the size of the group. Hence relatively large groups of equally trusting agents become immune to be convinced of a different posture.

2. Table 2 reports the minimum number of cycles, found among each series of 100 computational experiments, to indoctrinate the full group, this table shows that for some relatively large groups, and in a few cases, an indoctrinator is still able to convince the group. For example, for a group of 20 agents (including the indoctrinator), an indoctrinator of charisma 10 convinced the group in 55 cycles, although the average number of cycles found for this case was 2638 cycles.

3. Table 3 reports the maximum number of cycles to indoctrinate the full group, these are the maximum number of cycles found among each series of 100 computational experiments. The dashes correspond to the cases when the indoctrinator was unable to convince the group.

4. Table 4 reports the cases when the indoctrinator was convinced of a different posture. For example, an indoctrinator of charisma 2 is always convinced of a different posture by groups of 12 or more agents. While an indoctrinator of charisma 3, was convinced by groups of 12, 14 or 16 agents in few cases; but it always was convinced by groups of 18 or more agents. Indoctrinators with charisma 4 or greater are not persuaded to change their opinion.

In Figures 2(a) and 2(b), just to illustrate the dynamics, we present two examples of the time evolution of the preferences of groups of 16 agents under the presence of an indoctrinator of charisma 10, Figures 2(c) and 2(d) present the evolution of the number of agents in each of the basin options: The number of agents in basin $(-300°, 60°)$ are represented by the red line, agents in basin $(60°, 180°)$ by the blue line, and agents in the basin $(180°, 300°)$ by the green line.

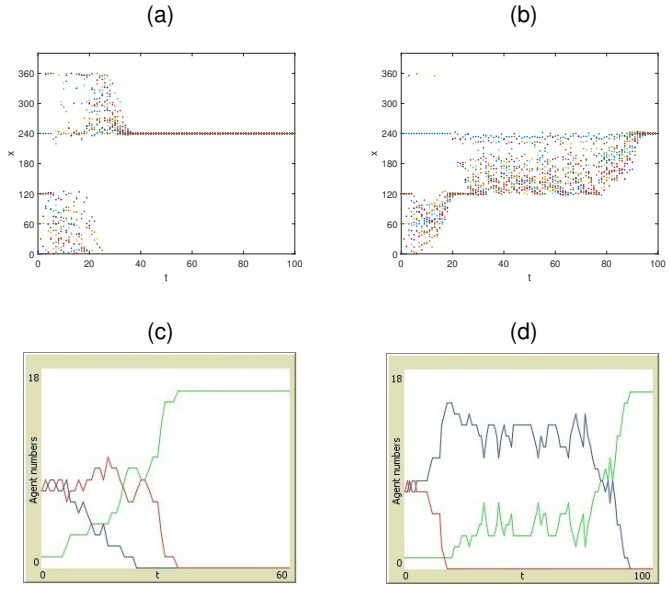

Figure 2 Figures (a) and (b) show the evolution of the opinion preferences of a group of 16 agents. Initially, there are two subgroups each one in a consensus around opinions $0°$ and $120°$, an indecisive agent between those two postures with a $60°$ opinion, and indoctrinator with charism 10 suporting opinion $240°$. Here t denotes the number of cycles, and x the preference regarding the options. In Figure 2(a) the group is indoctrinated after 33 cycles while in Figure 2(b) the group is indoctrinated after 91 cycles. Notice that on figures 2(a) and 2(b), the values $0°$ and $360°$ should be identified, the graphic is on a cylinder. Figures 2(c) and 2(d) show the evolution of the agent numbers in each attraction basin. Respectively, red, blue and green lines represents the number of agents in the basin corresponding to the attractors $0°$, $120°$ and $240°$. Figure 2(c) correspond to the time series 2(a), while 2(d) to 2(b).

Table 1 Average indoctrination time and standard deviation vs group size for different charismatic indoctrinators

charisma	2		3		4		5		10	
Agents	$\bar{T}$	σ	$\bar{T}$	σ	$\bar{T}$	σ	$\bar{T}$	σ	$\bar{T}$	σ
4	17.29	5.56	13.94	3.27	13.8	3.3	13.86	2.88	13.96	5.15
6	22.92	6.29	21.96	5.41	20.75	4.96	19.86	4.62	19.73	3.80
8	33.91	4.56	31.72	6.30	27.90	5.34	27.18	5.40	26.12	4.46
10	30.6	3.61	49.35	12.71	35.82	6.96	32.91	5.62	31.08	5.74
12	-	-	230.63	227.65	55.27	23.39	45.07	13.36	37.38	7.33
14	-	-	-	-	137.89	79.56	68.27	29.86	51.77	14.61
16	-	-	-	-	1412.43	1398.77	252.45	196.98	79.05	36.17
18	-	-	-	-	48676	55111	3604	3854	256.8	203.73
20	-	-	-	-	-	-	114712	101086	2638	2535
22	-	-	-	-	-	-	-	-	63464	54877

Table 2 Minimum time for indoctrination vs group size for different charismatic indoctrinators

Agents \ Charisma	2	3	4	5	10
4	8	8	8	7	8
6	14	11	13	11	12
8	27	14	18	14	17
10	25	25	23	24	22
12	-	23	28	20	19
14	-	31	29	29	29
16	-	19347	39	27	26
18	-	-	673	94	45
20	-	-	-	1388	55
22	-	-	-	-	383

Table 3 Maximum time for indoctrination vs group size for different charismatic indoctrinators

Agents \ Charisma	2	3	4	5	10
4	32	23	25	23	50
6	47	39	41	32	29
8	43	53	43	43	37
10	35	98	49	51	45
12	-	1614	192	113	58
14	-	-	436	174	104
16	-	-	6448	1088	230
18	-	-	419114	24151	1119
20	-	-	-	291994	11328
22	-	-	-	-	250165

Table 4 Indoctrinator is convinced by the group in less than 100 cycles

Agents \ Charisma	2	3
4	6 %	0 %
6	64 %	0 %
8	89 %	0 %
10	95 %	0 %
12	100 %	1 %
14	100 %	3 %
16	100 %	3 %
18	100 %	9 %
20	100 %	9 %
22	100 %	24 %

CONCLUSIONS

In this paper, we have used the model proposed in Medina-Guevara *et al.* (2017) to investigate the influence of an indoctrinator, a very persuasive agent, on a polarized group made up of two factions of equal size. Each faction supports a unique position than the indoctrinator does. In this sense, the opinion space is a circle where the agents express their preferences regarding three equidistant options. To distinguish these options on the circle, the model employs a system of difference equations that introduces three attractors, which are then identified with the options. The interaction between the agents is in pairs, which is why it is necessary to have an even total number of agents, so we introduce an undecided agent between the two factions to complete that even number of agents.

Following Medina-Guevara *et al.* (2019), to ensure that the indoctrinator is a very persuasive agent, we have made all agents in the group give a high weight to his opinion. While, among themselves, the agents give the opinion of their peers the same weight that they give to their own. To measure the persuasive strength of the indoctrinator, the definition of charisma was also adopted, which is the ratio between the weights mentioned, see eq. (8).

In the model, each faction of agents has the possibility to convince its members back, as well as to persuade the others to adopt its position. So groups can offer resistance to changing their minds.

From the results shown in the previous section, it can be seen that:

1. The average number of temporal steps to indoctrinate a group grows with the size of the group, indeed large groups become immune to the indoctrinator's attempts to persuade them, as long as its agents are free to interact with any other agent in the group.

2. Uncharismatic indoctrinators can be convinced to take the stance of the winning faction.

3. Very charismatic indoctrinators are stubborn and cannot be persuaded to adopt a different opinion, no matter how large groups they interact with.

Acknowledgments

The authors appreciate the invitation to participate in EDIESCA 2022.

Availability of data and material

Not applicable.

Conflicts of interest

The authors declare that there is no conflict of interest regarding the publication of this paper.

LITERATURE CITED

Boccaletti, S., A. N. Pisarchik, C. I. Del Genio, and A. Amann, 2018 *Synchronization: from coupled systems to complex networks*. Cambridge University Press.

Caponigro, M., A. C. Lai, and B. Piccoli, 2015 A nonlinear model of opinion formation on the sphere. Discrete & Continuous Dynamical Systems **35**: 4241.

Dong, Y., M. Zhan, G. Kou, Z. Ding, and H. Liang, 2018 A survey on the fusion process in opinion dynamics. Information Fusion **43**: 57–65.

Hegarty, P., A. Martinsson, and E. Wedin, 2016 The hegselmann-krause dynamics on the circle converge. Journal of Difference Equations and Applications **22**: 1720–1731.

Medina-Guevara, M., J. E. Macías-Díaz, A. Gallegos, and H. Vargas-Rodríguez, 2017 On s1 as an alternative continuous opinion space in a three-party regime. Journal of Computational and Applied Mathematics **318**: 230–241.

Medina-Guevara, M., H. Vargas-Rodríguez, and P. Espinoza-Padilla, 2019 (cmmse paper) a finite-difference model for indoctrination dynamics. Mathematical Methods in the Applied Sciences **42**: 5696–5707.

Medina Guevara, M. G., H. Vargas Rodríguez, P. B. Espinoza Padilla, and J. L. Gozález Solís, 2018 Evolution of electoral preferences for a regime of three political parties. Discrete Dynamics in Nature and Society **2018**.

Noorazar, H., K. R. Vixie, A. Talebanpour, and Y. Hu, 2020 From classical to modern opinion dynamics. International Journal of Modern Physics C **31**: 2050101.

Zha, Q., G. Kou, H. Zhang, H. Liang, X. Chen, *et al.*, 2020 Opinion dynamics in finance and business: a literature review and research opportunities. Financial Innovation **6**: 1–22.

Zhang, Z., S. Al-Abri, and F. Zhang, 2021 Dissensus algorithms for opinion dynamics on the sphere. In *2021 60th IEEE Conference on Decision and Control (CDC)*, pp. 5988–5993, IEEE.

Zhang, Z., S. Al-Abri, and F. Zhang, 2022 Opinion dynamics on the sphere for stable consensus and stable bipartite dissensus. IFAC-PapersOnLine **55**: 288–293.

How to cite this article: Medina-Guevara, M. G., Kurmyshev, E., and Vargas-Rodriguez, H. Dynamics of Indoctrination in Small Groups around Three Options. *Chaos Theory and Applications*, 4(4), 241-245, 2022.

CHAOS
Theory and Applications
in Applied Sciences and Engineering

e-ISSN: 2687-4539
RESEARCH ARTICLE
Vol.4 / No.4 / 2022 / pp.246-266
Special Issue (EDIESCA 2022)
https://doi.org/10.51537/chaos.1187427

Occurrence of Complex Behaviors in the Uncontrolled Passive Compass Biped Model

Essia Added [a,1], **Hassène Gritli** [a,b,2] **and Safya Belghith** [a,3]

[a]Laboratory of Robotics, Informatics and Complex Systems (RISC Lab, LR16ES07), National Engineering School of Tunis, University of Tunis El Manar, BP. 37, Le Belvédère, 1002 Tunis, Tunisia, [b]Higher Institute of Information and Communication Technologies, University of Carthage, 1164 Borj Cedria, Tunis, Tunisia.

ABSTRACT It is widely known that an appropriately built unpowered bipedal robot can walk down an inclined surface with a passive steady gait. The features of such gait are determined by the robot's geometry and inertial properties, as well as the slope angle. The energy needed to keep the biped moving steadily comes from the gravitational potential energy as it descends the inclined surface. The study of such passive natural motions could lead to ideas for managing active walking devices and a better understanding of the human locomotion. The major goal of this study is to further investigate order, chaos and bifurcations and then to demonstrate the complexity of the passive bipedal walk of the compass-gait biped robot by examining different bifurcation diagrams and also by studying the variation of the eigenvalues of the Poincaré map's Jacobian matrix and the variation of the Lyapunov exponents. We reveal also the exhibition of some additional results by changing the inertial and geometrical parameters of the bipedal robot model.

KEYWORDS
Compass biped robot
Passive dynamic walking
Poincaré map
Characteristic multipliers
Complexity
Chaos
Bifurcations
Bubbles
Lyapunov exponents

INTRODUCTION

The history of chaos theory began more than a century ago, in 1900, when mathematicians like Henri Poincaré studied the intricate motions of moving bodies (Walter 2014). Edward Lorenz finds the first chaotic weather system, sometimes known as an odd attractor, at the start of the 1960s. The paper "*Period three indicates chaos*" was an article written by Tien-Yien Li and James A. Yorke in 1975 that first used the word chaos (Li and Yorke 2004). And in 1990, James A. Yorke, Edward Ott, and Celso Grebogi introduced the idea of controlling chaos (Grebogi *et al.* 1997; Ott *et al.* 1990). The first application of chaos is the management of erratic behavior in systems and circuits (Andrievskii and Fradkov 2003, 2004). More applications and methods for analyzing and controlling chaos in engineering systems can be found for example in (Andrievskii and Fradkov 2003, 2004; Boccaletti *et al.* 2000; Fradkov and Evans 2005; Fradkov *et al.* 2006; Guanrong 2021; Harrison *et al.* 2022; Sprott 2020; Xiaoting *et al.* 2022; Yang and Zhou 2014).

Manuscript received: 16 October 2022,
Revised: 14 December 2022,
Accepted: 23 December 2022.

[1]addedessia@gmail.com
[2]grhass@yahoo.fr (**Corresponding author**)
[3]safya.belghith@enit.utm.tn

There are many applications for chaos (Andrievskii and Fradkov 2004; Boubaker and Jafari 2019; Grassi 2021; Jun 2022), but a few come to mind, such as in the engineering (Vibration control and circuit stabilization) (Akgul *et al.* 2016; Azar *et al.* 2017; Jimenez *et al.* 2009; Volos *et al.* 2017; Yang and Zhou 2014), in the computers (Encryption and packet switching in computer networks) (Beritelli *et al.* 2000). Additionally, in the world of medicine, there are techniques for analyzing heart rhythms (Ferreira *et al.* 2011), environment study (Aricioğlu and Berk 2022), enzyme-substrate reactions in a brain waves model via a biological snap oscillator (Vaidyanathan *et al.* 2018), predicting irregular heartbeats (Firth 1991), observation of performance of asynchronous machine (Öztürk 2020), stepper motor (Miladi *et al.* 2021), and controlling them. Moreover, in the field of mechanics and robotics, there are some applications of chaos in complex systems like the mechanical oscillators (Buscarino *et al.* 2016; Gritli and Belghith 2018a; Khraief Haddad *et al.* 2017), the mobile robots (Sambas *et al.* 2016; Vaidyanathan *et al.* 2017; Volos *et al.* 2012, 2013), and also the bipedal walking robots (Gritli and Belghith 2017a, 2018b; Iqbal *et al.* 2014; Montazeri Moghadam *et al.* 2018). The chaotic systems have been considered as important and attractive areas of research that have constantly evolved over the years which have an unpredictable behavior while changing the some parameters.

For a few years, the scientific community's and manufacturers' interest in mobile robotics has not waned. This sort of robot has a wide range of uses. There are primarily service robotics jobs (manoeuvrings, package distribution, and so on), as well as monitoring or obtaining information on the task environment of manufacturing carried out in a hostile or dangerous setting for humans (Bekey and Goldberg 2012).

In light of this, legged mobile robots have a lot of promise. The fundamental reason is that the employment of paws increases a mobile robot's overall mobility (Chevallereau *et al.* 2009; Goswami and Vadakkepat 2019; Meng and Song 2022). Indeed, only specifically equipped sites (roads, corridors, platforms) or areas with low inclination are accessible to a wheeled or tracked robot (fields, orchards). In steep situations, locations packed with obstructions on the ground, or urban spaces meant for people (issues with stairs, doorsteps, and side-walk), the legs are the optimum mode of locomotion. On rough floors, using the legs provides for a smoother movement and better performance than using the wheels (Meng and Song 2022).

Walking is a mode of locomotion for the lower limbs (the legs) of the body during which the subject always has at least one foot on the ground. This locomotion type gives birth to an alternation between the phase of simple support (one foot on the ground) and the phase of double support (two feet on the ground). Among biped walking mammals, human is the only one to adopt the erect attitude as its natural position that we want to imitate. Walking robots come in a variety of shapes and sizes: bipeds (Chevallereau *et al.* 2009; Reher and Ames 2021; Westervelt *et al.* 2007) and humanoids (Goswami and Vadakkepat 2019), etc.

McGeer developed a type of walking robots called passive dynamic walkers in the 1990s that can walk steadily down a slope without the aid of any actuators (McGeer 1990). In a lot of cases, impulsive hybrid nonlinear dynamics are used to describe bipedal walking robots (Chevallereau *et al.* 2009; Grizzle *et al.* 2001; Westervelt *et al.* 2007). Here, we are referring to impulsive mechanical systems that make stiff or even jarring interactions with particular surfaces. Using a biped robot that resembles a human is important to accurately examine the walking phenomenon. Particularly, articulated mechanical systems that experience collisions with the walking surface are designated as bipedal robots (Chevallereau *et al.* 2009; Westervelt *et al.* 2007).

In the present research work, we are interested in passive biped robots, and specially the compass-type bipedal robot, which is the simplest device that can more faithfully replicate human walking (Collins *et al.* 2005; Deng *et al.* 2017; Garcia *et al.* 2000, 1998; Kuo 2007; Miladi *et al.* 16-19 March 2015). It consists of two rigid legs with no knees and ankles, and it produces punctual contacts with the ground while walking.

The walk of a bipedal robot is modeled by a hybrid impulsive nonlinear dynamics (Fathizadeh *et al.* 2019; Goswami *et al.* 1998; Iqbal *et al.* 2014), which is considered complex and which can generate periodic cycles, quasi-periodic behaviors, chaotic motions and several types of bifurcation, including the period-doubling bifurcation, the cyclic-fold bifurcation, and the Neimark-Sacker bifurcation (called also the torus bifurcation), as for example in (Added and Gritli 2022, 2023; Added *et al.* 2021a,c; Fathizadeh *et al.* 2018; Goswami *et al.* 1998; Gritli and Belghith 2016a,b, 2017a,b, 2018b; Gritli *et al.* 2012, 2011, 2018; Jun 2022; Makarenkov 2020; Montazeri Moghadam *et al.* 2018; Nourian Zavareh *et al.* 2018). The existence and study of the period-doubling bifurcations exhibited in the biped robots' walking has been widely realized in the literature using the principle of Poincaré maps and also by determining its analytical expression like in (Znegui *et al.* 2020a, 2021) and also by using it in the chaos control (Znegui *et al.* 2020b). In (Added and Gritli 2022, 2023; Added *et al.* 2021b), a further study of the period-doubling bifurcations and their route to chaos has been realized. Moreover, in (Added and Gritli 2022), the numerical proof of the existence of the Neimark-Sacker bifurcation in the passive compass-gait bipedal robot has been achieved. The existence of such bifurcation has been demonstrated via only one set of parameters of the compass robot. In (Added *et al.* 2021a), an additional study of the complex motions of the passive bipedal gait of the compass walker has been realized using mainly bifurcation diagrams. Some unforeseen behaviors like the bubbles have been developed. A study of these behaviors and other motions including chaos, bifurcations and chaos in bubbles, has been also presented in (Added *et al.* 2021c).

The objective of this work is to further investigate the passive dynamic walking of the compass-type bipedal robot by mathematically modeling this dynamics for both phases: the swinging phase and the simple support phase, and simulating it numerically in order to observe the different complex behaviors. However, faced to the complexity of this task by observing chaos and bifurcations that appear for certain modification of the biped robot's parameters that has been recently started in (Added and Gritli 2022, 2023; Added *et al.* 2021a,b,c), then a thorough analysis of gait stability of the biped robot is necessary to proceed with and hence develop the analysis of this type of legged walking bipedal robots. We are then going to highlight the diversity of the complex behaviors covered by the fact of walking passively down sloped surfaces.

In previous articles, we have presented a variety of control methods based on tracking the passive dynamic walking and tracking a certain created trajectory with spline or Bezier functions (Added and Gritli 2020a,b; Added *et al.* 2021b, 2022a,b) to control the chaotic behavior in the bipedal walking of the compass-gait walker. Some other techniques like the OGY control and the delayed-feedback control methods have been widely employed for the suppression of chaos (Gritli *et al.* 2015, 2013; Iqbal *et al.* 2014; Znegui *et al.* 2020b).

Additionally, in order to analyze the walking behavior of the biped robot, it is crucial to apply the Poincaré map approach to determine therefore the fixed point for each walking gait due to the complexity of the impulsive hybrid nonlinear dynamics. By simulating this complex dynamics, an analysis of the behavior of the bipedal walking of the compass robot will be achieved by modifying its inertial and geometrical parameters and also the slope angle of the walking surface. Such analysis will be realized by means of the bifurcation diagrams that will reveal the presence of the period-doubling bifurcation, the Neimark-Sacker bifurcation, the cyclic-fold bifurcation and chaos. In addition, our analysis of the passive bipedal walking will be carried out by drawing the attractors in the phase planes and via the Poincaré section, and also by drawing the tendency of the eigenvalues of the Jacobian matrix of the Poincaré map. Some novel complex behaviors will be revealed in the bifurcation diagrams.

Our main contributions in this paper are summarized as follows:

- Analysis of chaos and bifurcations in the impulsive hybrid nonlinear dynamics of the passive dynamic walking of the compass bipedal robot under variation of two (bifurcation) parameters, namely the slope angle of the inclined walking surface and the length of the lower-half segment.
- Analysis and demonstration, via bifurcation diagrams, of existence of some period-doubling routes to chaos, period-

remerging scenario and bifurcation of bubbles (period bubbling).
- Investigation of the different motions by plotting and studying the resulting attractors in the phase planes and the Poincaré sections.
- Study of the stability of the period-1 walking gaits of the compass bipedal robot via the eigenvalues of the Jacobian matrix of the Poincaré map, and hence study of the occurrence of the period-doubling bifurcation and the Neimark-Sacker bifurcation.
- Use of the spectrum of Lyapunov exponents in the analysis of the scenario of period-doubling route to chaos. This study will be realized for only one case of the bifurcation diagram by varying only one parameter: the slope angle.

The remaining structure of this paper is as follows. A quick introduction of the compass-type bipedal robot and the mathematical model of its walking phases can be found in the second section. Then, by describing the Poincaré map approach in the third section for the localization of the period-1 fixed points, we will be interested in the hunting of a one-periodic bipedal walk of the compass robot using. The bifurcation diagrams and the analysis of various attractors in the fourth section are used to offer a study of the compass-type bipedal gait and to show the novel exhibited complex walking behaviors. The conclusion and a few upcoming projects are covered in the fifth and last Section.

PASSIVE DYNAMIC WALKING OF THE COMPASS BIPEDAL ROBOT

Geometric structure of the compass robot

Figure 1 shows a graphical presentation of the compass-gait biped robot, with Table 1 listing the significant parameters in the dynamics description. This biped robot is a type of rigid mechanical system with unilateral configuration space constraints (Chevallereau *et al.* 2009; Gritli *et al.* 2013; Westervelt *et al.* 2007).

The compass-type bipedal robot is made up of two legs that are exactly identical: a right leg and a left leg, as well as a frictionless hip that connects the two legs. The two legs are depicted as stiff bars without knees and ankles. The mass m of each leg is concentrated at a distance b from the mass m_h of the hip.

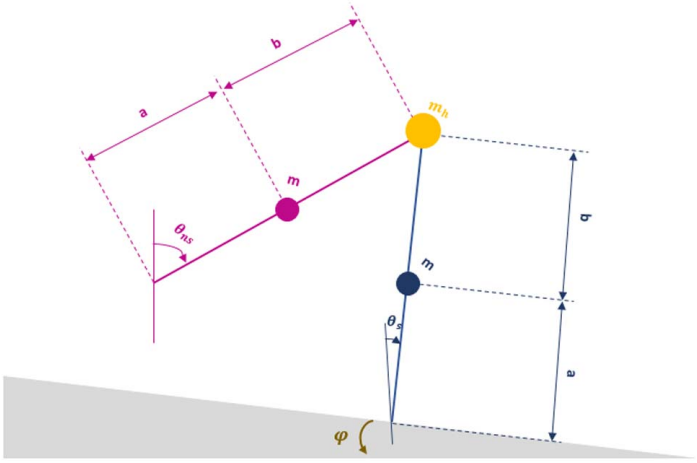

Figure 1 The passive compass bipedal robot walking down an inclined surface of angle φ. Here, θ_s and θ_{ns} stand respectively for the support angle of the support/stance leg, and the nonsupport angle of the swing leg. These angles are defined with regard to the vertical lines. Moreover, the positive angles are calculated in the counterclockwise direction.

Table 1 Significant parameters used in the dynamics description of the passive compass-type biped walker.

Notation	Value	Unit
a	0.5	m
b	0.5	m
l	1	m
m	5	Kg
m_h	10	Kg
g	9.8	ms^{-2}

The compass robot performs a passive walk without any external activity and relies solely on gravity for a suitable initial state and a corresponding slope φ. The passive walk of the compass robot contains two phases: a swing phase and a double-support phase or impact phase, which is a very fast transition phase. The compass-type bipedal robot can be modeled as a double pendulum in the first case with the stance leg stationary on the ground as a pivot and the other leg swinging above the ground as it walks down the hill. When the swing leg reaches the ground, the impulsive transition phase begins (and occurs instantaneously). As a result, the prior support leg departs the ground, and hence a new swing phase is developed.

We assume that the impact is totally inelastic and that there is no sliding at the point of contact between the leg and the ground (Gritli *et al.* 2015; Znegui *et al.* 2020a). In Figure 1 and in the sequel, θ_s is the angle of the support leg, whereas θ_{ns} is the angle of the swing leg. These two angles establish together the compass walk configuration. Note that positive angles are computed counterclockwise.

Modeling of the bipedal walk of the compass robot

The hybrid model of the compass-gait biped robot's passive dynamic walking combines of the nonlinear differential equation (3) for the swing phase and the nonlinear algebraic equation (7) for the impact phase.

Swing phase dynamics

Let $q = [\theta_{ns}\ \theta_s]^{\mathrm{T}}$ be the compass-gait biped robot's vector of generalized coordinates. According to (Znegui *et al.* 2020a), only one natural unilateral restriction is applied to this biped robot, namely

$$\mathcal{L}_1(q) = \theta_{ns} + \theta_s + 2\varphi \geq 0 \tag{1}$$

which corresponds to the distance between the hip of the swing leg and the ground. Thus, this constraint (1) represents the situation where and when the swing leg is upper the ground. This ensures that during bipedal walking, the unilateral restriction $\mathcal{L}_1 \geq 0$ is always satisfied.

The motion of the compass-gait biped robot can be defined as follows, by considering some basic assumptions (Gritli *et al.* 2015; Znegui *et al.* 2020a). Indeed, during the swing phase, we employ

the Euler-Lagrange method to determine the biped robot's dynamic model. The following is the expression for Euler-Lagrange equation for an uncontrolled robotic system, and therefore for the passive compass bipedal robot.

$$\frac{d}{dt}\frac{\partial \mathcal{L}(q,\dot{q})}{\partial \dot{q}} - \frac{\partial \mathcal{L}(q,\dot{q})}{\partial q} = 0 \tag{2}$$

From this previous expression (2), we get the following nonlinear differential equation:

$$\mathcal{M}(q)\ddot{q} + \mathcal{H}(q,\dot{q})\dot{q} + \mathcal{G}(q) = 0 \tag{3}$$

where $\mathcal{M}(q)$ is the inertia matrix:

$$\mathcal{M}(q) = \begin{bmatrix} mb^2 & -mlb\cos(\theta_s - \theta_{ns}) \\ -mlb\cos(\theta_s - \theta_{ns}) & (m+m_h)l^2 + ma^2 \end{bmatrix} \tag{4}$$

the matrix $\mathcal{H}(q,\dot{q})$ includes Coriolis and centrifugal forces:

$$\mathcal{H}(q,\dot{q}) = \begin{bmatrix} 0 & mbl\sin(\theta_s - \theta_{ns})\dot{\theta}_s \\ -mbl\sin(\theta_s - \theta_{ns})\dot{\theta}_{ns} & 0 \end{bmatrix} \tag{5}$$

and $\mathcal{G}(q)$ is the vector of gravitational torques:

$$\mathcal{G}(q) = \begin{bmatrix} -gmb\sin(\theta_{ns}) \\ g\left[(m+m_h)l + ma\right]\sin(\theta_s) \end{bmatrix} \tag{6}$$

It is worth noting that the control input, saying u, in the nonlinear dynamics (2) of the bipedal walking of the compass biped robot was not introduced, and then it is zero, $u = 0$. As a result, the compass bipedal robot is not controlled, and the swing phase, and consequently the complete bipedal walking, is hence entirely passive

Impact phase dynamics

The angular momentum conservation approach is used to determine the dynamics of the impact phase (Added *et al.* 2021b; Goswami *et al.* 1996, 1998). For this, we will use the two signs "+" and "−" that will be placed to the right of a variable to refer to the value of that variable, respectively, just after and just before the impact of the biped robot's swing leg with the ground.

The impact phase begins when the swing phase ends, which occurs when the compass walker's swing leg makes contact with the walking surface. When the swing leg encounters the walking surface, the angular momentum is conserved according to the following algebraic equation (Added *et al.* 2021b; Goswami *et al.* 1996, 1998):

$$\mathcal{Q}^+(q^+)\dot{q}^+ = \mathcal{Q}^-(q^+)\dot{q}^- \tag{7}$$

with $\dot{q}^+$ and $\dot{q}-$ are the angular velocities just after and just before the impact, where:

$$\mathcal{Q}^+(q) = \begin{bmatrix} mb(b - l\cos(\theta_s - \theta_{ns})) \\ mb^2 \\ ma^2 + m_h l^2 + ml(l - b\cos(\theta_s - \theta_{ns})) \\ -mlb\cos(\theta_s - \theta_{ns}) \end{bmatrix} \tag{8}$$

and

$$\mathcal{Q}^-(q) = \begin{bmatrix} -mab & l(m_h l + 2ma)\cos(\theta_s - \theta_{ns}) - mab \\ 0 & -mab \end{bmatrix} \tag{9}$$

Furthermore, when the impact with the ground occurs, a switching between the two legs happens. This situation is described by means of the following relation:

$$q^+ = \mathcal{R}q^- \tag{10}$$

where $\mathcal{R}$ is a constant matrix and is defined like so:

$$\mathcal{R} = \begin{bmatrix} 0 & 1 \\ 1 & 0 \end{bmatrix} \tag{11}$$

Relying on expressions of matrices $\mathcal{Q}^-(q)$ and $\mathcal{Q}^-(q)$, and by taking into consideration expressions (10) and (11), it is easy to demonstrate that the relation (7) can be recast as follows:

$$\dot{q}^+ = \left\{\mathcal{Q}^+(q^-)\right\}^{-1}\mathcal{Q}^-(q^-)\dot{q}^- \tag{12}$$

Impact conditions

According to the results in (Znegui *et al.* 2020a) and relying on the unilateral constraint (1), we can note the following condition:

$$\mathcal{L}_1(q) = 2\varphi + \theta_s + \theta_{ns} = 0 \tag{13}$$

which is the first impact condition and which reveals the case where the swing leg hits the walking surface.

Moreover, to ensure that the impact with the walking surface happens, we should add the following condition:

$$\mathcal{L}_2(q,\dot{q}) = \frac{d\mathcal{L}_1(q)}{dt} = \frac{\partial \mathcal{L}_1(q)}{\partial q}\dot{q} < 0 \tag{14}$$

which is the second impact condition revealing the case where the swing leg descends towards the walking surface.

In addition, in order to guarantee that the impact occurs after a complete swing phase, we add the following inequality constraint

$$\mathcal{L}_3(q) = \sin(\theta_{ns}) - \sin(\theta_s) > 0 \tag{15}$$

which is the third impact condition defining the case where the swing leg is opposite to (or it is in front of) the support leg.

Then, by arranging the previous expressions (13), (14) and (15), the impact conditions of the swing leg with the walking surface are defined by the following set:

$$\begin{cases} \mathcal{L}_1(q) = 2\varphi + \theta_{ns} + \theta_s = 0 \\ \mathcal{L}_2(q,\dot{q}) = \frac{\partial \mathcal{L}_1(q)}{\partial q}\dot{q} < 0 \\ \mathcal{L}_3(q) = \sin(\theta_{ns}) - \sin(\theta_s) > 0 \end{cases} \tag{16}$$

Complete dynamic model

The continuous dynamics presented in (3), the discrete dynamics presented in form of the two algebraic equations (12) and (10), and the set of impact conditions (16) form together the impulsive hybrid nonlinear dynamics of the passive dynamic walking model of the compass biped robot. Let $x = [q\ \dot{q}]^{\mathrm{T}}$ be the state vector.

Then, these previous expressions are grouped together to form the following impulsive hybrid nonlinear model:

$$\begin{cases} \dot{x} = f(x) \text{ if } x \in \Omega \\ x^{+} = h(x^{-}) \text{ if } x \in \Delta \end{cases} \tag{17}$$

where

$$\begin{cases} \Omega = \{x \in \mathbb{R}^{2n} : \mathcal{L}_1(x) > 0\} \\ \Delta = \{x \in \mathbb{R}^{2n} : \mathcal{L}_1(x) = 0; \mathcal{L}_2(x) < 0; \mathcal{L}_3(x) > 0\} \end{cases} \tag{18}$$

where here $n = 2$, and in (17),

$$f(x) = \begin{bmatrix} \dot{q} \\ -\mathcal{M}^{-1}(q)\left(\mathcal{H}(q,\dot{q})\dot{q} + \mathcal{G}(q)\right) \end{bmatrix} \tag{19a}$$

$$h(x) = \begin{bmatrix} \mathcal{R}q \\ \left\{\mathcal{Q}^{+}(q)\right\}^{-1}\mathcal{Q}^{-}(q)\dot{q} \end{bmatrix} \tag{19b}$$

Moreover, it is straightforward to show that the functions $\mathcal{L}_1(x)$ and $\mathcal{L}_2(x)$ are expressed like so:

$$\mathcal{L}_1(x) = \mathcal{C}_1 x + 2\varphi \tag{20a}$$

$$\mathcal{L}_2(x) = \mathcal{C}_2 x \tag{20b}$$

where

$$\mathcal{C}_1 = \begin{bmatrix} 1 & 1 & 0 & 0 \end{bmatrix} \tag{21a}$$

$$\mathcal{C}_2 = \begin{bmatrix} 0 & 0 & 1 & 1 \end{bmatrix} \tag{21b}$$

In addition, it is easy to show that the function $\mathcal{L}_2(x)$ is equivalent to:

$$\mathcal{L}_2(x) = \mathcal{C}_1 \dot{x} \tag{22}$$

IDENTIFICATION AND STABILITY OF THE ROBOT BIPED'S PERIODIC MOVEMENT

In this section, we will develop expressions of the fundamental solution matrix, the jump matrix, and the monodromy matrix, and use them to find a fixed point of the periodic movement of the compass-type bipedal robot.

Fundamental solution matrix

The first equation in the hybrid impulsive dynamic model (17) results from continuous behavior, whereas the second equation results from the discrete behavior. We consider first the nonlinear differential equation $\dot{x} = f(x)$, which proposes as a solution, which is expressed in terms of flow, defined like so:

$$x(t) = \phi(t, x_0) \tag{23}$$

and $x_0 = \phi(t_0, x_0)$, to be the initial condition.

It is simple to show that:

$$\dot{x} = f(x(t)) = \frac{dx(t)}{dt} = \frac{d\phi(t, x_0)}{dt} \tag{24}$$

Then, it is possible to write the following expressions:

$$\begin{cases} \dot{\phi}(t, x_0) = f(\phi(t, x_0)) \\ \phi(t_0, x_0) = x_0 \end{cases} \tag{25}$$

The derivative of these previous expressions in (25) with respect to the initial condition x_0, yields:

$$\begin{cases} \frac{\partial \dot{\phi}(t,x_0)}{\partial x_0} = \frac{\partial f(\phi(t,x_0))}{\partial x}\frac{\partial \phi(t,x_0)}{\partial x_0} \\ \frac{\partial \phi(t_0,x_0)}{\partial x_0} = \mathcal{I}_{2n} \end{cases} \tag{26}$$

where here and in the sequel $\mathcal{I}_{2n}$ stands for the identity matrix with dimension $(2n \times 2n)$.

We pose $\Phi(t, x_0)$ to be the fundamental solution matrix, which is expressed as follows:

$$\Phi(t, x_0) = \frac{\partial \phi(t, x_0)}{\partial x_0} \tag{27}$$

Then, the derivative of this matrix with respect to time leads to the following expression:

$$\dot{\Phi}(t, x_0) = \frac{\partial \dot{\phi}(t, x_0)}{\partial x_0} \tag{28}$$

Therefore, we can write the model (26) as follows:

$$\begin{cases} \dot{\Phi}(t, x_0) = \mathcal{J}(x)\Phi(t, x_0) \\ \Phi(t_0, x_0) = \mathcal{I}_{2n} \end{cases} \tag{29}$$

where $\mathcal{J}(x)$ is the Jacobian matrix of the nonlinear function $f(x)$, and is defined like so:

$$\mathcal{J}(x) = \frac{\partial f(\phi(t, x_0))}{\partial x} \tag{30}$$

The fundamental solution matrix $\Phi(t, x_0)$ is simple to calculate for continuous systems. However, its calculation is quite difficult for systems that are discontinuous or even show discontinuities, such as the impulsive hybrid dynamic systems as our biped robot's case. This problem to solve calls for the calculation of the jump matrix, as it will be explained in the next paragraph.

Jump matrix

The biped robots exhibit discontinuities as a result of the impact event in the Jacobian matrix during the transition of the state vector that results in a discontinuity or even a jump in the fundamental solution matrix $\Phi(t, x_0)$.

Let pose $\Phi^{+}(t, x_0)$ to be the fundamental solution matrix immediately after the impact, and $\Phi^{-}(t, x_0)$ to be the fundamental solution matrix immediately before the impact. The relation between $\Phi^{+}(t, x_0)$ and $\Phi^{-}(t, x_0)$ is obtained by means of the jump matrix $\mathcal{S}(x(\tau^{+}), x(\tau^{-}))$, as follows:

$$\Phi^{+}(t, x_0) = \mathcal{S}(x(\tau^{+}), x(\tau^{-}))\Phi^{-}(t, x_0) \tag{31}$$

Therefore, finding expression of the jump matrix $\mathcal{S}(x(\tau^{+}), x(\tau^{-}))$ is our goal in the next part.

Let posing for simplicity $x(\tau^{+}) = x^{+}$ and $x(\tau^{-}) = x^{-}$ with τ^{+} and τ^{-} are the moments right after and right before the impact. Moreover, we pose f^{+} to be the vector f immediately after the impact, and f^{-} to be the vector f immediately before the impact.

For simplicity, let us use in the next the following notations:

$$\begin{cases} \Phi^+ = \Phi(\tau^+, x_0) \\ \Phi^- = \Phi(\tau^-, x_0) \\ f^+ = f(x(\tau^+)) \\ f^- = f(x(\tau^-)) \end{cases} \tag{32}$$

As the flow $\phi(t, x_0)$ depends on t and x_0, it is then easy to write the following expression:

$$d\phi(t, x_0) = \frac{\partial \phi(t, x_0)}{\partial x_0} dx_0 + \frac{\partial \phi(t, x_0)}{\partial t} dt \tag{33}$$

Thus, we can write the relation:

$$\frac{d\phi(t, x_0)}{dx_0} = \frac{\partial \phi(t, x_0)}{\partial x_0} + \frac{\partial \phi(t, x_0)}{\partial t} \frac{dt}{dx_0} \tag{34}$$

Let us consider expressions (24) and (27), and posing $\tau_{x_0} = \frac{dt}{dx_0}$. Then, relation (34) can be reformulated as follows:

$$\frac{d\phi(t, x_0)}{dx_0} = \Phi(t, x_0) + f(\phi(t, x_0))\tau_{x_0} \tag{35}$$

Then, we can write for $t = \tau^-$ and $t = \tau^+$, the following expressions:

$$\begin{cases} \frac{dx(\tau^-)}{dx_0} = \Phi(\tau^-, x_0) + f(x(\tau^-))\tau_{x_0} \\ \\ \frac{dx(\tau^+)}{dx_0} = \Phi(\tau^+, x_0) + f(x(\tau^+))\tau_{x_0} \end{cases} \tag{36}$$

Then, using notation (32), expressions in (36) become:

$$\begin{cases} \frac{dx^-}{dx_0} = \Phi^- + f^-\tau_{x_0} \\ \\ \frac{dx^+}{dx_0} = \Phi^+ + f^+\tau_{x_0} \end{cases} \tag{37}$$

According to the second equation of the model (17), we have $x^+ = h(x^-)$. Then, it follows that:

$$\frac{dx^+}{dx_0} = \frac{dh(x^-)}{dx_0} = \frac{\partial h(x^-)}{\partial x^-} \frac{dx^-}{dx_0} \tag{38}$$

We pose $h_x^- = \frac{\partial h(x^-)}{\partial x^-}$. Then, relation (38) is rewritten like so:

$$\frac{dx^+}{dx_0} = h_x^- \frac{dx^-}{dx_0} \tag{39}$$

Therefore, based on the two results in (37), we can write from relation (39), the following expression:

$$\Phi^+ + f^+\tau_{x_0} = h_x^-(\Phi^- + f^-\tau_{x_0}) \tag{40}$$

According to the first impact condition in the set Δ in (18), we can write the following expression:

$$\frac{\partial \mathcal{L}_1(x^-)}{\partial x^-} \frac{dx^-}{dx_0} = 0 \tag{41}$$

Using expression (20a), and according to (41), it follows that:

$$\mathcal{C}_1 \frac{dx^-}{dx_0} = 0 \tag{42}$$

Therefore, relying on the first relation in (37), we obtain from the previous relation (42), the following expression:

$$\mathcal{C}_1(\Phi^- + f^-\tau_{x_0}) = 0 \tag{43}$$

Relying on the dynamics of the swing phase (24), we have:

$$\mathcal{C}_1 f^- = \mathcal{C}_1 \dot{x}^- \tag{44}$$

Moreover, relying on expression (22), it follows that (44) is recast like so:

$$\mathcal{C}_1 f^- = \mathcal{L}_2(x^-) \tag{45}$$

Then, according to the impact conditions describing the set Δ in (18), and then by considering the second condition $\mathcal{L}_2(x) < 0$, we obtain hence the following inequality:

$$\mathcal{C}_1 f^- < 0 \tag{46}$$

Accordingly, by taking into account this previous condition (46), and from the relation (43), expression of the quantity τ_{x_0} is defined as follows: :

$$\tau_{x_0} = \frac{-\mathcal{C}_1}{\mathcal{C}_1 f^-} \Phi^- \tag{47}$$

Hence, based on the equations (40) and (47), we can write the following relation:

$$\Phi^+ = (h_x^- - \frac{(h_x^- f^- - f^+)\mathcal{C}_1}{\mathcal{C}_1 f^-})\Phi^- \tag{48}$$

Therefore, compared to relation (31), the following expression describes the jump matrix:

$$\mathcal{S}(x^+, x^-) = h_x^- - \frac{(h_x^- f^- - f^+)\mathcal{C}_1}{\mathcal{C}_1 f^-} \tag{49}$$

Monodromy matrix

Let the set or hyperplan Δ describes our choice of the Poincaré section. Starting from the initial condition x_0 ($x_0 \in \Delta$), then the system trajectory will return to the Poincaré section Δ. The time required between two consecutive intersections with the Poincaré section is $T_r(x_0)$, which is called as the return time to the Poincaré section. For a one-periodic trajectory, the return time is the same as the period of the trajectory, and it defines the step period of the walking gait of the compass bipedal robot.

It is important to note that since the impact of the swing leg of the robot with the walking surface is instantaneous, then we can write the following relation:

$$T_r(x_0) = \tau^+ = \tau^- \tag{50}$$

For a 1-periodic trajectory and according to the equation (31), the monodromy matrix, namely Φ^+, is defined by the following relation:

$$\Phi^+ = \mathcal{S}(x^+, x^-)\Phi^- \tag{51}$$

where:

$$\Phi^- = \Phi(T_r(x_0), x_0) = \left. \frac{\partial f(\phi(t, x_0))}{\partial \phi(t, x_0)} \right|_{t=\tau^-} \tag{52}$$

Notice that $\Phi(T_r(x_0), x_0)$ is the fundamental solution matrix $\Phi(t, x_0)$, which is the solution of the differential system (29), and evaluated at the first return time $T_r(x_0)$. Then, we stress that the fundamental solution matrix $\Phi(t, x_0)$ depends on the values of

the state vector x just before (x^-) and just after (x^+) the impact event. These two states x^- and x^+ are completely different, and hence they will give us two different values of the fundamental solution matrix $\Phi(t, x_0)$ at the impact that are related via relation (48). Therefore, this sudden and non-continuous change in values of the fundamental solution matrix causes a discontinuity.

It is worth to mention that the search for the one-periodic walk for the compass-type biped robot lies in the search for a one-periodic fixed point of the period-1 limit cycle.

Finding a period-1 fixed point

The period-1 fixed point is the solution of the following equation:

$$\mathcal{F}(x_0) = \mathcal{P}(x_0) - x_0 = \phi(T_r(x_0), x_0) - x_0 = 0 \tag{53}$$

To determine the solutions of this equation (53), we use the numerical Newton-Raphson algorithm. We choose an initial estimate of x_0 as an initial condition, then we iterate the Poincaré map only once to find the flow $\phi(\tau^+, x_0)$.

Algorithm

The search algorithm for a period-1 fixed point is based on the following iterative scheme:

$$x_0^{k+1} = x_0^k - \left\{\mathcal{DF}(x_0^k)\right\}^{-1} \mathcal{F}(x_0^k) \tag{54}$$

where $\mathcal{DF}(x_0^k)$ is the Jacobian of the function $\mathcal{F}$ presented in the equation (53).

The algorithm stops when the norm of $\mathcal{F}(x_0^k)$ will be lower than a certain fixed threshold.

Expression of the Jacobian matrix $\mathcal{DF}(x_0)$

To solve the equation (54), the Jacobian matrix $\mathcal{DF}(x_0^k)$ must be first calculated. This matrix is defined by the following expression:

$$\mathcal{DF}(x_0) = \frac{d\mathcal{F}(x_0)}{dx_0} \tag{55}$$

Then, using relation (53), we have:

$$\mathcal{DF}(x_0) = \frac{d}{dx_0}(\phi(T_r(x_0), x_0) - x_0) \tag{56}$$

Thus, we obtain the following expression:

$$\mathcal{DF}(x_0) = \frac{d\phi(T_r(x_0), x_0)}{dx_0} - \mathcal{I}_{2n} \tag{57}$$

Expression of the quantity $\frac{d}{dx_0}\phi(T_\tau(x_0), x_0)$

Relying on expression (33), we can write the following relation:

$$d\phi(T_r(x_0), x_0) = \frac{\partial\phi(T_r(x_0), x_0)}{\partial x_0} dx_0 + \frac{\partial\phi(T_r(x_0), x_0)}{\partial T_r(x_0)} dT_r(x_0) \tag{58}$$

Then, we obtain the following expression of the quantity $\frac{d\phi(T_\tau(x_0), x_0)}{dx_0}$:

$$\frac{d\phi(T_\tau(x_0), x_0)}{dx_0} = \frac{\partial\phi(T_\tau(x_0), x_0)}{\partial x_0} + \frac{\partial\phi(T_\tau(x_0), x_0)}{\partial T_\tau(x_0)} \frac{dT_r(x_0)}{dx_0} \tag{59}$$

The previous expression can be rewritten like so:

$$\frac{d\phi(T_\tau(x_0), x_0)}{dx_0} = \Phi(T_\tau(x_0), x_0) + f(x(T_r(x_0))) \frac{dT_r(x_0)}{dx_0} \tag{60}$$

where $\Phi(T_\tau(x_0), x_0)$ is the fundamental solution matrix $\Phi(t, x_0)$ evaluated at the return time $T_\tau(x_0) = \tau^+$, and then $\Phi(T_\tau(x_0), x_0) = \Phi^+$. Moreover, we have $f(x(T_r(x_0))) = f(x(\tau^+)) = f^+$.

Then, the equation (57) becomes:

$$\mathcal{DF}(x_0) = \Phi(T_\tau(x_0), x_0) + f(x(T_\tau(x_0))) \frac{dT_\tau(x_0)}{dx_0} - \mathcal{I}_{2n} \tag{61}$$

The only unknown in this expression (61) is the quantity $\frac{dT_r(x_0)}{dx_0}$, which will be determined in the next section.

Expression of the quantity $\frac{dT_r(x_0)}{dx_0}$

Let us reconsider the two first impact conditions in the impact set Δ defined in (18):

$$\mathcal{L}_1(x) = \mathcal{C}_1 x + 2\varphi = 0 \tag{62a}$$
$$\mathcal{L}_2(x) = \mathcal{C}_2 x < 0 \tag{62b}$$

For a period-1 fixed point, we should have $x_0 = \phi(T_r(x_0), x_0)$. Then, the two impact conditions in (62a) and (62b) are recast as follows:

$$\mathcal{L}_1(\phi(T_r(x_0), x_0)) = \mathcal{C}_1\phi(T_r(x_0), x_0) + 2\varphi = 0 \tag{63a}$$
$$\mathcal{L}_2(\phi(T_r(x_0), x_0)) = \mathcal{C}_2\phi(T_r(x_0), x_0) < 0 \tag{63b}$$

The derivative of the first constraint (63a) with respect to x_0 is as follows:

$$\frac{d\mathcal{L}_1(\phi(T_r(x_0), x_0))}{dx_0} = \frac{\partial\mathcal{L}_1(\phi(T_r(x_0), x_0))}{\partial x_0} + \frac{\partial\mathcal{L}_1(\phi(T_r(x_0), x_0))}{\partial T_r(x_0)} \frac{dT_r(x_0)}{dx_0} = 0 \tag{64}$$

Moreover, we can write the following relations:

$$\frac{\partial\mathcal{L}_1(\phi(T_r(x_0), x_0))}{\partial x_0} = \frac{\partial\mathcal{L}_1(\phi(T_r(x_0), x_0))}{\partial\phi(T_r(x_0), x_0)} \frac{\partial\phi(T_r(x_0), x_0)}{\partial x_0} \tag{65a}$$
$$\frac{\partial\mathcal{L}_1(\phi(T_r(x_0), x_0))}{\partial T_r(x_0)} = \frac{\partial\mathcal{L}_1(\phi(T_r(x_0), x_0))}{\partial\phi(T_r(x_0), x_0)} \frac{\partial\phi(T_r(x_0), x_0)}{\partial T_r(x_0)} \tag{65b}$$

According to expression (63a), we obtain:

$$\frac{\partial\mathcal{L}_1(\phi(T_r(x_0), x_0))}{\partial\phi(T_r(x_0), x_0)} = \mathcal{C}_1 \tag{66}$$

Then, the two expressions (65a) and (65a) become:

$$\frac{\partial\mathcal{L}_1(\phi(T_r(x_0), x_0))}{\partial x_0} = \mathcal{C}_1 \frac{\partial\phi(T_r(x_0), x_0)}{\partial x_0} \tag{67a}$$
$$\frac{\partial\mathcal{L}_1(\phi(T_r(x_0), x_0))}{\partial T_r(x_0)} = \mathcal{C}_1 \frac{\partial\phi(T_r(x_0), x_0)}{\partial T_r(x_0)} \tag{67b}$$

Then, relation (64) is recast as follows:

$$\mathcal{C}_1 \frac{\partial\phi(T_r(x_0), x_0)}{\partial x_0} + \mathcal{C}_1 \frac{\partial\phi(T_r(x_0), x_0)}{\partial T_r(x_0)} \frac{dT_r(x_0)}{dx_0} = 0 \tag{68}$$

This expression (68) is rewritten like so:

$$\mathcal{C}_1\Phi(T_r(x_0), x_0) + \mathcal{C}_1 f(x(T_r(x_0))) \frac{dT_r(x_0)}{dx_0} = 0 \tag{69}$$

Accordingly, as $\mathcal{C}_1 f(x(T_r(x_0))) = \mathcal{C}_1 f^-$, and based on the condition (46), we can obtain expression of the quantity $\frac{dT_\tau(x_0)}{dx_0}$ as follows:

$$\frac{dT_\tau(x_0)}{dx_0} = \frac{-\mathcal{C}_1}{\mathcal{C}_1 f(x(T_\tau(x_0)))} \Phi(T_\tau(x_0), x_0) \tag{70}$$

We substitute expression (70) into the equation (61), then we get expression of the matrix $\mathcal{DF}(x_0)$ as follows:

$$\mathcal{DF}(x_0) = (\mathcal{I}_{2n} - \frac{f(x(T_r(x_0)))\mathcal{C}_1}{\mathcal{C}_1 f(x(T_r(x_0)))})\Phi(T_r(x_0), x_0) - \mathcal{I}_{2n} \quad (71)$$

or under its simplified version

$$\mathcal{DF}(x_0) = (\mathcal{I}_{2n} - \frac{f^-\mathcal{C}_1}{\mathcal{C}_1 f^-})\Phi^+ - \mathcal{I}_{2n} \quad (72)$$

It is important to show that the Jacobian matrix of the Poincaré map $\mathcal{P}$ is defined as follows:

$$\mathcal{DP}(x_0) = (\mathcal{I}_{2n} - \frac{f^-\mathcal{C}_1}{\mathcal{C}_1 f^-})\Phi^+ \quad (73)$$

ANALYSIS OF THE COMPASS-TYPE BIPEDAL ROBOT'S PASSIVE WALK

The impulsive hybrid nonlinear system describing the compass-gait biped walker's walking dynamics is thought to be difficult to analyze and can produce complex appealing behaviors. The cascade of repeated period-doubling bifurcations and their consequent route to chaos is the most prevalent behavior revealed in the passive dynamic walking of the compass-gait bipedal walker as it moves down the walking surface. All circumstances must be taken into consideration in order to more accurately resemble humans especially the physically handicapped which are more and more apparent. When the knee is not in the middle of the leg, for instance, the length of the shank and the thigh are not equal, which shifts the center of gravity from its typical location. We shall analyze this situation by walking on various slope angles of surfaces. To achieve this, we will use bifurcation diagrams to demonstrate novel exhibited behaviors by changing two parameters: the length a of the lower-half segment of the two legs (see Figure 1) and the slope φ of the inclined walking surface.

Analysis via bifurcation diagrams

Complex exhibited behavior with respect to the slope angle φ

In this section, we adjust the slope angle φ of the walking surface and we calculate the new walking step of the compass biped robot while maintaining constant the other geometrical characteristic parameters listed in Table 1.

A conventional bifurcation diagram is shown in Figure 2(a) that illustrates the period-doubling scenario exhibited for the parameter $a = 0.5$. The diagram starts with a 1-periodic behavior for φ values between 0° and 4.385°, then changes to a 2-periodic behavior as indicated by the two red arrows, then to a 4-periodic gait, to a 8-periodic gait, and so on, until reaching chaos, which is framed in green.

Similarly, and by fixing another value of the parameter $a = 0.87$, we obtain the bifurcation diagram in Figure 2(b). This diagram shows a period-doubling phenomenon as a route to chaos. Such scenario begins at the value $\varphi = 7.552^\circ$ and doubles until chaos, and ends with the fall of the bipedal robot (for $\varphi \approx 11^\circ$). The difference between the two first diagrams (Figure 2(a) and Figure 2(b)) is that for $a = 0.87$, the biped robot's passive gait returns to another periodic behavior to start another period-doubling scenario to chaos instead of falling after the initial formation of chaos, as it has been occurred in Figure 2(a). This new period-doubling scenario will be finished around the value of $\varphi = 9.864^\circ$. This phenomenon reveals the appearance of periodicity window that was born within the chaotic regime contrary to the bifurcation diagram in Figure 2(a).

Furthermore, for the parameter $a = 0.881$, we observe from Figure 2(c) that the band of φ-values in which chaos occurs is quite narrow, which is another feature that is revealed. Such band occurs between $\varphi = 10.79$ and $\varphi = 10.93$. That is to say, as soon as chaos sets in, the robot falls fairly quickly.

Figure 2(d) illustrates a different kind of bifurcation scenario and then another phenomenon. It is found that the period doubles from 1-periodic to 2-periodic to 4-periodic up to 8-periodic behavior. After that, a remerging-period bifurcation is developed before going back to one-periodic behavior. The bipedal robot falls down at the point $\varphi = 12.21^\circ$, shortly after the Neimark-Sacker bifurcation (NSB), which will be clearer in the next diagram.

In Figure 2(e), and for the parameter $a = 0.895$, the period-doubling schema has been changed and reduced to a single period-doubling bifurcation follows by another one. Thus, the 1-periodic gait is bifurcated into a 2-periodic gait and it returns again to the 1-periodic gait via the period-doubling bifurcation. Thus, by increasing the bifurcation parameter φ, a Neimark-Sacker bifurcation is hence produced giving rise to the formation of a quasi-periodic behavior. Further analysis of this Neimark-Sacker bifurcation will be realized in the sequel.

In the bifurcation diagram of Figure 2(f) depicted for $a = 0.95$, only the period-1 passive gait was observed. Moreover, the single and attractive element in this bifurcation diagram is the zoomed-out red-circled part that reveals occurrence of the Neimark-Sacker bifurcation. As in Figure 2(e), this bifurcation demonstrates how, for $\varphi = 7.7^\circ$, the behavior changes from a 1-periodic to quasi-periodic. The quasi-periodic behavior occurs in a very small interval of slopes, which is not clear in the bifurcation diagram of Figure 2(f), compared to that in Figure 2(e).

Complex exhibited behavior with respect to the lower-leg segment length a

In this part, we maintain the other geometrical properties stated in the Table 1 while adjusting the lower-leg segment length a and calculating the new walking stride of the compass biped robot. The simulation results for different values of the bifurcation parameter a are illustrated in Figure 3.

It can be reported from the bifurcation diagrams in Figure 3 that every minor change in the value of the parameter a can result in a significant change in the walking behavior of the compass robot. Moreover, in all these bifurcation diagrams in Figure 3, the passive gaits exhibit a 1-periodic behavior for the values of a greater than the value 0.5°.

A single period-doubling bifurcation from 1-periodic gait to 2-periodic gait is seen in Figure 3(a) for $\varphi = 0.1^\circ$. In the other diagrams, it gradually alters.

Figure 3(b) shows the exhibited phenomenon for $\varphi = 0.54^\circ$ and demonstrates how the robot's behavior or step period changes from 2-periodic to 4-periodic as a result of the emergence of tiny bubbles.

For $\varphi = 0.56^\circ$ in Figure 3(c), the periodicity is clearly obvious. The bipedal robot falls down as a result of the Neimark-Sacker bifurcation at the end of this period doubling.

Figure 3(d) depicts further bubbles that form within these final ones. In the center of these bubbles, we notice a 16-periodic behavior. It is therefore pretty obvious that within these bubbles and by raising the value of φ, we find a period doubling that can lead to chaos, as shown in Figure 3(e) for $\varphi = 0.6^\circ$, followed by a remerging-period bifurcation to go back to 2-periodic, which finishes at the Neimark-Sacker bifurcation. A classical period-doubling bifurcation from 1-periodic gait to chaotic one can be seen in Figure 3(f) for the parameter $\varphi = 0.61^\circ$.

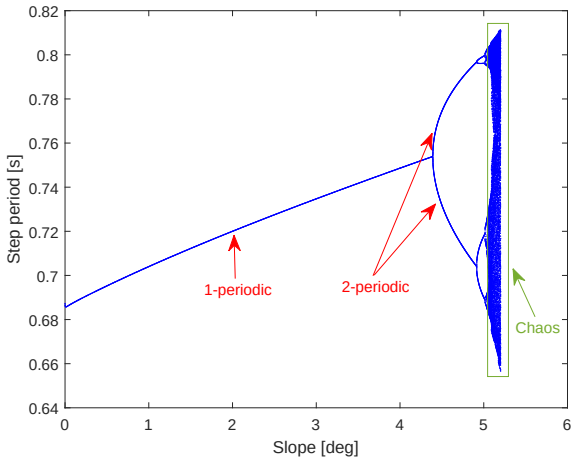

(a) $a = 0.5$

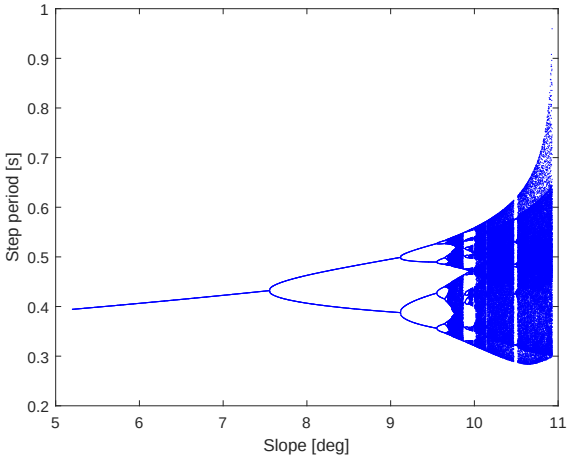

(b) $a = 0.87$

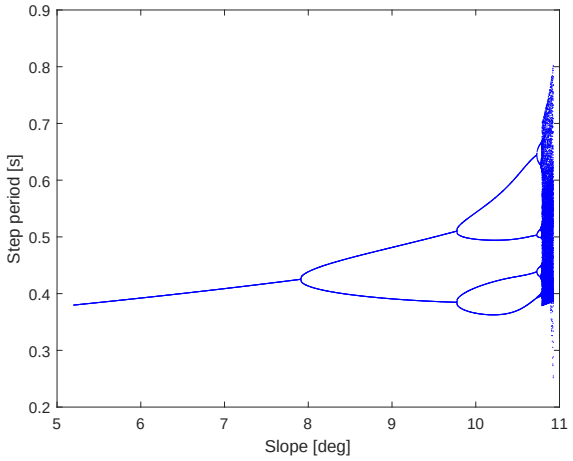

(c) $a = 0.881$

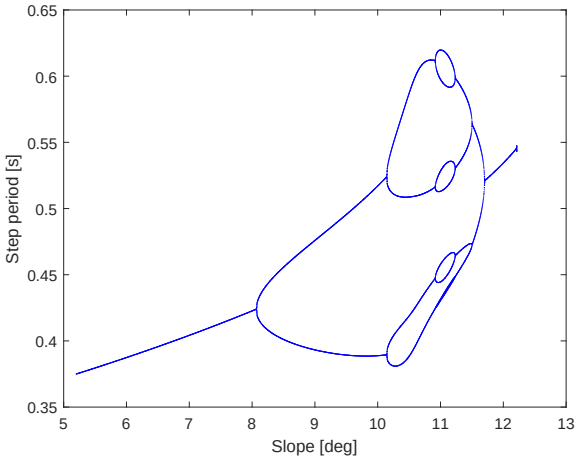

(d) $a = 0.8846$

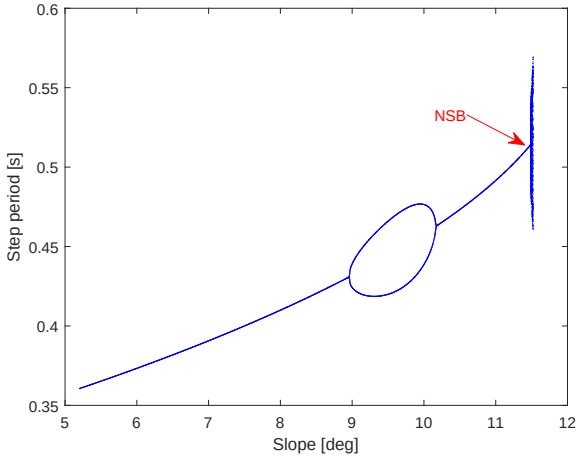

(e) $a = 0.895$

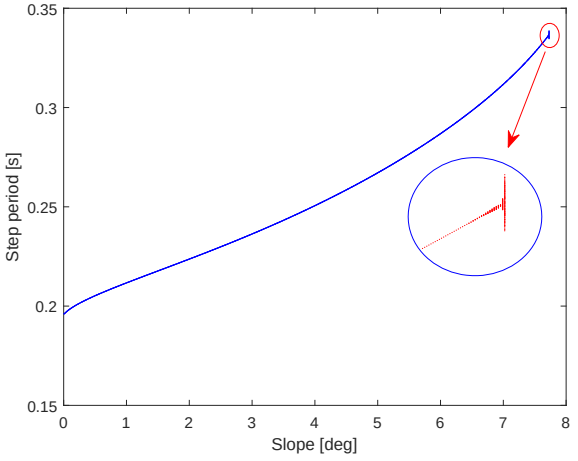

(f) $a = 0.95$

Figure 2 Bifurcation diagrams of the step period of the bipedal's walking plotted by varying the slope angle φ for (a) $a = 0.5$ showing the classical period-doubling bifurcation (PDB) route from 1-periodic to chaos, (b) for $a = 0.87$ showing the PDB with a large part of chaos containing bifurcation/periodicity windows, (c) for $a = 0.881$ showing also the PDB with a compass robot that falls down quickly after chaos, (d) for $a = 0.8864$ showing succession of the PDB and the remerging-period bifurcation followed by the Neimark-Sacker bifurcation (NSB), (e) for $a = 0.895$ showing a bubble that is the result of the 1-PDB and the 1-remerging-period bifurcation also followed by the NSB in a wide interval, and (f) for $a = 0.95$ showing the NSB.

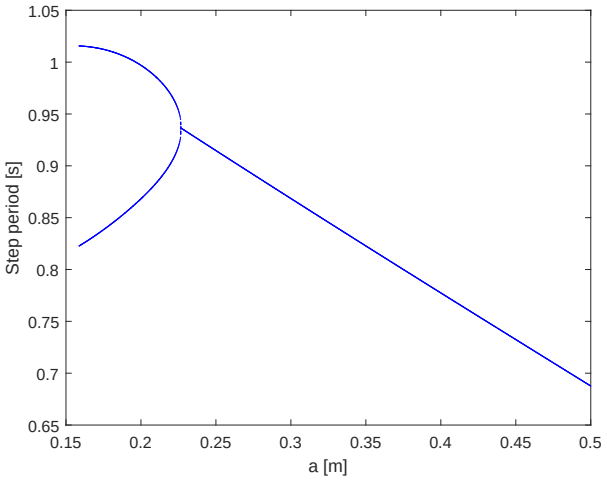

(a) $\varphi = 0.1^\circ$

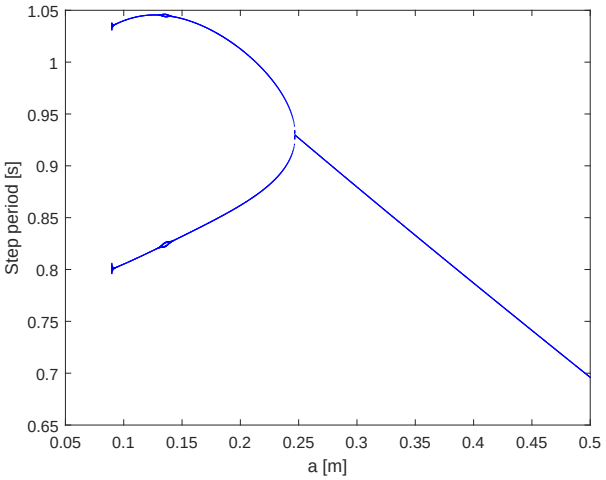

(b) $\varphi = 0.54^\circ$

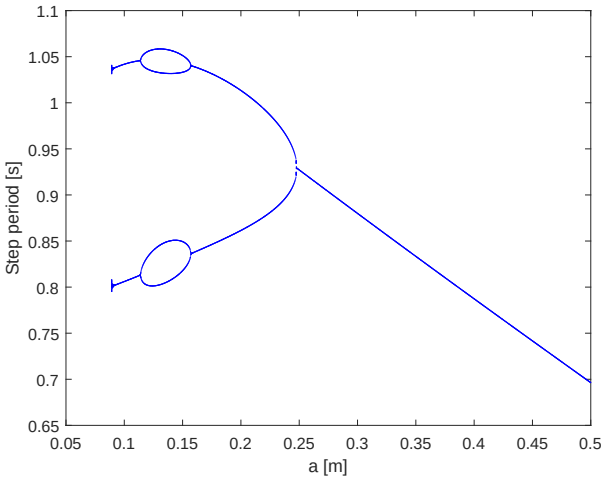

(c) $\varphi = 0.56^\circ$

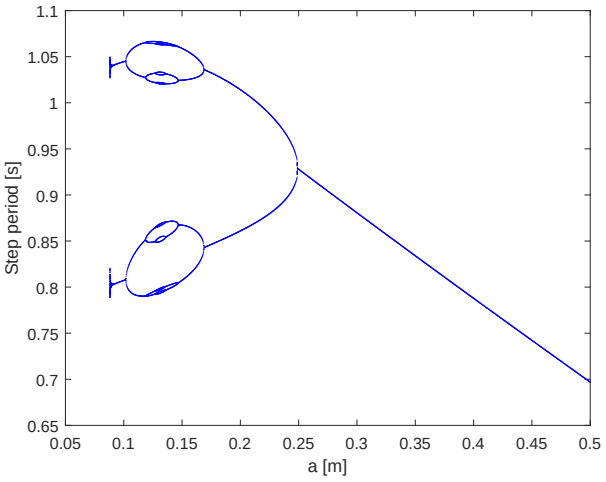

(d) $\varphi = 0.59^\circ$

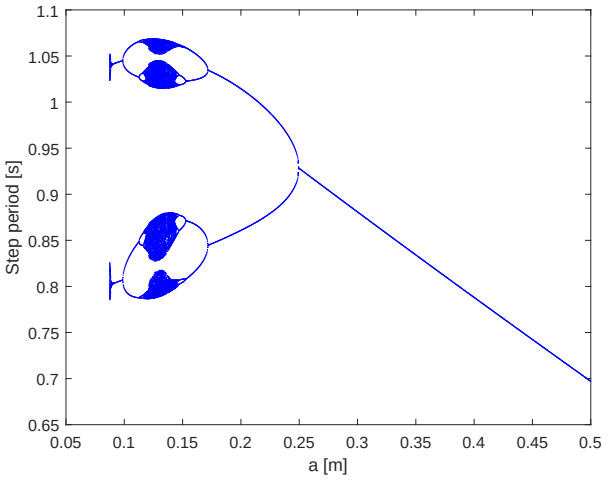

(e) $\varphi = 0.6^\circ$

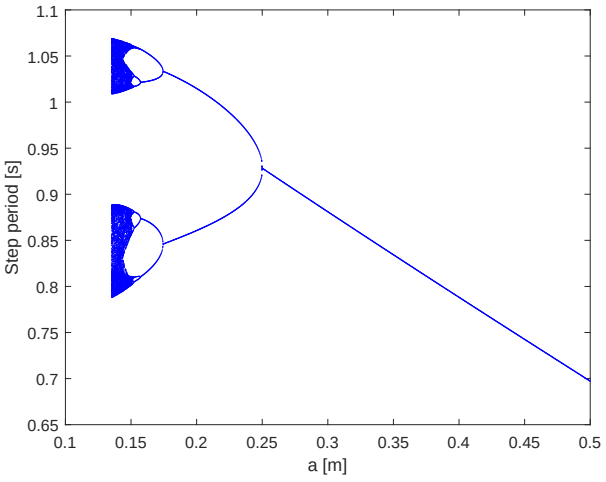

(f) $\varphi = 0.61^\circ$

Figure 3 Bifurcation diagrams plotted by varying the lower-leg segment length a for (a) $\varphi = 0.1^\circ$ showing the 1-PDB, (b) for $\varphi = 0.54^\circ$, (c) for $\varphi = 0.56^\circ$, (d) for $\varphi = 0.59^\circ$, (e) for $\varphi = 0.6^\circ$ showing the succession of the PDB route to chaos and the remerging-period bifurcation from chaos followed by the NSB, and (f) for $\varphi = 0.61^\circ$ showing the PDB ended by the fall of the bipedal robot.

Remark 1 *In addition to the step period, there are other descriptors of the passive dynamic walking of bipedal robots such as the step length, the average speed of each walking step, the mechanical energy, the angular positions and angular velocities just after/before the impact event with the ground (Goswami et al. 1996, 1998). The study of the apex can refer to the complexity of the bipedal walking as in (Gupta and Kumar 2017; Xie et al. 2020). The study of the apex consists in seeking the maximum position of the hip that can be reached by the biped robot while walking. Thus, such maximum position is such that the vertical speed of the hip is zero.*

It is straightforward to find that the vertical position of the hip of the compass robot is defined by the following expression:

$$z_{hip} = l\cos(\theta_s) \tag{74}$$

Thus, the vertical speed of the hip is defined as follows:

$$\dot{z}_{hip} = -l\dot{\theta}_s \sin(\theta_s) \tag{75}$$

Therefore, to obtain a zero vertical speed of the hip, we should have $\dot{z}_{hip} = 0$*, and then we should obtain:*

$$\dot{\theta}_s \sin(\theta_s) = 0 \tag{76}$$

Obviously, either $\sin(\theta_s) = 0$ *or* $\dot{\theta}_s = 0$ *to verify equality constraint (76). Relying on the structure of the compass robot, only the angular position* $\theta_s = 0$ *is realizable. Moreover, the angular position of the stance leg is always in variation as seen in the attractors in Figure 9. It can be seen that the angular velocity of the stance leg is always negative (*$\dot{\theta}_s < 0$*). Therefore, the angular velocity of the stance leg* $\dot{\theta}_s$ *cannot be 0. Hence, the only feasible solution that verifies the equality condition (76) is:*

$$\theta_s = 0 \tag{77}$$

Then, we should look for the descriptors of the passive bipedal walking of the compass robot such that the condition (77) is satisfied. Actually, this equality constraint (77) defines a new Poincaré section on which we look for new observation of the dynamics of the bipedal walking of the compass robot. Figure 4 shows two bifurcation diagrams revealing the complex behavior of the passive bipedal walking of the compass robot at its apex position while varying the slope angle φ *and with* $a = 0.5$*. Figure 4(a) reveals the walking time, whereas Figure 4(b) illustrates the angular velocity of the stance leg at the apex position. Notice that for* $a = 0.5$*, the bifurcation diagram at the impact of the swing leg with the ground was given by Figure 2(a) with* $a = 0.5$*. It is clear that by comparing the bifurcation diagram in Figure 2(a) with that in Figure 4(a), the behavior is almost similar, where the classical period-doubling route to chaos was revealed. However, in Figure 4(a), the (median) walking time at the apex position is almost constant while varying the slope angle* φ*. In contrast, in Figure 2(a), the (median) step period increases with respect to the increase of the slope* φ*. This result shows that the swing phase that happens just after the apex becomes longer by increasing the slope parameter* φ*.*

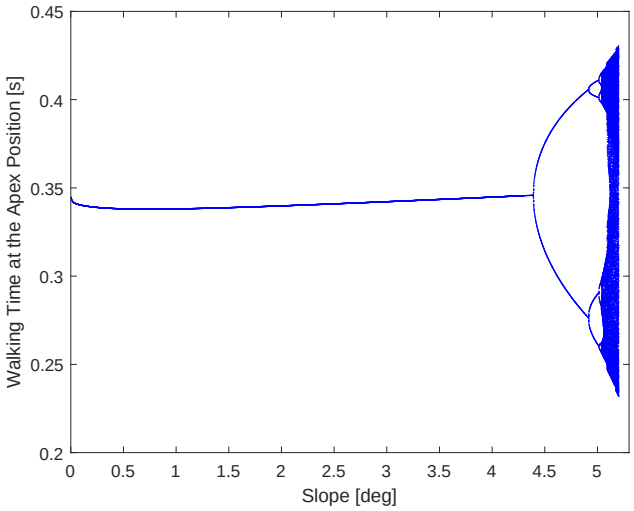

(a) $a = 0.82$

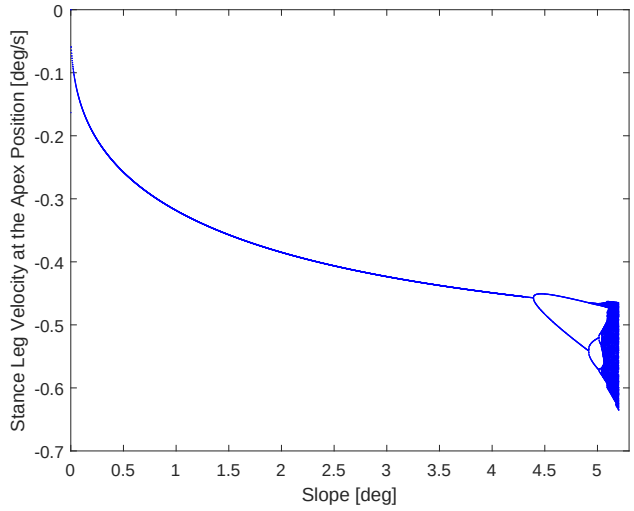

(b) $a = 0.83$

Figure 4 Bifurcation diagrams revealing the behavior of the bipedal walking at the apex position of the compass robot: (a) the walking time, and (b) the angular velocity of the stance leg. Here, the bifurcation parameter is the slope angle φ and the other parameter a was fixed to the nominal value $a = 0.5$.

Analysis of complex and strange behaviors

Figure 5, which is an addition to the previous section's illustrations, reveals a different phenomenon. By comparing the two figures, it seems that they are identical, with the exception that in Figure 5(a), there is some missing component that was present in Figure 5(b) and that was disappeared at the value $\varphi = 9.008°$ in Figure 5(a).

The same previous observation can be seen in Figure 6 by considering the bifurcation parameter a. For $\varphi = 0.605°$, the passive gait shows a classical period-doubling route to chaos, as seen in Figure 6(a). This exhibited behavior ends at the value $a = 0.133$, which provokes the fall of the bipedal robot. However, by slightly decreasing the value of the slope angle to $\varphi = 0.604°$, we see a completely different phenomenon. Indeed, a period-doubling route to chaos was first generated by decreasing the bifurcation parameter a. By decreasing further a, an inverse period-doubling scenario from chaos to a period-2 gait was observed. This period-2 gait was disappeared at the value $a = 0.0877$.

Accordingly, a very slight change in the value of the slope φ induces an almost different bifurcation diagram by varying the parameter a. As in Figure 5 by moving from the value $a = 0.83$ to $a = 0.82$ and where a complete part of the bifurcation diagram was disappeared, in Figure 6 and by changing/increasing the value of the slope from $\varphi = 0.604°$ to $\varphi = 0.604°$, a complete part of the bifurcation diagram was also disappeared without any explanation.

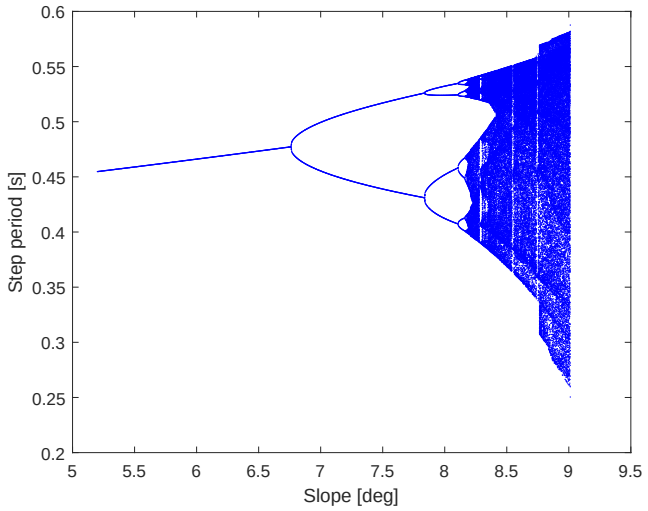

(a) $a = 0.82$

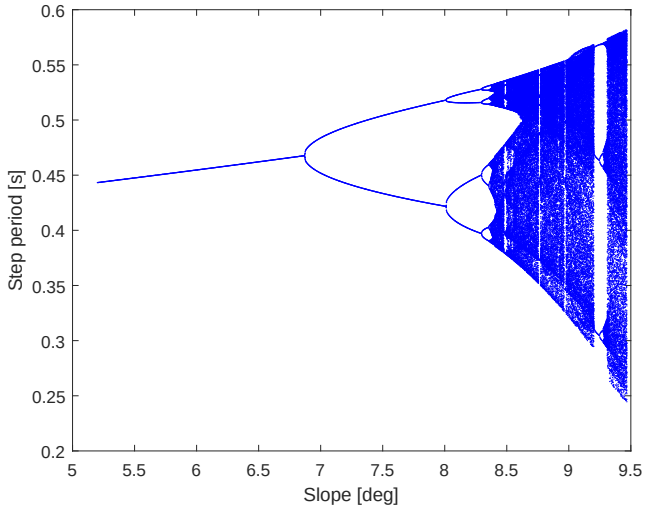

(b) $a = 0.83$

Figure 5 Bifurcation diagrams of the step period plotted by varying the slope angle φ for (a) $a = 0.82$ and (b) $a = 0.83$, showing the large variation of the step period (walking behavior) with respect to a tiny variation of the parameter a, which confirms the chaotic/strange nature of the passive walking dynamics of the compass bipedal robot. A large periodicity window appears in the bifurcation diagram (b). Such window and the result behavior leading to the formation of chaos was not observed in the bifurcation diagram (a).

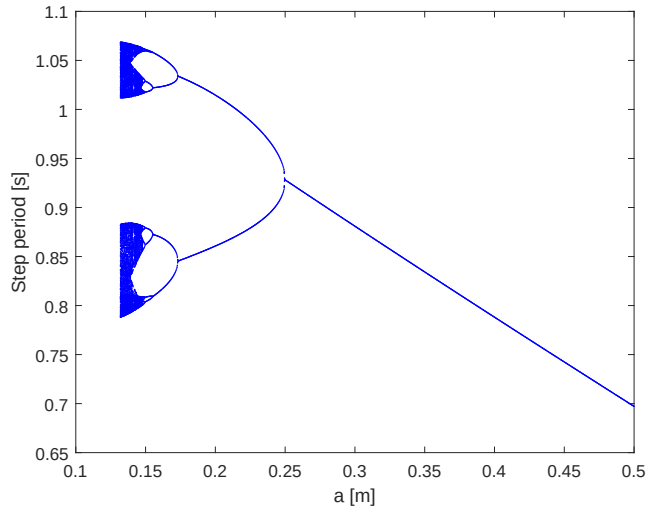

(a) $\varphi = 0.605^\circ$

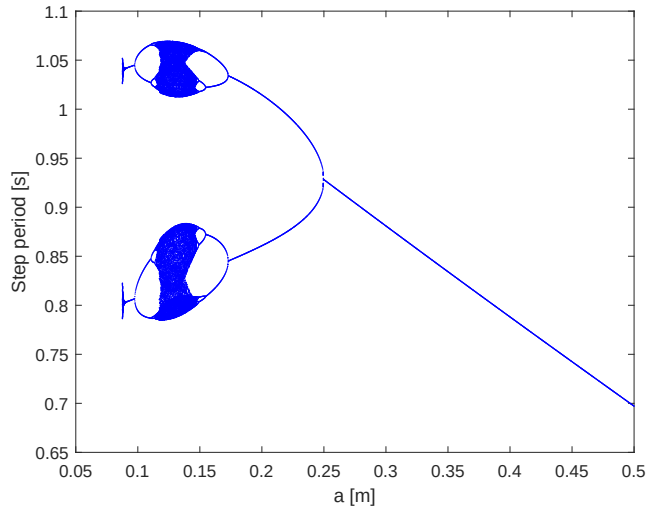

(b) $\varphi = 0.604^\circ$

Figure 6 Bifurcation diagrams of the step period plotted by varying the parameter a for (a) $\varphi = 0.605^\circ$ and (b) $\varphi = 0.604^\circ$, showing the sudden disappearance of some region/part of steady gaits of the passive compass robot. Such disappeared part is that located at the left side of the bifurcation diagram revealing the period-remerging scenario from chaos to the period-2 gait to the quasi-periodic gait. Such abrupt disappearance of these phenomena was occurred under a small variation of the slope angle φ.

Analysis via the characteristic multipliers

In addition to the stable solutions shown in the bifurcation diagram of Figure 5(a), we also presented the unstable solutions in the same plot as seen in Figure 7(a). These unstable solutions were represented by a dotted magenta line with the designation p1-ULC, which began at the first period-doubling bifurcation at the value of $\varphi = 6.771^\circ$. This shaky solution comes to an end at or near the value of $\varphi = 18^\circ$. The persistence of this unstable solution long after the biped robot has fallen suggests the presence of additional isolated components, which are depicted in Figure 5(b).

Figure 7(b) shows the evolution of the eigenvalues of the Jacobian matrix of the Poincaré map calculated via expression (71). This diagram in Figure 7(b) provides a strong support for this previous observation. We can see that the green eigenvalue takes values above the value 1, which is shown by a dotted line in black. Note that the value $\varphi = 6.771^\circ$ marks the birth of the bifurcation. This eigenvalue continues to vary even after the end of chaos at the value of $\varphi = 9.01^\circ$, which reveals the continued appearance of solutions but that is evident that they are unstable. According to the stability condition, as long as the characteristic multipliers lie inside the unit circle, the periodic solution is asymptotically stable. As φ is increased, a real characteristic multiplier moves out of the

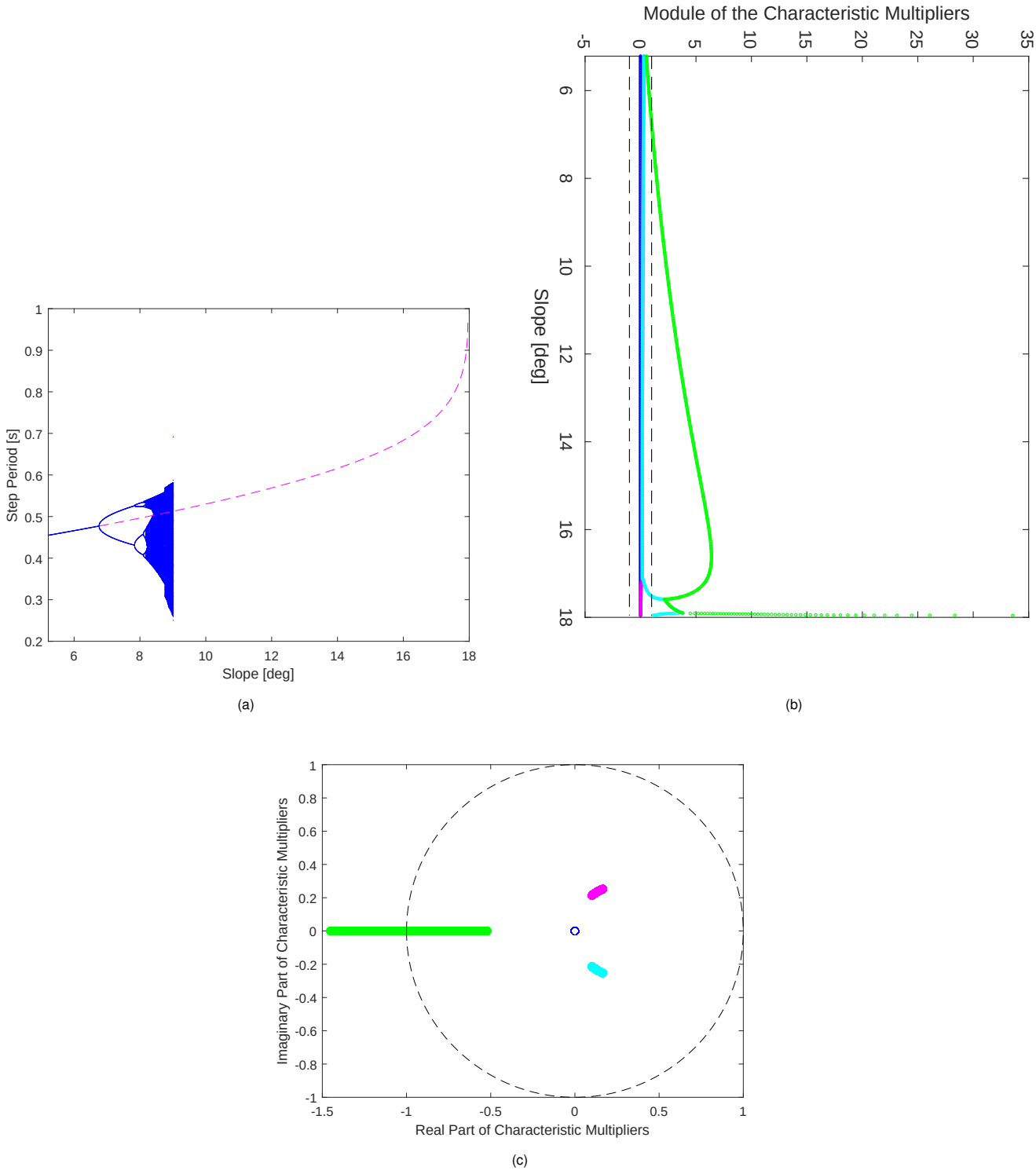

Figure 7 (a) Bifurcation diagram of the step period for $a = 0.82$ by varying the slope angle φ showing the period-1 unstable limit cycle (marked as p1-ULC), (b) Variation of the module of the eigenvalues of the Jacobian matrix of the Poincaré map, and (c) Variation of the loci of the characteristic multipliers with respect to the unit circle, as varying the slope angle φ for the fixed parameter $a = 0.82$.

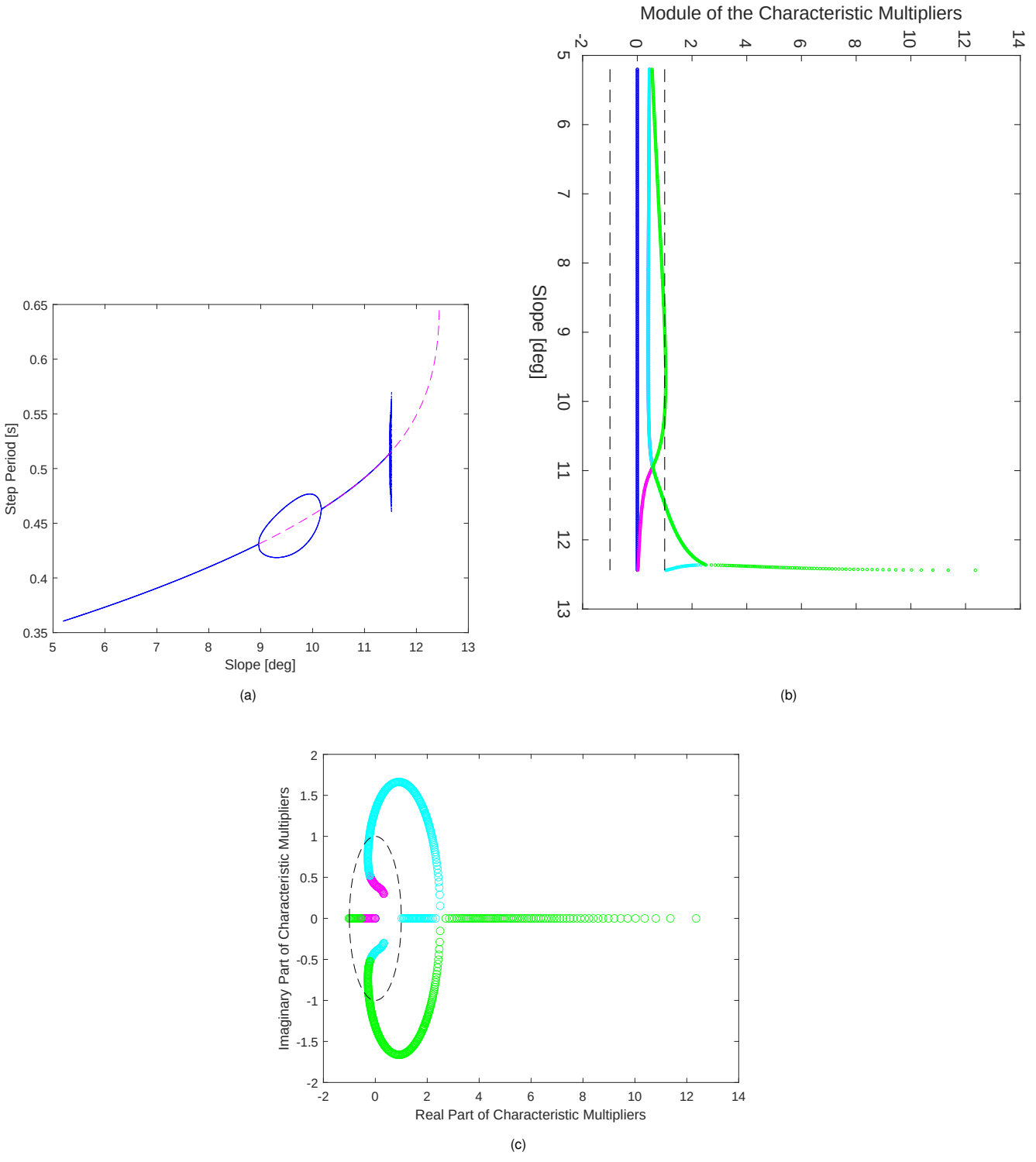

Figure 8 (a) Bifurcation diagram of the step period for the fixed parameter $a = 0.895$ by varying the slope angle φ showing the period-1 unstable limit cycle, (b) Variation of the module of the Jacobian matrix eigenvalues of the Poincaré map, and (c) Variation of the loci of the characteristic multipliers with respect to the unit circle, as varying the slope angle φ for $a = 0.895$.

unit circle through -1, indicating a period-doubling bifurcation. We observe in Figure 7(a) that the green eigenvalue leaves the unit circle via the real axis via the point -1, to mark hence the appearance of the period-doubling bifurcation and hence the beginning of the period-doubling scenario.

In Figure 8(a), we added the unstable solutions to the diagram that is shown in Figure 2(e) with a dashed magenta line. We see that the stable solution ends with a Neimark-Sacker bifurcation, but the diagram continues to evolve with unstable solutions until $\varphi = 12.44^\circ$. This Neimark-Sacker bifurcation is presented by the two eigenvalues green and cyan which take values greater than 1 in Figure 8(b), which presents the module of the eigenvalues of the Jacobian matrix of the Poincaré map. To show the Neimark-Sacker bifurcation well, we have presented the loci characteristic multipliers in Figure 8(c) where we see the location and variation of all the eigenvalues with respect to the unit circle.

Analysis through attractors

From a certain initial condition and for a set of parameters φ and a, the trajectory of the compass bipedal robot finally settles into an attractor state (in the state space). It can be a straightforward equilibrium point, a periodic trajectory (represented by a limit cycle in the phase plane or a some distinct points in the Poincaré section), a quasi-periodic trajectory (represented by a torus in the phase plane or a closed curve (like a closed circle) in the Poincaré section), or a strange/chaotic attractor, which is a type of trajectory on which a system moves from one situation to another without ever settling.

Attractors in the phase plane

Examples of periodic attractors in the phase plane and for different values of the two parameters a and φ, are shown in Figure 9(a), Figure 9(b), Figure 9(c), Figure 9(d) and Figure 9(e). They present respectively a 1-periodic attractor represented by a single closed trajectory, a 2-periodic attractor, a 4-periodic attractor, a 6-periodic attractor and an 8-periodic attractor.

We stated that the first attractor in Figure 9(a) plotted for $\varphi = 4^\circ$ clearly demonstrates that the step period of the biped robot's locomotion for $a = 0.5$ is 1-periodic as shown by a red arrow in Figure 2(a). The same remark for the second 2-periodic attractor of Figure 9(b), which supports the findings in Figure 2(b) for all the values of the parameter φ between 8.944° and 10.19° for $a = 0.895$ inside the bubble. The 4-periodic shape of Figure 9(c) is the attractor of the 4-periodic behavior of the compass-type bipedal robot shown in Figure 2(d) for $a = 0.8846$ and for the values of φ between 10.5° and 10.92°. The 6-periodic attractor in Figure 9(d) exhibited for $a = 0.87$ and $\varphi = 10.48^\circ$ reveals the 6-periodic behavior of the compass robot presented in Figure 2(b). For $a = 0.881$, which is comparable to what is depicted in Figure 2(c), we depict in Figure 9(e) an 8-periodic attractor.

Examples of chaotic attractors are shown in Figure 10(a), Figure 10(b), Figure 10(c) and Figure 10(d). All these diagrams present chaotic attractors, which are characterized by an infinity of unstable limit cycles embedded within it. These figures support what was reported about the bifurcation diagrams in the previous subsection.

Attractors in the Poincaré section

A useful methodology for investigating dynamic systems, such as the bipedal compass robot, is the Poincaré section. We concentrate on certain location along the system's trajectory that correlates to the point where the trajectory meets the hyperplan, which is the Poincaré section, rather than the continuous trajectory where the attractor is traced in the plane phase. For instance, if we have a 1-periodic behavior, we find a single point at which the 1-period trajectory intersects the Poincaré section. If we have a 2-periodic behavior, we find 2 points at which the system's trajectory intersects with the Poincaré section

We notice new shapes for the attractors in the Poincaré section in Figure 11. Due to the infinite number of points, a chaotic attractor is shown in the first plot in Figure 11(a). Additionally, Figure 11(b) displays an infinite number of points, but they all diverge outward, which is what attracts the behavior that is almost periodic due to the Neimark-Sacker bifurcation (NSB).

Analysis via Lyapunov exponents

The calculation of Lyapunov exponents is a numerical method that proves the existence of bifurcation in nonlinear dynamical systems. Moreover, they reveal the sensitive dependence of the dynamic system on neighboring initial conditions. Furthermore, the sign of the largest Lyapunov exponents demonstrates the type of the generated attractor, which can be either periodic or quasi-periodic or chaotic.

The computation of the spectrum of Lyapunov exponents for continuous-time as well as discrete-time dynamical systems has been widely investigated in several research works. A nonlinear dynamic system of dimension n has n Lyapunov exponents and for a smooth nonlinear dynamical system, the computation of the Lyapunov exponents becomes classic nowadays. For the hybrid impulsive nonlinear dynamics of the passive compass bipedal robot, and since the dimension of the state vector x is 4, then we have 4 Lyapunov exponents. Nevertheless, because of the impulsive and hybrid feature of the bipedal dynamics (17) of the passive compass robot, the computation of the Lyapunov exponents is complicated (Gritli and Belghith 2015, 2016a; Gritli *et al.* 2012). The calculation of the spectrum of Lyapunov exponents depends chiefly on the jump matrix $\mathcal{S}(x^+, x^-)$ that was defined by expression (49), and then on the fundamental solution matrix $\Phi^+(t, x_0)$. The computation of the spectrum of Lyapunov exponents for the passive compass bipedal robot and also for the semi-passive torso-driven bipedal robot has been achieved previously in (Gritli *et al.* 2012) and also using the explicit analytical expression of the controlled hybrid Poincaré map (Gritli and Belghith 2015, 2016a).

The variation of the four Lyapunov exponents λ_1, λ_2, λ_3, and λ_4 is shown in Figure 12(a) by adopting the lower-leg segment length $a = 0.5$ and then by varying the slope parameter φ from the value 4°. Evolution of the two largest Lyapunov exponents λ_1 and λ_2 with respect to φ is depicted in Figure 12(b). The largest Lyapunov exponent λ_1 is presented in blue whereas λ_2 is colored in red. When λ_1 takes the value 0 and while the other exponents are negative for the slope angle φ varies between 4° and 5.03°, this situation indicates hence that the passive bipedal walking of the compass robot is periodic. As it was presented in Figure 2(a), and for this same interval of the values of φ, we have a period doubling schema towards chaos. In Figure 12, this period-doubling scenario is presented by a succession of parabolic shapes formed by the two Lyapunov exponents λ_2 and λ_3. Each intersection of the second exponent λ_2 with the first one λ_1 i.e. with the value of 0, indicates the presence of a period-doubling bifurcation.

For the values of $\varphi > 5.03^\circ$ and referring to Figure 2(a), chaos starts to happen. In Figure 12, this complex behavior is presented by a positive value of the largest Lyapunov exponent λ_1. As φ increases, λ_1 increases as well. Furthermore, when the walking behavior is chaotic, the second Lyapunov exponent λ_2 takes the

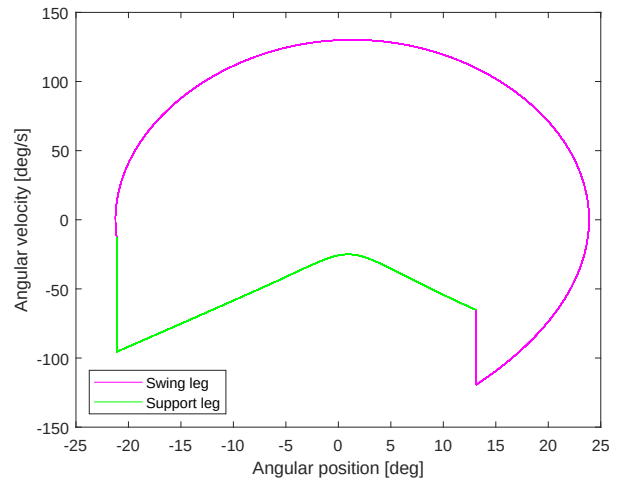

(a) 1-periodic attractor

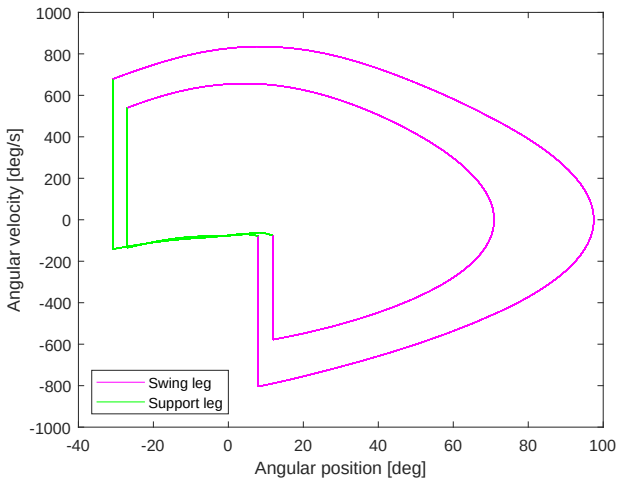

(b) 2-periodic attractor

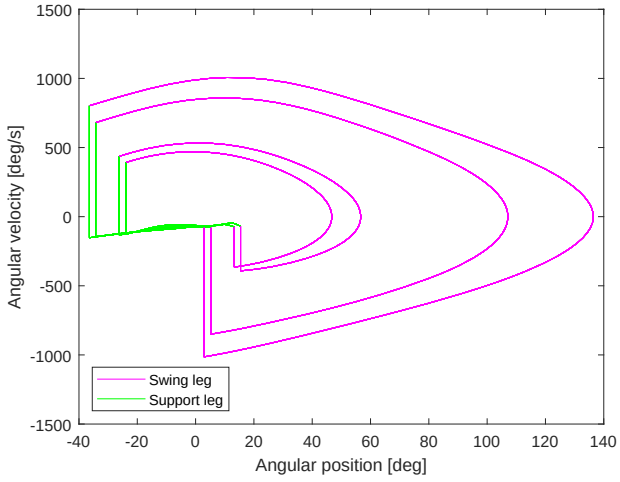

(c) 4-periodic attractor

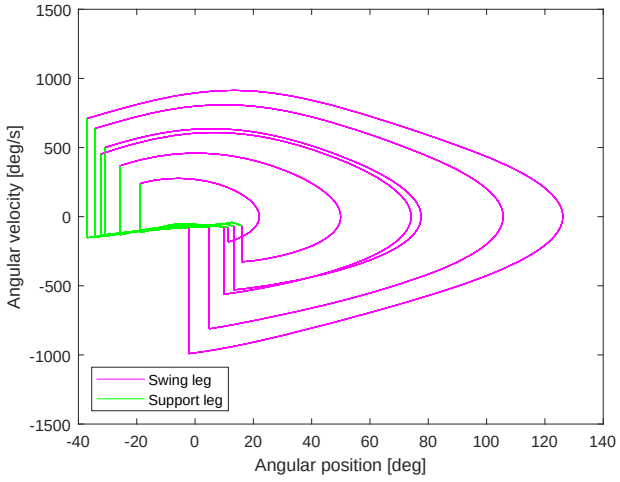

(d) 6-periodic attractor

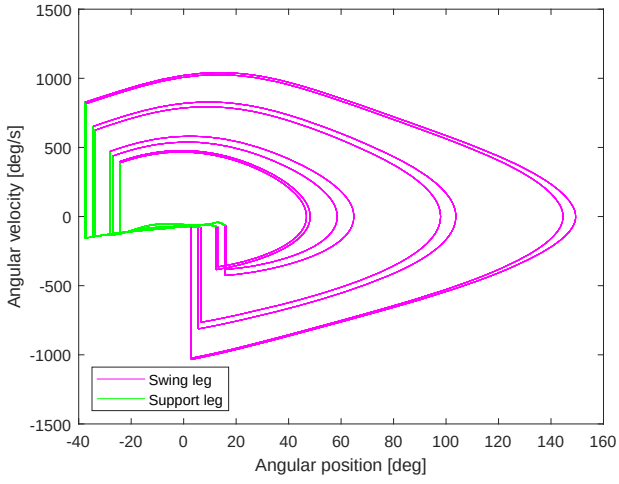

(e) 8-periodic attractor

Figure 9 Attractors in the phase plane: (a) A 1-periodic attractor for $a = 0.5$ and $\varphi = 4^\circ$, (b) A 2-periodic attractor for $a = 0.895$ and $\varphi = 9.5^\circ$, (c) A 4-periodic attractor for $a = 0.8846$ and $\varphi = 10.5^\circ$, (d) A 6-periodic attractor for $a = 0.87$ and $\varphi = 10.48^\circ$, and (e) An 8-periodic attractor for $a = 0.881$ and $\varphi = 10.75^\circ$.

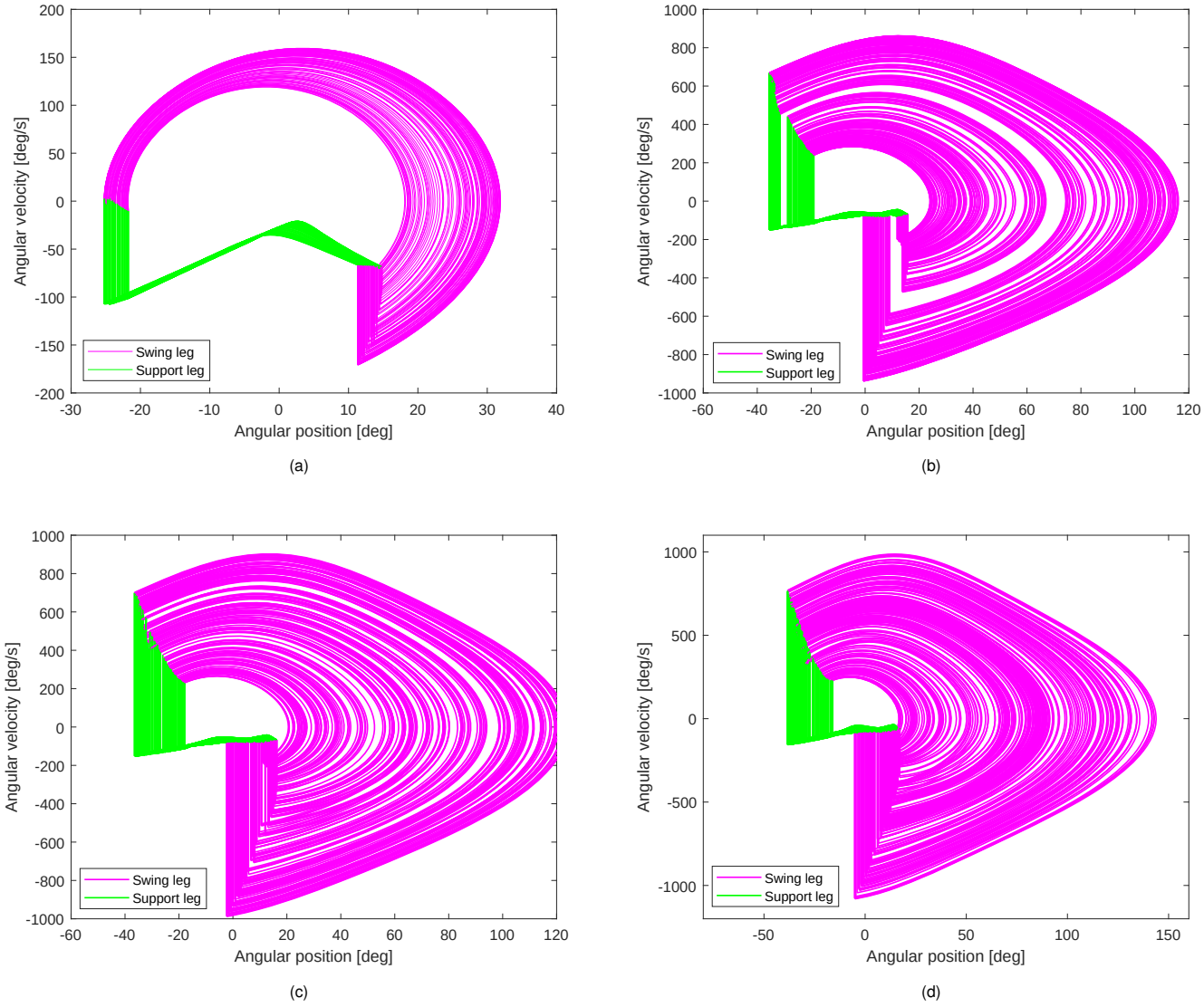

Figure 10 Chaotic attractors in the phase plane for (a) $a = 0.5$ and $\varphi = 5.2°$, (b) $a = 0.87$ and $\varphi = 9.85°$, (c) $a = 0.87$ and $\varphi = 10.1°$, and (d) $a = 0.87$ and $\varphi = 10.6°$. The portrait in (a) reveals the classical chaotic attractor that was observed for the classical parameter $a = 0.5$. The other plots show that the chaotic attractor becomes larger by varying/increasing the slope angle φ.

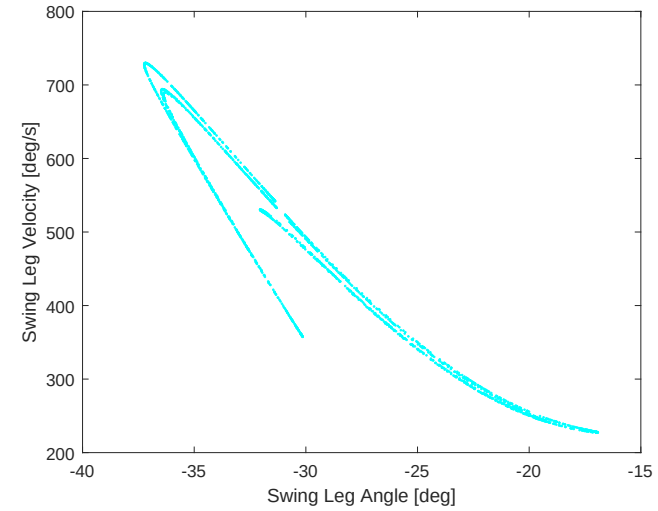

(a) A chaotic attractor

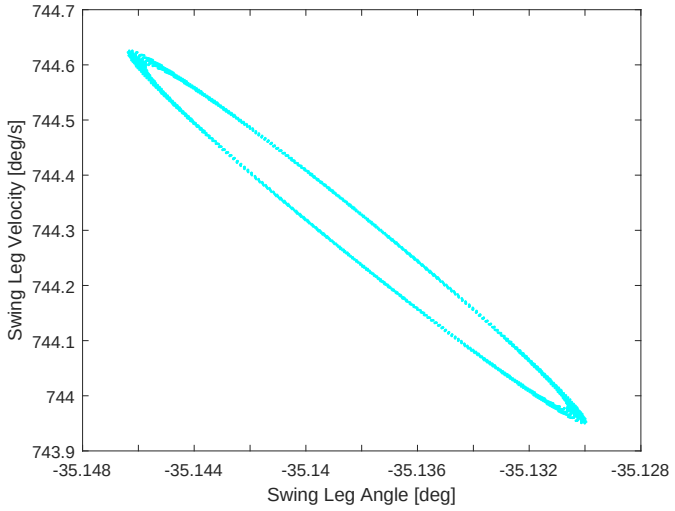

(b) A quasi-periodic attractor

Figure 11 Attractors in the Poincaré section for (a) chaotic attractor for $a = 0.87$ and $\varphi = 10.3°$, and (b) NSB attractor for$a = 0.8846$ and $\varphi = 12.21°$.

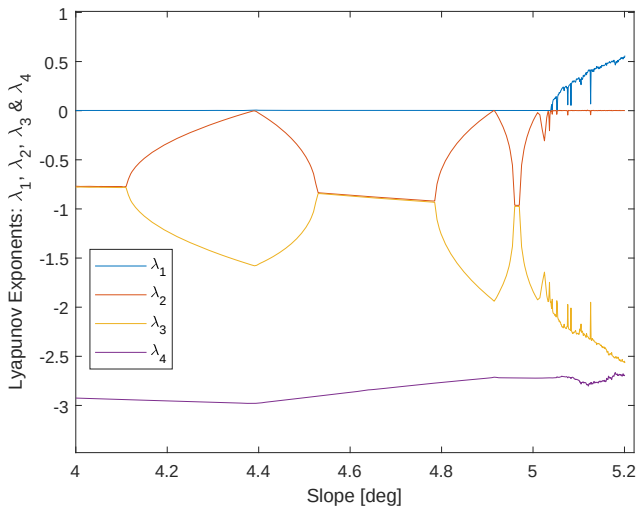

(a) $\lambda_1, \lambda_2, \lambda_3$ & λ_4

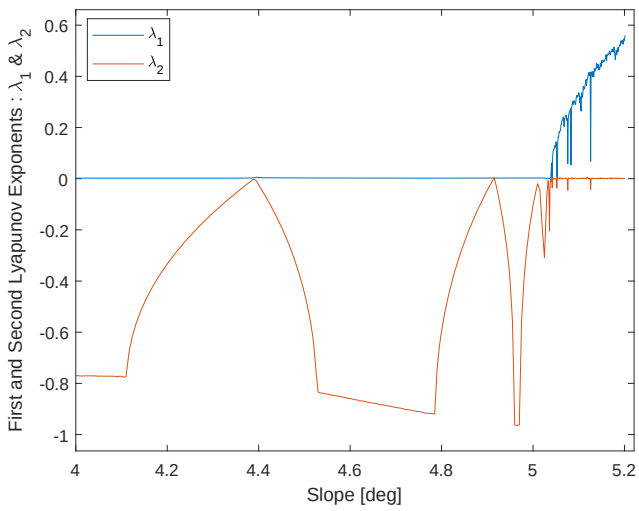

(b) λ_1 & λ_2

Figure 12 Variation of the Lyapunov exponents for $a = 0.5$ and by varying the slope angle of the walking surface φ from the value $4°$. (a) reveals the four Lyapunov exponents λ_1, λ_2, λ_3, and λ_4, whereas (b) shows the two largest Lyapunov exponents λ_1 and λ_2.

value 0, while the two other Lyapunov exponents λ_3 and λ_4 remain always negative.

It is important to note that within the chaotic regime, that is for $\varphi > 5.03°$, there are some fluctuations of the largest Lyapunov exponent λ_1 to zero. This behavior indicates the existence of periodicity windows inside the chaotic regime.

CONCLUSIONS

In this research study, we analyzed the passive gait of a planar biped robot using a motion that resembled a compass. We employed the bifurcation diagrams, the Poincaré sections, the phase planes and the variation of the characteristic multipliers to investigate the exhibited behaviors. Two different bifurcation parameters were considered: the parameter a which is the length of the lower leg segment and the parameter φ which is the slope angle of the inclined walking surface. We presented different simulation results to analyze the complex behavior of the passive dynamic bipedal walking of the compass robot. We demonstrated how the value of the parameter a can alter the stability and the overall behavior of the bipedal robot. We showed how the traditional period-doubling route to chaos can be transformed into a completely different behavior under some slight variation of the two parameters φ and a. In addition, we showed that the passive gait of the compass robot reveals the exhibition of the Neimark-Sacker bifurcation and hence the existence of the quasi-periodic passive gaits.

In our future research, the objective is to analyze the compass-gait walker's passive motion using the explicit analytical representation of the Poincaré map (Znegui *et al.* 2020a, 2021). In addition, our goal is to achieve an in-depth study of the Lyapunov exponents for different bifurcation diagrams and then for different scenarios that were presented in this paper.

Acknowledgments

The authors would like to thank the Ministry of Higher Education and Scientific Research (Ministère de l'Enseignement Supérieur et de la Recherche Scientifique (MESRS)), Tunisia, for technical and financial support under the PEJC Project no. 20PEJC 06-02.

Availability of data and material

Not applicable.

Conflicts of interest

The authors declare that there is no conflict of interest regarding the publication of this paper.

LITERATURE CITED

Added, E. and H. Gritli, 2020a Control of the passive dynamic gait of the bipedal compass-type robot through trajectory tracking. In *2020 20th International Conference on Sciences and Techniques of Automatic Control and Computer Engineering (STA)*, pp. 155–162.

Added, E. and H. Gritli, 2020b Trajectory design and tracking-based control of the passive compass biped. In *2020 4th International Conference on Advanced Systems and Emergent Technologies (IC_ASET)*, pp. 417–424.

Added, E. and H. Gritli, 2022 Birth of the Neimark–Sacker bifurcation for the passive compass-gait walker. In *Advances in Nonlinear Dynamics*, edited by W. Lacarbonara, B. Balachandran, M. J. Leamy, J. Ma, J. A. Tenreiro Machado, and G. Stepan, pp. 683–697, Cham, Springer International Publishing.

Added, E. and H. Gritli, 2023 A further analysis of the passive compass-gait bipedal robot and its period-doubling route to chaos. In *New Perspectives on Nonlinear Dynamics and Complexity*, edited by D. Volchenkov and A. C. J. Luo, pp. 11–30, Cham, Springer International Publishing.

Added, E., H. Gritli, and S. Belghith, 2021a Additional complex behaviors, bifurcations and chaos, in the passive walk of the compass-type bipedal robot. IFAC-PapersOnLine **54**: 111–116, 6th IFAC Conference on Analysis and Control of Chaotic Systems CHAOS 2021.

Added, E., H. Gritli, and S. Belghith, 2021b Further analysis of the passive dynamics of the compass biped walker and control of chaos via two trajectory tracking approaches. Complexity **2021**: 5533451 (39 pages).

Added, E., H. Gritli, and S. Belghith, 2021c Further analysis of the passive walking gaits of the compass biped robot: Bifurcations and chaos. In *2021 18th International Multi-Conference on Systems, Signals & Devices (SSD)*, pp. 160–165.

Added, E., H. Gritli, and S. Belghith, 2022a Trajectory tracking-based control of the chaotic behavior in the passive bipedal compass-type robot. The European Physical Journal Special Topics **231**: 1071–1084.

Added, E., H. Gritli, and S. Belghith, 2022b Trajectory tracking control of the compass-type bipedal robot gait via an improved PD+ controller. In *2022 5th International Conference on Advanced Systems and Emergent Technologies (IC_ASET)*, pp. 482–488.

Akgul, A., S. Hussain, and I. Pehlivan, 2016 A new three-dimensional chaotic system, its dynamical analysis and electronic circuit applications. Optik - International Journal for Light and Electron Optics **127**: 7062 – 7071.

Andrievskii, B. R. and A. L. Fradkov, 2003 Control of chaos: Methods and applications. I. Methods. Automation and Remote Control **64**: 673–713.

Andrievskii, B. R. and A. L. Fradkov, 2004 Control of chaos: Methods and applications. II. Applications. Automation and Remote Control **65**: 505–533.

Aricioğlu, M. A. and O. N. Berk, 2022 A comparative proposal on learning the chaos to understand the environment. Chaos Theory and Applications **4**: 19 – 25.

Azar, A. T., C. Volos, N. A. Gerodimos, G. S. Tombras, V.-T. Pham, *et al.*, 2017 A novel chaotic system without equilibrium: Dynamics, synchronization, and circuit realization. Complexity **2017**: 7871467.

Bekey, G. A. and K. Y. Goldberg, 2012 *Neural networks in robotics*, volume 202. Springer Science & Business Media.

Beritelli, F., E. Di Cola, L. Fortuna, and F. Italia, 2000 Multilayer chaotic encryption for secure communications in packet switching networks. In *WCC 2000-ICCT 2000. 2000 International Conference on Communication Technology Proceedings (Cat. No. 00EX420)*, volume 2, pp. 1575–1582.

Boccaletti, S., C. Grebogi, Y.-C. Lai, H. Mancini, and D. Maza, 2000 The control of chaos: theory and applications. Physics Reports **329**: 103–197.

Boubaker, O. and S. Jafari, 2019 *Recent Advances in Chaotic Systems and Synchronization: From Theory to Real World Applications*. Emerging Methodologies and Applications in Modelling, Identification and Control, Elsevier, first edition.

Buscarino, A., C. Famoso, L. Fortuna, and M. Frasca, 2016 A new chaotic electro-mechanical oscillator. International Journal of Bifurcation and Chaos **26**: 1650161.

Chevallereau, C., G. Bessonnet, G. Abba, and Y. Aoustin, 2009 *Bipedal Robots: Modeling, Design and Walking Synthesis*. John Wiley & Sons, Wiley-ISTE, first edition.

Collins, S., A. Ruina, R. Tedrake, and M. Wisse, 2005 Efficient bipedal robots based on passive-dynamic walkers. Science **307**: 1082–1085.

Deng, K., M. Zhao, and W. Xu, 2017 Passive dynamic walking with a torso coupled via torsional springs. International Journal of Humanoid Robotics **13**: 1650024.

Fathizadeh, M., H. Mohammadi, and S. Taghvaei, 2019 A modified passive walking biped model with two feasible switching patterns of motion to resemble multi-pattern human walking. Chaos, Solitons & Fractals **127**: 83 – 95.

Fathizadeh, M., S. Taghvaei, and H. Mohammadi, 2018 Analyzing bifurcation, stability and chaos for a passive walking biped model with a sole foot. International Journal of Bifurcation and Chaos **28**: 1850113.

Ferreira, B. B., A. S. de Paula, and M. A. Savi, 2011 Chaos control applied to heart rhythm dynamics. Chaos, Solitons & Fractals **44**: 587–599.

Firth, W., 1991 Chaos–predicting the unpredictable. BMJ: British Medical Journal **303**: 1565.

Fradkov, A. L. and R. J. Evans, 2005 Control of chaos: Methods and applications in engineering. Annual Reviews in Control **29**: 33–56.

Fradkov, A. L., R. J. Evans, and B. R. Andrievsky, 2006 Control of chaos: Methods and applications in mechanics. Philosophical Transactions of The Royal Society A **364**: 2279–2307.

Garcia, M., A. Chatterjee, and A. Ruina, 2000 Efficiency, speed, and scaling of two-dimensional passive-dynamic walking. Dynamics and Stability of Sytems **15**: 75–99.

Garcia, M., A. Chatterjee, A. Ruina, and M. Coleman, 1998 The simplest walking model: Stability, complexity, and scaling. Journal of Biomechanical Engineering **120**: 281–288.

Goswami, A., B. Thuilot, and B. Espiau, 1996 *Compass-like biped*

robot. Part I: Stability and bifurcation of passive gaits, volume 2996. Technical Report, INRIA.

Goswami, A., B. Thuilot, and B. Espiau, 1998 Study of the passive gait of a compass-like biped robot: Symmetry and chaos. International Journal of Robotics Research **17**: 1282–1301.

Goswami, A. and P. Vadakkepat, 2019 *Humanoid Robotics: A Reference*. Springer Netherlands, first edition.

Grassi, G., 2021 Chaos in the real world: Recent applications to communications, computing, distributed sensing, robotic motion, bio-impedance modelling and encryption systems. Symmetry **2021**: 2151.

Grebogi, C., Y.-C. Lai, and S. Hayes, 1997 Control and applications of chaos. Journal of the Franklin Institute **334**: 1115–1146, Visions of Nonlinear Mechanics in the 21st Century.

Gritli, H. and S. Belghith, 2015 Computation of the Lyapunov exponents in the compass-gait model under OGY control via a hybrid Poincaré map. Chaos, Solitons & Fractals **81**: 172–183.

Gritli, H. and S. Belghith, 2016a Bifurcations and chaos in the semi-passive bipedal dynamic walking model under a modified OGY-based control approach. Nonlinear Dynamics **83**: 1955–1973.

Gritli, H. and S. Belghith, 2016b Displayed phenomena in the semi-passive torso-driven biped model under OGY-based control method: Birth of a torus bifurcation. Applied Mathematical Modelling **40**: 2946–2967.

Gritli, H. and S. Belghith, 2017a Walking dynamics of the passive compass-gait model under OGY-based control: Emergence of bifurcations and chaos. Communications in Nonlinear Science and Numerical Simulation **47**: 308–327.

Gritli, H. and S. Belghith, 2017b Walking dynamics of the passive compass-gait model under OGY-based state-feedback control: Analysis of local bifurcations via the hybrid Poincaré map. Chaos, Solitons & Fractals **98**: 72 – 87.

Gritli, H. and S. Belghith, 2018a Diversity in the nonlinear dynamic behavior of a one-degree-of-freedom impact mechanical oscillator under OGY-based state-feedback control law: order, chaos and exhibition of the border-collision bifurcation. Mechanism and Machine Theory **124**: 1–41.

Gritli, H. and S. Belghith, 2018b Walking dynamics of the passive compass-gait model under OGY-based state-feedback control: Rise of the Neimark–Sacker bifurcation. Chaos, Solitons & Fractals **110**: 158 – 168.

Gritli, H., S. Belghith, and N. Khraeif, 2012 Intermittency and interior crisis as route to chaos in dynamic walking of two biped robots. International Journal of Bifurcation and Chaos **22**: 1250056.

Gritli, H., S. Belghith, and N. Khraeif, 2015 OGY-based control of chaos in semi-passive dynamic walking of a torso-driven biped robot. Nonlinear Dynamics **79**: 1363–1384.

Gritli, H., N. Khraeif, and S. Belghith, 2011 Cyclic-fold bifurcation in passive bipedal walking of a compass-gait biped robot with leg length discrepancy. In *2011 IEEE International Conference on Mechatronics*, pp. 851–856.

Gritli, H., N. Khraeif, and S. Belghith, 2013 Chaos control in passive walking dynamics of a compass-gait model. Communications in Nonlinear Science and Numerical Simulation **18**: 2048–2065.

Gritli, H., N. Khraief, and S. Belghith, 2018 Complex walking behaviours, chaos and bifurcations of a simple passive compass-gait biped model suffering from leg length asymmetry. International Journal of Simulation and Process Modelling **13**: 446–462.

Grizzle, J. W., G. Abba, and F. Plestan, 2001 Asymptotically stable walking for biped robots: Analysis via systems with impulse effects. IEEE Transaction on Automatic Control **46**: 51–64.

Guanrong, C., 2021 Chaos theory and applications: a new trend. Chaos Theory and Applications **3**: 1–2.

Gupta, S. and A. Kumar, 2017 A brief review of dynamics and control of underactuated biped robots. Advanced Robotics **31**: 607–623.

Harrison, R. C., A. OLDAG, E. PERKİNS, *et al.*, 2022 Experimental validation of a chaotic jerk circuit based true random number generator. Chaos Theory and Applications **4**: 64–70.

Iqbal, S., X. Z. Zang, Y. H. Zhu, and J. Zhao, 2014 Bifurcations and chaos in passive dynamic walking: A review. Robotics and Autonomous Systems **62**: 889–909.

Jimenez, A., E. N. Sanchez, G. Chen, and J. P. Perez, 2009 Real-time chaotic circuit stabilization via inverse optimal control. International Journal of Circuit Theory and Applications **37**: 887–898.

Jun, M., 2022 Chaos theory and applications: the physical evidence, mechanism are important in chaotic systems. Chaos Theory and Applications **4**: 1–3.

Khraief Haddad, N., S. Belghith, H. Gritli, and A. Chemori, 2017 From hopf bifurcation to limit cycles control in underactuated mechanical systems. International Journal of Bifurcation and Chaos **27**: 1750104.

Kuo, A. D., 2007 The six determinants of gait and the inverted pendulum analogy: A dynamic walking perspective. Human Movement Science **26**: 617 – 656.

Li, T.-Y. and J. A. Yorke, 2004 Period three implies chaos. In *The theory of chaotic attractors*, pp. 77–84, Springer.

Makarenkov, O., 2020 Existence and stability of limit cycles in the model of a planar passive biped walking down a slope. Proceedings of the Royal Society A: Mathematical, Physical and Engineering Sciences **476**: 20190450.

McGeer, T., 1990 Passive dynamic walking. International Journal of Robotics Research **9**: 62–82.

Meng, M. Q.-H. and R. Song, 2022 Legged mobile robots for challenging terrains. Biomimetic Intelligence and Robotics **2**: 100034.

Miladi, Y., A. Chemori, and M. Feki, 16-19 March 2015 The compass-like biped robot revisited: Nonlinear control of the disturbed passive dynamic walking. In *2015 IEEE 12th International Multi-Conference on Systems, Signals Devices (SSD15)*, pp. 1–7, Mahdia, Tunisia.

Miladi, Y., N. Derbel, and M. Feki, 2021 Optimal control based on multiple models approach of chaotic switched systems, application to a stepper motor. International Journal of Automation and Control **15**: 240–258.

Montazeri Moghadam, S., M. Sadeghi Talarposhti, A. Niaty, F. Towhidkhah, and S. Jafari, 2018 The simple chaotic model of passive dynamic walking. Nonlinear Dynamics **93**: 1183–1199.

Nourian Zavareh, M., F. Nazarimehr, K. Rajagopal, and S. Jafari, 2018 Hidden attractor in a passive motion model of compass-gait robot. International Journal of Bifurcation and Chaos **28**: 1850171.

Ott, E., C. Grebogi, and J. A. Yorke, 1990 Controlling chaos. Physical review letters **64**: 1196–1199.

Reher, J. and A. D. Ames, 2021 Dynamic walking: Toward agile and efficient bipedal robots. Annual Review of Control, Robotics, and Autonomous Systems **4**: 535–572.

Sambas, A., S. Vaidyanathan, M. Mamat, W. Sanjaya, and D. S. Rahayu, 2016 A 3-d novel jerk chaotic system and its application in secure communication system and mobile robot navigation. In *Advances and applications in Chaotic systems*, pp. 283–310, Springer.

Sprott, J., 2020 Do we need more chaos examples? Chaos Theory

and Applications **2**: 49 – 51.
Vaidyanathan, S., M. Feki, A. Sambas, and C.-H. Lien, 2018 A new biological snap oscillator: its modelling, analysis, simulations and circuit design. International Journal of Simulation and Process Modelling **13**: 419–432.
Vaidyanathan, S., A. Sambas, M. Mamat, and W. M. Sanjaya, 2017 A new three-dimensional chaotic system with a hidden attractor, circuit design and application in wireless mobile robot. Archives of Control Sciences **27**: 541–554.
Volos, C., A. Akgul, V.-T. Pham, I. Stouboulos, and I. Kyprianidis, 2017 A simple chaotic circuit with a hyperbolic sine function and its use in a sound encryption scheme. Nonlinear Dynamics **89**: 1047–1061.
Volos, C. K., I. M. Kyprianidis, and I. N. Stouboulos, 2012 A chaotic path planning generator for autonomous mobile robots. Robotics and Autonomous Systems **60**: 651–656.
Volos, C. K., I. M. Kyprianidis, and I. N. Stouboulos, 2013 Experimental investigation on coverage performance of a chaotic autonomous mobile robot. Robotics and Autonomous Systems **61**: 1314–1322.
Walter, S., 2014 Poincaré on clocks in motion. Studies in History and Philosophy of Science Part B: Studies in History and Philosophy of Modern Physics **47**: 131–141.
Westervelt, E. R., J. W. Grizzle, C. Chevallereau, J.-H. Choi, and B. Morris, 2007 *Feedback control of dynamic bipedal robot locomotion*. Taylor & Francis/CRC, London.
Xiaoting, Y., Y. Liguo, and W. Zhouchao, 2022 Stability and hopf bifurcation analysis of a fractional-order leslie-gower prey-predator-parasite system with delay. Chaos Theory and Applications **4**: 71–81.
Xie, Y., B. Lou, A. Xie, and D. Zhang, 2020 A review: Robust locomotion for biped humanoid robots. Journal of Physics: Conference Series **1487**: 012048.
Yang, D. and J. Zhou, 2014 Connections among several chaos feedback control approaches and chaotic vibration control of mechanical systems. Communications in Nonlinear Science and Numerical Simulation **19**: 3954–3968.
Znegui, W., H. Gritli, and S. Belghith, 2020a Design of an explicit expression of the Poincaré map for the passive dynamic walking of the compass-gait biped model. Chaos, Solitons & Fractals **130**: 109436.
Znegui, W., H. Gritli, and S. Belghith, 2020b Stabilization of the passive walking dynamics of the compass-gait biped robot by developing the analytical expression of the controlled Poincaré map. Nonlinear Dynamics **101**: 1061–1091.
Znegui, W., H. Gritli, and S. Belghith, 2021 A new Poincaré map for analysis of complex walking behavior of the compass-gait biped robot. Applied Mathematical Modelling **94**: 534–557.
Öztürk, H., 2020 A novel chaos application to observe performance of asynchronous machine under chaotic load. Chaos Theory and Applications **2**: 90 – 97.

How to cite this article: Added, E., Gritli, H., and Belghith, S. Occurrence of Complex Behaviors in the Uncontrolled Passive Compass Biped Model. *Chaos Theory and Applications*, 4(4), 246-266, 2022.

CHAOS
Theory and Applications
in Applied Sciences and Engineering

e-ISSN: 2687-4539
RESEARCH ARTICLE
Vol.4 / No.4 / 2022 / pp.267-273
Special Issue (EDIESCA 2022)
https://doi.org/10.51537/chaos.1196851

The Wonder World of Complex Systems

J.L. Echenausía-Monroy *,[1], **J.R. Cuesta-García** *,[2] **and J. Pena Ramirez** *,[3]
*Applied Physics Division, Center for Scientific Research and Higher Education at Ensenada, CICESE. Carr. Ensenada-Tijuana 3918, Zona Playitas, Ensenada, 22860, B. C., México.

ABSTRACT

Complex systems pervade nature and form the core of many technological applications. An exciting feature of these systems is that they exhibit a wide range of temporal behaviors, ranging from collective motion, synchronization, pattern formation, and chaos, among others. This has not only caught the attention of scientists, but also the interest of a wider audience. Consequently, our goal in this work is to provide a simple but descriptive explanation of some concepts related to complex systems. Specifically, the reader embarks on a journey that begins in the 17th century with the discovery of synchronization by Dutch scientist Christiaan Huygens and ends in the chaotic world explored by meteorologist Edward Lorenz around 1963. The journey is filled with examples, including synchronized clocks and metronomes, electronic fireflies that flash harmoniously, and even a chaotic dress.

KEYWORDS

Complex systems
Synchronization
Chaos
Emergent behavior
Collective behavior
Chaotic dynamics

INTRODUCTION

The term *complex system* is increasingly used nowadays. It is is used for describing phenomena ranging from our daily lives to behaviors typical of the scientific field, and has implications for social sciences, anthropology, mathematics, and biology, to name a few (Ottino 2003; Larsen-Freeman and Cameron 2008). This interdisciplinary field of science aims to study, characterize, and understand complex systems, their interactions, physical/biological effects, and the mechanisms that produce their particular behaviors (Huerta-Cuéllar *et al.* 2022).

It is relatively easy to identify a complex system using climate as an example, but it is somewhat more complex to clearly define the concept itself. This is because this definition changes depending on the field of application and adapts to the research subject's own needs. For example, in computer science, a complex system may refer to the computational time required by the processor to estimate the solution, while in biology it may refer to the interactions between different species in a wild area.

Although different definitions can be found in the literature, complex systems have in common the fact that they consist of various interconnected, interdependent, adaptive, and temporally changing actors whose interactions lead to emergent phenomena (Ladyman *et al.* 2013). In general, we can define a complex system as an organized and inseparable entity that consists of different interconnected parts and, considered as a whole, exhibits properties and behaviors that do not result from the sum of the individual parts or behaviors of any of its elements.

In other words, it is possible to know each of the agents that are part of a Complex System (CS), as well as their independent dynamics, but since they are interconnected and interact with each other, behaviors arise that are not very obvious based on individual knowledge of each element. Because of this peculiarity, complex systems are studied as living entities where it is necessary to consider all the elements and interactions that make them up. Let us take as an example the flight of a bird compared to the flight of a flock (Wang and Lu 2019). We can study individually the behavior of a bird and the mechanisms it needs to take to the skies.

We are able to understand the mechanics of wing flapping, the dynamics of the airflow that allows it to fly, the density and distribution of its feathers, and the limitations of the bird when flying at higher altitudes or speeds. Knowing all this about a single bird, one cannot predict (without prior knowledge) that a flock of birds (of the same species) will behave in such a way and form the flight patterns necessary to fly long distances or to protect the young from predators. This lack of answers in extrapolating data is the prerequisite for studying complex systems as living entities, and it is the behavior that arises from the interactions between them that we call emergent behavior, i.e., it is impossible to obtain

Manuscript received: 31 October 2022,
Revised: 14 December 2022,
Accepted: 23 December 2022.

[1]echenausia@cicese.mx (**Corresponding author**)
[2]jcuesta@cicese.mx
[3]jpena@cicese.mx

said result by studying and interacting only one of the entities that make up the CS.

Once the concept of complex system is defined, realize that they are present in many of the phenomena that surround us, that we are a part of them, and that this type of behavior exists in our bodies. Classic examples of complex systems can be found in something as mundane as the behavior of climate, which is one of the most studied complex systems. The behavior of stocks and all currencies, or the dynamics of planets and galaxies are examples of complex systems. The brain behavior and the transmission of information by neurons are examples of CS's which takes place in our bodies. The transmission of electrical energy, traffic in the air and on land are also clear examples of complex systems.

Note that in each of these examples it is possible to know the behavior of the individual elements that compose the CS, but we cannot estimate their behavior on the basis of individual dynamics. Take the example of land traffic in a city: it is possible to know the number of vehicles, the layout of roads and their traffic direction, the position of stop signs and traffic lights. But even with all this information and knowledge of the individual elements, it is impossible to predict the exact location and timing of a traffic jam. To understand the complex traffic system, one must study it as a living entity.

The rest of the article deals with two of the most common behaviors in complex systems: Synchronization and Chaos. Equations and proofs are deliberately omitted, and the text focuses on describing and explaining the main ideas about these behaviors. These are in turn illustrated with everyday references and illustrated with videos of simple experiments that the reader can consult on the Internet. The last part of the paper draws some preliminary conclusions.

SYNCHRONIZATION

In our time we speak more and more often of synchronization. We speak of synchrony between a user's cell phone, his TV and his computer. We also speak of synchronization in sports, for example synchronized swimming or rowing, and even in electronic transfers with dynamic keys linked to the cell phone number. Although the meaning of synchronization yields something obvious and commonplace, it can be defined as the coincidence in time of two or more events resulting from the interaction between two dynamic entities, which can be of almost any kind and nature. This makes synchronization an omnipresent behavior that can be found everywhere. The occurrence of synchronized behavior is very common in nature, with examples in biology, ecology, climatology, sociology, technology, and even art (Pikovsky *et al.* 2003; Strogatz 2004; Osipov *et al.* 2007).

To show how widespread this exciting phenomenon is, let us consider the universe, and in particular the Moon, which orbits our planet. The Moon spins on its own axis (rotation) at the same speed it spins around the Earth (translation), in other words, the Moon's rotation and translation speeds are synchronized. Because of this timing, we always see the same side of the moon. This behavior is also found in the animal kingdom. Have you ever observed birds flying in a "V" formation and flapping their wings at the same time? This allows them to use less energy and travel greater distances. Another example of synchronization in animals is a school of fish. A school is a group of synchronized fish that all move at the same speed and in the same direction as their nearest neighbors. Fish join together in schools for two main reasons: to protect themselves and to migrate. Just like birds that migrate or cyclists that group together, fish move in sync to move faster and expend less energy, which helps them survive.

People also synchronize, for example, the members of an orchestra playing in perfect synchronicity. A ballet performing a routine in time to the music, and even at the Olympic Games synchronization is present. There is also a symphony of synchronized rhythms in our bodies. For example, each beat of our heart is controlled by thousands of pacemaker cells that send out electrical impulses that stimulate the heart cells and cause them to contract or relax in a perfectly synchronized rhythm.

The first precursor in literature dealing with the concept of synchronization is the work of the extraordinary Dutch scientist Christiaan Huygens, mathematician, physicist and inventor of the pendulum clock (Pena Ramirez and Nijmeijer 2020). In 1665, Huygens noticed that two pendulum clocks suspended side by side from a crossbeam showed a kind of sympathy, that is, the pendulums of each clock swung at the same frequency, and when disturbed, they returned to the same rate of oscillation after about thirty minutes. In his writings Huygens points out that the main reason for this fact is the connection between the clocks, the crossbar being the said means of communication. Figure 1 shows the original hand drawing made by Huygens. It shows two pendulum clocks suspended from a wooden rod supported by two chairs.

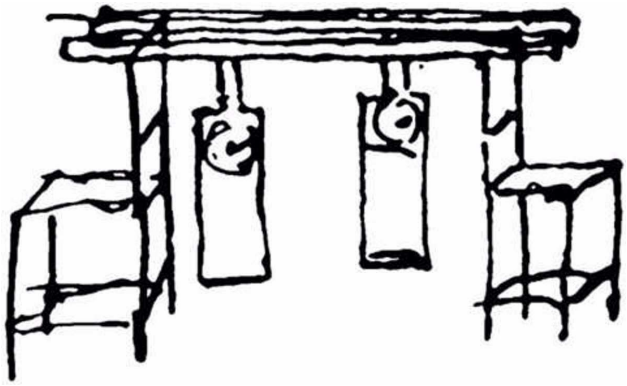

Figure 1 Synchronization scheme developed by Huygens for two pendulum clocks

To demonstrate in a simple way the synchronization between two inanimate objects, and inspired by the same Huygens experiment, we consider three monumental pendulum clocks (they are known as monumental clocks because this type of mechanism is used in towers, churches, obelisks and other monuments) (Pena Ramirez *et al.* 2016). Two of them are connected by a simple wooden rod, while the third has no connection with the other two, see Figure 2 and (Echenausía-Monroy 2022g). Some time after the clocks are set in motion, the two connected mechanisms synchronize, their pendulums working at the same time and in the same direction, while the third clock is free and never follows the rhythm or time of the two synchronized clocks. This illustrates three important points:

- *Synchronization is ubiquitous and can be found in living and inanimate systems;*
- *For synchronization you need at least two systems, agents, complex systems or dynamic units to be synchronized;*
- *For the phenomenon to appear, there must be a means of communication: physical, optical, acoustic, gravitational, electronic, etc.*

Regardless of the size of the object, synchronization is possible. Now consider metronomes, variable frequency pendulum

Figure 2 Modern version of the Huygens experiment, synchronizing two monumental clocks. Note that the means of communication between the two clocks is the orange wooden stick.

clocks that help music students keep time. These metronomes are mounted on a suspended floor structure, with the base free to move depending on the tension of the struts supporting it. When the metronomes are put into operation, they transmit their motion to the base on which they stand, which starts moving according to the number of metronomes. After a certain time, the base transmits this movement back to the metronomes and serves as a means of communication (coupling), giving the metronomes a synchronized response, see Figure 3 and (Echenausía-Monroy 2022c).

Figure 3 Hanging platform with synchronized metronomes (Echenausía-Monroy 2022c).

This phenomenon is similar to that observed when crossing a suspension bridge, where the movement of the pedestrians causes the bridge itself to vibrate so that it sways in the direction of travel, or to the phenomenon observed at the inauguration of the Millennium Bridge in London (2000), where the bridge swayed to the same extent as the pedestrians due to the lightness of the tensioners and the large number of visitors.

As with the size transition between monumental clocks and metronomes, it is possible to reduce the number of clocks and the size of the base to achieve a synchronous response. Now consider three metronomes on a 50 cm board standing on two cans of iced tea. If the clocks operate according to the scheme described, synchronization will occur between the metronomes as they transfer their motion to the table, causing the cans to move slightly and act in place of the struts. After a short time, this transfer of motion will cause the metronomes to operate at the same time and in the same direction. The experimental setup is shown in Figure 4, and the operation can be found in (Echenausía-Monroy 2022i).

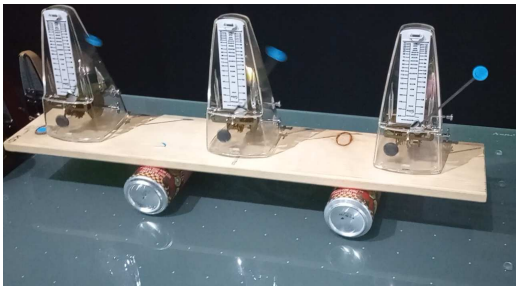

Figure 4 Experimental set-up to synchronize 3 metronomes.

As mentioned earlier, synchronization is not an unknown phenomenon in the animal kingdom; take fireflies, for example. These small insects, which are capable of biologically producing light (bioluminescence), are one of the many examples where synchronization occurs in animals (Buck and Buck 1976). During the breeding season, fireflies migrate to specific forested regions that meet certain climatic conditions. Once there, the males, like males of almost all species, try to attract the attention of females, in this case by the brightness and rhythm of their light. As expected, there is not just one male and one female, but hundreds of them, which leads to the males "seeing" each other. The fact that they see the light of the other male fireflies causes them to synchronize the rhythm of their blinking.

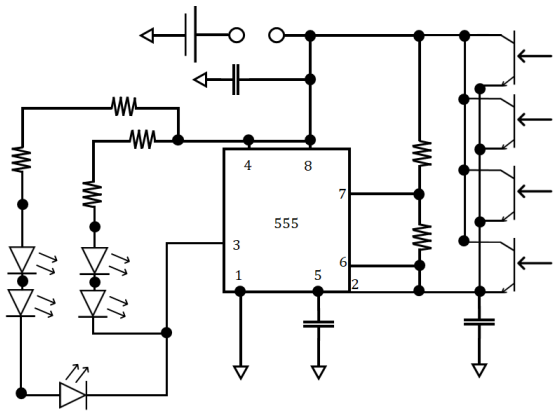

Figure 5 Electronic design of a firefly that can synchronize in four directions.

Using the electronic circuit shown in Figure 5, cf. (Arellano-Delgado *et al.* 2015), it is possible to electronically reproduce the behavior of a firefly. And in turn, it is possible to mimic the synchronization of these insects without having to enter their reproductive habitats. So these are friendly and didactic devices with which we show that synchronization is ubiquitous and that the type of communication between systems does not matter, as long as there is one, synchronization will emerge. In Figure 6 you can see the electronic firefly, and in (Echenausía-Monroy 2022h) you can see its operation in a beehive.

Figure 6 Electronic firefly that can synchronize in four directions. The picture shows the circuit without components and the final version.

It should be noted that in the above examples, the systems completely synchronize: the pendulums of the monumental clocks oscillate in harmony, moving in the same direction and with the same amplitudes; the electronic fireflies fire in unison, i.e., at the same frequency and with the same intensity, and also, the triplet of metronomes keep a rhythmic behavior such that their pendulums move with the same amplitude, frequency, and phase. However, many other types of synchronous motion can also be observed, like for example, the pendulum clocks moving at the same frequency but in opposite direction, a phenomenon called anti-phase synchronization, the electronic fireflies flashing at the unison but with different light intensities, which is referred to as frequency synchronization, and in the triplet of metronomes, they can produce a synchronized rotating wave: the metronomes oscillate a the same frequency and amplitude, but the pendulums of the metronomes have a phase difference of 120 degrees between them (Martens *et al.* 2013; Goldsztein *et al.* 2021).

Finally, it is important to note that in all the experiments described above, we can formally explain the onset of spontaneous synchronization using mathematical tools such as Lyapunov stability theory, the master stability function approach, or perturbation methods such as Poincaré's method (Ramirez and Nijmeijer 2016).

CHAOS

In the wonder world of complex systems (Cuesta-García 2022; Echenausía-Monroy 2022j), we are mostly dealing with nonlinear systems. This means that the dynamics of these systems are described by equations of motion with nonlinear terms, such as multiplications between variables of the same system, powers with degree greater than two, special nonlinear functions such as trigonometric or Piece Wise Linear (PWL) functions, to name a few (Drazin and Drazin 1992; Echenausía-Monroy *et al.* 2020). This type of complex systems does not respond to the superposition principle, where the system response cannot be decomposed as the sum of two or more responses corresponding to the number of system variables. In this type of system, it is possible to find chaotic behaviors or chaotic dynamics.

When we speak of "chaos" in science, we do not refer to the Greek cosmological stories that point to what existed before the existence of everything "*before the gods and the elemental forces there was CHAOS*". Nor do we refer to the absence of rules or order. Colloquially, chaos is often confused with examples such as a teenager's messy room, the actions of an angry mob, the behavior of an elementary school class when the teacher is absent for more than three minutes, or the mental disaster left behind after failing to conquer a summer love.

Mathematical chaos, which is generated by deterministic equations, is bounded aperiodic behavior that cannot be predicted. Also, a particular feature of chaotic behavior, which in general tends to be of oscillatory nature, is a high sensitivity to initial conditions, i.e., for two arbitrarily close starting points, the distance between the generated trajectories will exponentially diverge in time, see e.g. (Sprott 2010; Devaney 2018). When we say it is aperiodic, it simply means that there is no recurrence pattern and it is not known when the event occurs. When we say it is sensitive to initial conditions, it means that a small change at the beginning can cause a very large change over time. The first person to discover chaos was the famous polymath Henry Poincaré when he was working on solving the three-body problem (Chenciner 2015). A cinematic allusion to chaos is found in the first Jurassic Park movie, where Dr. Ian Malcolm (played by Jeff Goldblum) explains that chaos is unpredictable, citing as an example the trajectory of two drops of water in the hand of a beautiful lady.

This unpredictable behavior is also known as the "butterfly effect," which also appears in pop culture in the movie of the same name (The Butterfly Effect, starring Ashton Kutcher). In this movie, the protagonist travels to his past and can change certain events. Changing a small event in his past causes very big changes in his future, which is the essence of the Butterfly Effect.

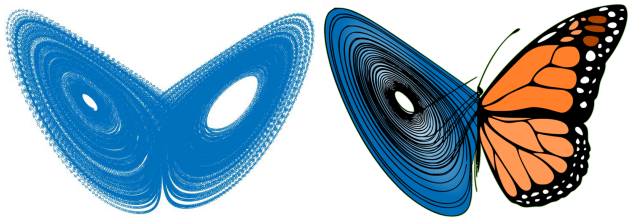

(a) (b)

Figure 7 (a) Numerically determined Lorenz attractor for $\sigma = 10$, $r = 28$, $b = 8/3$ and all initial conditions are set to one. (b) Analogy of the Lorenz butterfly with the attractor formed by the system of the same name.

Edward Lorenz, an American mathematician and meteorologist, discovered this behavior in 1963 when he studied and reduced a system of twelve differential equations that described climatological behavior (Lorenz 1963). Lorenz programmed these equations into a computer and analyzed the results, which were accurate to six decimal places. He then took a value that the computer had already provided as a system solution and set it as the initial value so that the computer could "get on" with the simulation. After running the simulation again, Lorenz made himself a cup of coffee. When he returned, he hoped that the graphs he received were the same or very similar to the original ones. To his surprise, the results seemed to match at first, but after a while they diverged and no longer matched. Thus Lorenz proved sensitivity to initial conditions, and the analogy to the butterfly effect was born, summed up in Lorenz's maxim: "Does the flap of a butterfly's wings in Brazil set off a tornado in Texas?". The mathematical model of the Lorenz system is described by the folowing set of equations

$$\begin{aligned} \dot{x} &= -\sigma(x+y), \\ \dot{y} &= x(r-z)-y, \\ \dot{z} &= xy-bz, \end{aligned} \tag{1}$$

which is derived from the simplified equations of convection rolls in the dynamical equations of the Earth's atmosphere (see (Lorenz 2000; Ambika 2015) and references therein for further information). The state variables (x, y, z) describe the behavior of the velocity and the direction of circulation of the convection rolls for state x, y is proportional to the temperature difference between the updrafts and downdrafts, and z is proportional to the deviation of the vertical temperature gradient from linearity. If the state variables of this system of equations are plotted on the $x - z$ plane, the result is a so-called attractor resembling the shape of a butterfly (Figure 7).

To easily introduce and demonstrate the concept of the butterfly effect, imagine a touch screen onto which a numerical simulation of the Lorenz attractor is projected. Since the butterfly effect is based on changing the initial conditions of the system, the simulation considers the touch point (on the touch screen) as the initial condition, so that when you repeatedly touch "the same point", you get different trajectories of the Lorenz system under different colors, which initially agree in their behavior, but diverge over time and follow completely different paths. Figure 8 shows an experiment based on the demonstration of the butterfly effect, the video of this experiment is available on (Echenausía-Monroy 2022f).

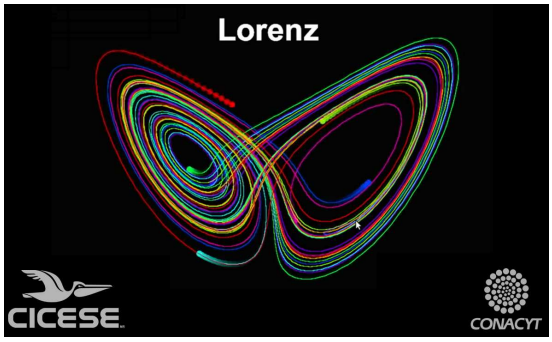

Figure 8 Experimental setup of the touchscreen to illustrate the butterfly effect of the Lorenz attractor.

Chaos is not only found in systems as complex as climate, but can also be observed in relatively simple models. Consider the behavior of a pendulum, like that of a wall clock, which behaves in a completely predictable, periodic, and monotonic manner; it always moves from left to right as long as the clock has a battery. Now, if the pendulum is disconnected from the clock, it will only move from left to right for a certain amount of time until it loses its energy and stops moving. If you attach another pendulum to the end of the system, you get a double pendulum. Since you know the behavior of a simple pendulum, you can assume that the new system will behave similarly to the first one. Surprisingly, the double pendulum follows unpredictable paths that change depending on the starting point of the pendulum, i.e., it shows chaotic behavior.

To observe the behavior of a double pendulum, consider its construction attached to an ultraviolet light-sensitive screen with a UV LED at the bottom. This allows visualization of the trajectories of the system when the pendulum is started in very similar positions, and the effects of initial conditions. Figure 9 shows the trajectory of the photoluminescent double pendulum, and the video of the experiment in operation can be found at (Echenausía-Monroy 2022b).

Figure 9 Double pendulum working with UV led placed on the tip of the second join. The image was taken with ISO 125 and a shutter speed of 4 seconds.

Chaos is not a phenomenon unique to weather or mechanical systems; rather, it is a quantifiable property (see (Wolff 1992; Abraham *et al.* 2013) and the references therein). As mentioned earlier, it is a phenomenon that surrounds us and that we can take advantage of. Take, for example, the logistic map, described by Eq. (2):

$$x_{n+1} = r x_n (1 - x_n), \tag{2}$$

which is one of the most studied complex systems in discrete time and has been applied in studying the dynamics of population growth (see (May 2004) for more information). In 2003, Professor Kazuyuki Aihara, a professor emeritus at the University of Tokyo, found that the bifurcation diagram of the logistic map (the behavior over time when a parameter changes) has a shape that resembles the silhouette of a dress, as shown in Figure 10 (a). This result was presented at Tokyo Fashion Week later that year ((Bulletin 2019)) and gave us a new perspective on the applications of chaos in our lives. A version of Aihara's chaotic dress can be seen in Figure 10 (b). For a 360° view, see (Echenausía-Monroy 2022e).

It has already been mentioned that there are chaotic dynamics in our body, which include the behavior of neurons. An example of this is the Hindmarsh-Rose model (HR), which describes the behavior of a single neuron in terms of axion potentials and the sodium-calcium channels that activate them (see (Shilnikov and Kolomiets 2008; Barrio *et al.* 2017) for more information). Although this complex system describes the behavior of a neuron and its excitatory agents, it is possible to take this model as a basis and use it to improve daily life.

Imagine a homemade blender spinning at a certain speed in the same direction. If we give the same blender a chaotic behavior, that is, it spins randomly in one direction or another and for different periods of time, it is possible to obtain a much faster homogeneous shake. This is exactly what Ricardo Núñez, an experimentalist researched based at CICESE, did when he developed a chaotic stirrer based on the Chua system. His idea, like Lorenz's discovery, was based on the morning coffee in the office and the time it takes to dissolve the different ingredients we add to the invigorating drink. As a result, he obtained a stirrer that homogenizes solutions

(a) (b)

Figure 10 (a) Section of interest from the bifurcation diagram of the logistic map by varying parameter r in Eq. (2). (b) Dress based on the logistic map designed by the authors. The original dress presented by Prof. Ahihara can be found at (Bulletin 2019).

more efficiently and in less time than a conventional one, Figure 11. For a video of the chaotic mixer in action, see (Echenausía-Monroy 2022d), and for more information, see (Núñez-Pérez 2022).

(a)

(b)

Figure 11 Stirrers mixing honey in water. The periodic shaker is shown on the left and the shaker based on a chaotic system is shown on the right. (a) 4 seconds of shaking versus (b) 12 seconds (Núñez-Pérez 2022).

In the last section, we described examples of how chaos occurs in our environment, how we can observe it, and how it can even help us in our daily lives. But for those of us who explore this exciting area of mathematics and physics, chaos has a beauty all its own. Each of the behaviors and models described can be represented by systems of equations. These, in turn, can be observed geometrically through so-called "attractors" that can be interpreted as the face of any system. In these chaotic attractors the whole beauty of chaos is shown. For example, consider the work of the Swiss artist "*Chaotic Atmospheres*", who has projected in his portfolio various chaotic attractors as graphic works of art, which you can find at (Atmospheres 2022). With the same idea and using 3D printing, it is possible to turn a system of differential equations into something tangible and bring chaos to the real plane, as seen in Figure 12, where four 3D-printed chaotic attractors are shown. This is not only a clear example of the use of technology to provide new educational tools, but also serves to explain and teach complex concepts such as chaos to people with visual impairments. Printed attractors can be found at (Echenausía-Monroy 2022a).

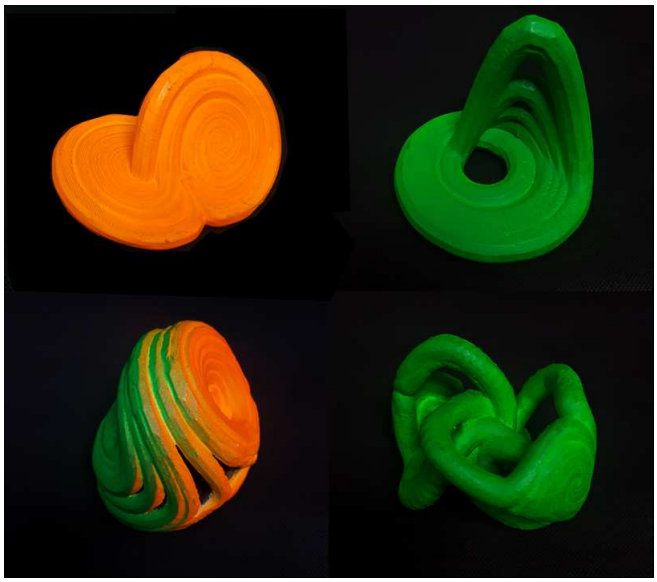

Figure 12 Chaotic attractors printted in 3D. (a) Lorenz, (b) Rössler, (c) Dequan Li, and (d) Thomas attractor.

Finally, it should be noted that the chaotic behavior discussed in this section and the phenomenon of synchronization presented in the previous section are two related concepts. Indeed, a pair or network of chaotic systems can synchronize provided they are suitably coupled, as shown in the pioneering work of Fujisaka and Yamada (Fujisaka and Yamada 1983).

CONCLUSION

It is our believe that the examples presented in this work may be useful for introducing concepts from complex systems like synchronization, emergent behavior and chaos, to non specialist and to further motivate the excitement for investigating these systems in the new generations.

Acknowledgments

This work was part of a museographic exhibition at "Caracol Museo de Ciencias" in Ensenada, Mexico. This work was supported by project "*Análisis, control y sincronización de sistemas complejos con interconexiones dinámicas y acoplamientos flexibles*" A1-S-26123, funded by CONACYT.

J.L.E.M. thanks CONACYT for financial support (CVU-706850, project: A1-S-26123). J.L.E.M. also thanks J.P.R. for the opportunity to complete a postdoctoral fellowship at CICESE.

Availability of data and material

Not applicable.

Conflicts of interest

The authors declare that there is no conflict of interest regarding the publication of this paper.

LITERATURE CITED

Abraham, N. B., A. M. Albano, A. Passamante, and P. E. Rapp, 2013 *Measures of complexity and chaos*, volume 208. Springer Science & Business Media.

Ambika, G., 2015 Ed lorenz: father of the 'butterfly effect'. Resonance **20**: 198–205.

Arellano-Delgado, A., C. Cruz-Hernández, R. López Gutiérrez, and C. Posadas-Castillo, 2015 Outer synchronization of simple firefly discrete models in coupled networks. Mathematical Problems in Engineering **2015**.

Atmospheres, C., 2022 Strange attractors: Visualisation of chaotic equations. https://chaoticatmospheres.com/mathrules-strange-attractors.

Barrio, R., S. Ibáñez, and L. Pérez, 2017 Hindmarsh–rose model: Close and far to the singular limit. Physics Letters A **381**: 597–603.

Buck, J. and E. Buck, 1976 Synchronous fireflies. Scientific American **234**: 74–85.

Bulletin, U.-T.-I., 2019 Fashionable mathematics. https://issuu.com/utokyo-iis/docs/utokyo-iis_bulletin_vol4/2?e=33831841/76398422.

Chenciner, A., 2015 Poincaré and the three-body problem. In *Henri Poincaré, 1912–2012*, pp. 51–149, Springer.

Cuesta-García, J. R., 2022 El maravilloso mundo de los sistemas complejos: web site. https://complexity-net.org/.

Devaney, R. L., 2018 *An introduction to chaotic dynamical systems*. CRC press.

Drazin, P. G. and P. D. Drazin, 1992 *Nonlinear systems*. Number 10, Cambridge University Press.

Echenausía-Monroy, J. L., 2022a The beauty of chaos. https://youtu.be/Uou-FS_eHjM.

Echenausía-Monroy, J. L., 2022b Chaos and the double pendulum. https://youtu.be/SoNFulHypJQ.

Echenausía-Monroy, J. L., 2022c Hanging platform to synchronize metronomes. https://youtu.be/R-IcZJg1Qlo.

Echenausía-Monroy, J. L., 2022d Improving the shaker with chaos. https://youtu.be/hLdpnUWPdjM.

Echenausía-Monroy, J. L., 2022e Logistics dress: Chaos in fashion. https://youtu.be/GTsJ4Kg14TU.

Echenausía-Monroy, J. L., 2022f Lorenz and the butterfly effect. https://youtu.be/uYQvuNjVjBM.

Echenausía-Monroy, J. L., 2022g Monumental clocks synchronized. https://youtu.be/eQn3kzP8HU0.

Echenausía-Monroy, J. L., 2022h Synchronized electronic fireflies. https://youtu.be/yDTQx0rLvik.

Echenausía-Monroy, J. L., 2022i Synchronized metronomes on ice tea cans. https://youtu.be/Ng1bhcEaD-k.

Echenausía-Monroy, J. L., 2022j The wonder world of complex systems. https://youtu.be/eX3oShdvKFM.

Echenausía-Monroy, J. L., J. H. García-López, R. Jaimes-Reátegui, and G. Huerta-Cuéllar, 2020 Parametric control for multiscroll generation: Electronic implementation and equilibrium analysis. Nonlinear Analysis: Hybrid Systems **38**: 100929.

Fujisaka, H. and T. Yamada, 1983 Stability theory of synchronized motion in coupled-oscillator systems. Progress of theoretical physics **69**: 32–47.

Goldsztein, G. H., A. N. Nadeau, and S. H. Strogatz, 2021 Synchronization of clocks and metronomes: A perturbation analysis based on multiple timescales. Chaos: An Interdisciplinary Journal of Nonlinear Science **31**: 023109.

Huerta-Cuéllar, G., E. Campos Cantón, and E. Tlelo-Cuautle, 2022 *Complex Systems and Their Application (2022)*. (Eds.) Springer Cham, Switzerland.

Ladyman, J., J. Lambert, and K. Wiesner, 2013 What is a complex system? European Journal for Philosophy of Science **3**: 33–67.

Larsen-Freeman, D. and L. Cameron, 2008 *Complex systems and applied linguistics*. Oxford University Press Oxford.

Lorenz, E., 2000 The butterfly effect. World Scientific Series on Nonlinear Science Series A **39**: 91–94.

Lorenz, E. N., 1963 Deterministic nonperiodic flow. Journal of Atmospheric Sciences **20**: 130–141.

Martens, E. A., S. Thutupalli, A. Fourriere, and O. Hallatschek, 2013 Chimera states in mechanical oscillator networks. Proceedings of the National Academy of Sciences **110**: 10563–10567.

May, R. M., 2004 Simple mathematical models with very complicated dynamics. In *The Theory of Chaotic Attractors*, pp. 85–93, Springer.

Núñez-Pérez, R. F., 2022 Prototipo de un nuevo mezclador electrónico pseudocaótico. Ingeniería, investigación y tecnología **23**.

Osipov, G. V., J. Kurths, and C. Zhou, 2007 *Synchronization in oscillatory networks*. Springer Science & Business Media.

Ottino, J. M., 2003 Complex systems. American Institute of Chemical Engineers. AIChE Journal **49**: 292.

Pena Ramirez, J. and H. Nijmeijer, 2020 The secret of the synchronized pendulums. Physics World **33**: 36.

Pena Ramirez, J., L. A. Olvera, H. Nijmeijer, and J. Alvarez, 2016 The sympathy of two pendulum clocks: beyond huygens' observations. Scientific reports **6**: 1–16.

Pikovsky, A., J. Kurths, M. Rosenblum, and J. Kurths, 2003 *Synchronization: a universal concept in nonlinear sciences*. Number 12, Cambridge university press.

Ramirez, J. and H. Nijmeijer, 2016 The poincaré method: A powerful tool for analyzing synchronization of coupled oscillators. Indagationes Mathematicae **27**: 1127–1146.

Shilnikov, A. and M. Kolomiets, 2008 Methods of the qualitative theory for the hindmarsh–rose model: A case study–a tutorial. International Journal of Bifurcation and Chaos **18**: 2141–2168.

Sprott, J. C., 2010 *Elegant chaos: algebraically simple chaotic flows*. World Scientific.

Strogatz, S., 2004 *Sync: The emerging science of spontaneous order*. Penguin UK.

Wang, X. and J. Lu, 2019 Collective behaviors through social interactions in bird flocks. IEEE Circuits and Systems Magazine **19**: 6–22.

Wolff, R. C., 1992 Local lyapunov exponents: looking closely at chaos. Journal of the Royal Statistical Society: Series B (Methodological) **54**: 353–371.

How to cite this article: Echenausía-Monroy, J. L., Cuesta-García, J. R., and Ramirez, J. P. The Wonder World of Complex Systems. *Chaos Theory and Applications*, 4(4), 267-273, 2022.

CHAOS
Theory and Applications
in Applied Sciences and Engineering

e-ISSN: 2687-4539
RESEARCH ARTICLE
Vol.4 / No.4 / 2022 / pp.274-284
Special Issue (EDIESCA 2022)
https://doi.org/10.51537/chaos.1214569

A Chaotification Model Based on Modulo Operator and Secant Functions for Enhancing Chaos

Nikolaos Charalampidis[*], **Christos Volos**[*], **Lazaros Moysis**[*,β] **and Ioannis Stouboulos**[*]

[*]Laboratory of Nonlinear Systems - Circuits & Complexity, Physics Department, Aristotle University of Thessaloniki, Thessaloniki, Greece, [β]Department of Mechanical Engineering, University of Western Macedonia, Kozani, Greece.

ABSTRACT Many drawbacks in chaos-based applications emerge from the chaotic maps' poor dynamic properties. To address this problem, in this paper a chaotification model based on modulo operator and secant functions to augment the dynamic properties of existing chaotic maps is proposed. It is demonstrated that by selecting appropriate parameters, the resulting map can achieve a higher Lyapunov exponent than its seed map. This chaotification method is applied to several well-known maps from the literature, and it produces increased chaotic behavior in all cases, as evidenced by their bifurcation and Lyapunov exponent diagrams. Furthermore, to illustrate that the proposed chaotification model can be considered in chaos-based encryption and related applications, a voice signal encryption process is considered, and different tests are being used with respect to attacks, like brute force, entropy, correlation, and histogram analysis.

KEYWORDS
Chaotic map
Chaotification
Secant functions
Modulo operator
Lyapunov exponent
Sound encryption
Fuzzy entropy

INTRODUCTION

Chaos theory, as a mathematical discipline aims to study the dynamic behavior of systems that are highly sensitive to the initial conditions and parameter values (Grassi 2021). Chaos can be found basically in almost all fields from natural and social sciences, to engineering, and medicine, even economics (Nagashima *et al.* 2019). As a result chaos theory has evolved to a large attraction for researchers, and the past decades is continuously being studied, due to a number of appealing characteristics such as randomness, and unpredictability, nonlinearity, and initial condition sensitivity, which over the years led to many interesting and varying applications. Examples of chaos applicability can be found in robotics (Petavratzis *et al.* 2022), weather forecast (Mammedov *et al.* 2022), pandemic crisis management (Borah *et al.* 2022), information security (Fadil *et al.* 2022), circuits (Xiu *et al.* 2022), and signal processing (Abd *et al.* 2022).

Generally in chaos-based applications, and in particular cryptography, better chaotic properties are imperative, since they imply enhanced performance or security. However, many classic chaotic maps like the logistic map and the sine map exhibit weaknesses. For instance, simple phase portraits which makes it easy to identify their equilibrium points. This allows potential attackers to predict the chaotic sequence and the parameter values just by analyzing the equilibrium points (Shahi *et al.* 2022; Wang *et al.* 2022). Another example is low chaos complexity, which in turn leads to degradation of the chaotic behavior (Liu *et al.* 2021). Furthermore, small regions of chaos also constitutes a weakness, since within an interval of the control parameter values, only a subset is admitted for use, leading to limited applicability of the chaotic map (Zeraoulia 2012). Consequently, achieving strong chaos with enhanced performance has the potential to vastly improve chaos theory research into the development of related applications.

In this direction, optimization methods to increase Lyapunov exponents of chaotic systems are developed, for example via differential evolution and particle swarm optimization algorithms (de la Fraga *et al.* 2012; Adeyemi *et al.* 2022). The reason for that is because the Lyapunov exponent measures the sensitivity of the initial conditions for a chaotic map to small changes (Bovy 2004). Additionally, since positive Lyapunov exponent values indicate chaos, the higher they are the more complex a chaotic system is regarded.

Furthermore, as of recent, there is a movement to develop families of chaotic systems, often called chaotification models (Moysis *et al.* 2022a), that holistically improve the chaotic behavior for any given existing chaotic map. To do so, the goal is to prove that a

Manuscript received: 5 December 2022,
Revised: 22 December 2022,
Accepted: 27 December 2022.

[1]nicharala@physics.auth.gr (**Corresponding author**)
[2]volos@physics.auth.gr
[3]lmousis@physics.auth.gr
[4]stouboulos@physics.auth.gr

chaotification model can achieve higher Lyapunov exponent values than the existing chaotic maps, and verify that with numerical experiments. Such examples are to combine any map with a cosine function (Natiq *et al.* 2019), a sine function (Hua *et al.* 2018), a sine and cosecant functions (Li *et al.* 2021), a cascade sine operation (Wu 2021), an internal perturbation model (Dong *et al.* 2021), a remainder operation addition (Moysis *et al.* 2022b), or the modulo operator, which has been shown to be effective in improving chaotic behavior (Ablay 2022; Zhang *et al.* 2022).

Influenced by this, a chaotification model based on the modulo operation and secant function to strengthen the complexity of existing chaotic maps is constructed. Its structure is comprised of the secant function, which influences directly the output of existing chaotic maps, acting as a chaotification agent, and the modulo operator, which limits the set of possible output values. To assess the model's performance, a theoretical analysis based on the Lyapunov exponent is conducted. Additionally, four one-dimensional chaotic maps acting as seed maps are applied to the model, leading to four new chaotic maps. The chaos complexity of these maps is then evaluated through common tools for studying the dynamical behavior of chaotic systems, namely phase, bifurcation, Lyapunov exponent diagrams, and the fuzzy entropy.

Moreover, to illustrate an application of the proposed chaotification model, a voice signal encryption technique is designed based on one of the new chaotic maps. This map is used to shuffle, and modulate the signal to obtain the ciphered signal. This voice signal encryption technique's security is validated and tested using a variety of tests and measures such as histogram, and key space and sensitivity analysis, approximate entropy, spectral distortion, log-likelihood, and signal to noise ratio.

The outline of the paper is as follows: Section 2 presents the proposed chaotification model, and the theoretical analysis of its performance. Section 3 introduces four new chaotic maps. In Section 4 the dynamics of the new maps is discussed. Section 5 considers the application of voice encryption. In Section 6 the encryption performance is discussed. Section 7 conclusions are presented, along with a suggestion for future research based on the shortcomings of the suggested model.

CHAOTIFICATION MODEL BASED ON MODULO OPERATOR AND SECANT FUNCTIONS

In this section is introduced the proposed chaotification model and are presented various examples of modified chaotic maps to illustrate the model's effectiveness.

Concept of the chaotification model

The proposed chaotification model uses a double nonlinear transformation based on the modulo operator and secant function to improve the chaotic properties and complexity of existing chaotic maps as shown in Fig. 1.

Consider the modulo operator $\mod(\cdot, N)$, and the secant function $sc(\cdot) = \frac{1}{\cos(\cdot)}$, then the chaotic system is of the following form:

$$x_{i+1} = mod(a \cdot sc(b \cdot F(x_i)), N) \tag{1}$$

where x_i is the input, $a, b \in \mathbb{R}^+$ are the system's parameters, $F(x_i)$ the existing chaotic maps, and $N \in \mathbb{N}^*$ the control parameter that limits the map's values in the interval $[0, N]$.

The following aspect primarily reflects the augmentation of the chaotic complexity of the resulting new maps. The chaotification model expands the chaotic range of one dimensional chaotic

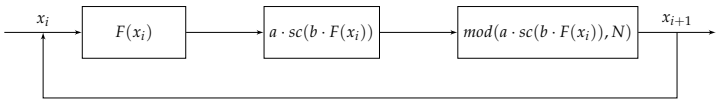

Figure 1 Structure of the chaotification model based on modulo operator and secant functions.

maps. Meaning that the modified maps have larger control parameter range than before. This will be confirmed theoretically and experimentally.

Lyapunov exponent analysis

One of the most well-known tools for studying the quantitative behavior of chaotic systems is the Lyapunov exponent. The Lyapunov exponent for a dynamical system of the form $x_{i+1} = f(x_i)$ is defined as follows:

$$\lambda = \lim_{n\to\infty} \frac{1}{n} \sum_{i=0}^{n-1} \ln \mid \dot{f}(x_i) \mid \tag{2}$$

When $\lambda > 0$ implies existence of chaos. Furthermore, a greater Lyapunov exponent is an indication of a more complex chaotic behavior.

By the definition of Lyapunov exponent a chaos complexity analysis of the proposed chaotification method can be derived. The derivative in Eq. (2) is known that is the slope of the tangent line at any given point $(x_i, f(x_i))$ of the chaotic system's curve. In addition, the modulo operator has an inherent property that allows it to translate a curve's part that is outside the phase space inside of it without alterations.

Therefore, without loss of generality, the modulo operator can be disregarded, and the chaotification model in (1) be regarded as

$$x_{i+1} = \mathcal{M}(x_i) = a \cdot sc(b \cdot F(x_i)). \tag{3}$$

Hence, the following theorem is proven.

Theorem 1. *The proposed map (1) achieves a higher Lyapunov exponent (LE) compared to its source map $F(x_i)$, for appropriate choice of parameters a, b.*

Proof. This proof is inspired by (Zhang *et al.* 2022; Li *et al.* 2021). Consider two initial conditions y_0 and x_0, where x_0 differs from y_0 by a small number $\epsilon > 0$. Then, after iterating once are obtained y_1 and x_1. Their difference is computed as follows,

$$\begin{aligned}
&|y_1 - x_1| = |\mathcal{M}(y_0) - \mathcal{M}(x_0)| \\
&= |a \cdot sc(b \cdot F(y_0)) - a \cdot sc(b \cdot F(x_0))| \\
&= \left| \left(\frac{a \cdot sc(b \cdot F(y_0)) - a \cdot sc(b \cdot F(x_0))}{F(y_0) - F(x_0)} \right) \left(\frac{F(y_0) - F(x_0)}{y_0 - x_0} \right) (y_0 - x_0) \right| \\
&= \left| \left(\frac{a \cdot sc(b \cdot F(y_0)) - a \cdot sc(b \cdot F(x_0))}{F(y_0) - F(x_0)} \right) \right| \left| \left(\frac{F(y_0) - F(x_0)}{y_0 - x_0} \right) \right| |y_0 - x_0|.
\end{aligned} \tag{4}$$

Because from hypothesis $y_0 \to x_0$, consequently $F(y_0) \to F(x_0)$, then

$$\lim_{y_0 \to x_0} \left| \left(\frac{F(y_0) - F(x_0)}{y_0 - x_0} \right) \right| \approx \frac{dF}{dx}|_{x_0}$$

$$\lim_{F(y_0) \to F(x_0)} \left| \left(\frac{a \cdot sc(b \cdot F(y_0)) - a \cdot sc(b \cdot F(x_0))}{F(y_0) - F(x_0)} \right) \right| \approx \frac{d\mathcal{M}}{dx}|_{F(x_0)}$$

Therefore,

$$|y_1 - x_1| \approx \left|\frac{d\mathcal{M}}{dx}|_{F(x_0)}\right| \left|\frac{dF}{dx}|_{x_0}\right| |y_0 - x_0|. \tag{5}$$

In similar way, after iterating for a second time y_2 and x_2 are obtained. Their difference is calculated as

$$\begin{aligned}
&|y_2 - x_2| = |\mathcal{M}(y_1) - \mathcal{M}(x_1)| \\
&= |a \cdot sc(b \cdot F(y_1)) - a \cdot sc(b \cdot F(x_1))| \\
&= \left|\left(\frac{a \cdot sc(b \cdot F(y_1)) - a \cdot sc(b \cdot F(x_1))}{F(y_1) - F(x_1)}\right)\left(\frac{F(y_1) - F(x_1)}{y_1 - x_1}\right)(y_1 - x_1)\right| \\
&= \left|\left(\frac{a \cdot sc(b \cdot F(y_1)) - a \cdot sc(b \cdot F(x_1))}{F(y_1) - F(x_1)}\right)\right| \left|\left(\frac{F(y_1) - F(x_1)}{y_1 - x_1}\right)\right| |y_1 - x_1| \\
&\approx \left|\frac{d\mathcal{M}}{dx}|_{F(x_1)}\right| \left|\frac{dF}{dx}|_{x_1}\right| \left|\frac{d\mathcal{M}}{dx}|_{F(x_0)}\right| \left|\frac{dF}{dx}|_{x_0}\right| |y_0 - x_0|.
\end{aligned} \tag{6}$$

After iterating for the n^{th} time and y_n and x_n are obtained, their difference can be computed as

$$\begin{aligned}
|y_n - x_n| &= |\mathcal{M}(x_{n-1}) - \mathcal{M}(x_{n-1})| \\
&\approx \prod_{i=0}^{n-1} \left|\frac{d\mathcal{M}}{dx}|_{F(x_i)} \frac{dF}{dx}|_{x_i}\right| |y_0 - x_0|.
\end{aligned} \tag{7}$$

The average divergence after n iterations will be denoted $\Delta_{\mathcal{M}}(x)$, and is calculated as follows:

$$\begin{aligned}
\Delta_{\mathcal{M}(x)} &= \left|\frac{y_n - x_n}{y_0 - x_0}\right|^{\frac{1}{n}} \\
&= \left(\prod_{i=0}^{n-1} \left|\frac{d\mathcal{M}}{dx}|_{F(x_i)} \frac{dF}{dx}|_{x_i}\right|\right)^{\frac{1}{n}}
\end{aligned} \tag{8}$$

Hence, from equation (2) the Lyapunov exponent of $\lambda_{\mathcal{M}(x)}$ can be obtained.

$$\begin{aligned}
\lambda_{\mathcal{M}(x)} &= \lim_{n\to\infty} \ln(\Delta_{\mathcal{M}(x)}) \\
&= \lim_{n\to\infty} \frac{1}{n} \ln\left(\prod_{i=0}^{n-1} \left|\frac{d\mathcal{M}}{dx}|_{F(x_i)} \frac{dF}{dx}|_{x_i}\right|\right) \\
&= \lim_{n\to\infty} \frac{1}{n} \sum_{i=0}^{n-1} \ln\left|\frac{d\mathcal{M}}{dx}|_{F(x_i)} \frac{dF}{dx}|_{x_i}\right| \\
&= \lim_{n\to\infty} \frac{1}{n} \sum_{i=0}^{n-1} \ln\left|\frac{ab\dot{F}(x_i)\sin(bF(x_i))}{\cos^2(bF(x_i))}\right| \\
&= \lim_{n\to\infty} \frac{1}{n} \sum_{i=0}^{n-1} \left(\ln|ab\dot{F}(x_i)\sin(bF(x_i))| - \ln\left|\cos^2(bF(x_i))\right|\right) \\
&= \lim_{n\to\infty} \frac{1}{n} \sum_{i=0}^{n-1} \left(\ln|ab\dot{F}(x_i)\sin(bF(x_i))|\right) \\
&\quad - \lim_{n\to\infty} \frac{1}{n} \sum_{i=0}^{n-1} \left(\ln\left|\cos^2(bF(x_i))\right|\right) \\
&= \lambda + \ln|a| + \lim_{n\to\infty} \frac{1}{n} \sum_{i=0}^{n-1} \left(\ln|b\sin(bF(x_i))|\right) \\
&\quad - \lim_{n\to\infty} \frac{1}{n} \sum_{i=0}^{n-1} \left(\ln\left|\cos^2(bF(x_i))\right|\right) \\
&= \lambda + \ln|\,a\,| + \lambda_{\mathcal{C}(x)} + \gamma
\end{aligned} \tag{9}$$

where

$$\lambda = \lim_{n\to\infty} \frac{1}{n} \sum_{i=0}^{n-1} \ln|\dot{F}(x_i)|,$$

$$\gamma = -\lim_{n\to\infty} \frac{1}{n} \sum_{i=0}^{n-1} \left(\ln\left|\cos^2(bF(x_i))\right|\right),$$

and

$$\lambda_{\mathcal{C}(x)} = \lim_{n\to\infty} \frac{1}{n} \sum_{i=0}^{n-1} \left(\ln|b\sin(bF(x_i))|\right)$$

Notice that since $0 \le \cos^2(b(F(x_i))) \le 1$ then $\gamma \ge 0$, and $\ln|a| > 0$ iff $a > 1$. Furthermore, it can be noticed that $\ln|b\sin(bF(x_i))| > 0$ iff $|b\sin(bF(x_i))| > 1$ as such $|b| > \frac{1}{|\sin(bF(x_i))|}$, and because $b \in \mathbb{R}^+$, $b > \frac{1}{|\sin(bF(x_i))|}$. Thus, $\lambda_{\mathcal{C}(x)} > 0$ if and only if, $b > \frac{1}{|\sin(bF(x_i))|}$. However, because b is depended on $F(x_i)$ it is very difficult to identify a particular set of values for b from this condition.

Similarly to (Li *et al.* 2021) in order to identify values for the parameter b such that $\lambda_{\mathcal{C}(x)} > 0$, design the chaotic map

$$x_{i+1} = -\cos(bx_i). \tag{10}$$

with corresponding Lyapunov exponent

$$\lim_{n\to\infty} \frac{1}{n} \sum_{i=0}^{n-1} \left(\ln|b\sin(bx_i)|\right)$$

According to the bifurcation and Lyapunov exponent diagram of Eq. (10) depicted in Fig. 2, the map exhibits chaotic behavior with respect to parameter b for a variety of values. For example, $b = 1$ or 20. Thus, it can be concluded that for the same value of parameter b, $\lambda_{\mathcal{C}(x)} > 0$.

Hence, the chaotic properties based on the above analysis can be summarized as follows:

1. When $\lambda > 0$ and $\lambda_{\mathcal{M}(x)} > \lambda > 0$. In this case, the generated new map shows chaos and has larger Lyapunov exponent than the seed map.

2. If $\lambda < 0$, and $\lambda > -(\lambda_{\mathcal{C}(x)} + \gamma + \ln|a|)$. In this case also the generated new map shows chaos.

3. When $\lambda < 0$, and $\lambda \le -(\lambda_{\mathcal{C}(x)} + \gamma + \ln|a|)$. Then the generated new map does not have chaotic behavior.

Hence, it has been proved that the proposed chaotification model can improve the complexity of the seed map and the modified map can obtain larger Lyapunov exponents.

EXAMPLES OF NEW CHAOTIC MAPS

To showcase our previous result, the logistic map, the sine map, the sine sine map, and the cosine logistic map are used as seeds, yielding four new chaotic maps of the form (1). It should be noted that all initial conditions are set $x_0 = 0.1$. Furthermore, the parameter b when directly multiplied with a seed map's control parameter is set $b = 1$, if not then b can take any positive real number under the condition that the value of b is within a chaotic region of the map $x_{i+1} = -\cos(bx_i)$.

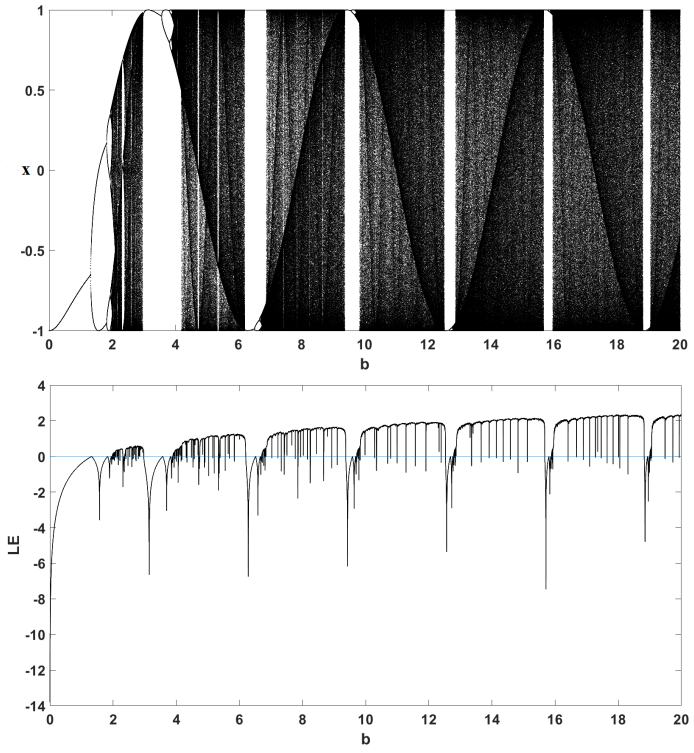

Figure 2 The bifurcation and Lyapunov exponent diagram of Eq. (10) with respect to b.

Modified logistic map

Consider the Logistic map $F(x_i) = rx_i(1 - x_i)$ as a seed map to Eq. (1), then the following map is obtained:

$$x_{i+1} = mod(a \cdot sc(brx_i(1 - x_i)), N) \tag{11}$$

Modified sine map

Let the Sine map $F(x_i) = \eta \sin(\pi x_i)$ be a seed map to Eq. (1), then the following map is obtained:

$$x_{i+1} = mod(a \cdot sc(b\eta \sin(\pi x_i)), N) \tag{12}$$

Modified sine sine map

If the Sine Sine map $F(x_i) = \sin(\pi\eta \sin(\pi x_i))$ is considered as a seed map to Eq. (1), then the following map is obtained:

$$x_{i+1} = mod(a \cdot sc(b \sin(\pi\eta \sin(\pi x_i))), N) \tag{13}$$

Modified cosine logistic map

Consider the Cosine Logistic map $F(x_i) = k \cos(rx_i(1 - x_i))$ as a seed map to Eq. (1), then a new modified map is obtained:

$$x_{i+1} = mod(a \cdot sc(bk \cos(rx_i(1 - x_i))), N) \tag{14}$$

PERFORMANCE EVALUATION

To evaluate the behavior of the new chaotic maps the following tools are used:

Phase diagrams

By projecting the inputs and outputs, phase diagrams can provide a qualitative portray of the behavior of chaotic maps. Irregularities in the phase diagram imply that the map's behavior is less predictable.

In Figs. 3, 4, 5, 6 the phase diagrams of the new chaotic maps and the phase diagrams of their corresponding seed maps are presented. It can be observed that while the shape of the seed maps' phase diagrams is distinguishable, the shape of the modified chaotic maps' phase diagram is indistinguishable. This means that the fixed points of the modified maps can not be obvious, contrary to the fixed points of the seed maps. As such, the task of predicting the parameters and states becomes considerably more difficult. Hence, the complexity of the new maps is higher.

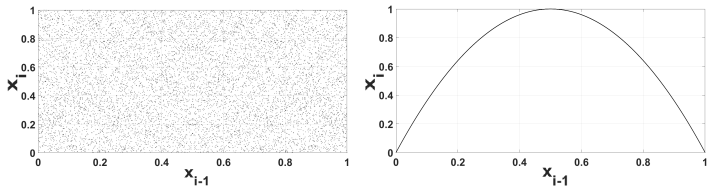

Figure 3 On the left the phase diagram of the modified Logistic map (11) is depicted, where $r = 4$, $a = 2 \cdot 10^6$, $b = 1$ and $N = 1$. On the right the phase diagram of the Logistic map, where $r = 4$.

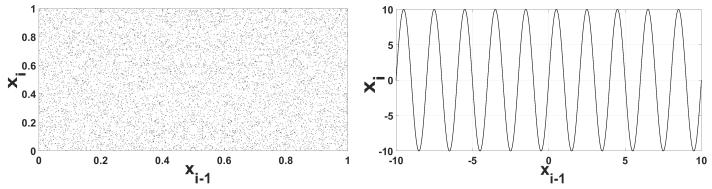

Figure 4 On the left the phase diagram of the modified sine map (12) is depicted, where $\eta = 10$, $a = 2 \cdot 10^6$, $b = 1$ and $N = 1$. On the right the phase diagram of the sine map, where $\eta = 10$.

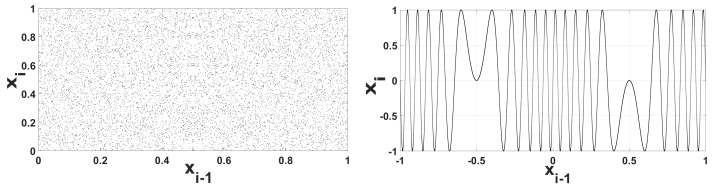

Figure 5 On the left the phase diagram of the modified sine sine map (13) is depicted, where $\eta = 10$, $a = 2 \cdot 10^6$, $b = 20$ and $N = 1$. On the right the phase diagram of the sine sine map, where $\eta = 10$.

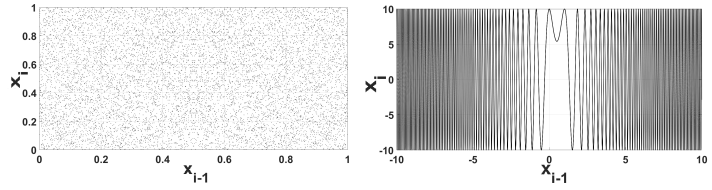

Figure 6 On the left the phase diagram of the modified cosine logistic map (14) is depicted, where $k = 10$, $a = 2 \cdot 10^6$, $b = 1$, $r = 4$ and $N = 1$. On the right the phase diagram of the cosine logistic map, where $k = 10$ and $r = 4$.

Bifurcation diagrams

By projecting the outputs with respect to the system's parameters, bifurcation diagrams shows the qualitative behavior of the system. Provides an insight on when, and the conditions under which the system enters or exits chaos.

From the comparison of the bifurcation diagrams in Figs. 7, 8, 9, 10 between the new maps and their classic counterparts, it can be seen that the enhanced maps exhibit larger regions of chaotic behavior, as well as the set of values is in the whole interval $[-1, 1]$. Therefore, it can be concluded that the modified maps exhibit more complicated behavior than their seed maps.

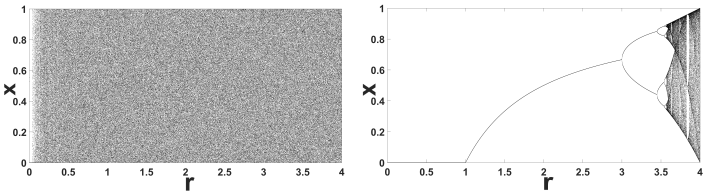

Figure 7 On the left the bifurcation diagram of the modified logistic map (11) with respect to r is depicted, where $a = 2 \cdot 10^6$, $b = 1$ and $N = 1$. On the right the bifurcation diagram of the Logistic map with respect to r.

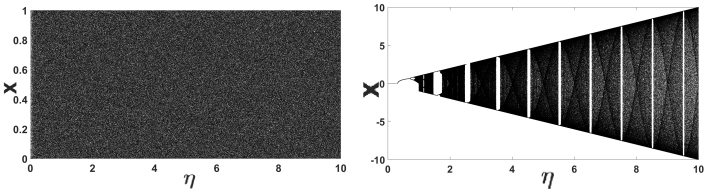

Figure 8 On the left the bifurcation diagram of the modified sine map (12) with respect to η is depicted, where $a = 2 \cdot 10^6$, $b = 1$ and $N = 1$. On the right the bifurcation diagram of the Sine map with respect to η.

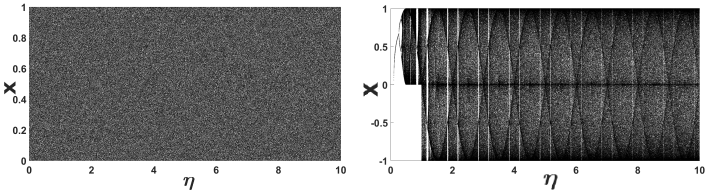

Figure 9 One the left the bifurcation diagram of the modified sine sine map (13) with respect to η is depicted, where $a = 2 \cdot 10^6$, $b = 20$ and $N = 1$. On the right the bifurcation diagram of the Sine Sine map with respect to η.

Lyapunov exponent diagrams

The Lyapunov exponent describes the average divergence of trajectories that begin from almost the same initial conditions. A positive Lyapunov exponent suggests that two neighboring trajectories in a dynamical system exponentially separate in each iteration, becoming different trajectories as time approaches infinity. As such, a positive Lyapunov exponent suggests chaos, and large Lyapunov exponent values indicate high complexity.

In Fig. 12, it can be seen that there exists a small region where the modified sine map (12) exhibits periodic behaviour. However, this is not visible to the corresponding bifurcation diagram

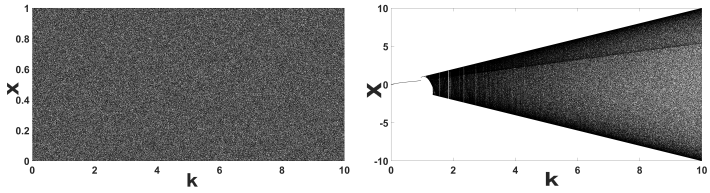

Figure 10 On the left the bifurcation diagram of the modified cosine logistic map (14) with respect to k is depicted, where $a = 2 \cdot 10^6$, $b = 1$, $r = 4$ and $N = 1$. On the right the bifurcation diagram of the cosine cogistic map with respect to k.

8, because the size of the region is much smaller than the overall interval in which the bifurcation diagram is plotted.

In addition, Figs. 11, 12, 13, 14 a comparison between the Lyapunov exponent diagrams of the modified chaotic maps and their original counterparts are presented. Immediately, from the high Lyapunov exponent values of the modified maps becomes apparent that they exhibit more complex behaviors than their seed maps.

Furthermore, from a first glance it seems that the modified maps mostly overcome chaos degradation, something very desirable in chaos based encryption. However, next it will be shown that this is not the case.

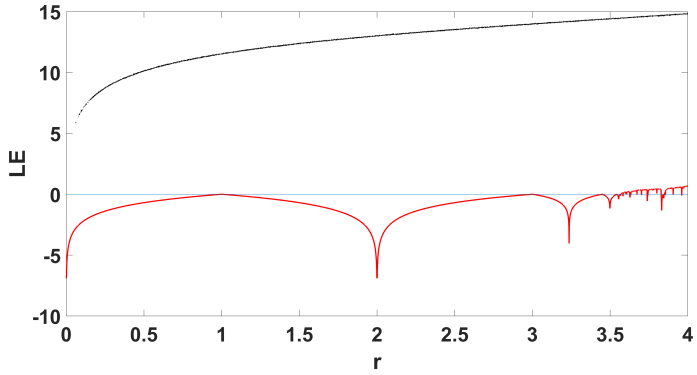

Figure 11 The Lyapunov exponent diagrams of the modified Logistic map (11) (black) and the Logistic map (red).

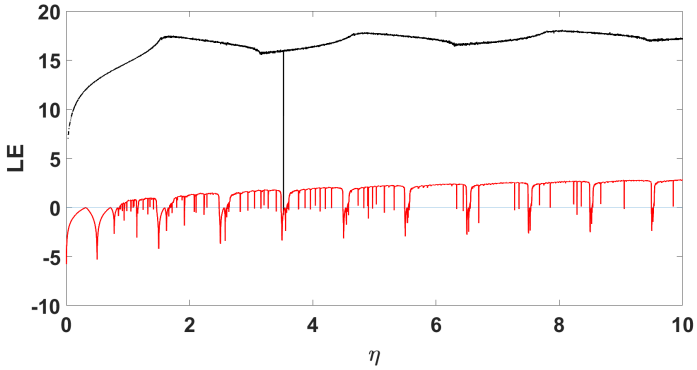

Figure 12 The Lyapunov exponent diagrams of the modified Sine map (12) (black) and the Sine map (red).

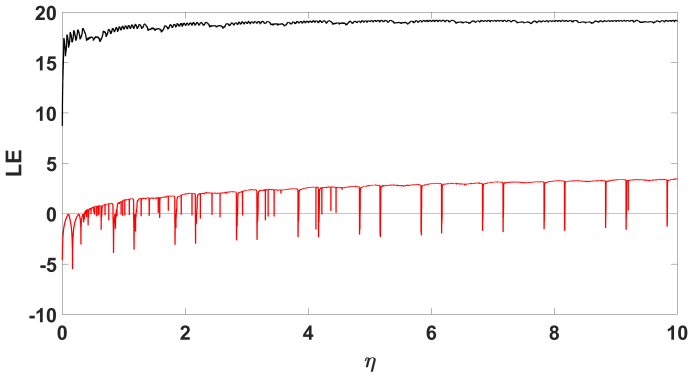

Figure 13 The Lyapunov exponent diagrams of the modified Sine Sine map (13) (black) and the Sine Sine map (red).

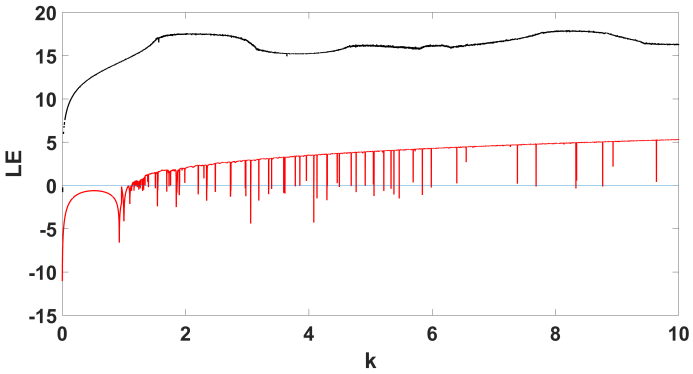

Figure 14 The Lyapunov exponent diagrams of the modified cosine logistic map (14) (black) and the cosine logistic map (red).

Fuzzy entropy

Like approximate, and sample entropy, fuzzy entropy is another measure to assess the complexity of a dynamical system based on fuzzy logic. High values of fuzzy entropy indicate high complexity. The reason for using fuzzy over sample entropy is because the complexity estimate is computed via the Gaussian function (Chen *et al.* 2009; Alawida *et al.* 2022; Dong *et al.* 2021),

$$\Theta(w_{i,j}^m, t) = \exp\{\frac{-(w_{i,j}^m)^2}{t}\} \tag{15}$$

where m is the embedding dimension which is set to 2, t is the tolerance value set to be $t = 0.15 * std(x)$, where $std(x)$ is the standard deviation of the time-series, and $w = \max_{(i,j)\in(0,m-1)} |x(i) - x(j)|$ the maximum distance between two sequences of length m.

In Figs. 15,17,19,21 a comparison of the fuzzy entropy values between the modified chaotic maps, and their classic counterparts is presented. It can be seen that the modified maps indeed display higher complexity than their counterparts. However, an undesirable effect in chaos cryptography that is not visible in the Lyapunov exponent diagrams depicted in Figs. 11, 12, 13, 14 becomes apparent, chaos degradation. This degradation in small periodic windows making it impossible to identify them in the bifurcation or Lyapunov exponent diagrams. Additionally, Fig. 17 verifies the periodic behavior of the modified sine map (12) presented in Fig. 12.

Furthermore, to investigate further these small periodic windows, and better understand the systems' behavior, the fuzzy entropy values were computed with respect to two parameters of the modified maps depicted in Figs. 16, 18, 20, 22. Again these diagrams verify that the modified chaotic maps exhibit a more complex behavior than their counterparts. However, the periodic windows, due to their size are not clearly visible in the diagrams.

Hence, despite the higher complexity of the new maps, a challenging problem is to modify the proposed chaotification technique in such way that chaos degradation is limited or absent.

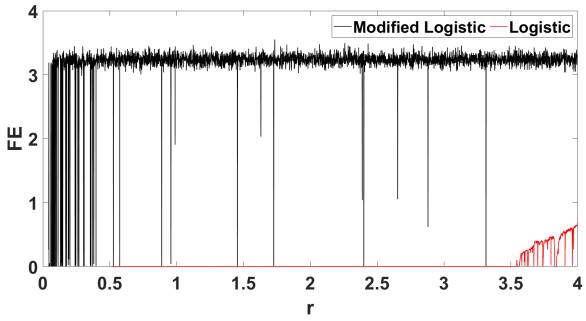

Figure 15 Fuzzy entropy comparison between the modified logistic map (11) with $a = 2 \cdot 10^6$, $b = 1$ and $x_0 = 0.1$, and the classic logistic map.

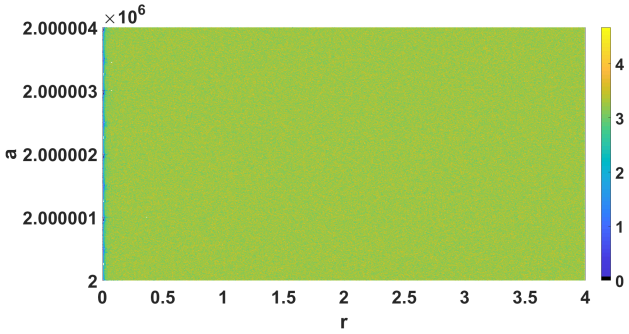

Figure 16 Fuzzy entropy of the modified logistic map (11) with respect to two parameters r, a with initial conditions $x_0 = 0.1$ and $b = 1$.

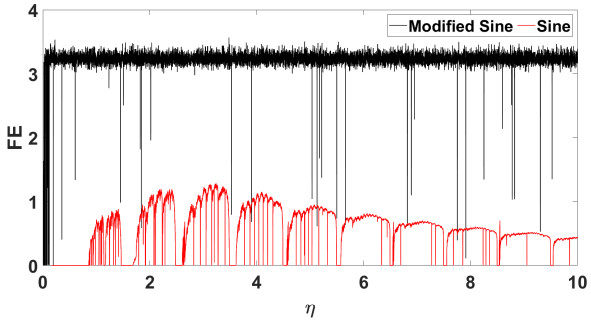

Figure 17 Fuzzy entropy comparison between the modified sine map (12) with $a = 2 \cdot 10^6$, $b = 1$ and $x_0 = 0.1$, and the classic sine map.

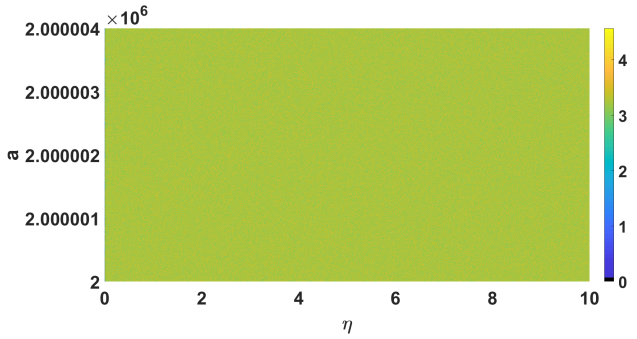

Figure 18 Fuzzy entropy of the modified sine map (12) with respect to two parameters η, a with initial conditions $x_0 = 0.1$ and $b = 1$.

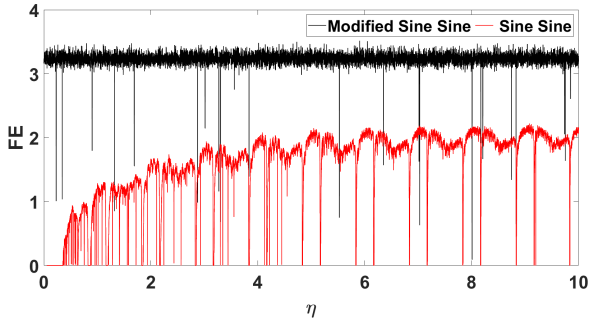

Figure 19 Fuzzy entropy comparison between the modified sine sine map (13) with $a = 2 \cdot 10^6$, $b = 20$ and $x_0 = 0.1$, and the classic sine sine map.

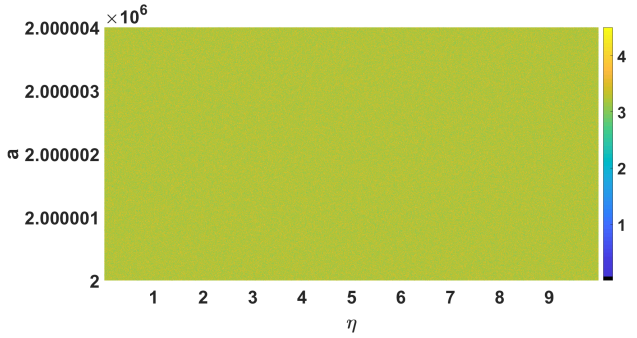

Figure 20 Fuzzy entropy of the modified sine sine map (13) with respect to two parameters η, a with initial conditions $x_0 = 0.1$ and $b = 20$.

ENCRYPTION OF SOUND SIGNAL

In this section the encryption of a sound signal is presented. The encryption consists of two parts, a sample shuffling, and a modulation of the source signal. The simulated signals are depicted in Fig. 23. As a source signal was used the poem *Three Things* by *Ella Wheeler Wilcox*. It can be downloaded by archive.org.

Step 1: A permutation to the source signal is performed. To do that consider two chaotic sequences of the form (11) with parameters (x_0, a_x, b_x, r_x) and (y_0, a_y, b_y, r_y) of same length as the samples of the source signal n. Consider also a sequence $z = \text{mod}\ (x + y, 1)$ with length n. Then, consider a vector $\mathcal{P}$ of length n, that takes its values in the interval $[1, n]$, applying the following

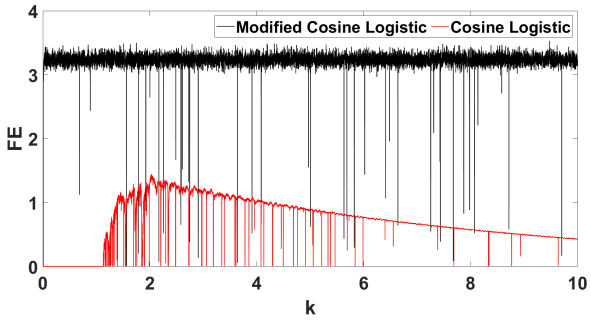

Figure 21 Fuzzy entropy comparison between the modified cosine logistic map (14) with $a = 2 \cdot 10^6$, $b = 1$, $r = 4$ and $x_0 = 0.1$, and the cosine logistic map with $r = 4$.

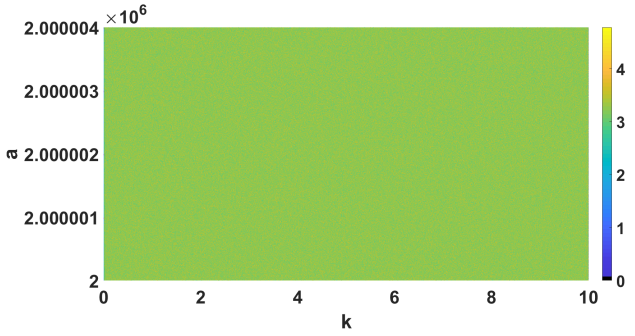

Figure 22 Fuzzy entropy of the modified cosine logistic map (14) with respect to two parameters k, a with initial conditions $x_0 = 0.1$ and parameter values $r = 4$ and $b = 1$.

rule, $p_i = \lceil \text{ mod } (10^{12} z_i, n) \rceil$ for $i = 1, \ldots, n$, where $\lceil \cdot \rceil$ is the ceiling operator. If $p_i = p_j$ for $i, j = 1, \ldots, n$, then p_j is rejected until all locations in the vector are unique. Then $\mathcal{P}$ provides the permutation order of the source signal. For example, let $p_1 = 200$, then the 1^{st} element of the source signal will move to the 200^{th} position. This is process is repeated until all elements in the source signal are repositioned and a new $\tilde{\mathcal{P}}$ signal is obtained.

Step 2: Then a modulation to the permuted signal is performed to obtain the final encrypted signal. To do that consider a chaotic sequence of any of the forms (11), (12), (13), (14) of length n. In this scenario it was chosen the chaotic map (11) with parameters (q_0, a_q, b_q, r_q). Finally, the encrypted signal is obtained by,

$$\mathcal{E} = \tilde{\mathcal{P}} + cos(\pi q).$$

Then the ciphered signal can be transmitted, and the receiver can reconstruct the original signal by solving

$$\tilde{\mathcal{P}} = \mathcal{E} - cos(\pi q)$$

and reversing step 1.

ENCRYPTION PERFORMANCE

A series of tests are run on the original, permuted, and encrypted signals to evaluate the performance of the encryption algorithm. Table 1 summarizes the results of the simulation performed in Matlab R2019a. The encryption key values are $x_0 = 0.2$, $y_0 = 0.8$, $q_0 = 0.1$, $a_x = 2 \cdot 10^6$, $a_y = 2 \cdot 10^6$, $a_q = 2 \cdot 10^6$, $b_x = 1$, $b_y = 1$, $b_q = 1$, $r_x = 3$, $r_y = 4$, $r_q = 5$.

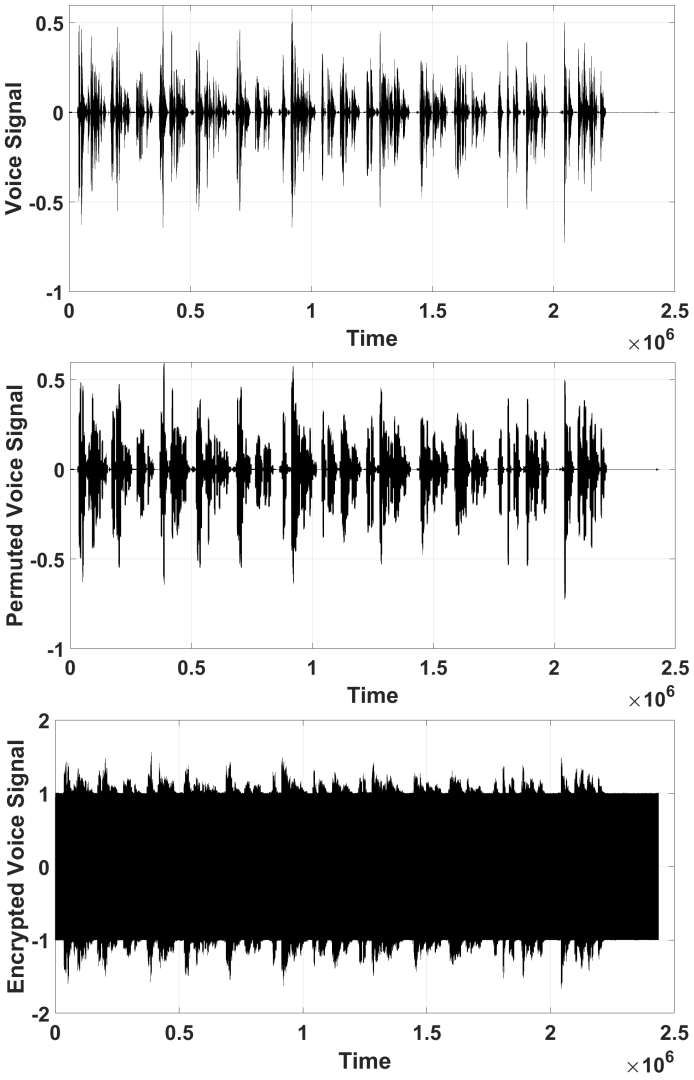

Figure 23 Original voice signal, permuted signal, and encrypted signal.

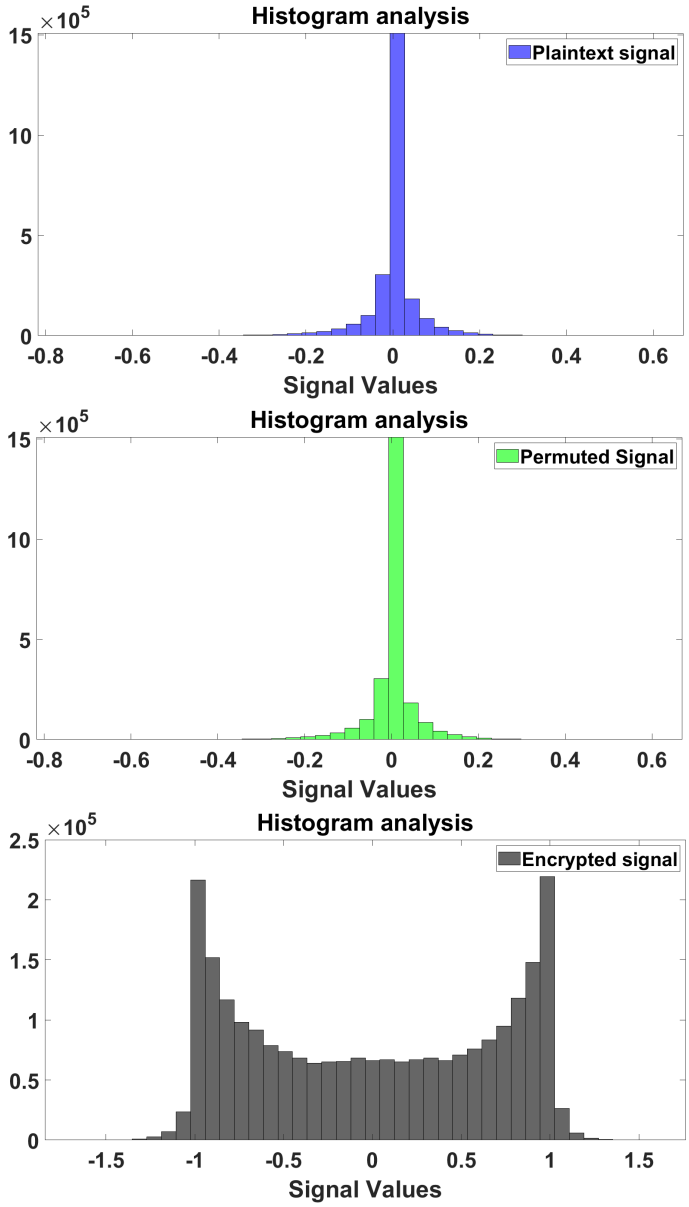

Figure 24 Histograms of the Original, Permuted, and Encrypted Signal.

Histogram

The original, permuted, and encrypted signal histograms are depicted in Fig. 24. As it can be observed contrary to the normal-like distributions of the original and permuted histograms, the encrypted signal exhibits a more complex histogram. As such, the hidden information is successfully masked. It should be noted that the original and permuted histograms are alike, since the values of the original signal were not altered but only shuffled.

Structural Similarity Index

The structural similarity (Algarni *et al.* 2021) between two signals is computed by,

$$SSIM = \frac{(2\mu_x\mu_y + S_1)(2cov(x,y) + S_2)}{(\mu_x^2 + \mu_y^2 + S_1)(var^2x + var^2y + S_2)} \tag{16}$$

where μ_x, μ_y the mean of the original and encrypted (or permuted) signals respectively, $varx$, $vary$ their variances, and $cov(x,y)$ their cross-covariance. It should be noted that S_1, S_2 are set to small values, in order to ensure stable results when the denominator is close to zero.

The structural similarity index value is in the interval $[-1,1]$, with 1 implying matched signals, and 0 when the signals have no similarity. Therefore, if the value is closing to zero, then the encryption is better. The structural similarity index between the original and the permuted signal is equal to 0.1253, and between the original and the encrypted signal is equal to 0.0019. Hence, since these values are close to zero, it can be concluded that the encryption is good.

Log-Likelihood Ratio

The Log-Likelihood Ratio estimates the encryption reliability (Elshamy *et al.* 2015). It assumes the segment can be depicted by a pth order all-pole linear predictive coding model,

$$x_i = \sum_{m=1}^{p} a_m x_{i-m} + G_x u_i \tag{17}$$

where x_i is the i^{th} signal sample, $a_m,\ m = 1, ..., p$ the coefficients of the all-pole filter, G_x is the filter gain, and u_i is an appropriate signal excitation input. Then the Log-Likelihood Ration is given by,

$$LLR = \left| \log \left(\frac{\mathbf{a}_x \mathbf{R}_y \mathbf{a}_x^T}{\mathbf{a}_y \mathbf{R}_z \mathbf{a}_y^T} \right) \right| \tag{18}$$

where $\mathbf{a}_x,\ \mathbf{a}_y$ the vectors of the Linear Prediction Coefficients of the form $[1\ a_1\ a_2\ \dots\ a_m]$ of the original signal, and the encrypted, or permuted signal respectively, and $\mathbf{R}_y$ the autocorrelation matrix of the encrypted or permuted signal. High Log-Likelihood Ratio values suggest a successful encryption. In order to short the computational time because the original signal is comprised by about 2.4 million samples, the original and encrypted (or permuted) signals were split to several segments, then the Log-Likelihood Ratio was computed as the mean value of the Log-Likelihood Ratio values of those segments. As such, the Log-Likelihood Ratio among the original and permuted signals is computed 2.5940 with variance 1.3347 and standard deviation 1.1553. Between the original and encrypted signals the Log-Likelihood Ration is 2.5930 with variance 1.3419 and standard deviation 1.1584. Since the values are both high, it can be concluded that the encryption is successful.

Signal to Noise Ration

The signal-to-noise ratio is another metric used to assess the quality of an encryption (Mosa *et al.* 2011). The signal-to-noise ratio is given by,

$$SNR = 10 \log_{10} \frac{\sum_{i=1}^{N} x_i^2}{\sum_{i=1}^{N} (x_i - y_i)^2} \tag{19}$$

where x, y are the original and encrypted (or permuted, decrypted) signals respectively. High positive signal-to-noise ratio value indicate strong relation between the two signals, while low negative signal-to-noise ratio value imply mismatch between the signals. The signal-to-noise ratio among the original and the decrypted signals is 306.8672. Therefore, indicating that the decryption is successful. The signal-to-noise ratio between the original and permuted signals is -3.0148, and among the original and encrypted signals is -21.6418. Hence, also from this measure it can be deduced that the encryption is good.

Correlation Coefficient

The correlation coefficient (Renza *et al.* 2019; Algarni *et al.* 2021) among two signals is given by,

$$r_{xy} = \frac{cov(x, y)}{\sqrt{var(x)}\sqrt{var(y)}} \tag{20}$$

where $cov(x, y)$ is the covariance of the two signals and $var(x), var(y)$ their variances. The correlation coefficient takes its values in the interval $[0, 1]$. When the value is close to zero means that the two signals are uncorrelated. The correlation coefficient between the original and the permuted signal is -0.0010, between the original and the encrypted signal is -0.00047, in both of these cases is implied uncorrelated signals, while the correlation coefficient between the original and the decrypted signal is 1, and that is because they are identical, as it should.

Spectral Distortion

The spectral distortion is the measure to quantify the mismatch between two signals (Renza *et al.* 2019). Therefore, spectral distortion can be used to compare the original sound with the permuted, encrypted, and the decrypted sounds. It is given by,

$$SD = \frac{1}{N} \sum_{i=0}^{N-1} |V_{x,i} - V_{y,i}| \tag{21}$$

where $V_{x,i}, V_{y,i}$ are the spectrum of the signals in decibels at any given point in time i. When the spectral distortion value is high, a higher difference between the two signals is implied, and when the spectral distortion value is equal to zero the two signals are matched. As such, large values of spectral distortion are indicative of a good encryption, and zero or close to zero value implies successful decryption. The spectral distortion among the original and permuted signals is 29.3021, between the original and encrypted signals is 36.7113, and among the original and decrypted signals is $3.7596 \cdot 10^{-12} \approx 0$. Hence, it can be deduced that the encryption is good as well that the decryption is successful.

Approximate Entropy

The approximate entropy proposed in (Pincus 1991) provides an indication for the complexity of a time series. The higher the approximate entropy of a time series, the more complex it is considered (Liu *et al.* 2021). As a result, the approximate entropy value of the encrypted signal must be greater than that of the original. The approximate entropy of the original signal is 0.6235, 1.9402 after the permutation is performed, and 1.9696 for the encrypted one, indicating that the encrypted signal has the highest approximate entropy. It should be noted that the original, permuted, and encrypted signals were divided into several sub-signals for computational reasons, and their approximate entropy is computed as the mean approximate entropy of those sub-signals. The variance for each signal is 0.2453, 0.0561, and 0.0011, and the standard deviation is 0.4953, 0.2369, and 0.0342 respectively.

Key space and Sensitivity

Every encryption system must be robust to brute force attacks. This requires that the key space be higher than 2^{100} (Alvarez and Li 2006). Three chaotic maps (11) are used in the proposed encryption system, with parameters (x_0, a_x, b_x, r_x), (y_0, a_y, b_y, r_y) and (q_0, a_q, b_q, r_q), given that for this map the parameter b is set to be always 1. As a result, the system has 9 parameters. For a precision of 16 digits, the upper bound for the key space is computed as $10^{9 \cdot 16} = 10^{144} = (10^3)^{48} \approx (2^{10})^{48} = 2^{480}$. Note, that since the map (11) exhibits periodic windows in very small regions with respect to its control parameters the actual key space is less than 2^{480}. However, the requirement to resist brute force attacks is still met.

Moreover, since this encryption system is chaos-based, any minor change in the parameter values will result in a flawed decryption process. As a result, any encrypted signal can only be decrypted by the receiver only as long as the given keys are precisely known.

Table 1 Performance of the encryption scheme

Signals	Original Sound	Permuted Sound	Encrypted Sound	Decrypted Sound
Structural Similarity Index	-	0.1253	0.0019	1
Log-Likelihood Ratio	-	2.5940	2.5930	-
Signal Noise Ratio	-	−3.0148	−21.6418	306.8672
Correlation Coefficient	-	−0.0010	−0.00047	1
Spectral Distortion	0	29.3021	36.7113	$3.7596 \cdot 10^{-12}$
Approximate Entropy	0.6235	1.9402	1.9696	0.6235

CONCLUSION

In this work, a new chaotification method is proposed by using a double nonlinear transformation based on the modulo operator and secant function to enhance the chaotic behavior and complexity of existing chaotic maps. The theoretical analysis based on the Lyapunov exponent revealed that for a given seed map applied on the proposed chaotification model, the modified map can achieve higher Lyapunov exponent values than the original map. As a result, the proposed chaotification technique can enlarge the chaotic region of a one-dimensional chaotic map while also improving its dynamic properties. To validate this theoretical result, numerical experiments were applied using as seed maps, the logistic, sine, sine sine, and the cosine logistic maps, through well-known tools for studying the dynamical behavior of chaotic systems, namely the phase diagrams, bifurcation diagrams, Lyapunov exponent diagrams, and the fuzzy entropy. From these experiments it was shown that indeed the modified maps exhibit larger chaotic regions, higher lyapunov exponents, indistinguishable phase diagrams. Therefore, the chaotification technique improves the dynamic properties of the seed maps. However, the fuzzy entropy showed chaos degradation in the new maps which is in the form of small periodic windows. These periodic windows are not a desirable property, especially in chaos based encryption. As such, a modification of the chaotification technique must be considered. A possible modification which will be studied is as follows:

$$x_{i+1} = \mod\left(a \cdot \frac{1}{(b\cos(F(x_i)) + c)}, N\right)$$

where parameter c is small in order to guarantee consistent performance when the denominator is close to zero.

Moreover, to illustrate a practical application of the proposed chaotification model, a voice encryption scheme was designed. The system is based on a permutation, and a modulation process both derived by the modified logistic map 11. A variety of tests and measures were used to showcase that the resulting encrypted signal is both random and secure.

Furthermore, for future research the implementation of this proposed encryption scheme on digital hardware, such as ARM processors, FPGA, and microcontrollers will be considered. When it comes to digital implementation of chaos-based cryptography techniques, the problem of chaotic map reproducibility from one device to another arises. Given the nonlinear nature of the maps, computational accuracy is of the utmost importance. One round-off error in the least significant digits can lead to completely different trajectories throughout various devices even with exact initial conditions and control parameter values (Teh *et al.* 2020; Sayed *et al.* 2020). Therefore, the output replication problem across different devices becomes apparent. In addition, an investigation of the increased computational effort by the modulo operator and the secant function in comparison to the classic maps is of interest.

Finally, it is intended to extent our results to multidimensional chaotic maps, and construct new hyperchaotic systems.

Availability of data and material

Not applicable.

Conflicts of interest

The authors declare that there is no conflict of interest regarding the publication of this paper.

LITERATURE CITED

Abd, M. H., G. A. Al-Suhail, F. R. Tahir, A. M. Ali Ali, H. A. Abbood, *et al.*, 2022 Synchronization of monostatic radar using a time-delayed chaos-based fm waveform. Remote Sensing **14**: 1984.

Ablay, G., 2022 Lyapunov exponent enhancement in chaotic maps with uniform distribution modulo one transformation. Chaos Theory and Applications **4**: 45–58.

Adeyemi, V.-A., E. Tlelo-Cuautle, F.-J. Perez-Pinal, and J.-C. Nuñez-Perez, 2022 Optimizing the maximum lyapunov exponent of fractional order chaotic spherical system by evolutionary algorithms. Fractal and Fractional **6**: 448.

Alawida, M., J. S. Teh, A. Mehmood, A. Shoufan, *et al.*, 2022 A chaos-based block cipher based on an enhanced logistic map and simultaneous confusion-diffusion operations. Journal of King Saud University-Computer and Information Sciences .

Algarni, A. D., N. F. Soliman, H. A. Abdallah, A. El-Samie, and E. Fathi, 2021 Encryption of ecg signals for telemedicine applications. Multimedia Tools and Applications **80**: 10679–10703.

Alvarez, G. and S. Li, 2006 Some basic cryptographic requirements for chaos-based cryptosystems. International journal of bifurcation and chaos **16**: 2129–2151.

Borah, M., A. Gayan, J. S. Sharma, Y. Chen, Z. Wei, *et al.*, 2022 Is fractional-order chaos theory the new tool to model chaotic pandemics as covid-19? Nonlinear Dynamics pp. 1–29.

Bovy, J., 2004 Lyapunov exponents and strange attractors in discrete and continuous dynamical systems. Theoretica Phys. Project, Catholic Univ. Leuven, Flanders, Belgium, Tech. Rep **9**: 1–19.

Chen, W., J. Zhuang, W. Yu, and Z. Wang, 2009 Measuring complexity using fuzzyen, apen, and sampen. Medical engineering & physics **31**: 61–68.

de la Fraga, L. G., E. Tlelo-Cuautle, V. Carbajal-Gómez, and J. Munoz-Pacheco, 2012 On maximizing positive lyapunov exponents in a chaotic oscillator with heuristics. Revista mexicana de física **58**: 274–281.

Dong, C., K. Rajagopal, S. He, S. Jafari, and K. Sun, 2021 Chaotification of sine-series maps based on the internal perturbation model. Results in Physics **31**: 105010.

Elshamy, E. M., E.-S. M. El-Rabaie, O. S. Faragallah, O. A. Elshakankiry, A. El-Samie, *et al.*, 2015 Efficient audio cryptosystem based on chaotic maps and double random phase encoding. International Journal of Speech Technology **18**: 619–631.

Fadil, E., A. Abass, and S. Tahhan, 2022 Secure wdm-free space optical communication system based optical chaotic. Optical and Quantum Electronics **54**: 1–14.

Grassi, G., 2021 Chaos in the real world: Recent applications to communications, computing, distributed sensing, robotic motion, bio-impedance modelling and encryption systems. Symmetry **13**: 2151.

Hua, Z., B. Zhou, and Y. Zhou, 2018 Sine chaotification model for enhancing chaos and its hardware implementation. IEEE Transactions on Industrial Electronics **66**: 1273–1284.

Li, Y., X. He, and D. Xia, 2021 A chaotification model based on sine and cosecant functions for enhancing chaos. Modern Physics Letters B **35**: 2150258.

Liu, L., H. Xiang, and X. Li, 2021 A novel perturbation method to reduce the dynamical degradation of digital chaotic maps. Nonlinear Dynamics **103**: 1099–1115.

Mammedov, Y. D., E. U. Olugu, and G. A. Farah, 2022 Weather forecasting based on data-driven and physics-informed reservoir computing models. Environmental Science and Pollution Research **29**: 24131–24144.

Mosa, E., N. W. Messiha, O. Zahran, A. El-Samie, and E. Fathi, 2011 Chaotic encryption of speech signals. International Journal of Speech Technology **14**: 285–296.

Moysis, L., D. N. Butusov, A. Tutueva, V. Ostrovskii, I. Kafetzis, *et al.*, 2022a Introducing chaos and chaos based encryption applications to university students-case report of a seminar. In *2022 11th International Conference on Modern Circuits and Systems Technologies (MOCAST)*, pp. 1–6, IEEE.

Moysis, L., I. Kafetzis, M. S. Baptista, and C. Volos, 2022b Chaotification of one-dimensional maps based on remainder operator addition. Mathematics **10**: 2801.

Nagashima, H., Y. Baba, and M. Nakahara, 2019 *Introduction to chaos: physics and mathematics of chaotic phenomena*. CRC Press.

Natiq, H., S. Banerjee, and M. Said, 2019 Cosine chaotification technique to enhance chaos and complexity of discrete systems. The European Physical Journal Special Topics **228**: 185–194.

Petavratzis, E., C. Volos, L. Moysis, H. Nistazakis, A. Giakoumis, *et al.*, 2022 Experimental coverage performance of a chaotic autonomous mobile robot. In *2022 11th International Conference on Modern Circuits and Systems Technologies (MOCAST)*, pp. 1–4, IEEE.

Pincus, S. M., 1991 Approximate entropy as a measure of system complexity. Proceedings of the National Academy of Sciences **88**: 2297–2301.

Renza, D., S. Mendoza, *et al.*, 2019 High-uncertainty audio signal encryption based on the collatz conjecture. Journal of Information Security and Applications **46**: 62–69.

Sayed, W. S., A. G. Radwan, H. A. Fahmy, and A. El-Sedeek, 2020 Software and hardware implementation sensitivity of chaotic systems and impact on encryption applications. Circuits, Systems, and Signal Processing **39**: 5638–5655.

Shahi, S., F. H. Fenton, and E. M. Cherry, 2022 Prediction of chaotic time series using recurrent neural networks and reservoir computing techniques: A comparative study. Machine Learning with Applications **8**: 100300.

Teh, J. S., M. Alawida, and Y. C. Sii, 2020 Implementation and practical problems of chaos-based cryptography revisited. Journal of Information Security and Applications **50**: 102421.

Wang, B., J. Liu, M. O. Alassafi, F. E. Alsaadi, H. Jahanshahi, *et al.*, 2022 Intelligent parameter identification and prediction of variable time fractional derivative and application in a symmetric chaotic financial system. Chaos, Solitons & Fractals **154**: 111590.

Wu, Q., 2021 Cascade-sine chaotification model for producing chaos. Nonlinear Dynamics **106**: 2607–2620.

Xiu, C., J. Fang, and X. Ma, 2022 Design and circuit implementations of multimemristive hyperchaotic system. Chaos, Solitons & Fractals **161**: 112409.

Zeraoulia, E., 2012 *Robust chaos and its applications*, volume 79. World Scientific.

Zhang, Z., H. Zhu, P. Ban, Y. Wang, and L. Y. Y. Zhang, 2022 Buffeting chaotification model for enhancing chaos and its hardware implementation. IEEE Transactions on Industrial Electronics .

How to cite this article: Charalampidis, N., Volos, C., Moysis, L., and Stouboulos, I. A Chaotification Model Based on Modulo Operator and Secant Functions for Enhancing Chaos. *Chaos Theory and Applications*, 4(4), 274-284, 2022.